

# Interfacial engineering for competitive Dye-Sensitized Solar Cells production

Présentée le 21 mai 2021

Faculté des sciences de base  
Laboratoire des sciences photomoléculaires  
Programme doctoral en chimie et génie chimique

pour l'obtention du grade de Docteur ès Sciences

par

**Natalie FLORES DIAZ**

Acceptée sur proposition du jury

Prof. K. Sivula, président du jury  
Prof. U. A. Hagfeldt, Dr S. M. Zakeeruddin, directeurs de thèse  
Prof. P. Cameron, rapporteuse  
Prof. E. Gibson, rapporteuse  
Prof. M. K. Nazeeruddin, rapporteur

# Acknowledgements

I want to specially thank my home university, **Universidad de Costa Rica** (UCR), the “Oficina de Asuntos Internacionales y de Cooperación Externa” from UCR, and the “Red de Investigación en Eficiencia Energética y Energías Renovables” (**RIDER**) from UCR, for granting me with a full scholarship to complete my Ph.D. studies at **EPFL**.

I will be forever grateful for this unique opportunity.

The completion of this thesis would not have been possible without my supervisor Prof. Anders Hagfeldt. I want to thank him for always being kind and encouraging for my work and ideas, showing me that bad or unwanted results are always a constant in academic research. Still, perseverance must prevail and can lead to good and exciting findings.

I want to extend my kind gratitude to:

My co-supervisor, Prof. Shaik M. Zakeeruddin, for his support and corrections on manuscripts helped me improve my writing skills.

Prof. Marina Freitag for being a great mentor.

Yamileth Damazzio for her support with my scholarship during these past 4 years.

Heidi Francelet for her support and encouraging words during my Ph.D. at EPFL

Sandy Sánchez for being such a good advisor and working partner.

Yameng Ren for fruitful collaborations and conversations about DSSCs.

Nathalia Verissimo, for proof-reading my thesis and for being a great office mate.

Simone Hagfeldt, for proof-reading and especially for always having nice and cheerful words for me.

Olivier Ouellette for proof-reading part of my thesis.

Felix Eickermeyer for very productive discussions about EIS.

Nikolaos Vlachopoulos for helping me with electrochemical measurements.

Jovana Milic for her support and collaboration.

Jean-David Decoppet for always helping me in the lab.

Special thanks to Hui-Seon, Yasemin, Jessi, and Jeannette for making my first years an unforgettable time.

To all the LSPM and LPI friends and extended family, especially to Nathalia, Elsa, Algirdas, Emilija, Jun, Viktor, Felix, Olivier, Amelie, Lukas, Loï, Thomas, Vicky, Fanny, Kasia, Audi, Kazu, Anwar, Massaud and Ji-Youn.

Silvia for being there for me since the very beginning.

Laura for bringing some Costarrican warm to Lausanne.

Sandy and Ana for being there through bad and good, will be always grateful for your friendship.

Silvia and Thomas for always having a spot for me.

Felix and Sol for opening the doors of their lovely family to me.

My Lausanne friends, for making these years more than incredible, Eirini, Hazel, Andreas, Dora, Roger, Isinsu, Maria, Klaus, Sina, Javier, Alex, Jisoo, Jihyun, Nora, Alejandra, Luciano, Andrea, and Esteban, Elisa, Jimena, Allen, Tatiana, Carmer, Javier and Jimena&Pali from not so far away in Europe.

My aunt Emilia, for being one of my biggest supports during my European stay.

The Flores family for their support and encouragement.

My friends in Costa Rica, who were there for me through good and bad, Sofi, Su, Lay, Kari, Fo, Adri, Natalie, Jenny, Pri, Aima, Nela, Marco, Victor, Naty, Fabio, Michael, Jorge, Elías.

Last but not least, my family, Karla, David, Miriam, and Carlos. It was you who made me miss Costa Rica so much; it was you whom I thought about anytime I saw something new and exciting. Your support means the world to me, and I can't express enough how much I love you. Without your unconditional support from miles away and different time zones, I would not have made it.

Lausanne, le 14 Avril 2021

“A mis padres Miriam Díaz Segura y Carlos Flores Fallas, con cariño, les dedico otro triunfo”



# Abstract

Green energy production is crucial to reducing CO<sub>2</sub> emissions and reaching the Paris agreement goals. As society transitions to a circular economy, renewable energy technologies will play a crucial role in our energy decarbonization.

Dye-sensitized solar cells (DSSCs) can be designed in various colors and transparency for building-integrated photovoltaics (BIPV). They have gained a lot of attention owing to its remarkably high power conversion efficiency (PCE) under indoor lighting, with PCEs up to 34% under 1000 lux.

To improve the performance of DSSCs, different approaches to study and reduce the interfacial recombination of the electrons from the conduction band (CB) of the semiconductor to the electrolyte were implemented in this thesis. The studied methods lead to minimized power losses in the devices.

One of the approaches was the introduction of the radical AZADO (AZ<sup>+0</sup>) to an electrolyte with [Co(bpy)<sub>3</sub>]<sup>2+/3+</sup> to form the tandem electrolyte containing two redox species in the liquid electrolyte. DSSCs with tandem electrolytes showed increased open-circuit voltages (V<sub>OC</sub>) values of 1009 mV, while the one-mediator electrolytes showed lower performance. The V<sub>OC</sub> enhancement was determined to result from the higher redox potential of (AZ<sup>+0</sup>) and the slower electron recombination rate. Our findings demonstrate the advantages of tandem electrolytes and indicate that further work could improve the V<sub>OC</sub> and overall performance of DSSCs.

To decrease the solvent's volatility and increase the recombination resistance in cobalt-based electrolytes, we implemented the in-situ photopolymerization of a thiol-siloxane with an acrylate monomer, such as PEGMA and PEGDA, through a click thiol-ene reaction. The formed hyperbranched networks were denoted HB1 (thiol-siloxane and PEGMA) and HB2 (thiol-siloxane and PEGMA). Electrolytes containing 20% of HB1 and HB2 in the cobalt electrolyte retained the liquid electrolyte up to 98% of their initial weight until 150 °C. The highest performance was achieved using 10%(v/v) of HB1 with a V<sub>OC</sub> of 875 mV, short-circuit current (J<sub>SC</sub>) of 14.75 mAcm<sup>-2</sup>, and fill-factor (FF) of 0.66 for a PCE of 8.52% under AM1.5, comparable to a PCE of 9.36% for the cobalt reference electrolyte. An upward-shift in the CB of TiO<sub>2</sub> compared to the cobalt reference was observed for all the HB-electrolytes. In addition, they presented longer electron lifetimes than the Co<sup>3+/2+</sup> electrolyte, explaining the

higher  $V_{OC}$  values for the HB electrolytes. Electrical impedance spectroscopy (EIS) analysis showed that the HB polymers suppress the interfacial electron recombination and enhance the photovoltaic performance under low light intensity leading to a PCE of 23.19% under 1000 lux for devices containing 15% of HB1 compared to 20.37% for the Co-reference.

We then developed a new dye, R7, with a strong electron-donating PAH core and BPT2 as the central building block and a bulkier HF donor to decrease electron recombination at the interface  $TiO_2$ /electrolyte. We found that in the presence of a copper electrolyte, the dye R7 outperformed devices with the blue dye R6. EIS revealed that the bulky HF-donor introduction effectively suppressed the electron recombination between the  $TiO_2$  surface and the redox shuttle. Additionally, we employed a co-sensitized system of R7+Y123 to reach the outstanding parameters of  $J_{SC}$  of  $16.15\text{ mAcm}^{-2}$ ,  $V_{OC}$  of 1035 mV, FF of 0.76 to achieve a top PCE of 12.7%. To the best of our knowledge, this is the highest for copper-based DSSCs using a blue photosensitizer.

Lastly, we studied interfacial phenomena in DSSCs with carbon counter electrodes (CCEs) and copper-based electrolytes to determine the feasibility of the production of monolithic DSSCs with copper-based hole-transporting materials. We found that the electron transport in devices with CCEs to be in the same order of magnitude as those with PEDOT. However, the devices with CCEs presented a decrease of 2 orders of magnitude in the recombination resistance, resulting in decreased  $V_{OC}$  and  $J_{SC}$  and leading to a PCE of 17% compared to 24.5% for PEDOT devices under 1000 lux illumination.

## Keywords

Dye-sensitized solar cells, tandem redox electrolytes, aza-adamantane, hyperbranched polymers, photopolymerization, dye engineering, thiol-ene reaction, Hagfeldt donor, R7, carbon counter electrodes, monolithic structure.

# Résumé

La production d'énergie verte est essentielle pour réduire les émissions de CO<sub>2</sub> et atteindre les objectifs de l'accord de Paris. Avec la transition vers une économie circulaire, les technologies des énergies renouvelables joueront un rôle crucial dans notre décarbonation énergétique.

Les cellules solaires à colorant, ou DSSC, sont considérées comme une technologie émergente prometteuse. Elles peuvent être conçues dans différentes couleurs et transparences pour le photovoltaïque intégré au bâtiment (BIPV). En raison de leur efficacité de conversion de puissance (PCE) remarquablement élevée sous éclairage intérieur, atteignant 34% sous 1000 lux, elles ont attiré beaucoup d'attention auprès des chercheurs et du public.

Pour améliorer les performances des DSSC, nous avons mis en œuvre différentes approches pour étudier et réduire la recombinaison interfaciale des électrons de la bande de conduction du semi-conducteur à l'électrolyte. Nos méthodes permettent de minimiser les pertes de puissance dans les cellules solaires.

L'une des approches consiste en l'introduction du radical AZADO (AZ<sup>+•/0</sup>) dans un électrolyte avec [Co(bpy)<sub>3</sub>]<sup>2+/3+</sup> pour former l'électrolyte en tandem contenant deux espèces redox dans l'électrolyte liquide. Les DSSC avec des électrolytes en tandem ont montré des valeurs de V<sub>OC</sub> accrues jusqu'à 1009 mV, tandis que les électrolytes à médiateur unique ont montré des performances inférieures. L'amélioration des V<sub>OC</sub> a été déterminée comme résultant du potentiel redox plus élevé du médiateur (AZ<sup>+•/0</sup>) et du taux de recombinaison électronique réduit. Nos résultats démontrent les avantages des électrolytes en tandem et indiquent que des travaux supplémentaires pourraient améliorer le V<sub>OC</sub> et la performance globale des DSSC.

Pour diminuer la volatilité du solvant et augmenter la résistance à la recombinaison dans les électrolytes à base de cobalt, nous avons mis en œuvre la photopolymérisation in-situ d'un thiol-siloxane avec un monomère acrylate, tel que PEGMA et PEGDA, via une réaction click thiol-ène. Les réseaux hyper-ramifiés formés sont notés HB1 (thiol-siloxane et PEGMA) et HB2 (thiol-siloxane et PEGDA). Les électrolytes contenant 20% de HB1 et HB2 dans l'électrolyte au [Co(bpy)<sub>3</sub>]<sup>2+/3</sup> ont conservé l'électrolyte liquide jusqu'à 98% de leur poids initial jusqu'à une température de 150 ° C. Les performances les plus élevées ont été obtenues en utilisant 10% (v/v) de HB1, per-

mettant d'atteindre un  $V_{OC}$  de 875 mV, un  $J_{SC}$  de 14.75  $\text{mAcm}^{-2}$  et un FF de 0,66 pour un PCE de 8,52% sous AM1.5, comparable à un PCE de 9.36 % pour l'électrolyte de référence au cobalt. Un déplacement vers le haut de la bande de conduction (CB) du  $\text{TiO}_2$  par rapport à la référence de cobalt a été observé pour tous les électrolytes HB. En outre, ils ont présenté des durées de vie des électrons plus longues que l'électrolyte au Co, expliquant les valeurs de  $V_{OC}$  plus élevées pour les électrolytes HB. L'analyse EIS a montré que les polymères HB suppriment la recombinaison électronique interfaciale et améliorent les performances photovoltaïques sous faible intensité lumineuse, conduisant à un PCE de 23,19% sous 1000 lux pour les dispositifs contenant 15% de HB1 contre 20,37% pour la co-référence.

Nous avons également développé un nouveau colorant, nommé R7, constitué d'un noyau de PAH donneur d'électrons fort et de BPT2 comme bloc de construction central ainsi qu'un donneur HF plus volumineux pour diminuer la recombinaison d'électrons à l'interface  $\text{TiO}_2$ /électrolyte. Nous avons constaté qu'en présence d'un électrolyte de cuivre, le colorant R7 surpassait les cellules solaires utilisant R6. L'EIS a révélé que l'introduction du donneur volumineux HF supprimait efficacement la recombinaison électronique entre la surface de  $\text{TiO}_2$  et la navette redox. De plus, nous avons utilisé un système co-sensibilisé de R7+Y123 pour atteindre les paramètres exceptionnels de  $J_{SC}$  de 16.15  $\text{mAcm}^{-2}$ ,  $V_{OC}$  de 1035 mV, FF de 0.76, menant à un PCE supérieur de 12.7%. À notre connaissance, il s'agit de l'efficacité la plus élevée pour les DSSC à base de cuivre utilisant un photosensibilisateur bleu.

Finalement, nous avons étudié les phénomènes interfaciaux en DSSC avec des contre-électrodes en carbone (CCE) et des électrolytes à base de cuivre pour déterminer la faisabilité de la production de DSSC monolithiques avec les matériaux de transport de trous à base de cuivre. Nous avons constaté que le transport d'électrons dans les cellules avec CCE était du même ordre de grandeur que pour ceux avec PEDOT. Cependant, les appareils avec CCE ont présenté une diminution de 2 ordres de grandeur de la résistance à la recombinaison, entraînant une diminution des  $V_{OC}$  et  $J_{SC}$  et menant à un PCE de 17%, comparé à 24.5% pour les cellules basées au PEDOT sous 1000 lux d'éclairage.

## Mots-clés

Cellules solaires sensibilisées aux colorants, électrolytes redox en tandem, aza-adamantane, polymères hyper-ramifiés, photopolymérisation, technique des colorants, réaction thiol-ène, donneur Hagfeldt, R7, contre-électrode en carbone, structure monolithique

# Abbreviations

PV	Photovoltaic devices
PCE	Power conversion efficiency
CIGS	CuInGaS
OPV	Organic photovoltaics
QDSSC	Quantum Dots Solar Cells,
ETA	Extremely Absorbent Cells
DSSC	Dye-Sensitized Solar Cells,
PSC	Perovskite Solar Cells
HOMO	Highest occupied molecular orbital
LUMO	Lowest unoccupied molecular orbital
CB	Conduction band
CE	Counter electrode
WE	Working electrode
TCO	Transparent conductive oxide
FTO	Fluorine doped tin oxide F:SnO <sub>2</sub>
PEDOT	Poly (3,4-ethylenedioxythiophene)
GNP	Graphene nanoplatelets
AM 1.5G	Air mass, standard lighting conditions
V <sub>oc</sub>	Open circuit voltage
PCE	Power conversion efficiency
IPCE	Incident photon to current conversion efficiency
SHE	Standard hydrogen electrode
LHE	Light harvesting efficiency
TAS	Transient absorption spectroscopy
EIS	Electrochemical impedance spectroscopy
HB	Hyperbranched polymers
MN	Monolithic

# Symbols

D	dye
$\nu$	frequency
h	Plank's constant
M	mediator
E	redox potential
$k_{et}$	electron transfer constant rate
$\Delta G^\ddagger$	activation energy
$\Delta G^0$	Free Gibbs energy
$\lambda$	reorganizational energy
$k_B$	Boltzmmman constant
T	temperature
$H_{AB}$	electronic coupling
$\beta$	constant for distance in electronic coupling
$r$	distance between donor and acceptor
P	power
I	current
J	current density
V	voltage
$V_{oc}$	open circuit voltage
$J_{sc}$	short circuit current density
FF	fill factor
$P_{in}$	incident power
m	ideality factor
$I_s$	saturation current
$R_{series}$	series resistance
$R_{shunt}$	shunt resistance
$J_{ph}$	photogenerated current density
$E_{F,TiO_2}$	Fermi level of TiO <sub>2</sub>
$E_{redox}$	redox potential

$q$	elementary charge
$n_{CB}$	electron concentration
$N_{CB}$	density of states in the CB
$E^0$	formal redox potential
$C_{ox}$	concentration of oxidized species
$C_{red}$	concentration of reduced species
$\varphi_{inj}$	electron injection efficiency
$\varphi_{coll}$	electron collection efficiency
$\varphi_{reg}$	dye regeneratio efficiency
$A$	absorbance
$^{Int}J_{SC}$	integrated short cuircuit current density
$k_{trans}$	electron transport constant
$k_{rec}$	electron recombination constant
$k_{inj}$	electron injection constant
$k_0$	relaxation constant
$I$	intensity
$\beta$	stretched exponential factor
$\varepsilon_{ox}$	extintion coefficient of the dye
$\tau_e$	electron lifetime
$Q_{oc}$	extracted charge
$n$	number of electrons transfer
$A_{electrode}$	electrode's surface area
$D_n$	diffusion coefficient
$J_{lim}$	Limiting current
$F$	Faraday's constat
$l$	distance between electrodes
$J_0$	Exchange current
$R$	gas constant
$R_{CT}$	charge transfer resistance
$Z$	impedance
$Z_W$	Warburg element
$R_{trans}$	transport resistance
$R_{CT}$	recombination resistance
$C_\mu$	chemical capacitance
DOS	density of states
$g(E)$	density of states

$\tau_e$	electron transport time in the transmission line
$L_n$	electron diffusion length



# Contents

<b>Acknowledgements.....</b>	<b>v</b>
<b>Abstract .....</b>	<b>viii</b>
<b>Keywords .....</b>	<b>ix</b>
<b>Résumé .....</b>	<b>x</b>
<b>Mots-clés .....</b>	<b>xi</b>
<b>Abbreviations.....</b>	<b>xii</b>
<b>Symbols .....</b>	<b>xiii</b>
<b>List of Figures .....</b>	<b>xix</b>
<b>List of Tables .....</b>	<b>xxv</b>
<b>List of Equations.....</b>	<b>xxvi</b>
<b>Chapter 1 Introduction.....</b>	<b>1</b>
1.1 Energy deployment .....	1
1.2 Solar Energy.....	2
1.3 Dye-Sensitized Solar cells .....	3
1.4 Components of a DSSC .....	6
1.4.1 Substrates .....	6
1.4.2 Semiconductor.....	6
1.4.3 Dyes .....	6
1.4.4 Electrolyte.....	7
1.4.5 Counter electrode.....	7
1.5 Thermodynamics of electron transfer .....	7
1.6 Characterization Techniques .....	9
1.6.1 J-V characteristic curves .....	9
1.6.2 IPCE .....	12
1.6.3 UV-Vis spectroscopy .....	14
1.6.4 TAS.....	14

1.6.5	Toolbox measurements .....	16
1.6.6	Cyclic voltammetry .....	17
1.6.7	EIS .....	19
1.6.8	FTIR .....	23
1.6.9	SEM .....	24
1.7	Redox mediators .....	24
1.7.1	Iodide .....	25
1.7.2	Cobalt mediators .....	26
1.7.3	Copper complexes .....	27
1.8	Interfacial engineering.....	28
<b>Chapter 2</b>	<b>Tandem redox systems for reduced back electron reactions .....</b>	<b>31</b>
2.1	Motivation .....	31
2.2	New stable organic radical 2-Azaadamantane-N-oxyl.....	33
2.3	Electrochemical characterization of the tandem electrolyte .....	36
2.4	Device optimization.....	38
2.5	Tandem electrolytes with Cu complexes.....	43
2.6	Conclusions.....	45
2.7	Supporting information .....	46
<b>Chapter 3</b>	<b>In-situ photopolymerization by thiol-ene “click” reaction in cobalt based electrolytes.....</b>	<b>55</b>
3.1	Motivation .....	55
3.2	Thiol-ene reaction .....	56
3.3	Electrochemical characterization .....	59
3.4	DSSC with HB polymers .....	61
3.5	Conclusions.....	68
3.6	Supporting Information .....	69
<b>Chapter 4</b>	<b>Engineering of a novel blue dye for decreased electron recombination.....</b>	<b>83</b>
4.1	Motivation .....	83
4.2	Dye characterization.....	84
4.3	DSSC employing the engineered R7 dye.....	87
4.4	Conclusions.....	93
4.5	Supporting Information .....	93
<b>Chapter 5</b>	<b>Carbon counter electrodes for copper-based DSSCs .....</b>	<b>107</b>
5.1	Motivation .....	107

5.2	FIRA processing .....	109
5.3	DSSC with CCE for indoor light harvesting.....	110
5.4	Monolithic DSSC based on copper electrolytes.....	113
5.5	Conclusions.....	115
5.6	Supporting information .....	116
<b>Chapter 6</b>	<b>Conclusions.....</b>	<b>119</b>
6.1	Achieved results .....	119
6.2	Future development.....	121
<b>References</b>	<b>.....</b>	<b>122</b>
<b>Curriculum Vitae</b>	<b>.....</b>	<b>133</b>

## List of Figures

<b>Figure 1.1.</b> (a) Schematic representation of a DSSC and (b) operation scheme. ....	3
<b>Figure 1.2.</b> Gerischer Diagram for electron transfer in DSSC. ....	8
<b>Figure 1.3.</b> Energetic parabolas for the Marcus normal and Inverted region .....	9
<b>Figure 1.4.</b> AST G173-03 reference spectra for AM1.5. ....	9
<b>Figure 1.5.</b> Characteristic J-V curve for a cobalt-based DSSC. ....	10
<b>Figure 1.6.</b> Equivalent circuit of a solar cell. ....	12
<b>Figure 1.7.</b> Typical IPCE curve for a DSSC employing a cobalt-based electrolyte. ....	13
<b>Figure 1.8.</b> UV-Vis spectra for the dye R7. ....	14
<b>Figure 1.9.</b> (a) schematic representation of a TAS set-up and (b) TAS measurements for a sample sensitized with XY1 and $\text{Co}(\text{bpy})_3^{3+/2+}$ electrolyte and with inert electrolyte. ....	15
<b>Figure 1.10.</b> (a) Electron lifetime vs. $EF, \text{TiO}_2$ and (b) charge extraction vs. $EF, \text{TiO}_2$ for DSSC with cobalt-based reference electrolyte and 10% of polymer HB2. ....	17
<b>Figure 1.11.</b> Cyclic voltammograms for the redox mediator $\text{Co}(\text{bpy})_3^{3+/2+}$ and the auxiliary redox mediator $\text{AZ}^+/\text{AZ}^0$ . ....	18
<b>Figure 1.12</b> Cyclic voltammetry with a rotating disk at 50 rpm. ....	18
<b>Figure 1.13.</b> Typical Nyquist plot for a DSSC with 10% of polymer in a cobalt-based electrolyte at 0.85 V. ....	20
<b>Figure 1.14.</b> The complete equivalent circuit for a DSSC including the transmission line. <sup>61</sup> ....	20
<b>Figure 1.15.</b> Simplification of the DSSC's equivalent circuit according to the voltage range, obtained from ZView®. ....	22
<b>Figure 1.16.</b> The equivalent circuit for symmetrical cells for electrochemical studies, obtained from ZView®. ....	23
<b>Figure 1.17.</b> FTIR spectra for a polymer mixture containing a polyacrylate and a siloxane. ....	24
<b>Figure 1.18.</b> Top-view image of a carbon-based counter electrode obtained by SEM. ....	24
<b>Figure 1.19.</b> Representation of the electronic configuration of $\text{Co}^{2+}$ and $\text{Co}^{3+}$ species. ....	26
<b>Figure 1.20.</b> Molecular structures of cobalt complexes employing as redox mediators in DSSC. ....	27
<b>Figure 1.21.</b> Molecular structures of copper complexes employing as redox mediators in DSSC. ....	28
<b>Figure 2.1.</b> Schematic representation of the energetic levels in DSSC employing tandem electrolytes. ....	33
<b>Figure 2.2.</b> Molecular structures of the radicals used as small donors in tandem redox systems .....	33
<b>Figure 2.3.</b> Cyclic voltammetry with a three-electrode cell with glassy carbon as the working electrode, a graphite rod as the counter electrode, and a non-aqueous reference electrode of $\text{Ag}/\text{AgCl}$ (2 M in ethanol) and a scan rate of $100 \text{ mV s}^{-1}$ of (a) $\text{AZ}$ 2 mM and (b) $[\text{Co}(\text{bpy})_3]^{2+}$ 2 mM and tandem mixture $[\text{Co}(\text{bpy})_3]^{2+} + \text{AZ}$ . ....	34

<b>Figure 2.4.</b> Schematic overview of the energetic levels in a DSSC with a tandem electrolyte $[\text{Co}(\text{bpy})_3]^{3+/2+} + \text{AZ}^{+/0}$ .....	35
<b>Figure 2.5.</b> Molecular structures of dyes tested with the tandem electrolyte. ....	35
<b>Figure 2.6.</b> Photocurrent density vs. voltage (J-V curves) for DSC with tandem electrolyte $\text{Co}(\text{bpy})_3$ 0.22 M + AZ 0.15 M and different sensitizers and PEDOT as CE. ....	36
<b>Figure 2.7.</b> Log(J) vs. potential plots for symmetrical cells containing tandem electrolytes. ....	37
<b>Figure 2.8.</b> (a) J-V curves for DSSC with tandem system electrolytes and PEDOT as CE. The Co ref electrolyte is composed of 0.25 M $\text{Co}(\text{bpy})_3\text{TFSI}_2$ , 0.05 M $\text{Co}(\text{bpy})_3\text{TFSI}_3$ , 0.1 M LiTFSI, and 0.5 M 4,5-nonylpyridine, and the tandem systems were prepared using a concentration of $\text{Co}(\text{bpy})_3^{2+}$ of 0.25 M, and the showed ratios of AZ. (b) light intensity current dependence. ....	39
<b>Figure 2.9.</b> IPCE curves for the tandem systems.....	40
<b>Figure 2.10.</b> (a) Charge extraction vs. Fermi level and (b) electron lifetime vs. Fermi level of DSSC containing tandem electrolyte systems. For both plots, the squares correspond to the $[\text{Co}(\text{bpy})_3]^{3+/2+}$ reference, the circles to Co/AZ 1:1, diamonds to Co/AZ 1:0.8, triangles to AZ/Co 1:0.9, and, inverted triangles to the $\text{AZ}^{+/0}$ electrolyte.....	41
<b>Figure 2.11.</b> EIS analysis. (a) Continuous lines with solid markers represent the charge transfer resistance $R_{\text{CT}}$ as a function of applied voltage, and the dotted lines with open markers the transport resistance $R_{\text{trans}}$ . (b) Voltage vs. DOS/cm <sup>-3</sup> .....	42
<b>Figure 2.12.</b> Transient absorption spectroscopy measurements of DSSC with tandem electrolytes.....	43
<b>Figure 2.13.</b> Schematic representation of the energetic levels in dye-sensitized solar cells.....	44
<b>Figure 2.14.</b> Photocurrent density vs voltage (J-V curves) for DSC with Y123 as sensitizer, PEDOT as CE and electrolytes with a) $\text{Cu}(\text{tmby})_2$ , b) $\text{Cu}(\text{tmby})_2 + \text{TEMPO}$ , and c) $\text{Cu}(\text{tmby})_2 + \text{TPPA}$ . ....	45
<b>Figure 2.15.</b> Plot of voltage vs time in a chronopotentiometry method (zero current) of (a) 2 mM $\text{Co}(\text{bpy})_3^{2+}$ , 0.5 mM $\text{Co}(\text{bpy})_3^{3+}$ , 0.1 M LiTFSI (dash-dotted black line), (b) 2 mM $\text{Co}(\text{bpy})_3^{2+}$ , 0.5 mM $\text{Co}(\text{bpy})_3^{3+}$ , 0.1 M LiTFSI, 2 mM AZ (dotted red line) and (c) 2 mM $\text{Co}(\text{bpy})_3^{2+}$ , 0.5 mM $\text{Co}(\text{bpy})_3^{3+}$ , 0.1 M LiTFSI, 2 mM AZ, 0.1 mM $\text{AZ}^+$ by adding the corresponding amount of $\text{NOBF}_4$ (solid blue line), and (d) excess of $\text{NOBF}_4$ .....	48
<b>Figure 2.16.</b> Current vs voltage plots measured with a rotatory disk electrode (a) calibration with $\text{Fe}(\text{CN})_6^{3-}$ and $\text{Fe}(\text{CN})_6^{4-}$ electrolyte and (b) tandem system electrolytes.....	49
<b>Figure 2.17.</b> Nyquist plots for symmetric cells containing the tandem electrolyte systems, at 0 V. ....	50
<b>Figure 2.18.</b> Nyquist plots under dark conditions for DSSC with electrolytes of a) $[\text{Co}(\text{bpy})_3]^{3+/2+}$ reference, b) Co/AZ 1:1, c) Co/AZ 1/0.8, d) AZ/Co 1:0.9 and e) $\text{AZ}^+/\text{AZ}$ electrolyte. ....	52
<b>Figure 2.19.</b> EIS analysis. (a) Nyquist plots at open-circuit voltage for each electrolyte system, (b) continuous lines with solid markers represent the charge transfer resistance $R_{\text{CT}}$ as a function of applied voltage, the dotted lines with open markers the transport resistance $R_{\text{trans}}$ , dash-dotted lines with and x marker represents capacitance, (c) electron lifetime and transport time vs density of states, DOS. For all the plots, the squares correspond to the $[\text{Co}(\text{bpy})_3]^{3+/2+}$ reference, the circles to Co/AZ 1:1, diamonds to Co/AZ 1/0.8, triangles to AZ/Co 1:0.9, and inverted triangles to the $\text{AZ}^+/\text{AZ}$ electrolyte. ....	53

<b>Figure 3.1.</b> Thiol-ene reaction and molecular structures of thiol-siloxane, polyacrylate monomers PEGMA, and PEGDA and simplified hyperbranched products, HB1 (PEGMA+thiolsiloxane) and HB2 (PEGDA+thiolsiloxane).....	57
<b>Figure 3.2.</b> (a) FTIR of electrolyte with HB1 (PEGMA + thiol-siloxane) in ACN from 0s to 240 s of UV curing. (b) FTIR of HB2 (PEGDA + thiol-siloxane) in ACN from 0s to 240 s of UV curing. ....	58
<b>Figure 3.3.</b> (a) FTIR of electrolyte with Co ref +HB1 (PEGMA+Thiolsiloxane) 20% (v/v) at 0s and after 120 s of UV curing.(b) FTIR of electrolyte with Co ref+HB2(PEGDA+Thiolsiloxane) 20% (v/v) at 0s and after 120 s of UV curing. The Co ref contains 0.23M Co(bpy) <sub>3</sub> TFSI <sub>2</sub> , 0.05 Co(bpy) <sub>3</sub> TFSI <sub>3</sub> , 0.1 M LiTFSI and 0.6 M 4,5-nonylpyridine.....	59
<b>Figure 3.4.</b> TGA analysis of the monomers, a [Co(bpy) <sub>3</sub> ] <sup>3+/2+</sup> reference electrolyte, and electrolytes containing 20% of HB1 and HB2. ....	59
<b>Figure 3.5.</b> (a) and (b) Representation of symmetric cells with the photopolymerized electrolytes, (c) Taffel plots, and (d) Nyquist plots at 0 V.....	60
<b>Figure 3.6.</b> Molecular structure of XY1-b used as the sensitizer for DSSCs with HB polymers.....	61
<b>Figure 3.7.</b> (a) J-V plots under 1.5 AM, (b) J-V plots under 0.5 Sun and (d) 0.1 Sun and (d) IPCE curves.....	62
<b>Figure 3.8.</b> (a) Charge extraction vs Fermi level (b) electron lifetime vs Fermi (c) V <sub>OC</sub> vs light intensity and (d) J <sub>SC</sub> vs light intensity of DSSC containing photopolymerized electrolytes. (e) Current density vs voltage for symmetric cells. The quasi-Fermi level was calculated by the relation E <sub>F-q</sub> =E <sub>redox</sub> -V <sub>OC</sub> .....	64
<b>Figure 3.9.</b> EIS analysis. (a) continuous lines with solid markers represent the charge transfer resistance R <sub>CT</sub> as a function of applied voltage, and the dotted lines with open markers the transport resistance R <sub>trans</sub> . (b) voltage vs. DOS/cm <sup>-3</sup> .....	65
<b>Figure 3.10.</b> Warburg resistance of Co <sup>3+</sup> in the studied electrolytes as a function of applied bias. ....	66
<b>Figure 3.11.</b> EIS analysis. (a) continuous lines with solid markers represent the charge transfer resistance R <sub>CT</sub> as a function of applied voltage and the dotted lines with open markers the transport resistance R <sub>trans</sub> . (b) voltage vs. DOS/cm <sup>-3</sup> .....	66
<b>Figure 3.12.</b> (a) J-V plots of 2.8 cm <sup>2</sup> devices under 1000 lux illumination, (b) charge transfer resistance R <sub>CT</sub> as function of applied voltage for solid markers and continuous lines, and transport resistance R <sub>trans</sub> for the dotted lines with open marker (c) electron lifetime $\tau_e$ as function of DOS/cm. ....	67
<b>Figure 3.13.</b> Nyquist plots for a device with Co-reference electrolyte at 1 sun illumination. ....	72
<b>Figure 3.14.</b> Nyquist plots for a device with 10% of HB1 electrolyte at 1 sun illumination.....	73
<b>Figure 3.15.</b> Nyquist plots for a device with 15% of HB1 electrolyte at 1 sun illumination.....	73
<b>Figure 3.16.</b> Nyquist plots for a device with 20% of HB1 electrolyte at 1 sun illumination.....	74
<b>Figure 3.17.</b> Nyquist plots for a device with 10% of HB2 electrolyte at 1 sun illumination.....	74
<b>Figure 3.18.</b> Nyquist plots for a device with 15% of HB2 electrolyte at 1 sun illumination.....	75
<b>Figure 3.19.</b> Nyquist plots for a device with 20% of HB2 electrolyte at 1 sun illumination.....	75
<b>Figure 3.20.</b> Nyquist plots for a device with Co-reference electrolyte at 0.1 sun illumination. ....	76

<b>Figure 3.21.</b> Nyquist plots for a device with 10% of HB1 electrolyte at 0.1 sun illumination.....	76
<b>Figure 3.22.</b> Nyquist plots for a device with 15% of HB1 electrolyte at 0.1 sun illumination.....	77
<b>Figure 3.23.</b> Nyquist plots for a device with 20% of HB1 electrolyte at 0.1 sun illumination.....	77
<b>Figure 3.24.</b> Nyquist plots for a device with 10% of HB2 electrolyte at 0.1 sun illumination.....	78
<b>Figure 3.25.</b> Nyquist plots for a device with 15% of HB2 electrolyte at 0.1 sun illumination.....	78
<b>Figure 3.26.</b> Nyquist plots for a device with 20% of HB2 electrolyte at 0.1 sun illumination.....	79
<b>Figure 3.27.</b> Nyquist plots for a device Co-reference electrolyte at 1000 lux illumination. ....	79
<b>Figure 3.28.</b> Nyquist plots for a device 15% of HB1 electrolyte at 1000 lux illumination.....	80
<b>Figure 3.29.</b> Nyquist plots for a device 15% of HB2 electrolyte at 1000 lux illumination.....	80
<b>Figure 3.30.</b> Light soaking aging at 60 °C and 1 Sun illumination .....	81
<b>Figure 4.1.</b> Molecular structures of the dyes Y123, R6, and R7.....	85
<b>Figure 4.2.</b> (a) Stationary UV-vis spectroscopies of R6 and R7 in THF (10 $\mu$ M). (b) LUMO energy levels (values above color bars), HOMO energy levels (value under color bars), and energy gaps ( $\Delta E_{LH}$ ) of the dye molecules. ....	85
<b>Figure 4.3.</b> (a) Cyclic voltammograms of R6 and R7 in THF. Scan rate: 5 mV s <sup>-1</sup> . The internal reference was decamethylferrocene (DMFc), and all potentials were calibrated with the standard ferrocene/ferrocenium (Fc/Fc <sup>+</sup> ) redox couple. (b) Cyclic voltammograms of R6 and R7 dyes adsorbed on the TiO <sub>2</sub> /FTO electrode in 0.1 M LiTFSI + acetonitrile, scan rate 10 mV/s.....	86
<b>Figure 4.4.</b> Contour plots of all the related S <sub>1</sub> ←S <sub>0</sub> transition molecular orbitals. The orbitals were calculated using DFT/B3LYP/C-PCM(THF). (Isovalue set to 0.03 a.u.). The large hexyl substituents were replaced with ethyl to improve computational efficiency. ....	87
<b>Figure 4.5.</b> (a) Current density-voltage ( <i>J</i> - <i>V</i> ) curves measured under simulated full sunlight conditions for DSSCs. (b) Incident photon-to-electron conversion efficiencies (IPCEs) at a set of wavelengths of incident monochromatic lights.....	88
<b>Figure 4.6.</b> (a) Charge extraction vs. voltage curves measured (b) electron lifetime vs. voltage of DSCs with the dyes R6, R7 and the co-sensitized system R7+Y123 and Cu(tmby) <sub>2</sub> <sup>2+/+</sup> electrolyte.....	90
<b>Figure 4.7.</b> Electrochemical impedance spectroscopy (EIS) analysis. (a) Continuous lines with solid markers represent the charge transfer resistance ( <i>R</i> <sub>CT</sub> ) as a function of the applied voltage. The dotted lines with solid markers represent the transport resistance ( <i>R</i> <sub>trans</sub> ), and the dashed lines with open markers represent the chemical capacitance. (b) Voltage vs. density of states (DOS). (c) Electron lifetime as a function of DOS. ....	91
<b>Figure 4.8.</b> Transient absorption spectra for a) R6 and R7 with inert electrolyte of 0.1 M LiTFSI and 0.6 M NMB in acetonitrile (ACN), b) with 0.2 M [Cu(tmby) <sub>2</sub> ] <sup>1+</sup> TFSI, 0.09 M [Cu(tmby) <sub>2</sub> ] <sup>2+</sup> (TFSI) <sub>2</sub> , 0.1 M LiTFSI and 0.6 M NMB in ACN. ....	92
<b>Figure 4.9.</b> Synthetic routes to R7. Reagents and conditions: (i) NBS, THF, R.T., 10 min.; (ii) bis(2',4'-bis(hexyloxy)-[1,1'-biphenyl]-4-yl)amine, Pd <sub>2</sub> (dba) <sub>3</sub> , P( <i>t</i> -Bu) <sub>3</sub> , NaOtBu, toluene, reflux, 12 h; (iii) NBS, THF, R.T., 8 h; (iv) butyl 4-(7-ethynylbenzo[ <i>c</i> ][1,2,5]thiadiazol-4-yl)benzoate,	

Pd <sub>2</sub> (dba) <sub>3</sub> , P( <i>t</i> -Bu) <sub>3</sub> , Cs <sub>2</sub> CO <sub>3</sub> , dioxane, reflux, 10 h; (v) KOH, THF/H <sub>2</sub> O (v/v, 3/1), reflux, 10 h; then phosphoric acid. ....	96
<b>Figure 4.10.</b> Molecular structure of bis(2',4'-bis(hexyloxy)-[1,1'-biphenyl]-4-yl)amine. ....	96
<b>Figure 4.11.</b> Molecular structure of R7. ....	97
<b>Figure 4.12.</b> <sup>1</sup> H NMR (500 MHz) spectrum of <b>3</b> in THF- <i>d</i> <sub>8</sub> . ....	99
<b>Figure 4.13.</b> <sup>13</sup> C NMR (125 MHz) spectrum of <b>3</b> in THF- <i>d</i> <sub>8</sub> . ....	99
<b>Figure 4.14.</b> High resolution mass spectrum (MALDI-TOF) of <b>3</b> . ....	100
<b>Figure 4.15.</b> ATR-FTIR spectrum of <b>3</b> . ....	100
<b>Figure 4.16.</b> UV-Vis spectroscopy of <b>3</b> in THF. ....	101
<b>Figure 4.17.</b> <sup>1</sup> H NMR (400 MHz) spectrum of R7 in THF- <i>d</i> <sub>8</sub> . ....	101
<b>Figure 4.18.</b> <sup>13</sup> C NMR (100 MHz) spectrum of R7 in THF- <i>d</i> <sub>8</sub> . ....	102
<b>Figure 4.19.</b> High resolution mass spectrum (MALDI-TOF) of R7. ....	102
<b>Figure 4.20.</b> ATR-FTIR spectrum of R7. ....	103
<b>Figure 4.21.</b> UV-Vis spectroscopy of R7 in THF. ....	103
<b>Figure 4.22.</b> Histogram of PCE of DSSCs with R6. ....	104
<b>Figure 4.23.</b> Histogram of PCE of DSSCs with R7. ....	104
<b>Figure 4.24.</b> Histogram of PCE of DSCs with R7 using Y123 as the cosensitizer. ....	105
<b>Figure 4.25.</b> Exponential fit of transient absorption spectra of dye R6. ....	105
<b>Figure 4.26.</b> Exponential fit of transient absorption spectra of dye R7. ....	106
<b>Figure 5.1.</b> (a) Schematic representation of a solid-state DSSC (b) Zombie cell employing a Cu complex as HTM. ....	108
<b>Figure 5.2.</b> (a) Schematic representation of the Flash Infrared Annealing set-up. (b) Used equipment. ....	109
<b>Figure 5.3.</b> SEM top view images of TiO <sub>2</sub> , ZrO <sub>2</sub> and Carbon top layers after annealing at FIRA at 450 °C, 500 °C and 400 °C respectively. ....	110
<b>Figure 5.4.</b> J-V curve for DSSCs with an active area of 2.8 cm <sup>2</sup> . ....	111
<b>Figure 5.5.</b> Electrochemical impedance spectroscopy (EIS) analysis. (a) Continuous lines with solid markers represent the charge transfer resistance ( <i>R</i> <sub>CT</sub> ) as a function of the applied voltage. The dotted lines with solid markers represent the transport resistance ( <i>R</i> <sub>trans</sub> ), and the dashed lines with open markers represent the chemical capacitance. (b) Voltage vs. density of states (DOS). (c) Electron lifetime as a function of DOS. ....	112
<b>Figure 5.6.</b> (a) Schematic representation and (b) cross-sectional SEM of a MN-DSSC with a CCE and copper complex mediator. ....	113
<b>Figure 5.7.</b> (a) J-V curve for MN-DSSCs under 1.5 AM and (b) J-V curve for a liquid-based DSSC. ....	114
<b>Figure 5.8.</b> Top view SEM images of (a) a carbon counter electrode and (b) MS-DSSC with a copper-complex as HTM. ....	115
<b>Figure 5.9.</b> Nyquist plots for a device Cu-reference electrolyte with CCE at 1000 lux illumination. ....	117



<b>Figure 5.10.</b> Nyquist plots for a device Cu-reference electrolyte with PEDOT CE at 1000 lux illumination.....	118
<b>Figure 5.11.</b> Nyquist plots at 700 mV for DSSCs fabricated with a copper-based electrolyte under 1000 lux. ....	118
<b>Figure 5.12.</b> Monolithic solar cells. ....	118
<b>Figure 6.1.</b> Rational design of new carbon-based materials with enhanced charge transfer properties. ....	121

## List of Tables

<b>Table 2.1</b> Characteristic parameters of DSSCs with tandem electrolyte Co+AZ (0.22 M/0.15 M) and different sensitizers. ....	36
<b>Table 2.2.</b> Characterization data of symmetric cells from Log(J) vs. potential plots and from EIS analysis .....	38
<b>Table 2.3</b> Characteristic parameters for the best DSSC using XY1 as sensitizer and the different tandem electrolytes.....	39
<b>Table 2.4.</b> Regeneration halftimes obtained from transient absorption spectroscopy measurements.....	43
<b>Table 2.5.</b> Diffusion coefficients of the actives species in acetonitrile, measured with a rotatory disk electrode.....	50
<b>Table 2.6.</b> Photovoltaic parameters of DSSC with the dye XY1, PEDOt as CE and different electrolyte systems. ....	51
<b>Table 3.1.</b> Characterization data of symmetric cells from Log(J) vs. potential plots and from EIS analysis .....	61
<b>Table 3.2.</b> Photovoltaic characteristic parameters for DSSC with photopolymerized electrolytes. ....	63
<b>Table 3.3.</b> Photovoltaic characteristic parameters for DSSC with photopolymerized electrolytes under 1000 lux illumination.....	68
<b>Table 4.1.</b> Data on frontier orbital energy levels and electronic absorptions. <sup>a</sup> .....	86
<b>Table 4.2.</b> Photovoltaic parameters of the best-performing devices under the simulated AM1.5G sunlight (100 mW cm <sup>-2</sup> ). ....	89
<b>Table 5.1.</b> Characteristic parameters of 2.8 cm <sup>2</sup> DSSC under 1000 lux illumination .....	111
<b>Table 5.2.</b> Characteristic parameters of devices DSSC under AM1.5. ....	114

## List of Equations

Equation 1.1. Dye excitation .....	4
Equation 1.2. Electron injection .....	4
Equation 1.3 Dye regeneration .....	5
Equation 1.4 Shuttle's regeneration .....	5
Equation 1.5 Recombination to the mediator .....	5
Equation.1.6 Recombination to the dye .....	5
Equation 1.7 Decay from the excited state.....	5
Equation 1.8 Driving force for dye regeneration .....	7
Equation 1.9 Redox potential of the mediator .....	7
Equation 1.10 Electron transfer rate .....	8
Equation 1.11 Electronic coupling .....	8
Equation 1.12 Activation energy.....	9
Equation 1.13 Power calculation .....	10
Equation 1.14. Power derivation .....	10
Equation 1.15 Maximum power .....	10
Equation 1.16 Fill factor calculation.....	10
Equation 1.17 Power conversion efficiency.....	11
Equation 1.18 dark current .....	11
Equation 1.19 Current density .....	11
Equation 1.20 Ideality factor.....	11
Equation 1.21 $V_{oc}$ dependence on the photocurrent.....	11
Equation 1.22 $V_{oc}$ determination .....	12
Equation 1.23 Fermi level determination .....	12
Equation 1.24 Nernst equation.....	12
Equation 1.25 IPCE determination.....	13
Equation 1.26 Light-harvesting efficiency.....	13
Equation 1.27 Integrated current density.....	13
Equation 1.28 Electron collection efficiency.....	13
Equation 1.29 Electron injection efficiency .....	14
Equation 1.30 Absorbance calculation .....	14
Equation 1.31 Lambert-Beer Law .....	14

Equation 1.32 Absorbance change in TAS.....	15
Equation 1.33 Absorbance decay.....	15
Equation 1.34 Dye regeneration efficiency.....	15
Equation 1.35 Injection efficiency.....	15
Equation 1.36 Electron lifetime .....	16
Equation 1.37 Charge extraction .....	16
Equation 1.38 Redox potential calculation from CV .....	17
Equation 1.39 Peak distance relation .....	17
Equation 1.40 Levich equation .....	18
Equation 1.41 Limiting current .....	18
Equation 1.42 Exchange current.....	19
Equation 1.43 AC voltage.....	19
Equation 1.44 AC current.....	19
Equation 1.45 Impedance calculation.....	19
Equation 1.46 Impedance as a complex number.....	19
Equation 1.47 Chemical capacitance .....	21
Equation 1.48 Density of states in the CB.....	21
Equation 1.49 Electron lifetime .....	22
Equation 1.50 Recombination resistance .....	22
Equation 1.51 Electron lifetime .....	22
Equation 1.52 Transport time .....	22
Equation 1.53 Density of states .....	23
Equation 1.54 Transport time.....	23
Equation 1.55 Electron diffusion length .....	23
Equation 2.1 Dye's regeneration by $AZ^0$ .....	34
Equation 2.2 Dye's regeneration by $Co^{2+}$ .....	34
Equation 2.3 Regeneration of AZ by $Co^{2+}$ .....	34
Equation 2.4 Diffusion coefficient from rotatory disk electrode .....	49

# Chapter 1 Introduction

## 1.1 Energy deployment

As we start 2021, after one year of the Covid-19 pandemic, we can see more than ever the disparities in our modern society and the real energy crisis we face. The pandemic's unprecedented measures included lockdowns for several months with substantially decreased economic and individual activities worldwide. From these measures, we expected that the energy consumption would drastically reduce. However, we still faced an annual increase of 1.3% global energy demand in 2020, just half of the annual increase in 2018 before the health crisis (2.8%), according to the statistical review of world energy 2020 from BP.<sup>1</sup> The increase in CO<sub>2</sub> emissions fell only down to 0.5% compared to 1.1% in 2018. The exceptional decrease during the present crisis is expected to be only temporary and to rebound by 2025 to the pre-Covid19 trends with a continuous increase in energy demand due to an (expected) boost in economic growth to overcome the global economic recession.<sup>2,3</sup> Several studies including different scenarios predict an increase in the energy demand up to 28% in 2040.<sup>4</sup>

The challenge to cover the increasing energy demand will grow in complexity as we must decrease CO<sub>2</sub> emissions to reach the targets specified in the Paris Agreement by the United Nations to limit the temperature increase to 1.5 °C.<sup>5</sup>

There is no single answer to solve the global climate crisis, therefore employing all possible technologies using clean energy is more critical than ever. The strategies to meet the CO<sub>2</sub> emission targets include research and development of renewable energy deployment technologies, energy efficiency implementation, and carbon capture.<sup>4-6</sup>

Several international policies and plans aiming to reach carbon-neutrality by 2050 have discussed the importance of implementing those strategies, such as the Energy Strategy 2050 from the Swiss Federal Council and the European Commission's Green Deal. We can only achieve these targets by the contribution of each stakeholder in the energy field to speed a radical transformation to shift from a fossil fuel-based to a renewable-based energetic matrix.<sup>2,6</sup>

Renewable energy sources such as hydro-, wind-, and solar power are vital for achieving a low carbon-based economy. The provision of clean energy is rapidly growing, but its share of the total energy usage is less than one-fifth of the current energy supply worldwide. Solar energy offers the best potential to increase the total share of renewable energy.

## 1.2 Solar Energy

The amount of energy reaching the earth's atmosphere from the sun is  $340 \text{ W/m}^2$  and approximately 600 TW reaching the earth's surface.<sup>7</sup> The conversion of only 10% of this energy into electrical energy could supply about 60 TW of clean energy. Harvesting solar energy with efficient photovoltaic devices (PV) capable of transforming solar energy into electricity is one of the best strategies to boost renewable energy use.

The first generation of PV solar cells is based on p-n junctions of monocrystalline silicon (c-Si), with record power conversion efficiencies (PCE) of 26.7 %.<sup>8</sup> This is the most market-mature PV technology and has seen an unprecedented decline in manufacturing costs and prices, reaching the consumer at final prices lower than \$ 0.1/W<sub>p</sub>. However, a further decrease in prices must be reached to make this technology accessible to a broader segment of the world population and beat oil-produced electricity prices.

The second generation of PV cells is based on p-n junctions of polycrystalline and amorphous silicon and other materials such as CdSe, CuInGaS (CIGS), and GaAs, among others. The record PCEs of 23.2% for polycrystalline Silicon cells, 21.2% for thin-film technologies, 27.8% for GaAs, 23.4% for CIGS, 22.12% for CdSe, according to the latest NREL chart. In recent years, the costs of these photovoltaic technologies have been significantly reduced. Silicon-based technologies, including mono and polycrystalline PV, currently account for 95% of the PV market. According to the Fraunhofer Institute for Solar Energy Systems (ISE), the installed PV cumulative capacity for 2020 was 635 GW.<sup>2</sup>

The thermodynamic limit establishes the maximum theoretical PCE for a solar cell, which depends on the material's bandgap. For crystalline silicon with a bandgap of 1.1 eV, the maximum theoretical PCE is around 31%.<sup>9,10</sup>

Traditionally, the third generation of solar cells also named emerging technologies include Organic Photovoltaics, OPV,<sup>11</sup> Quantum Dots Solar Cells, QDSSC,<sup>12</sup> Extremely Thin Absorbent Cells, ETA,<sup>13</sup> Dye-Sensitized Solar Cells, DSSC,<sup>14</sup> and hybrid organic/inorganic Perovskite Solar Cells, PSC.<sup>15</sup> It is estimated that these technologies could potentially exceed the theoretical efficiency limit or be produced at a low cost and a reduced carbon footprint.<sup>9</sup>

As the world's requirements for solar cells increase, mass-production in a sustainable fashion will be a decisive factor in the photovoltaics market. New technologies produced from cheap and environmentally friendly materials, reducing CO<sub>2</sub> emission from production and transport.<sup>2</sup> Third-generation PV technologies can be produced from inexpensive, earth-abundant materials and can potentially transform the energy sector by making renewable energy more accessible to society worldwide. Additionally, these solar cells' production can easily be integrated into a circular economy, which is also part of several climate actions such as a Circular Economic Action Plan (2020) proposed by the European Commission.<sup>16</sup>

Flexibility and affordability are some of the numerous benefits these technologies offer. Unlike silicon technology, they can be embedded into everyday objects such as clothes, electronic devices, or building materials. Progress towards making solar energy more sustainable has primarily involved developing more powerful light-absorbing materials.

### 1.3 Dye-Sensitized Solar cells

Dye-sensitized solar cells were first introduced in 1991 by Michael Grätzel and Brian O'Regan,<sup>17</sup> with a study reporting DSSC with a PCE of 7.12%, using TiO<sub>2</sub> nanoparticles in the anatase phase as semiconductor, sensitizing with a ruthenium dye, and using an electrolyte with the redox couple  $I_3^-/I^-$ . In recent publications, up to 14.3% efficiency has been achieved.<sup>18</sup> As mentioned above, DSSCs are considered third-generation cells since they have advantages such as low production and investment costs than other existing technologies. Variety in design, such as transparency, multiple color options, flexibility, and excellent performance under diffuse light.<sup>19</sup> The design and operation diagram of a DSSC is shown in Fig 1.1. DSSC has recently attracted much attention due to their remarkably high PCE under indoor illumination, up to 34% under 1000 lux.<sup>20</sup>

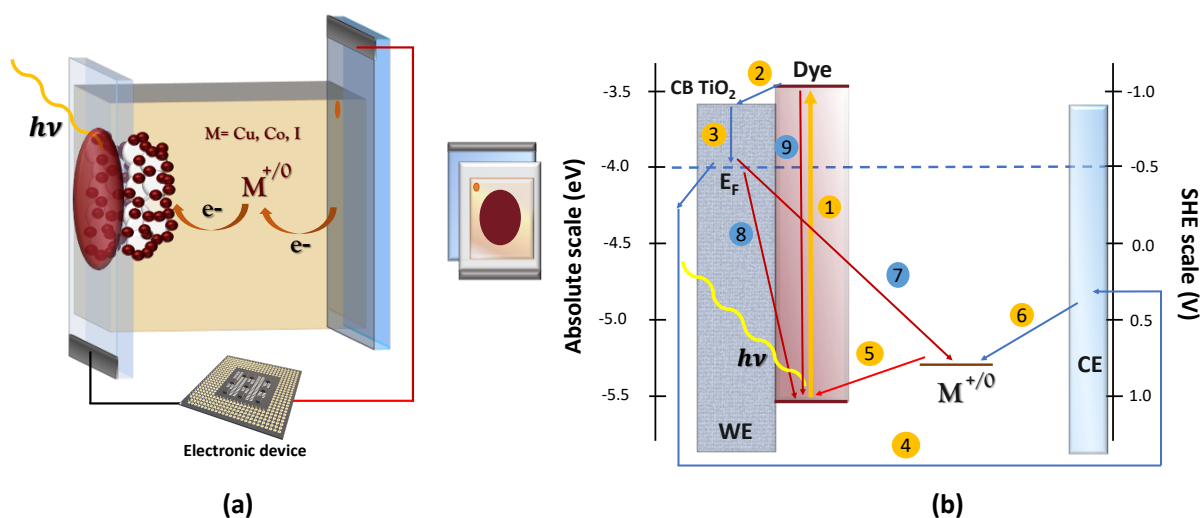


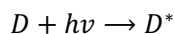
**Figure 1.1.** (a) Schematic representation of a DSSC and (b) operation scheme.

In general, DSSCs are composed of a photoanode, electrolyte, and counter electrode. The photoanode or working electrode (WE) is fabricated with a mesoporous-semiconductor such as TiO<sub>2</sub> deposited on a conducting-glass substrate (usually SnO<sub>2</sub>:F, FTO). The chemisorption of a monolayer of dye molecules sensitizes the semiconductor. The counter electrode (CE), placed on top of the WE, is composed of another glass substrate with a thin layer of an electrocatalytic material such as Pt, graphene, or poly(3,4-ethylenedioxythiophene) (PEDOT). The liquid electrolyte or solid hole transport material (HTM) is filled in between the two electrodes.<sup>21</sup>

Incoming light from the sun excites electrons from the HOMO of the dye to its LUMO. The excited electrons are later injected into the semiconductor's conduction band and transported through localized states into the FTO electrode, exiting the circuit.<sup>22</sup> The electron in the external circuit can provide power to electronic devices and then return to the system through the counter-electrode. After electron injection, the dye's oxidized form can be regenerated to the ground state by electron transfer from a redox couple in the electrolyte or by a hole transporting material (for all-solid DSSCs). The dye regeneration process is vital for the well-functioning of the cell. Therefore, the electrolyte plays a pivotal role in attaining high energy conversion efficiencies.

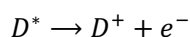
The redox couple  $I^-/I_3^-$  has been widely used because it presents significant recombination resistance and provides high electron lifetimes,<sup>23,24</sup> thus, high energy conversion efficiencies can be obtained.<sup>25</sup> Nevertheless, this redox couple has several disadvantages. This includes corrosiveness, light absorption in the visible range, sublimation, and a significant potential drop due to the mismatch of the redox potential of  $I^-/I_3^-$  and the highest occupied molecular orbital (HOMO) level of most sensitizers; limiting the open-circuit voltage,  $V_{OC}$ , to values between 0.7-0.8 V.<sup>26,27</sup>

Photoexcitation (step 1): the dye molecule absorbs energy from the photon from sunlight and goes from its ground state to its excited state. An electron is promoted from HOMO to LUMO with the energy of the absorbed photon.<sup>28</sup>



Equation 1.1. Dye excitation

Electron injection (step 2): the electron located in the LUMO of the dye is transferred to the conduction band (CB) of TiO<sub>2</sub> because it is slightly lower in energy (driving force), leaving the dye in its oxidized form. This reaction must be faster than the recombination reaction from Eq. 1.5 to avoid kinetic competition between these reactions.

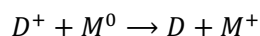


Equation 1.2. Electron injection



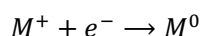
Charge transfer in TiO<sub>2</sub> (step 3): the electron is transported through the TiO<sub>2</sub> layer by trapping-detrapping random events to the FTO. From there, the electron passes through the external circuit to the counter electrode (step 4).

Dye Regeneration (step 5): in this step, the reduction of the dye's oxidized species occurs through the oxidation of the mediator M.



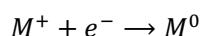
Equation 1.3 Dye regeneration

Mediator's regeneration (step 6): in this step, the redox mediator's oxidized species are reduced by electron transfer at the counter electrode, closing the circuit.



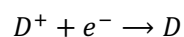
Equation 1.4 Shuttle's regeneration

Recombination of electrons with the electrolyte (step 7): The electrons in the CB of TiO<sub>2</sub> recombine with the mediator's oxidized state in the electrolyte. This process is faster than the recombination with the dye (step 8) because the Fermi level of M (redox potential) has a lower energy level than the oxidized state of the dye. This recombination is responsible for the dark current in cells.<sup>29</sup>



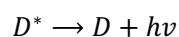
Equation 1.5 Recombination to the mediator

Recombination with the dye (step 8): electrons in the CB of the TiO<sub>2</sub> recombines with the dye's oxidized state, regenerating it and thereby decreasing the extracted photocurrent.



Equation.1.6 Recombination to the dye

Recombination by decay (step 9): The dye molecule returns from its excited state to its ground state, releasing the absorbed energy as heat.



Equation 1.7 Decay from the excited state

For proper cell operation and to obtain high efficiencies, the recombination reactions ( steps 7-9) must be slower than charge transport reactions in the desired direction.

## 1.4 Components of a DSSC

### 1.4.1 Substrates

As observed from Fig.1.1, a DSSC is composed of two glass substrates that must be transparent, have low sheet resistance, and good thermal and mechanical stability. Typically, a thin layer of a transparent conductive oxide (TCO), such as fluorine-doped tin oxide (F: SnO<sub>2</sub>, FTO), is deposited on the glass to decrease the sheet resistance.

### 1.4.2 Semiconductor

The most widely used semiconductor is TiO<sub>2</sub> in its anatase phase (bandgap of 3.2 eV). A mesoporous semiconductor with a large surface area is needed to increase dye loading. Generally, the working electrode (WE), or photoanode, is assembled by deposition of a TiO<sub>2</sub> “blocking” layer (approx.50 nm) in order to prevent contact of the electrolyte with the FTO and to reduce deleterious recombination of electrons at the substrate. The blocking layer can be deposited by chemical bath deposition, spray pyrolysis, sputtering and atomic layer deposition. Subsequently, a “light-absorbing” layer of TiO<sub>2</sub> with particle sizes between 20-40 nm is deposited using screen printing techniques. For devices employing Co and Cu complexes in the electrolyte, the light-absorbing layer’s typical thickness is approximately 4-5 μm. Successively a “scattering” layer, with particle sizes between 400 nm, of approximately 3-4 μm is deposited to decrease light reflection and losses. Lastly, a thin layer of TiO<sub>2</sub> (approximately 1 nm) is deposited by treatment with TiCl<sub>4</sub>, followed by a treatment sintering process at 450 °C.<sup>7</sup>

### 1.4.3 Dyes

The sensitizer must meet specific requirements, including good adsorption into the TiO<sub>2</sub> (by an anchoring group, such as -COOH). The LUMO of the dye must be at a higher energy level than the CB of TiO<sub>2</sub> to secure enough driving force for electron injection. The HOMO of the dye must be at a lower energy level (more positive) than the reduction potential of the redox mediator in the electrolyte for sufficient driving force for dye regeneration. It must have a high molar extinction coefficient and overlap with the solar spectrum and should be chemically stable in its oxidized state and with the solvent used for the electrolyte.

Traditionally, Ru-based dyes with high extinction coefficients were employed in DSSC with  $I_3^-/I^-$  for high photocurrents.<sup>30</sup> Nonetheless, for cobalt and copper complexes as redox mediators, the best-performing dyes are completely organic molecules, employing D- $\pi$ -A architectures that separate the HOMO in the acceptor group (anchored to TiO<sub>2</sub>) and the LUMO in the donor moiety. The extension of the  $\pi$  bridge increases the extinction

coefficient.<sup>31,32</sup> Dyes can be engineered to prevent interfacial recombination to the electrolyte, as will be presented in chapter 4.

## 1.4.4 Electrolyte

Generally, the liquid electrolytes employ organic solvents, or ionic liquids, or a quasi-solid matrix. Solid hole transport materials can also be used. The redox mediator in the electrolyte must be chemically and thermally stable. They must present high conductivity to secure a rapid diffusion of the charge carriers. On the other hand, the redox mediator should present slow recombination kinetics for Eq.1.5, and electrochemical reversibility. Some additives such as 4-tert-butylpyrine (TBP) are used to shift the CB of TiO<sub>2</sub> towards a higher energy level and decrease recombination, increasing the generated photovoltage. While lithium salts such as LiTFSI are known to shift the CB of TiO<sub>2</sub> towards a lower energy level, increasing the driving force for injection and the generated photocurrent.<sup>33,34</sup>

## 1.4.5 Counter electrode

Usually, Pt, PEDOT,<sup>35</sup> graphene nanoplatelets (GNP),<sup>36</sup> or carbon-based materials,<sup>37</sup> are deposited on the glass substrate. This reduces the glass substrate's resistance to values from 0.1-1  $\Omega/\text{cm}^2$ , compared to the bare FTO glass around 100  $\Omega/\text{cm}^2$ . Several review papers describe in detail each component of DSSC.<sup>32,38</sup>

## 1.5 Thermodynamics of electron transfer

The minimal driving force for regeneration is around 0.1-0.15 eV.<sup>39</sup> Employing a mediator with a high redox potential implies less energy loss in the dye-regeneration process, and higher photovoltage could be expected. Such is the case of Co and Cu mediators when compared to the  $I_3^-/I^-$  redox pair. Nonetheless, this also increases the driving force for the back recombination reactions of electrons from the TiO<sub>2</sub> CB or the FTO contact, increasing the dark currents and decreasing the  $V_{OC}$ .<sup>40</sup> The standard Gibbs free energy is the thermodynamic driving force for dye regeneration and can be calculated as:

$$\Delta G_{reg}^0 = E_F^{0'}(D^+/D^0) - E_{redox}$$

Equation 1.8 Driving force for dye regeneration

$$E_{redox} = E_F^{0'}(M^+/M^0)$$

Equation 1.9 Redox potential of the mediator

The Gerischer model can be used to represent the Gaussian distribution of energetic levels both for the dye and the redox mediator and is presented in Fig. 1.2, where  $E_{0-0}$  is the optical transition from the ground to the excited state of the sensitizer. For  $\text{Co}(\text{bpy})_3^{3+/2+}$ , the standard redox potential is 0.56 V, and most organic dyes have a HOMO level around 1.05 V and a LUMO around -1.14 V (higher than the CB edge of  $\text{TiO}_2$  around -0.5 V vs. SHE).

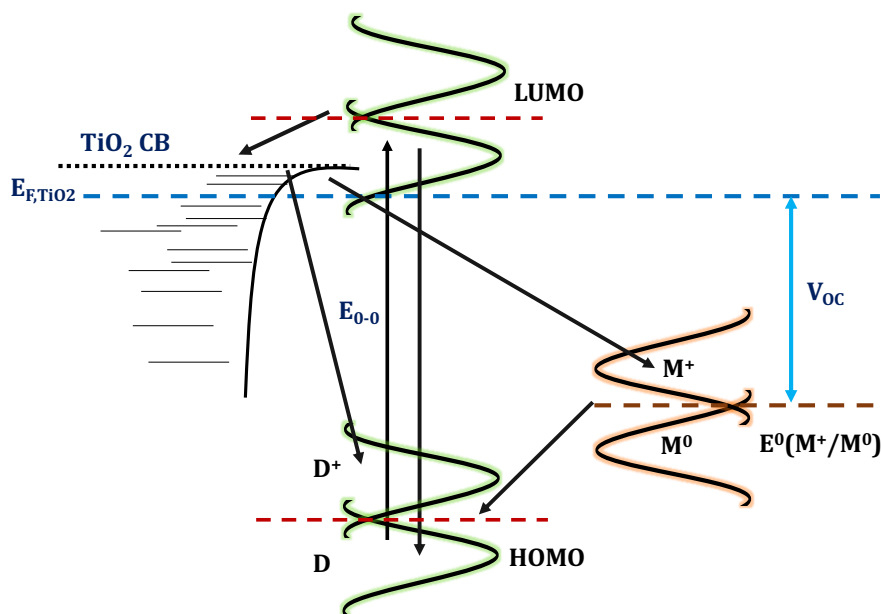


**Figure 1.2.** Gerischer Diagram for electron transfer in DSSC.

The Marcus theory can explain the electron transfer of outer-sphere species, where the rate of electron transfer,  $k_{et}$ , depends on the electronic coupling ( $H_{AB}$ ), the reorganization energy ( $\lambda$ ), and the Gibbs free energy for the transfer reaction ( $\Delta G^0$ ).<sup>41,42</sup> The reorganization energy accounts for two main contributions, the internal reorganization energy ( $\lambda_{in}$ ) due to the change in bond lengths and bond angles and the external reorganizational energy ( $\lambda_{os}$ ) due to the rearrangement of the solvent shell.<sup>43,44</sup> The electronic coupling decreases with the donor and acceptor's distance due to a lower probability of coupling. For non-adiabatic reactions, the electron transfer rate increases with the driving force, and the maximum rate is obtained at  $\Delta G^\ddagger=0$  and  $-\Delta G^0=\lambda$ . This behavior is denoted as the Marcus normal region. If the transfer rate decreases with the driving force, this behavior is denoted as the Marcus inverted region and is presented in Fig.1.3.

$$k_{et} = \frac{|H_{AB}|^2}{\sqrt{4\pi\lambda k_B T}} \exp\left(-\frac{(\Delta G^0 + \lambda)^2}{4\lambda k_B T}\right)$$

Equation 1.10 Electron transfer rate

$$|H_{AB}|^2 = |H_{AB}|^2(r = r_0) \exp[-\beta(r - r_0)]$$

Equation 1.11 Electronic coupling

$$\Delta G^\ddagger = \frac{(\Delta G^0 + \lambda)^2}{4\lambda}$$

Equation 1.12 Activation energy

For most cobalt and copper complexes, the dye regeneration rate falls in the Marcus normal region.<sup>45</sup>

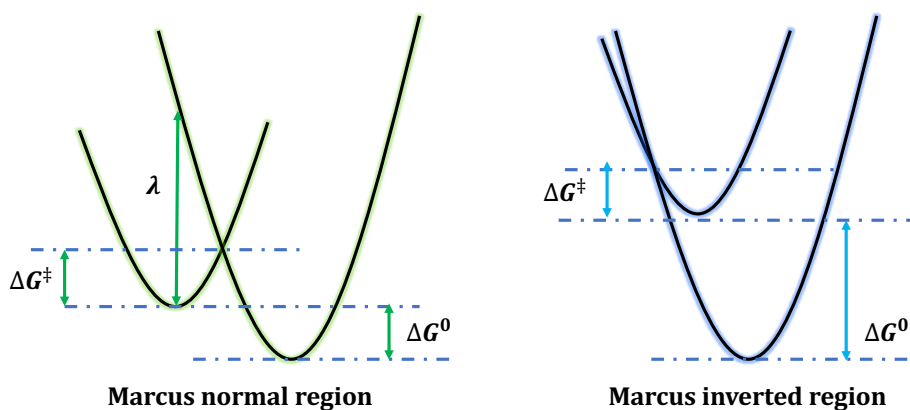


**Figure 1.3.** Energetic parabolas for the Marcus normal and Inverted region

## 1.6 Characterization Techniques

### 1.6.1 J-V characteristic curves

The solar spectrum can be approximated to a black-body radiation, an ideal body that absorbs all wavelength light. By convention, measurements of the efficiency of a solar cell are carried out to an AM (Air Mass) standard of 1.5 G, which simulates the conditions when the sun is at an elevation of 48° with the horizontal and the irradiance is 1000 W/m<sup>2</sup>, at room temperature (25 °C). The standard AM1.5 corresponds to an angle of incidence of 48°, which is chosen as the standard spectrum for solar-cell characterization.<sup>46</sup> The AM1.5 spectra is shown in Fig.1.4.

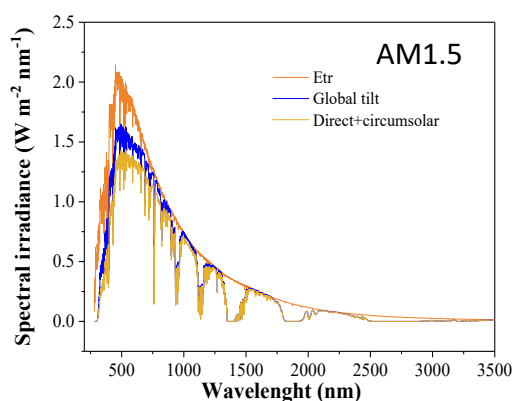


**Figure 1.4.** AST G173-03 reference spectra for AM1.5

The cell's load has an infinite resistance at open-circuit conditions, and the current is zero. Under standard lighting conditions (AM 1.5G), the open-circuit voltage,  $V_{OC}$ , is generated between the cell terminals and is the maximum voltage that the cell can reach. The short circuit current,  $I_{SC}$ , is the current generated under standard lighting conditions when the load has near-zero resistance, and in this case, the voltage is zero. The short circuit current density ( $J_{SC}$ ) normalized by the active area is the maximum current under illumination. A typical characteristic J-V is shown in Fig.1.5.

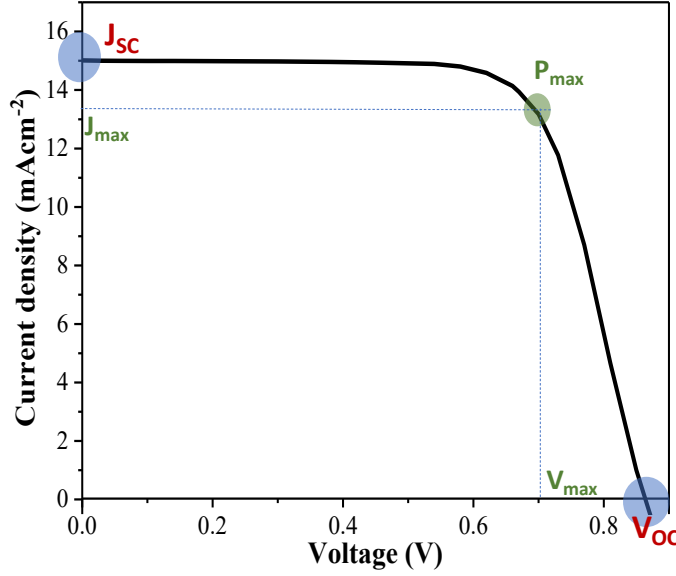


**Figure 1.5.** Characteristic J-V curve for a cobalt-based DSSC.

Using a resistive load  $R$ , the voltage,  $V$ , is smaller than  $V_{OC}$ , and the current density  $J$ , is smaller than the short-circuit current  $J_{SC}$ . The maximum generated power is calculated as:<sup>46</sup>

$$P = J V$$

Equation 1.13 Power calculation

$$dP = d(J V) = JdV + VdJ = 0$$

Equation 1.14. Power derivation

$$P_{max} = J_{max} V_{max}$$

Equation 1.15 Maximum power

The fill factor (FF) is defined as:

$$FF = \frac{P_{max}}{J_{SC} V_{OC}} = \frac{J_{max} V_{max}}{J_{SC} V_{OC}}$$

Equation 1.16 Fill factor calculation

The PCE ( $\eta$ ) is determined by the ratio of the maximum power and the incident power ( $P_{in}$ ) from the solar simulator at AM1.5.

$$PCE = \eta = \frac{J_{sc} V_{oc} FF}{P_{in}}$$

Equation 1.17 Power conversion efficiency

When applying a bias in the dark, a dark current density  $J_{dark}$  is generated in the opposite direction to the photo-generated current:

$$J_{dark} = J_s \left( e^{\frac{qV}{k_B T}} - 1 \right)$$

Equation 1.18 dark current

where  $J_s$  is the saturation current ranges from  $10^{-7}$ - $10^{-9}$  A,  $V$  the applied voltage,  $q$  the elementary charge,  $k_B$  the Boltzmann constant, and  $T$  the absolute temperature. Upon irradiation, the photogenerated current density  $J_{ph}$  is

$$J = J_{ph} - J_{dark} = J_{ph} - J_s \left( e^{\frac{qV}{m k_B T}} - 1 \right)$$

Equation 1.19 Current density

Where  $m$  is the ideality factor and the shunt resistance,  $R_{sh}$ , is the slope of the dark current vs. applied bias. The values for  $R_{shunt}$  should be as high as possible to avoid a shunt current  $J_{sh}$ , parasitic current. The series resistance  $R_{series}$ , on the contrary, should be as low as possible to allow the transport of the photogenerated current to the external circuit. The  $R_{series}$  estimates the overall resistance of the glass substrates and contacts. The short circuit current  $J_{sc}=J_{ph}$  when the applied bias  $V=0$ .<sup>47</sup>

$$J = J_{ph} - J_{dark} - J_{shunt} = J_{ph} - J_s \left( e^{\frac{qV}{m k_B T}} - 1 \right)$$

Equation 1.20 Ideality factor

At open circuit conditions, with no external load ( $J=0$ ), the  $V_{oc}$  can be obtained by eq 1.21, where can denote the photovoltage's dependence with the photogenerated current.<sup>48</sup> The general equivalent circuit of a solar cell is presented in Fig.1.6.

$$V_{oc} = \frac{m k_B T}{q} \ln \left( \frac{J_{ph}}{J_s} + 1 \right) \cong \frac{m k_B T}{q} \ln \left( \frac{J_{ph}}{J_s} \right)$$

Equation 1.21  $V_{oc}$  dependence on the photocurrent

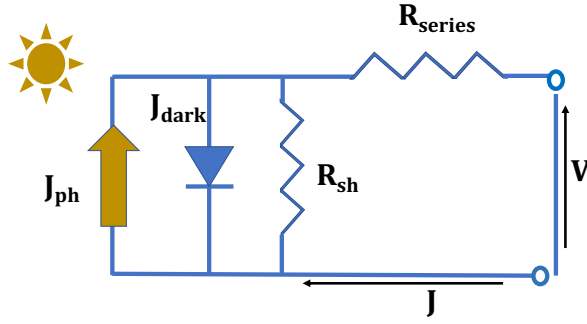


**Figure 1.6.** Equivalent circuit of a solar cell.

The  $V_{OC}$  is determined by the difference between the quasi-Fermi level of the  $TiO_2$  and the mediator's redox potential in the electrolyte.

$$V_{OC} = E_{F,TiO_2} - E_{redox}$$

Equation 1.22  $V_{OC}$  determination

Where normally the  $E_{F,TiO_2}$  value lies around -4.0 eV in the absolute scale,<sup>49,50</sup> and can be converted to the Standard Hydrogen Electrode (SHE) by the relation  $E_{F,TiO_2} = -4.5 \text{ eV} - e_o E_{redox}$ .<sup>51,52</sup>

The quasi-Fermi level of  $TiO_2$  depends on the electron density in the conduction band  $n_{CB}$ , and the density of states in the CB,  $N_{CB}$ ,<sup>53</sup> and can be obtained by:

$$E_{F,TiO_2} = E_{CB} - \frac{k_B T}{q} \ln \left( \frac{n_{CB}}{N_{CB}} \right)$$

Equation 1.23 Fermi level determination

The redox potential of the mediator can be obtained from the standard reduction potential  $E^{0'}$  (referred to SHE) and the concentration of the oxidized and reduced species by the Nernst equation as follows:

$$E_{redox} = E^{0'} - \frac{RT}{nF} \ln \left( \frac{C_{ox}}{C_{red}} \right)$$

Equation 1.24 Nernst equation

## 1.6.2 IPCE

The incident photon to current conversion efficiency (IPCE) corresponds to the photoelectric density produced in the external circuit under monochromatic illumination, divided by the incident photon flux.<sup>54</sup> It can be expressed



in terms of the light-harvesting efficiency (LHE), the electron injection efficiency  $\varphi_{inj}$ , the electron collection efficiency  $\varphi_{coll}$ , and the dye regeneration efficiency  $\varphi_{reg}$

$$IPCE = \frac{J_{sc}}{e \Phi(\lambda)} = 1240 \frac{J_{sc}}{\lambda P_{in}(\lambda)} = LHE \varphi_{inj} \varphi_{coll} \varphi_{reg}$$

Equation 1.25 IPCE determination

The light-harvesting efficiency of the dye depends on the absorption coefficient (A) as follows:

$$LHE = 1 - 10^{-A}$$

Equation 1.26 Light-harvesting efficiency

The integrated short circuit current density can be obtained from the integration of the IPCE at all the illuminated wavelengths according to Eq.1.27. A typical IPCE curve is presented in Fig.1.7.

$$^{Int}J_{sc} = \int IPCE(\lambda) e \varphi(\lambda) d(\lambda)$$

Equation 1.27 Integrated current density

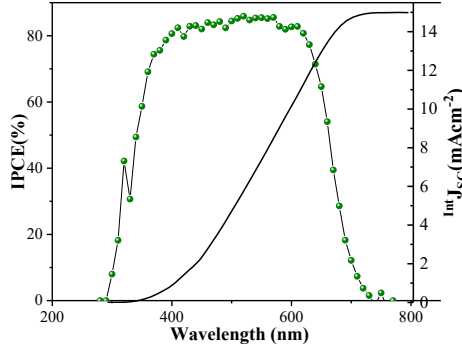


**Figure 1.7.** Typical IPCE curve for a DSSC employing a cobalt-based electrolyte.

The collection efficiency is determined by the competition of the transport of electrons constant rate and the recombination constant rate to the electrolyte.

$$\varphi_{coll} = \frac{k_{trans}}{k_{trans} + k_{rec}}$$

Equation 1.28 Electron collection efficiency

The injection efficiency is determined by injection rate (usually from Femto to Picoseconds) and the relaxation rate from the dye's excited state to the ground state (nanoseconds). All the rate constants are assumed to be pseudo-first-order.

$$\varphi_{inj} = \frac{k_{inj}}{k_{inj} + k_0}$$

Equation 1.29 Electron injection efficiency

### 1.6.3 UV-Vis spectroscopy

The absorption properties of dyes can be studied by UV-Visible spectroscopy.<sup>54</sup> The absorbance is calculated from the transmittance of the sample over a range of wavelength as Eq.1.30. An example of an UV-Vis spectra of a dye designed for DSSCs is presented in Fig.1.8.

$$A(\lambda) = -\log_{10}T(\lambda)$$

Equation 1.30 Absorbance calculation

The extinction coefficient can be estimated according to Lambert-Beer Law:

$$A = \varepsilon Cl$$

Equation 1.31 Lambert-Beer Law

Where  $C$  is the concentration and  $l$  is the path length.

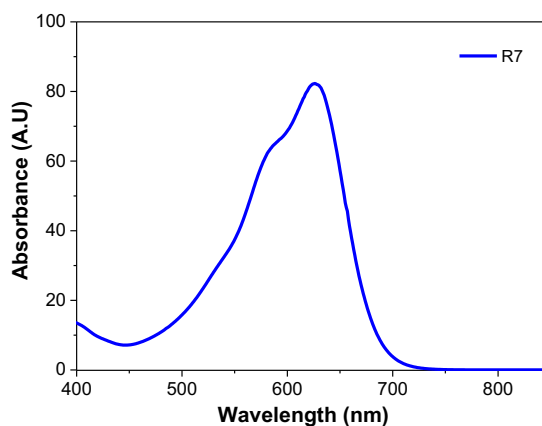


**Figure 1.8.** UV-Vis spectra for the dye R7.

### 1.6.4 TAS

The kinetics of dye regeneration and other dye photo-excited processes can be studied by transient absorption spectroscopy (TAS).<sup>55</sup> Pump pulses generated by a laser such as Nd:YAG, and a continuous probe pulse from a white light source are used to excite the sample and track the induced changes using silicon photodiodes or

photomultipliers as detectors over time, as shown in Fig.1.9. The change in absorbance is calculated from the probe's intensity change in the presence and without the pump as:

$$\Delta A(\lambda) = -\log \left( \frac{I(\lambda)_{pumped}}{I(\lambda)_{unpumped}} \right)$$

Equation 1.32 Absorbance change in TAS

The recombination halftime can be fitted from the absorption decay. The halftime corresponds to the time when the initial amplitude decreased to half, where  $\beta$  is the stretched exponential factor.

$$\Delta A(t) = \Delta A_{t_0} e^{-\left(\frac{t}{\tau}\right)^\beta}$$

Equation 1.33 Absorbance decay

The decay of the dye's excited state in the presence of the inert electrolyte ( $k_{rec}$ ) and with the redox mediator in the electrolyte allowing to obtain the regeneration efficiency is determined as:

$$\phi_{reg} = \frac{k_{reg}}{k_{reg} + k_{rec}} = 1 - \frac{k_{rec}}{k_{redox}} = 1 - \frac{\tau_{rec}}{\tau_{redox}}$$

Equation 1.34 Dye regeneration efficiency

The injection yield can also be determined from TAS in the range of nano-millisecond traces, from the ratio of oxidized molecules to the sum of absorbed photons.  $I_{ex}$  is the intensity of the pump laser,  $\epsilon_{ox}$  is the extinction coefficient of the dye according to Eq.1.35.

$$\phi_{inj} = \frac{\Delta A(\lambda)}{\epsilon_{ox}(\lambda) \times \phi_{LHE} \times I_{ex} \times 1000}$$

Equation 1.35 Injection efficiency

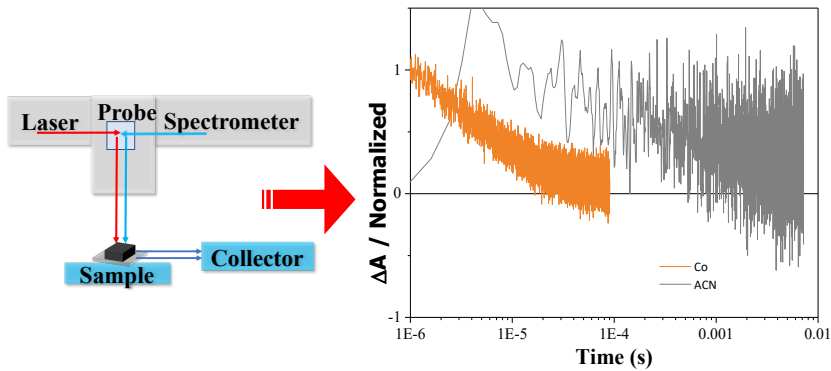


**Figure 1.9.** (a) schematic representation of a TAS set-up and (b) TAS measurements for a sample sensitized with XY1 and  $\text{Co(bpy)}_3^{3+/2+}$  electrolyte and with inert electrolyte.

The J-V curves' characterization only reflects the cell's behavior regarding the characteristic parameters  $J_{sc}$ ,  $V_{oc}$ , and FF to determine the overall performance and the PCE. The internal behavior can be studied by other techniques such as small light-perturbation voltage/current measurements and Electrochemical Impedance Spectroscopy (EIS).

## 1.6.5 Toolbox measurements

The lifetime measurements can provide valuable information about the electron lifetimes and interfacial electron recombination to the electrolyte. The DSSCs are kept at open-circuit conditions for electron lifetime measurements, and the  $V_{oc}$  decay is measured as a function of time at different light intensities after they are turned off.<sup>54</sup> The  $V_{oc}$  decay can be analyzed and fitted from:

$$\tau_e = \frac{-k_b T}{e} \left( \frac{dV_{oc}}{dt} \right)^{-1}$$

Equation 1.36 Electron lifetime

Charge extraction measurements at open circuit conditions can be used to determine the extracted charge,  $Q_{oc}$ , of a solar cell. The  $Q_{oc}$  is related to the stored charge in the  $TiO_2$  mesoporous layer upon irradiation. These studies are beneficial for determining CB shifts and comparing the  $V_{oc}$ 's behavior in different solar cells. The extracted charge at open circuit conditions can be calculated at different light intensities, and can be calculated as:

$$Q_{oc} = \int_{E_{F_0}}^{E_{F_n}} g(E) dE = m_c g_0 \left( \exp \left( \frac{E_{F_n} - E_{F_0}}{m_c k_b T} \right) - 1 \right)$$

Equation 1.37 Charge extraction

where  $m_c$  is the trap distribution parameter and is related to the average trap depth. From eq.1.36 we can note that the  $V_{oc}$  in a DSSC and the charge extraction are exponentially related to traps' distribution in the conduction band. Fig.1.10 illustrates the electron lifetime and charge extraction measurements for DSSCs.

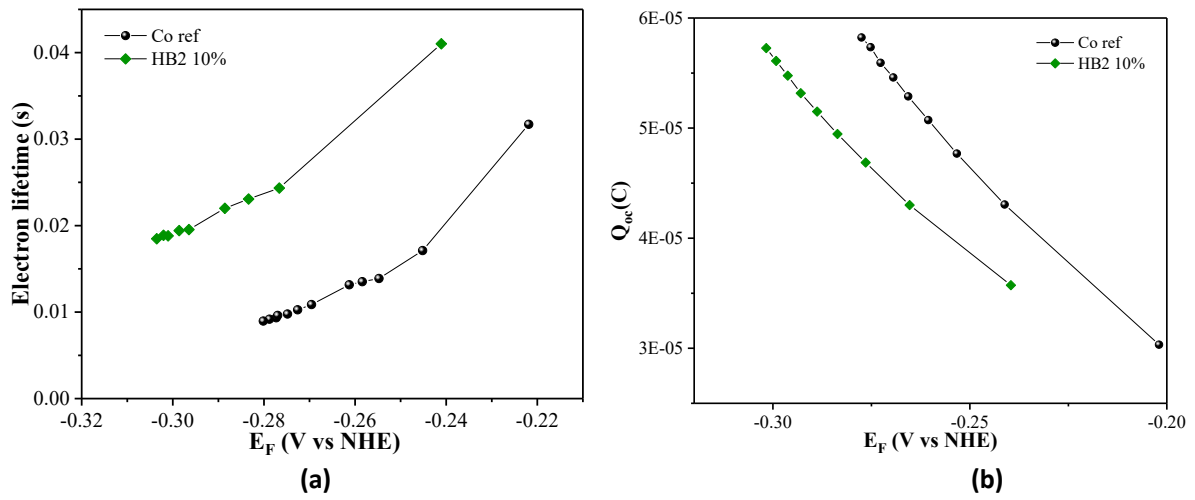


**Figure 1.10.** (a) Electron lifetime vs.  $E_{F,TiO_2}$  and (b) charge extraction vs.  $E_{F,TiO_2}$  for DSSC with cobalt-based reference electrolyte and 10% of polymer HB2.

## 1.6.6 Cyclic voltammetry

Cyclic voltammetry (CV) can be used to determine the redox potential of the redox mediators or the oxidation potential of dyes.<sup>56</sup> A typical voltammogram is shown in Fig.1.11.

The standard reduction potential  $E^{0'}$  (referred to SHE) used to determine the redox potential of the mediator with the Nernst equation (Eq 1.24), can be obtained from the half-wave potential,  $E_{1/2}$ , under standard conditions as the middle point of the oxidation and reduction peaks as shown in Eq.1.38.

$$E^{0'} = E_{1/2} = \frac{E_{p,o} + E_{p,r}}{2}$$

Equation 1.38 Redox potential calculation from CV

The electrochemical reversibility of the redox mediator can be determined from the distance in the oxidation and reduction peaks and the number of transferred electrons,  $n$ , as follows:

$$n|E_{p,o} - E_{p,r}| = 0.057 V$$

Equation 1.39 Peak distance relation

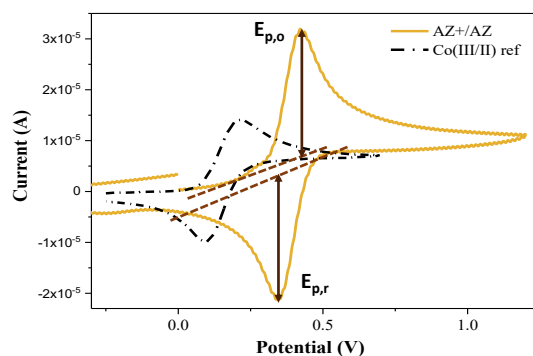


**Figure 1.11.** Cyclic voltammograms for the redox mediator  $\text{Co(bpy)}_3^{3+/2+}$  and the auxiliary redox mediator  $\text{AZ}^+/\text{AZ}^0$ .

The Levich equation estimates the diffusion coefficients of the active species in electrolytes according to the eq. 1.40.

$$i_L = \frac{zF}{1.61} c_i \nu^{-1/6} \omega^{1/2} D_i^{2/3}$$

Equation 1.40 Levich equation

Where  $i_L$  is the limiting current,  $c_i$  is the species' concentration,  $\nu$  the kinematic viscosity,  $\omega$  the rotation rate in  $\text{rad s}^{-1}$ , and  $D$  the diffusion coefficient. The typical shape of a CV using a rotating disk electrode is shown in Fig.1.12.

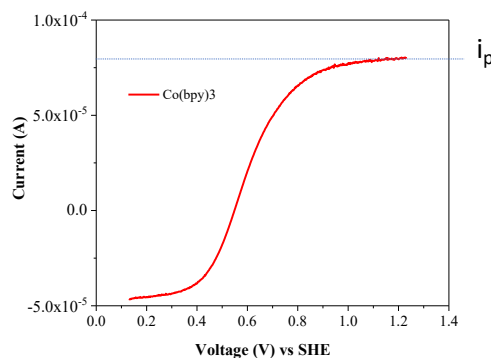


**Figure 1.12** Cyclic voltammetry with a rotating disk at 50 rpm

The electrochemical behavior of the redox species in the electrolyte can also be studied through symmetrical or dummy cells, enclosing the electrolyte under study into CE substrates. The  $J_{lim}$  can be obtained from cyclic voltammetry and be used to determine the diffusion coefficients of the species in the electrolyte.<sup>54</sup>

$$J_{lim} = \frac{2nFDn}{l}$$

Equation 1.41 Limiting current

Generally, the diffusion coefficients are determined by the minority species with sluggish electron transfer from the CE in complete devices. For iodide-based electrolytes, the concentration of  $I_3^-$  is used to determine the diffusion coefficient, the Co(III) species for cobalt-based electrolytes, and Cu(II) species for copper electrolytes.

From the same voltammograms, the exchange current,  $J_0$ , obtained at the intercept  $V=0$ , can be used to study the reversibility of electron-transfer at the CE. The charge transfer resistance,  $R_{CT}$ . Generally, values ranging from  $0.1-2 \Omega\text{cm}^2$  are obtained using PEDOT as a CE with cobalt and copper electrolytes.

$$J_0 = \frac{RF}{nR_{CT}}$$

Equation 1.42 Exchange current

## 1.6.7 EIS

Electrochemical impedance spectroscopy, EIS, is generally used to study in detail all the interfacial phenomena in DSSC. Small variations in  $V(\omega)$  and  $I(\omega)$ . EIS is a steady-state technique, where a small AC voltage perturbation produces a small change in the corresponding AC current, with a phase shift  $\varphi$ , compared to the applied voltage, as presented in eq. 1.43 and 44.

$$V(t) = V_m \sin(\omega t) = V_m \exp(i\omega t)$$

Equation 1.43 AC voltage

$$I(t) = I_m \sin(\omega t + \varphi) = I_m \exp(i\omega t)$$

Equation 1.44 AC current

The frequency is,  $f = \omega/2\pi$ . Thus, the impedance is a complex number, with  $Z'(\omega)$  being the real part and  $Z''(\omega)$  the imaginary part of the impedance.<sup>57</sup>

$$Z(\omega) = \frac{V_m}{I_m} \exp(i\varphi)$$

Equation 1.45 Impedance calculation

$$Z(\omega) = Z'(\omega) + Z''(\omega)$$

Equation 1.46 Impedance as a complex number

The measurements are conducted to ensure a linear dependence of  $I(\omega)$  and  $V(\omega)$  during the impedance measurement to avoid perturbation noises.<sup>58</sup> A frequency scan, from MHz to mHz at a given steady voltage, will produce a Nyquist plot as shown in Fig.1.13. Typically, these measurements are carried at a voltage range, e.g. 0-

1 V, resulting in a Nyquist plot for each voltage step. The Nyquist plots are fitted with an equivalent circuit to unveil all the resistive (R) and capacitive (C) elements that account for the interfaces of the cell's different components. The Warburg elements (W) describe processes of diffusion of active species in the electrolyte. The illumination or dark conditions are kept constant during the whole EIS scan, where a J-V curve can be measured simultaneously.

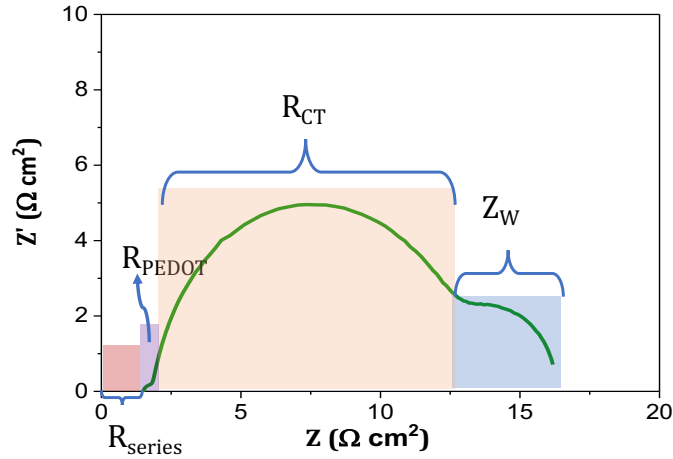


**Figure 1.13.** Typical Nyquist plot for a DSSC with 10% of polymer in a cobalt-based electrolyte at 0.85 V.

The complete equivalent circuit for a DSSC is shown in Fig.1.14, where the main components are the series resistance  $R_{series}$ , arising from the contacts and connections, and as stated before, should be as low as possible. The transport resistance ( $R_{trans}$ ) is the resistance opposed by the  $TiO_2$  mesoporous network to the electron transport on their random path to reach the FTO contact (transmission line) after injection from the dye. The recombination resistance ( $R_{CT}$ ) represents the resistance opposed to the recombination of the electrons from  $TiO_2$  to the electrolyte.<sup>59</sup>  $R_{trans}$  should be at least a couple of orders of magnitude lower than  $R_{CT}$  for a suitable performing device. The chemical capacitance at the  $TiO_2$ -electrolyte interface ( $C_\mu$ ) represents the accumulation of charges at that interphase.<sup>60</sup> The Nernst (Warburg) diffusion ( $Z_d$ ) corresponds to the electrolyte's resistance to the diffusion of the chemical species. Moreover, the counter-electrode resistance ( $R_{CE}$ ) accounts for the load resistance at the counter electrode.

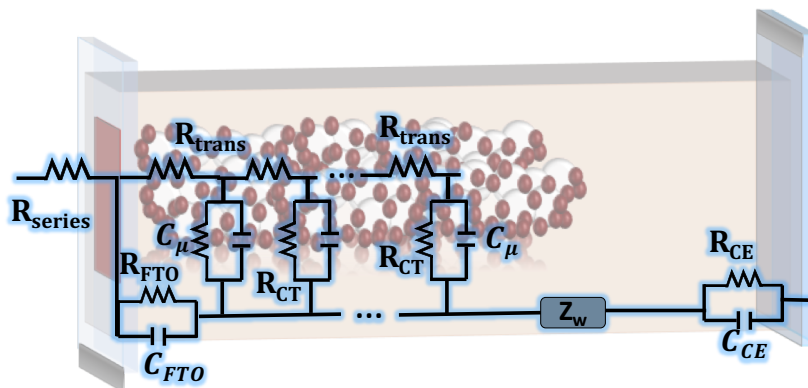


**Figure 1.14.** The complete equivalent circuit for a DSSC including the transmission line.<sup>61</sup>



When a bias change towards higher voltages is applied to a DSSC, the Fermi level of the  $\text{TiO}_2$  shifts towards the CB of the semiconductor, changing the electrons' chemical potential and increasing the chemical capacitance. Therefore,  $C_\mu$  is proportional to the density of available states (DOS), following an exponential trend as a function of the applied voltage. The increase in charge due to a small voltage disturbance ( $dV$ ) corresponds to the traps' filling at the semiconductor's Fermi level.

$$C_\mu = q \frac{dn}{dE_{Fn}}$$

Equation 1.47 Chemical capacitance

$$g(E) = \frac{N_L}{k_B T_0} \exp \left[ \frac{(E - E_{CB})}{k_B T_0} \right]$$

Equation 1.48 Density of states in the CB

The electron transport in the transmission line occurs through surface states by trapping-detrapping.<sup>60-62</sup> When a bias is applied to the semiconductor, the chemical capacitance is also loaded by surface states; this charge transfer produces resistance to recombination with the electrolyte in parallel with the chemical capacitance, as shown in the equivalent circuit in Fig. 1.14.

At dark conditions, an applied bias induces electron injection into the CB of  $\text{TiO}_2$ ; this is coupled with dark current from the movement of the ionic species of the electrolyte. In the dark, the semiconductor's Fermi level is in equilibrium with the redox system's potential. Under irradiation, the photogenerated electrons are injected into the  $\text{TiO}_2$ , shifting the Fermi level towards the CB, increasing the chemical capacitance, as mentioned above.<sup>63,64</sup>

The behavior of a DSSC varies with the applied voltage. At high applied voltages (close to the  $V_{OC}$ ), the  $\text{TiO}_2$  behaves like a conductor since most of the CB's traps are filled with electrons. The Fermi level gets closer to the CB edge of the semiconductor. At these conditions, the resistance  $R_{FTO}$  at the substrate is almost negligible. The  $R_{CT}$  to the electrons' recombination from the CB of the  $\text{TiO}_2$  to the electrolyte is the primary resistive process at the high voltage range. With an increasing number of electrons extracted into the external circuit and subsequently back to the CE, the ionic species  $Z_d$  mobility is sufficient to be observed at low-frequency values. The simplified equivalent circuit under high voltages is illustrated in Fig.1.15.

The electron occupation in the CB of  $\text{TiO}_2$  decreases at medium potentials, causing a resistance opposed by the  $\text{TiO}_2$  to transport electrons throughout the whole layer. This behavior is commonly denoted as the transmission line and is generally fitted with the Bisquert's transmission line model. The  $R_{CT}$  increases significantly at this potential range, and the Warburg element  $Z_d$  is no longer visible.

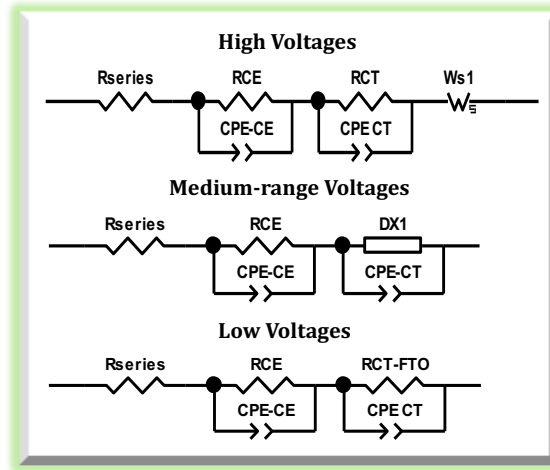


**Figure 1.15.** Simplification of the DSSC's equivalent circuit according to the voltage range, obtained from ZView®.

When the applied voltage is low, generally between 0-0.3 V, the  $\text{TiO}_2$  behaves as an insulating material, and the induced electrons in the system recombine with the electrolyte (dark current). Therefore, at low voltages, the most critical interface is the FTO / electrolyte, with high values for  $R_{\text{FTO}}$ .

From the analysis of the EIS measurements in the whole voltage range, important information can be calculated from the fitted values of  $R_{\text{CT}}$ ,  $R_{\text{trans}}$ ,  $C_{\mu}$  such as the electron lifetime  $\tau_e$ , the transport time  $\tau_{\text{trans}}$ , the DOS, electron diffusion coefficient  $D_n$ , and diffusion length,  $L_n$ . The  $C_{\mu}$  is adjusted to  $C_{\mu, \text{corrected}}$  by normalizing the obtained capacitance (**CPE-T**) by a simple relation accounting for the deviation of the constant phase element to the ideal behavior of a capacitive element (**CPE-P**) and the associated resistance. For example, the chemical capacitance at the interface with the electrolyte  $\text{CPE}_{\text{CT}}$  is corrected as  $C_{\mu, \text{corrected}} = ((R_{\text{CT}} * \text{CPE}_{\text{CT-T}})^{(\text{CPE}_{\text{CT-P}})}) / R_{\text{CT}}$ .

$$\tau_e = -\frac{k_B T}{q} \left( \frac{dV_{\text{OC}}}{dt} \right)^{-1}$$

Equation 1.49 Electron lifetime

$$R_{\text{CT}} = \frac{1}{A} \left( \frac{\partial j_{\text{rec}}}{\partial V} \right)^{-1}$$

Equation 1.50 Recombination resistance

$$\tau_e = R_{\text{CT}} C_{\mu, \text{corrected}}$$

Equation 1.51 Electron lifetime

$$\tau_{\text{trans}} = R_{\text{trans}} C_{\mu, \text{corrected}}$$

Equation 1.52 Transport time

$$DOS = \frac{6.4 \times 10^{18}}{\rho(1-d)} C_{\mu,corrected}$$

Equation 1.53 Density of states

$$\tau_{trans} = \frac{L^2}{D_n}$$

Equation 1.54 Transport time

$$L_n = \sqrt{D_n \tau_n}$$

Equation 1.55 Electron diffusion length

EIS is also used to study symmetrical or “dummy” cells fabricated with two CE substrates and filled with the electrolyte. In general, a frequency scan is set at 0 V, and the obtained Nyquist plots are simulated using the equivalent electrical model shown in Fig 1.16. The series resistance of the symmetric cell ( $R_{series}$ ), the charge-transfer resistance ( $R_{CT}$ ), and the diffusion resistance of the active species in the electrolytes ( $Z_W$ ) can be obtained from the EIS analysis. These measurements are helpful to characterize the behavior of the active species in liquid, polymeric, or ionic liquid electrolytes and to study the charge transfer at the interface of the chosen material as the counter electrode, e.g., PEDOT, Pt, functionalized materials, among others.

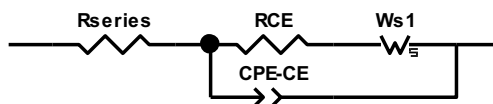


**Figure 1.16.** The equivalent circuit for symmetrical cells for electrochemical studies, obtained from ZView®.

## 1.6.8 FTIR

The functional groups from molecular species can be studied by Fourier Transformed Infrared Spectroscopy (FTIR).<sup>54</sup> The vibrational stretch of the bonds of different functional groups absorbs infrared radiation at specific frequencies that allow for its identification in the sample. An illustration of an FTIR spectrum is displayed in Fig.1.17, where the presence of a siloxane in a sample was determined by the peak at  $2600\text{ cm}^{-1}$  corresponding to the stretch of the Si-H bond.

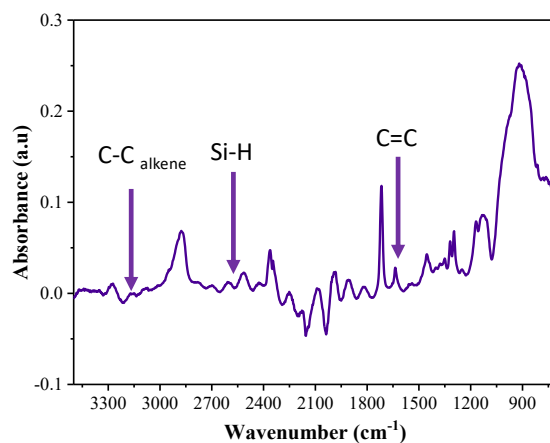


**Figure 1.17.** FTIR spectra for a polymer mixture containing a polyacrylate and a siloxane.

## 1.6.9 SEM

Scanning Electron Microscopy (SEM) can be used to study the morphology of samples by scanning the sample with a focused beam of electrons.<sup>54</sup> The electrons interact with the sample, and the signals can be used to reconstruct the surface's topology as the picture presented in Fig.1.18.

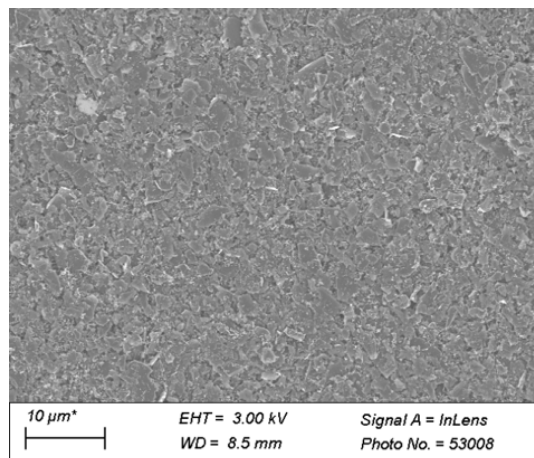


**Figure 1.18.** Top-view image of a carbon-based counter electrode obtained by SEM.

## 1.7 Redox mediators

One of the essential components in a DSSC is the redox mediator. It can significantly influence the main parameters in a DSSC,  $J_{sc}$ ,  $V_{oc}$ , FF, and PCE. The essential function of the redox pair is dye- regeneration, directly influencing the photogenerated current. Moreover, as stated before, the  $V_{oc}$  is controlled by the difference between the mediator's redox potential and the  $TiO_2$ 's Fermi level. The FF is also impacted by the CE material's ability to

transfer charge to the redox mediator efficiently. Another vital factor highly influenced by the used mediator is the diffusion of active species in the electrolyte, which depends on the active species' size. An appropriate redox mediator for high performing DSSCs must be stable and present electrochemical reversibility, afford fast regeneration kinetics, relatively high diffusion coefficients in the electrolyte's solvent, and low charge  $R_{CT}$  at the CE.<sup>65</sup>

## 1.7.1 Iodide

The widely studied mediator  $I^-/I_3^-$  possess a formal redox potential around 0.35-0.4V vs. SHE in ACN,<sup>66</sup> meets most of the criteria described above. Therefore, making it one of the most commonly used electrolytes since the early developments of DSSCs. Several complex reactions and the formation of unstable radicals are involved in dye regeneration by  $I^-/I_3^-$  and a potential drop around 0.3 eV.<sup>67,68</sup> Nonetheless, this mediator presents low recombination kinetics for the electrons from the CB of  $TiO_2$  to the  $I^-/I_3^-$  electrolyte with most ruthenium sensitizers long electron lifetimes, and high diffusion coefficients due to its small size.<sup>24,69</sup>

The halftimes ( $\tau_{1/2}$ ) for the regeneration of most ruthenium dyes by the  $I^-/I_3^-$  shuttle ranges from 10 ns to 10  $\mu$ s, while the  $\tau_{1/2}$  of the recombination of electrons from the  $TiO_2$ 's CB to the electrolyte has been estimated to be around 1  $\mu$ s and around 100 ns to 1ms for the recombination of electrons from the  $TiO_2$ 's CB to the oxidized state of the dye.<sup>70</sup> The recombination of electrons at the interface FTO: $TiO_2$  is normally negligible due to the presence of the "blocking layer" discussed in section 1.4.2, which passivates the surface and significantly reduces the electron recombination with the substrate.<sup>71,72</sup>

Outstanding performance on DSC devices with PCE from 11.0–11.75% employing ruthenium or Zn porphyrin sensitizers and Pt in the CE have been reported for  $I^-/I_3^-$ .<sup>73,74</sup> Recently, an ionic liquid electrolyte and the sensitizer C268 reached 1000 h of stability under light soaking at 60 °C and PCE of 10%.<sup>75</sup> While these redox pair is highly efficient, it's use in large area DSSCs is restricted due to solvent evaporation, leakage, corrosion at the metal contacts, the reaction with glass frit sealant, complexation of additives by  $I^-$ , sublimation of  $I_2$ , among others.<sup>76,77</sup>

Nonetheless, the critical disadvantage of  $I^-/I_3^-$ , is the substantial energy loss due to the difference of the HOMO level of dye with the redox potential of around 0.5 eV. This restricts the attainable  $V_{OC}$  and has been the main incentive to search for different redox mediators with higher redox potential.<sup>68</sup>

## 1.7.2 Cobalt mediators

Higher  $V_{OC}$  values can be reached by replacing iodide with transition metal complexes. Outer-sphere redox couples exhibit fast electron transfer rates, are chemically stable, and undergo minimal structural changes after the electron transfer steps (low reorganization energy).<sup>78,79</sup>

Cobalt complexes with bipyridine ligands have attracted significant attention in DSSC since their redox potential can be tuned by ligand engineering. The electronic structure of Co(II) is  $d^7$ , and high spin (HS) with a paramagnetic nature, whereas Co(III) is  $d^6$ , with a low spin state (LS), and diamagnetic nature. A representation of the electronic configuration of the  $Co^{2+}$  and  $Co^{3+}$  species is presented in Fig.1.19.

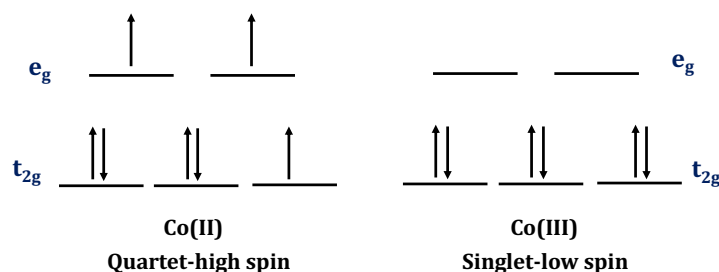


**Figure 1.19.** Representation of the electronic configuration of  $Co^{2+}$  and  $Co^{3+}$  species.

Mosconi et al., reported the calculation of the reorganization energy ( $\lambda$ ) by equilibrium solvation based on the dye's nature as the difference between the single-point energy of the complex with the product's geometry in the solution and the ground-state energy of the reactant cobalt complex. They found that high reorganizational energy is required in the electron transfer step from Co(III) to Co(II) due to the spin change from the Co(III) low-spin state to the Co(II) HS state. For instance, one of the most used cobalt complexes in DSSC,  $Co(bpy)_3^{3+/2+}$ , presents a higher  $\lambda$  of around 1.36 eV for the high-spin Co(II) species compared to around 0.63 eV for the Co(III) low spin state.<sup>80</sup> The energetic barrier for the spin change from  $Co(bpy)_3^{3+}$  to  $Co(bpy)_3^{2+}$  could slow the dye regeneration process due to slower electron transfer rates.<sup>81,82</sup> The amount of energy to undergo the spin change adds to the reorganizational energy to re-arrange Co-ligand length.

For most cobalt outer sphere complexes (Fig.1.20), the one-electron transfer kinetics is relatively fast and within the Marcus normal region, with higher regeneration rates with the increased driving force.<sup>83,84</sup>

The addition of bulkier groups in the ligand to provide steric hindrance decreases the recombination rates from the electrons in the CB of  $TiO_2$  to the cobalt mediator. Nonetheless, this will lead to mass-transport limitations in the electrolyte due to the increase in the complexes' size.<sup>42</sup>

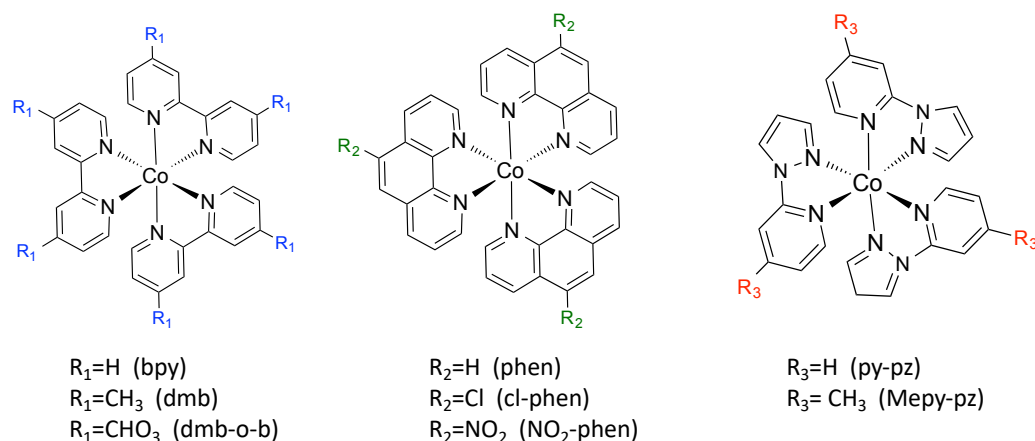


**Figure 1.20.** Molecular structures of cobalt complexes employing as redox mediators in DSSC.

High PCE's can be reached with organic dyes and cobalt complexes.<sup>85</sup> For instance, Yella et al. reported a porphyrin dye reaching PCEs of 12.5% under 1 sun illumination in the presence of  $\text{Co}(\text{bpy})_3^{3+/2+}$ .<sup>86</sup> Matthew et al. reported an engineered dye SM315 to decrease recombination, reaching a PCE of 13%.<sup>87</sup> Kakiage et al. reported the highest-performing DSSC to date, employing a new dye denoted ADEKA-1 with an alkoxysilyl-anchoring group and the mediator  $\text{Co}(\text{phen})_3^{3+/2+}$  reaching the outstanding PCE of 14.3%.<sup>18</sup> Co-based electrolytes' use is highly attractive to fabricate semi-transparent DSSC, making them appropriate for building-integrated photovoltaics (BIPV) applications. Thus, it is a motivation for our research in the following chapters.

### 1.7.3 Copper complexes

Copper complexes have gained ample attention in the past years due to the high performance attainable with their use. The electronic configuration of Cu(I) is  $d^{10}$ , generally forming four-coordinate complexes with tetrahedral geometry. The Cu(II) complexes are  $d^9$  and can adopt geometries such as distorted octahedral, square pyramidal, or trigonal bi-pyramidal. The kinetics for electron transfer steps in Cu(II/I) systems with distorted tetragonal geometry such as  $\text{Cu}(\text{dmp})_2^{2+/1+}$  is relatively fast. Due to the constraints of the structure formed with the ligands, they present minimal reorganization energies.<sup>88</sup>

One of the main advantages of using copper complexes is the decreased overpotential for dye-regeneration, leading to  $V_{\text{oc}}$ s exceeding 1 V. Additionally, the smaller size of these complexes (Fig.1.21) compared to cobalt mediators renders higher diffusion coefficients in the liquid electrolyte. However, these systems present higher recombination rates when compared to cobalt complexes. It has been demonstrated that for copper complexes, the kinetics of electron transfer, the diffusion coefficients, and the electrochemical properties are highly related to the Lewis base's presence in the electrolyte. For instance, 4-tert-butylpyridine (TBP) can coordinate into the Cu(II) species.<sup>89</sup>

The complex  $\text{Cu}(\text{tmby})_2^{2+/1+}$  with two additional methyl groups at 4,6-position have become one of the most employed copper mediators. It holds lower reorganizational energy than most cobalt complexes used in DSSCs, around 0.3 eV, and retains the coordination geometry of Cu(I) when oxidizing to Cu(II). This low  $\lambda$  compared to  $\text{Co}(\text{bpy})_3^{3+}$  (around 0.6 eV) indicates rapid self-exchange reactions and fast dye regeneration rates.

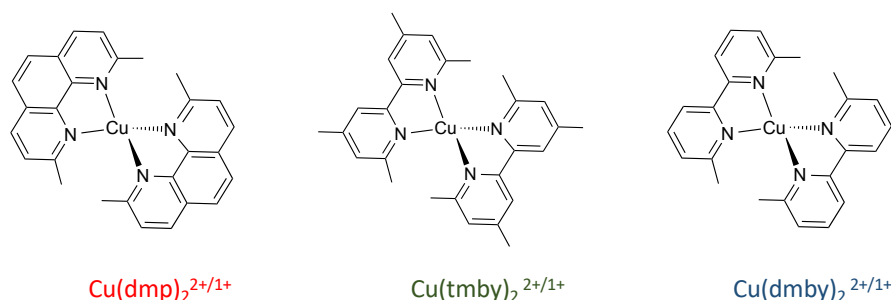


**Figure 1.21.** Molecular structures of copper complexes employing as redox mediators in DSSC.

DSSCs employing  $\text{Cu}(\text{tmby})_2^{2+/1+}$  have reached PCEs of 10% with  $V_{\text{oc}}$  around 1.01 V.<sup>90</sup> Recently, Michaels et al., reported the impressive PCE of 34% under 1000 lux, exceeding the performance of other photovoltaic technologies under these conditions.<sup>20</sup> These findings demonstrate that DSSCs are the best candidates for providing power to a range of electronic devices, including smartphones, tablets, and Internet of Things (IoT) related gadgets.

## 1.8 Interfacial engineering

This thesis aimed to use interfacial engineering to tune the electron transfer rates at the different interfaces DSSCs employing  $\text{Co}(\text{bpy})_3^{3+/2+}$  electrolytes and  $\text{Cu}(\text{tmby})_2^{2+/1+}$  electrolytes to enhance the performance of the devices.

To enhance the electron transfer at the interface dye/electrolyte, a tandem electrolyte employing a small electron donor denoted as AZADO ( $\text{AZ}^{+/0}$ ) in conjunction with  $\text{Co}(\text{bpy})_3^{3+/2+}$  was proposed. Additionally, this strategy was chosen to improve the dye regeneration rate. By improvement of the electrolyte's recombination resistance, it can be expected to increase the  $V_{\text{oc}}$  attainable by Co-based electrolytes. This work is presented in chapter 2.



In addition, in-situ photopolymerization of hyperbranched networks in the  $\text{Co}(\text{bpy})_3^{3+/2+}$  electrolyte was proposed to decrease the recombination at the interface  $\text{TiO}_2$ -electrolyte, to increase the  $V_{\text{OC}}$  and the performance under low light intensity. This work is presented in chapter 3.

Moreover, the high interfacial recombination of electrons from the  $\text{TiO}_2$  CB to copper-based electrolytes limits the performance of devices employing copper-complexes. To address this problem, a blue dye with a bulkier donor moiety leading to high-performing devices was engineered. This work is presented in chapter 4.

Finally, the charge transfer at the interface counter electrode/electrolyte for copper-based electrolytes employing carbon counter electrodes was studied. The performance of DSSC with liquid electrolytes was tested under indoor illumination conditions, intending to determine the feasibility of developing monolithic DSSC based on copper HTMs. This work is presented in chapter 5.



## Chapter 2 Tandem redox systems for reduced back electron reactions

This chapter is adapted from the paper:

***Tandem redox system with cobalt complex and 2-azaadamante-N-oxyl for fast dye regeneration and exceeding open circuit voltage 1 V***

Natalie Flores-Díaz, Hee-won Bahng, Nikolaos Vlachopoulos, Jacques-E. Moser, Shaik M. Zakeeruddin, Michael Grätzel, Anders Hagfeldt

<https://pubs.rsc.org/en/content/articlelanding/2019/TA/C9TA00490D#!divAbstract>

My contribution was all the device preparation and characterization, electrolytes characterization, and manuscript writing.

Hee-won Bahng contributed with the TAS measurements

Nikolaos Vlachopoulos contributed with setting up the cyclic voltammetry.

### 2.1 Motivation

As previously discussed,  $I^-/I_3^-$  has a broad range of applications used due to slow electron recombination and long electron lifetimes;<sup>23,24</sup> being able to attain high energy conversion efficiencies.<sup>25</sup> Conversely, this redox couple has many drawbacks such as corrosiveness, light absorption in the range, but most importantly, a mismatch of the  $I^-/I_3^-$  redox potential with that of the ground state of most dyes of interest for DSSCs. As a result, a significant energy loss occurs during dye regeneration, limiting the  $V_{oc}$  to values between 0.7-0.8 V for  $I^-/I_3^-$  redox electrolytes.<sup>26,27</sup>

Several studies have shown that the redox potential of  $[\text{Co}(\text{bpy})_3]^{3+/2+}$  (where bpy = 2,2'-bipyridine) is closer to the HOMO level of the most efficient dyes. Therefore, less driving force is needed for dye regeneration, resulting in higher open-circuit voltages and higher power conversion efficiencies. Notably, the impressive PCE of 14.3% was reached by the complex  $[\text{Co}(\text{phen})_3]^{3+/2+}$  with a co-sensitized organic dyes (ADEKA and LEG4) photoanode.<sup>18,91,92</sup>

Regardless, DSSCs featuring cobalt complex electrolytes typically show mass transport problems in the electrolyte due to the large size of the complexes, which decreases the dye regeneration rate, and thus results in devices of inferior efficiency.<sup>93</sup>

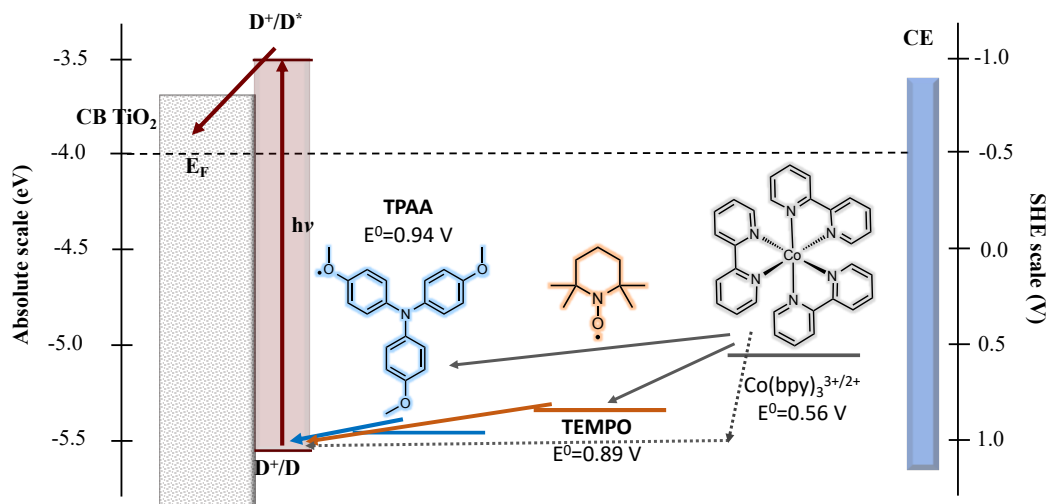
Various authors have demonstrated a different approach to mitigate the voltage loss during dye regeneration and to decrease mass-diffusion limitations of the redox complexes in the electrolyte by developing the so-called **tandem electrolytes**. These systems feature a second redox pair in the electrolyte with a more positive redox potential than that of either cobalt or copper complexes, often denoted as “auxiliary” mediators.

The auxiliary mediators (also known as small electron donors) are chosen to have a higher redox potential than the Co complex and thus, play a major role in increasing the  $V_{\text{OC}}$  of the devices due to an increase in the energetic difference between the Fermi level of  $\text{TiO}_2$  ( $E_{F,\text{TiO}_2}$ ) and the redox potential of the auxiliary redox mediator ( $E_{\text{redox}}$ ), increasing the  $V_{\text{OC}}$ , according to Eq. 1.22.

For instance, the organic stable radical (2,2,6,6-tetramethylpiperidin-1-yl)oxyl, TEMPO, with a redox potential of 0.89 V vs SHE,<sup>94,95</sup> was reported to increase the efficiency of DSSC as a tandem partner to  $[\text{Co}(\text{bpy})_3]^{3+/2+}$  compared to a  $[\text{Co}(\text{bpy})_3]^{3+/2+}$  alone. An increase in PCE from  $\eta=7.1\%$  to  $\eta=8.4\%$  was made possible by using a tandem electrolyte.<sup>96</sup>

Furthermore, a tandem electrolyte based on  $[\text{Co}(\text{bpy})_3]^{3+/2+}$  and the organic electron donor tris(p-anisyl)amine (TPPA) the latter with  $E^\circ = 0.94$  V vs SHE, achieved better DSSC metrics of  $V_{\text{OC}}=920$  mV,  $J_{\text{SC}}=15.5$   $\text{mAcm}^{-2}$ ,  $\text{FF}=73\%$  and  $\text{PCE}=10.5\%$  compared to  $V_{\text{OC}}=820$  mV,  $J_{\text{SC}}=13.9$   $\text{mAcm}^{-2}$ ,  $\text{FF}=72.4\%$  and  $\text{PCE}=8.3\%$  for the reference devices without TPPA.<sup>97</sup> A schematic representation of the mechanism for tandem electrolytes is shown in Fig. 2.1.

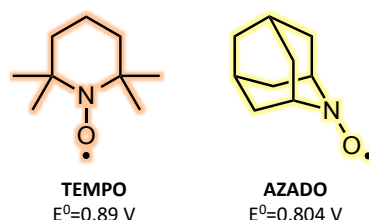
The oxidized species of the auxiliary mediators are regenerated by  $\text{Co}^{2+}$  species, which can also contribute to the dye regeneration. This overall effect of using tandem electrolytes is higher  $J_{\text{SC}}$  values due to the improved regeneration rates. Reducing the electron recombination rates at the  $\text{TiO}_2$ +dye/electrolyte interface is crucial to enhance the performance of DSSCs to efficiencies up to 17%. Engineering and optimization of tandem electrolytes and highly efficient sensitizers with fine-tuning of HOMO and LUMO levels could lead to highly efficient DSSCs.



**Figure 2.1.** Schematic representation of the energetic levels in DSSC employing tandem electrolytes.

## 2.2 New stable organic radical 2-Azaadamantane-N-oxyl

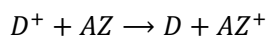
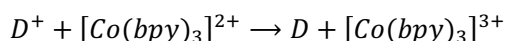
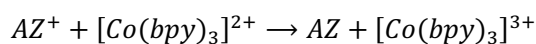
With the aim to increase the stability of the  $\text{TEMPO}^+$  cation in a tandem electrolyte, a TEMPO derivative was judiciously selected. This could potentially result in enhanced  $V_{\text{oc}}$  in the solar cells, leading to increased device performance. The organic radical 2-azaadamantane-N-oxyl, AZADO (abbreviated as AZ), as illustrated in Fig 2.2, was chosen as a donor with a higher steric impediment than TEMPO.<sup>98</sup> The bulkiness of AZADO offers higher stability to its oxidized form  $\text{AZADO}^+$ , as previously demonstrated by Kato et al.<sup>99</sup> The rigidity of AZADO prevents self-disproportionation from the abstraction of an  $\alpha$  H atom, which would lead to the formation of a double bond  $\text{C}=\text{N}$  at the head of the ring.<sup>99,100</sup> Moreover, the steric hindrance can provide higher recombination resistance in DSSCs, leading to higher electron lifetimes and enhanced photovoltage and device performance.



**Figure 2.2.** Molecular structures of the radicals used as small donors in tandem redox systems

In principle, the photo-oxidized dye can be regenerated by reacting either with AZ or with  $\text{Co}^{2+}$ . Given that AZ is a smaller molecule compared to the bulky cobalt complexes, the diffusion of AZ to the working electrode can be expected to be relatively fast. It can be reasonably assumed that dye regeneration to a large extent occurs ac-

cording to Eq. 2.1. The  $AZ^+$  species produced after dye-regeneration are preferentially reduced to AZ by the  $Co^{2+}$  species. The resulting  $Co^{3+}$  species diffuse to the counter electrode as depicted in the reaction from Eq.2.3, which at the same time can provide good protection to prevent the recombination reaction of CB electrons with  $AZ^+$ . The  $Co(II)$  species can also contribute to dye regeneration (Eq.2.2), and higher  $J_{SC}$  can be expected due to an overall increase in the regeneration rate.

Equation 2.1 Dye's regeneration by  $AZ^0$ Equation 2.2 Dye's regeneration by  $Co^{2+}$ Equation 2.3 Regeneration of AZ by  $Co^{2+}$ 

Cyclic voltammetry was performed to determine the redox potential of AZ and is depicted in Fig 2.3. The redox potentials were referenced first vs. the well-known couple ferrocene/ferrocenium and subsequently vs. the standard hydrogen electrode (SHE).<sup>101</sup> The redox potential for the organic donor  $AZ/AZ^+$  was determined to be 0.804 V vs. SHE, which is higher than the  $[Co(bpy)_3]^{3+/2+}$  mediator, with a redox potential of 0.56 V vs. SHE. This indicates an improvement in the difference between the mediator's redox potential and the Fermi level of  $TiO_2$ . As a result, higher  $V_{OC}$  could be reached employing a tandem electrolyte comprised of AZ and Co complexes.

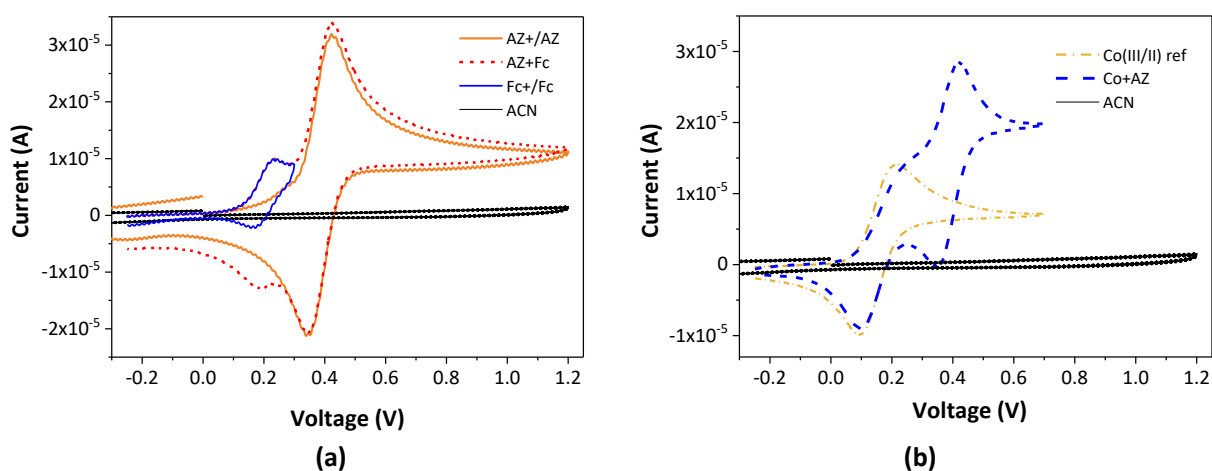


**Figure 2.3.** Cyclic voltammetry with a three-electrode cell with glassy carbon as the working electrode, a graphite rod as the counter electrode, and a non-aqueous reference electrode of Ag/AgCl (2 M in ethanol) and a scan rate of 100 mV s<sup>-1</sup> of (a) AZ 2 mM and (b)  $[Co(bpy)_3]^{2+}$  2 mM and tandem mixture  $[Co(bpy)_3]^{2+}$  + AZ.

Additionally, the recombination of electrons in the conduction band (CB) of the semiconductor to the  $AZ^+$  can be prevented by the steric hindrance from the Co complexes. This can result in longer electron lifetimes, enhanced photovoltage, and device performance. The proposed mechanism for DSSC bearing tandem electrolytes  $AZ+Co(bpy)_3$  is shown in Fig.2.4.

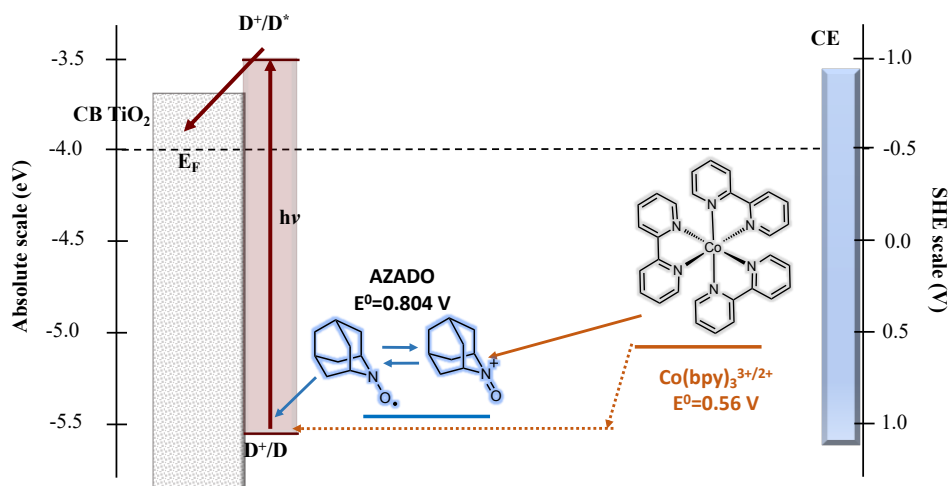


**Figure 2.4.** Schematic overview of the energetic levels in a DSSC with a tandem electrolyte  $[Co(bpy)_3]^{3+/2+}+AZ^{+/0}$ .

Different dyes with appropriate HOMO levels (Fig.2.5) were tested in DSSC with a tandem  $AZ+Co$  electrolyte to demonstrate that high  $V_{OC}$  values could be achieved by employing tandem systems  $AZ+Co(bpy)_3$ . The tandem electrolyte contained 0.22 M  $Co(II)$ , 0.05 M  $Co(III)$ , 0.15 M  $AZ$ , 0.5 M TBP, and 0.1 M of  $LiTFSI$ . The obtained J-V curves are presented in Fig.2.6.

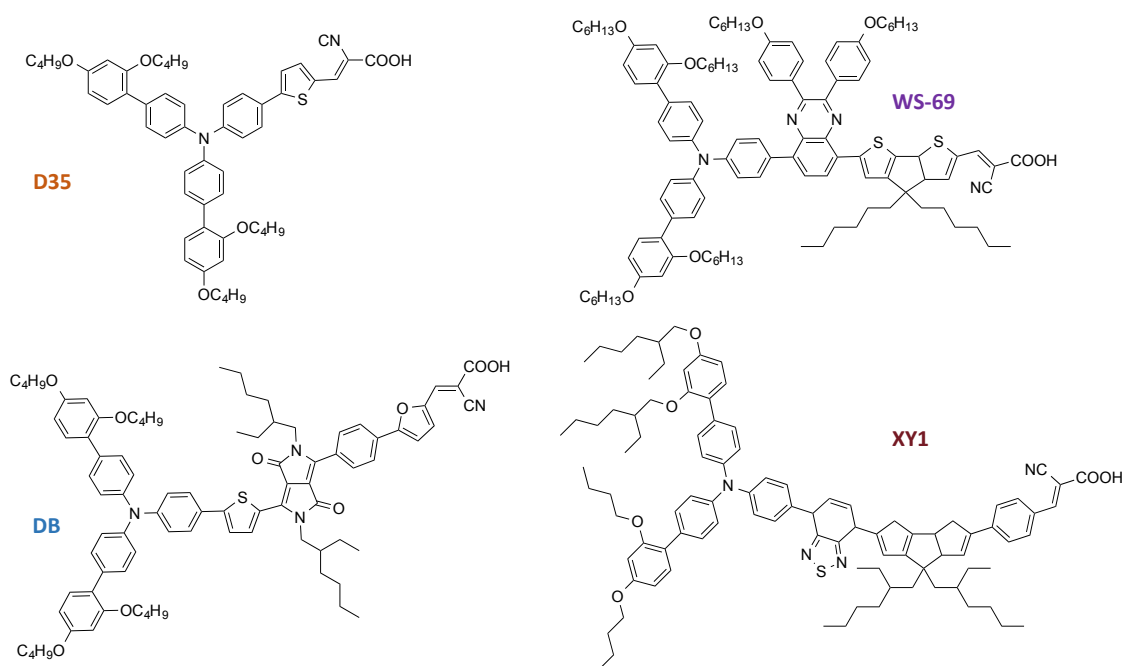


**Figure 2.5.** Molecular structures of dyes tested with the tandem electrolyte.

The characteristic parameters of the best-performing devices for various sensitizers are shown in Table.2.1. It was confirmed that the use of AZ in the redox mediator leads to high  $V_{OC}$  values surpassing 1 V for cells using XY1 as a sensitizer. Consequently, this dye was selected for further optimization of the system.

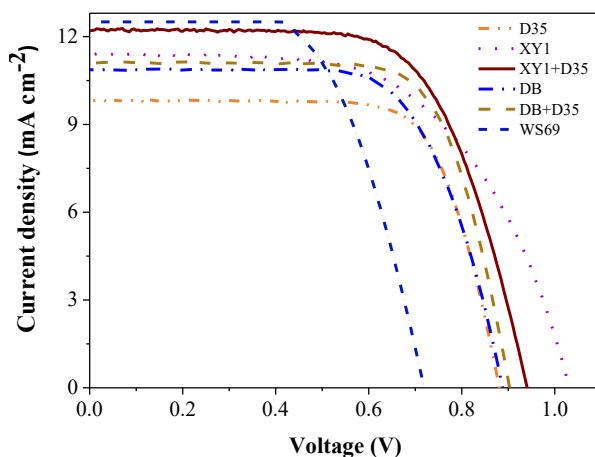


**Figure 2.6.** Photocurrent density vs. voltage (J-V curves) for DSC with tandem electrolyte  $\text{Co}(\text{bpy})_3$  0.22 M + AZ 0.15 M and different sensitizers and PEDOT as CE.

**Table 2.1** Characteristic parameters of DSSCs with tandem electrolyte Co+AZ (0.22 M/0.15 M) and different sensitizers.

Dye	$V_{OC}(\text{mV})$	$J_{SC}(\text{mA cm}^{-2})$	FF	$\eta(\%)$
D35 <b>Co ref</b>	910	8.43	0.67	$5.10^{102}$
D35 <b>Co+AZ</b>	868	9.74	0.74	6.43
XY1 <b>spiro-OMeTAD</b>	942	10.02	0.674	$6.69^{103}$
XY1 <b>Co+AZ</b>	1008	11.24	0.64	7.28
XY1 /D35 1:4 <b>Co+AZ</b>	920	12.21	0.70	8.06
DB <b>Co ref</b>	757	13.21	0.73	$7.3^{104}$
DB <b>Co+AZ</b>	893	11.01	0.67	6.74
DB /D35 3:4 <b>Co ref</b>	797	15.60	0.70	$8.7^{104}$
DB /D35 1:4 <b>Co+AZ</b>	902	11.10	0.72	7.37
WS69 <b>Co+AZ</b>	719	13.12	0.73	6.91

## 2.3 Electrochemical characterization of the tandem electrolyte

To study the electrochemical properties of the designed tandem electrolytes, symmetric cells bearing PEDOT as CE material and the designed tandem electrolytes were fabricated. The current density (log J) curves obtained as a function of voltage (V) are displayed in Fig.2.7. It provides different compositions of the active redox species to determine each component's effect in the tandem electrolytes.



Table 2.2 presents the electrochemical parameters obtained from the analysis of the corresponding Taffel plots. The limiting current remained relatively similar for most of the tandem systems. It was not possible to determine the diffusion coefficient for the individual components in the tandem electrolytes. Therefore, the limiting current accounts for the overall diffusion of all the ionic species in the mixed electrolyte.

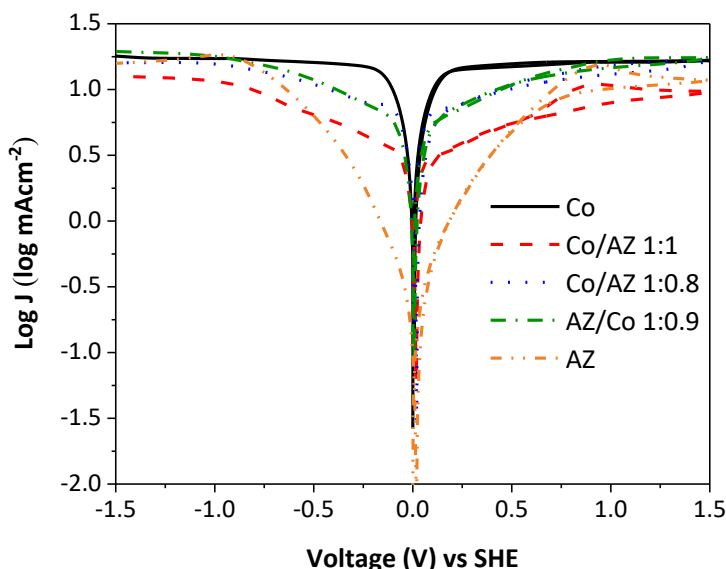


**Figure 2.7.** Log(J) vs. potential plots for symmetrical cells containing tandem electrolytes.

It is possible to observe from Fig.2.7 that AZ's addition to Co-based electrolytes reduced the exchange current,  $J_0$  (intercept at  $V=0$ ). The  $J_0$  is related to the reversibility of electron transfer with the reduced species at the CE. The addition of high concentrations of AZ decreased the electron transfer rate at the CE, resulting in higher charge transfer resistance,  $R_{CT}$ , at the PEDOT CE. The  $R_{CT}$  values were calculated according to Eq. 1.42.<sup>105</sup>

To confirm the Taffel plots' trends, we conducted EIS measurements in the symmetric cells, and the obtained Nyquist plots were fitted using the equivalent circuit from Fig.1.15. The values corresponding to the symmetric cell's series resistance,  $R_{series}$ , the charge-transfer resistance  $R_{CT}$ , and the diffusion resistance of the redox species in the tandem electrolytes,  $Z_w$ . The results are summarized in Table 2.2.

Additionally, a rotating disk electrode was used to determine the diffusion coefficients for the tandem electrolyte. The values provided in Table 2.2, account for the overall diffusion of the species  $Co^{2+}$  and AZ in each mixture, and it was not possible to associate the respective contribution of each species to the overall limiting current (Fig. 2.16). The obtained value for the  $Co(bpy)_3^{2+}$  species was  $7.26 \times 10^{-6} \text{ cm}^2 \text{ s}^{-1}$ , which is consistent with the values recorded by several authors.<sup>106,107</sup> The  $AZ^0$  species in the  $AZ^{+/0}$  electrolyte showed a diffusion coefficient of  $1.58 \times 10^{-5} \text{ cm}^2 \text{ s}^{-1}$ , as predicted from its smaller size compared to the cobalt complexes. In addition, we deter-

mined the diffusion coefficient of the  $AZ^+$  species (Table 2.5 in the experimental section) in the  $AZ^{+/0}$  electrolyte to be  $1.87 \times 10^{-7} \text{ cm}^2 \text{ s}^{-1}$ , which is two orders of magnitude slower than the diffusion coefficient of the  $AZ^0$  species. The low diffusion coefficient for  $AZ^+$  can contribute to the high  $R_{CT}$  at the PEDOT CE observed for the  $AZ^{+/0}$  electrolyte in the symmetrical cells. In a working DSSC under light irradiation, the  $AZ^+$  species generated after dye regeneration can be reduced back to AZ by a nearby  $Co^{2+}$  molecule, thus, the low diffusion coefficients observed for  $AZ^+$  species are not a limiting factor for the well-functioning of the cells.

**Table 2.2.** Characterization data of symmetric cells from Log(J) vs. potential plots and from EIS analysis

Electrolyte	$J_{lim}$ ( $\text{mAcm}^{-2}$ )	$J_0$ ( $\text{mAcm}^{-2}$ )	$R_s$ ( $\Omega\text{cm}^{-2}$ )	$R_{CT}$ ( $\Omega\text{cm}^{-2}$ )	$Z_w$ ( $\Omega\text{cm}^{-2}$ )	$D$ ( $\text{cm}^2 \text{ s}^{-1}$ )
$[Co(bpy)_3]^{3+/2+}$	16.71	8.87	7.53	0.34	7.14	$7.26 \times 10^{-6}$
Co/AZ 1:1	10.94	4.00	8.82	0.54	24.21	$1.39 \times 10^{-5}$
Co/AZ 1:0.8	16.26	7.17	8.20	0.28	15.09	$1.67 \times 10^{-5}$
AZ/Co 1:0.9	17.51	7.64	7.57	0.69	13.55	$1.40 \times 10^{-5}$
$AZ^+/AZ$	15.42	1.12	7.32	81.4	182.6	$1.54 \times 10^{-5}$

The EIS measurements obtained the same patterns observed from the Taffel plots. The system with AZ/Co 1:0.9 presented the lowest value of Nernst diffusion impedance,  $Z_w$  in the electrolyte among the three tandem electrolytes. This can be associated with lower resistance to the actives species' diffusion in the tandem electrolyte, resulting in higher diffusion coefficients.

## 2.4 Device optimization

To better understand each species' role in the tandem systems, different electrolyte compositions were employed in DSSCs. An equimolar ratio of  $Co^{2+}$  and AZ is denoted as (Co/AZ 1:1), an excess of  $Co^{2+}$  denoted as (Co/AZ 1:0.8), an excess of AZ denoted as (AZ/Co 1:0.9). From the J-V curves in Fig. 2.8, we can notice the  $V_{oc}$  and  $J_{sc}$  enhancement when using tandem electrolytes  $Co(bpy)_3+AZ$  compared to bare Co electrolyte, and the characteristic parameters are shown in Table 2.3. Fig.2.8(b) shows that there is a substantial difference in the cobalt reference electrolyte photocurrent at various light intensities, which is well-known to be due to the slow diffusion of the bulky complexes at high light intensities. It can be inferred that in complete devices, the addition of AZ molecules decreases the diffusion limitations typically presented by cobalt complexes, enhancing the dye regeneration rates and improving the linear dependence of photocurrent with the incident light.

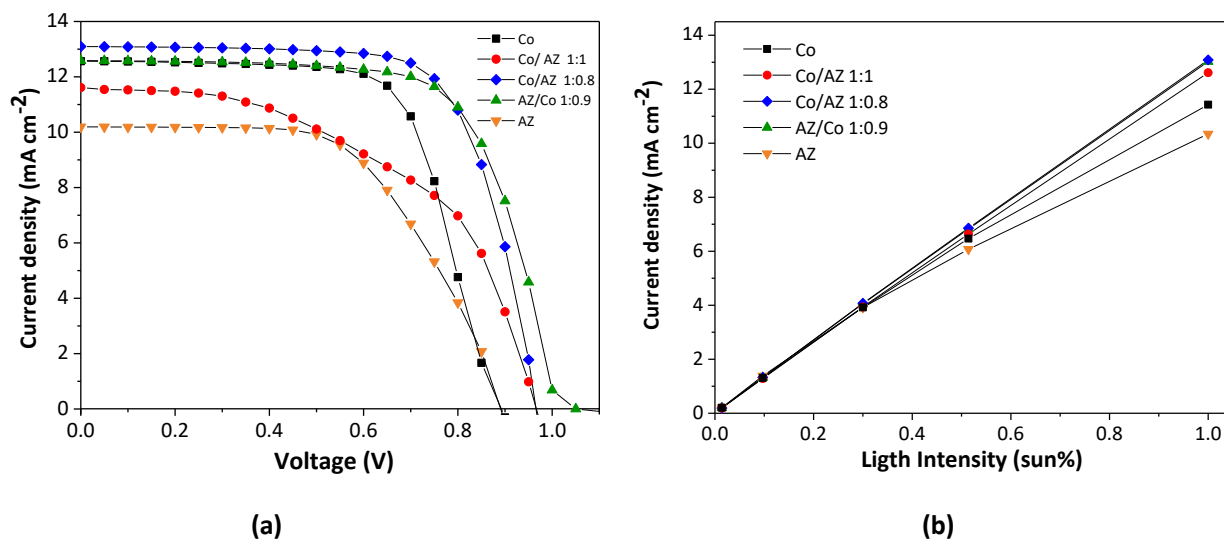


**Figure 2.8.** (a) J-V curves for DSSC with tandem system electrolytes and PEDOT as CE. The Co ref electrolyte is composed of 0.25 M Co(bpy)<sub>3</sub>TFSI<sub>2</sub>, 0.05 M Co(bpy)<sub>3</sub>TFSI<sub>3</sub>, 0.1 M LiTFSI, and 0.5 M 4,5-nonylpyridine, and the tandem systems were prepared using a concentration of Co(bpy)<sub>3</sub><sup>2+</sup> of 0.25 M, and the showed ratios of AZ. (b) light intensity current dependence.

The higher  $J_{SC}$  was reached by the tandem electrolyte composed of an excess of cobalt (II) (Co/AZ 1:0.8). This could be explained by the fact that there is enough Co(II) in the electrolyte to transfer charge to the AZ<sup>+</sup> molecules. It could also indicate that in the tandem system Co(II) also plays a role in the dye regeneration and indicates an enhancement in the dye regeneration rate compared to the Co-reference. For the tandem system with an excess of AZ (AZ/Co 1:0.9), a higher photovoltage exceeding 1 V was obtained. This indicates that AZ plays a significant role in determining the  $V_{OC}$  in the cell, as previously discussed.

**Table 2.3** Characteristic parameters for the best DSSC using XY1 as sensitizer and the different tandem electrolytes.

Electrolyte	$V_{OC}$ (mV)	$J_{SC}$ (mAcm <sup>-2</sup> )	FF	$\eta$ (%)
[Co(bpy) <sub>3</sub> ] <sup>3+/2+</sup>	896	12.87	0.69	7.96
Co/AZ 1:1	997	12.89	0.68	8.52
Co/AZ 1:0.8	968	13.23	0.71	9.15
AZ/Co 1:0.9	1007	13.16	0.69	8.97
AZ <sup>+</sup> /AZ	856	11.82	0.66	6.67

The non-linearity observed for the AZ<sup>+/0</sup> electrolyte Fig.2.8(b) can be explained by AZ's irreversibility at the CE, as demonstrated by the low exchange current at the PEDOT CE in Fig2.7. This irreversibility affects the FF drastically with the increase of light intensity. Even though the AZ molecules can easily reach the photoanode and regenerate the dye, the AZ<sup>+</sup> species are not effectively reduced at the CE. This causes a decrease in the AZ's concentra-

tion and the dye regeneration rate. The tandem system Co/AZ 1:1 presented the same behavior, which indicates that high concentrations of AZ increase the charge transfer resistance at the CE due to AZ's irreversibility mentioned above at the PEDOT CE.

The IPCE for the devices is presented in Fig.2.9. The Co/AZ 1:0.8 tandem system reached the highest IPCE value, agreeing with the high  $J_{SC}$  obtained by this system. Additionally, the IPCE depends on the light-harvesting efficiency, LHE, electron injection efficiency,  $\phi_{inj}$ , and charge collection efficiency,  $\phi_{cc}$ , as in Eq.1.25. The LHE is expected to be close to 100% due to the high molar extinction coefficient of XY1, at its maximum light absorbance. Thus, the  $\eta_{LHE}$  does not explain the differences observed in Fig 2.9. It should be noted, the electron collection efficiency and the electron injection efficiency are expected to directly affect the IPCE in tandem electrolytes. As demonstrated above, the tandem electrolytes presented faster regeneration of the dye molecules, increasing  $\phi_{inj}$ . A faster regeneration rate compared to the recombination rate increase since will increase  $\phi_{cc}$ .

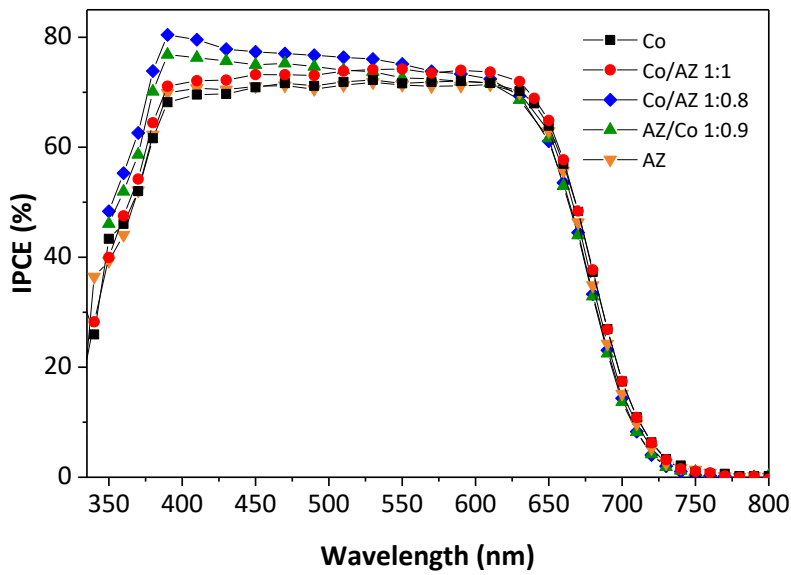


**Figure 2.9.** IPCE curves for the tandem systems

Under illumination, the  $V_{OC}$  for DSSC results from the difference of the quasi-Fermi level,  $E_{F,q}$ , of  $TiO_2$ , and the Nernst potential of the redox couple electrolyte. The  $E_{F,q}$  is determined by electron concentration at the conduction band, which also depends on the electron recombination rate from the CB to the electrolyte.

Charge extraction measurements as a function of light intensity were employed to uncover the  $V_{OC}$  differences for the tandem electrolytes. The obtained results are presented in Fig.2.10 as a function of  $E_{F,q}$ . The Eq. 1.23 was used to determine the quasi-Fermi level for devices with the  $[Co(bpy)_3]^{3+/2+}$  and  $AZ^+/AZ$  electrolyte.<sup>108</sup> For the tandem electrolytes, the  $E_{redox}$  was approximated as the average of the  $E_{redox}$  of  $AZ^{+/0}$  and  $[Co(bpy)_3]^{3+/2+}$ .

This estimation was supported by a chronopotentiometry method at zero current, Fig 2.15 (experimental section). The  $V_{OC}$  of a tandem electrolyte with 2 mM  $[Co(bpy)_3]^{3+}$ , 0.5 mM  $[Co(bpy)_3]^{3+}$ , 0.1 M LiTFSI, 2 mM AZ and 0.1 mM  $AZ^+$  was 0.62 V. Under illumination, the concentration of  $AZ^+$  is rather uncertain. However, the  $Co^{2+}$  species can rapidly reduce  $AZ^+$ , and the concentration of  $AZ^+$  in the electrolyte can be expected to be low. These measurements demonstrated that using the redox potentials' average is a good approximation to estimate the tandem electrolytes' redox potential level.

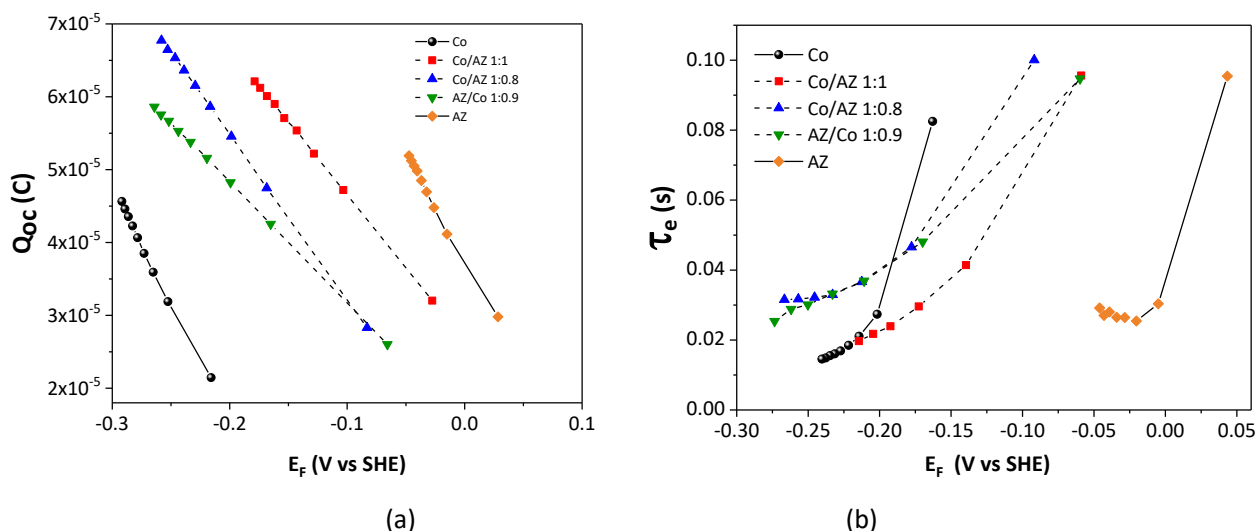


**Figure 2.10.** (a) Charge extraction vs. Fermi level and (b) electron lifetime vs. Fermi level of DSSC containing tandem electrolyte systems. For both plots, the squares correspond to the  $[Co(bpy)_3]^{3+/2+}$  reference, the circles to Co/AZ 1:1, diamonds to Co/AZ 1:0.8, triangles to AZ/Co 1:0.9, and, inverted triangles to the  $AZ^{+/0}$  electrolyte.

A downward shift compared to the  $[Co(bpy)_3]^{3+/2+}$  reference was observed for all the tandem electrolytes in Fig.2.10. The CB's shift could be associated with the adsorption of the  $AZ^+$  cations into the  $TiO_2$  layer, which are reduced to  $AZ^0$  by electrons from the CB, resulting in a decrease in the electron concentration in the CB of  $TiO_2$ .

However, from the J-V parameters, we found that this shift does not result in a  $V_{OC}$  decrease, which could be attributed to a "passivating effect" from the adsorption of  $AZ^+$  species in the  $TiO_2$ , decreasing the electron recombination rate to the electrolyte, improving the electron lifetime and, consequently, the  $V_{OC}$  of the devices. Moreover, even after the CB edge down-shift from the  $AZ^+$  adsorption, the CB edge still lies at values above 0 V vs. SHE.

It is significant to note from Fig 2.10(b), that all the tandem electrolytes presented longer electron lifetimes than the  $Co^{3+/2+}$  electrolyte, which indicates an even lower recombination rate for this system explaining the higher  $V_{OC}$  (exceeding 1 V) obtained for the tandem electrolytes. The differences observed in the IPCE measurements

can be explained by the slight down-shift of the CB of  $\text{TiO}_2$ , resulting in a larger driving force for electron injection from the LUMO of the dye to the CB of  $\text{TiO}_2$ . As a result, the  $\eta_{inj}$  is improved.

To better understand the improvement in  $V_{OC}$  observed in the devices bearing tandem electrolytes, EIS analysis was conducted on complete devices in the dark. The obtained Nyquist plots (Fig. 2.18) were fitted following the transmission-line model from Bisquert et al.,<sup>48</sup> to determine the recombination resistance for the electrons in the  $\text{TiO}_2$  conduction band to the electrolyte  $R_{CT}$ , the chemical capacitance  $C_\mu$ , and the transport resistance  $R_{trans}$ . The obtained results are presented in Fig. 2.11. The electron recombination and electron lifetime follow the same trends under illumination observed from Fig. 2.10. The tandem electrolytes presented improved recombination resistance and longer electron lifetimes than the cobalt reference.

In the high forward bias region, the tandem electrolyte Co/AZ 1:0.8 presented higher recombination resistance than the cobalt reference. This effect is more prominent from 900 mV to higher voltages. Additionally, all tandem electrolytes presented smaller  $R_{trans}$  than the cobalt reference. As expected from the IPCE curves, this explains an improvement in the electron collection efficiency. These findings explain that the highest performance in the J-V measurements for the tandem electrolyte results from improved  $R_{CT}$  and  $R_{trans}$ .

In Fig 2.11(b) we can note a slight upward shift of the CB edge for all the devices containing AZ compared to the cobalt reference, contrary to the behavior observed from the charge extraction measurements under illumination. These findings show that under dark conditions, the generated amount of  $\text{AZ}^+$  is minimal. The CB's displacement to lower energetic values under illumination can be attributed to the adsorption of the  $\text{AZ}^+$  cations into the  $\text{TiO}_2$  layer.

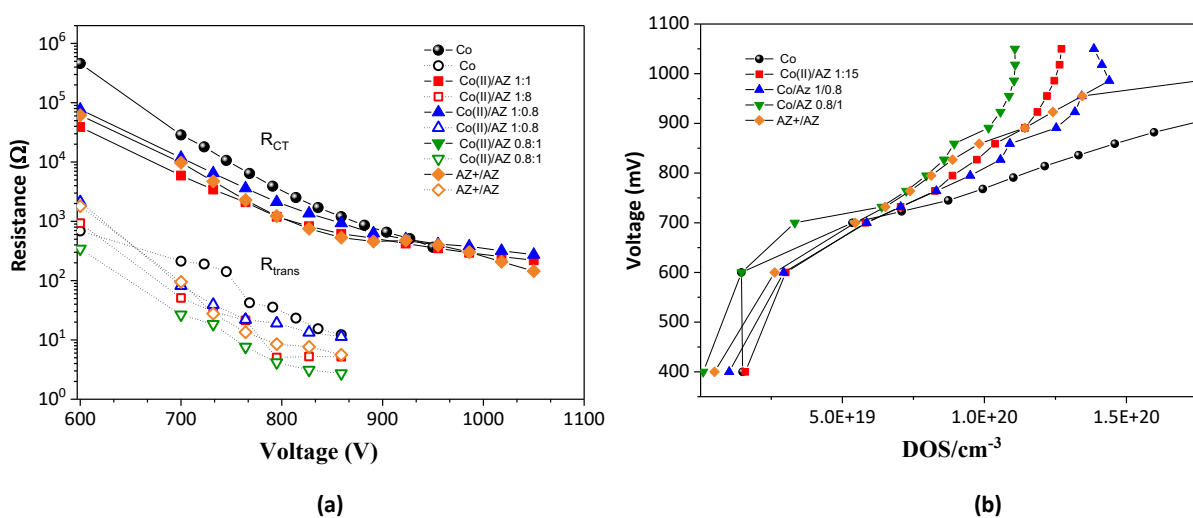


**Figure 2.11.** EIS analysis. (a) Continuous lines with solid markers represent the charge transfer resistance  $R_{CT}$  as a function of applied voltage, and the dotted lines with open markers the transport resistance  $R_{trans}$ . (b) Voltage vs.  $\text{DOS}/\text{cm}^{-3}$ .

Transient absorption spectroscopy measurements were performed to confirm the improved dye-regeneration rates by implementing tandem electrolytes in DSSC, and the results are presented in Fig.2.12. The regeneration half-times obtained from the decay-plot fitting are presented in Table 2.4. The regeneration halftimes for all the tandem electrolytes are faster than the cobalt reference. These results can be explained by the small size and high diffusion coefficients of AZ. Additionally, the  $\text{Co}^{2+}$  species contribute to the regeneration of the dye, resulting in improved regeneration rates. This is further proved by the fact that the regeneration halftimes for the  $\text{AZ}^{+/0}$  are slower than the tandem systems. The higher  $J_{\text{SC}}$  for the tandem electrolyte Co/AZ 1:0.8 can be explained by the fast regeneration half-time among the studied electrolytes.

**Table 2.4.** Regeneration halftimes obtained from transient absorption spectroscopy measurements.

Electrolyte	$\tau_{\text{reg.}}$ ( $\mu\text{s}$ )	$\eta_{\text{reg}}$ (%)
$[\text{Co}(\text{bpy})_3]^{3+/2+}$ ref.	6.29	99.22
Co/AZ (1:1)	2.81	99.65
Co/AZ (1:0.8)	2.13	99.73
AZ/Co (1:0.9)	2.45	99.69
AZ 0.25 M	3.58	99.56
Inert, ACN	0.81 ms ( $\tau_{\text{rec.}}$ )	-

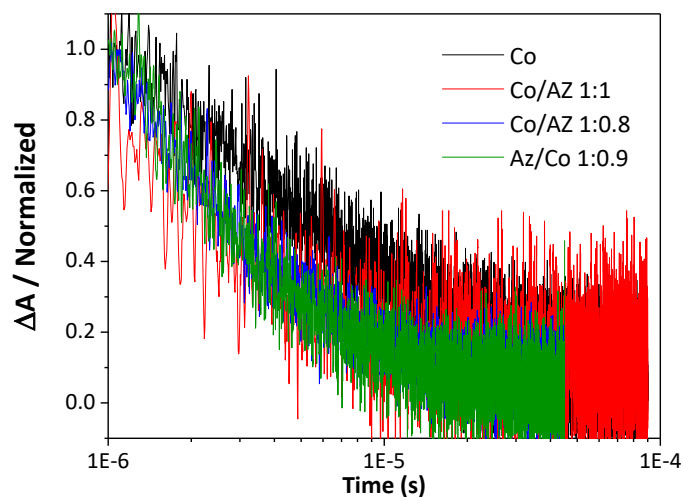


**Figure 2.12.** Transient absorption spectroscopy measurements of DSSC with tandem electrolytes.

## 2.5 Tandem electrolytes with Cu complexes

Recently, the introduction of copper complexes, with high redox potentials ranging between 0.87-0.97 V decreasing the driving force for dye regeneration to only 0.1 – 0.2V, has lead to remarkable performances with  $V_{\text{OC}}$  exceeding 1 V.<sup>109,110</sup> Even though the copper complexes absorb light in the visible region, conversion efficiencies

of 10% for liquid electrolytes,<sup>111</sup> and 11% for solid-state devices using copper complexes as hole transporter materials have been achieved.<sup>112</sup>

It has been previously reported that DSSCs based on  $\text{Cu}(\text{tmby})_2^{2+/1+}$  electrolyte with Y123 as a sensitizer show  $V_{\text{OC}}$  higher than 1 V with high power conversion efficiencies. As previously discussed, the use of small electron donors such as TEMPO and TPPA proved to enhance DSSC's performance when used in tandem electrolytes with cobalt complex. The energetic levels of the TEMPO (0.89 V) and TPPA (0.94 V) are slightly more positive than that of  $\text{Cu}(\text{tmby})_2$  (0.87 V) and have a relatively better match with the HOMO level of the dye Y123. Thus, it could be expected to further enhance the  $V_{\text{OC}}$  and the overall device performance by developing tandem electrolytes. In this regard, novel tandem electrolytes with  $\text{Cu}(\text{tmby})_2$ +TEMPO or  $\text{Cu}(\text{tmby})_2$ +TPPA were proposed, following a charge transfer mechanism as the one shown in Fig. 2.13.

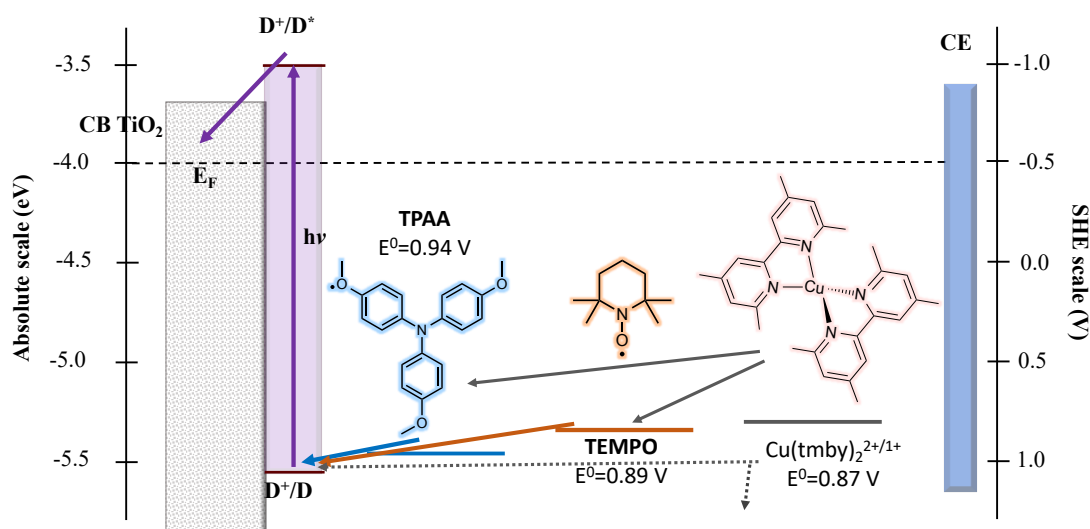


**Figure 2.13.** Schematic representation of the energetic levels in dye-sensitized solar cells.

For this purpose, DSSCs were fabricated by using Y123 as sensitizer, PEDOT as counter electrode (CE) in combination with the electrolytes; a)  $\text{Cu}(\text{tmby})_2\text{TFSI}$  as reference electrolyte (0.22 M of Cu(I), 0.04 M Cu(II), 0.5 M of TBP and 0.1 M of LiTFSI), and tandem electrolytes by adding b) 0.1 M of TEMPO and c) 0.1 M of TPPA to the reference electrolyte. The best performances are presented in Fig.2.14. It was observed that the addition of either TEMPO or TPPA to form tandem electrolytes with  $\text{Cu}(\text{tmby})_2$  decreased all the PV characteristic parameters of the cells compared to the copper reference cell. Even though the energetic levels of the small donors should allow a fast dye regeneration, the interactions of this species with the copper complexes retard this process, and low  $J_{\text{SC}}$  were obtained for the tandem systems. Also, the low FF indicates high recombination rates. Consequently, it is concluded that tandem electrolytes with copper complexes are not the best approach to optimize the dye regeneration over potential in DSSC.



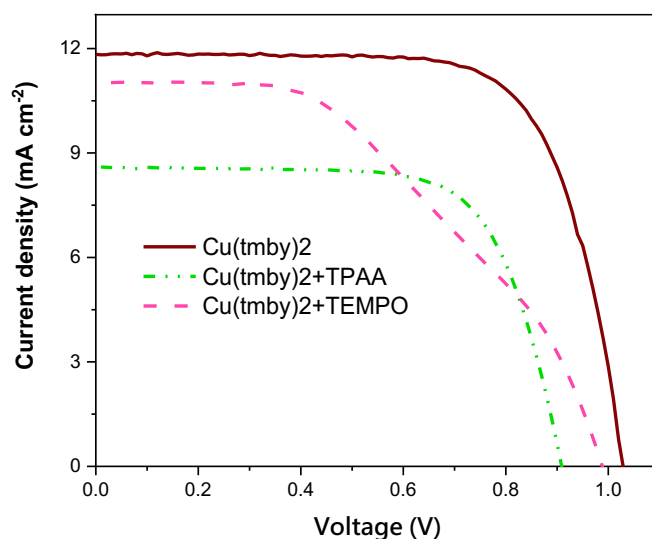


**Figure 2.14.** Photocurrent density vs voltage (J-V curves) for DSC with Y123 as sensitizer, PEDOT as CE and electrolytes with a)  $\text{Cu}(\text{tmby})_2$ , b)  $\text{Cu}(\text{tmby})_2 + \text{TEMPO}$ , and c)  $\text{Cu}(\text{tmby})_2 + \text{TPPA}$ .

**Table 2.5** Characteristic parameters for the best DSSC using Y123 as sensitizer and the different tandem electrolytes with the copper complex  $\text{Cu}(\text{tmby})_2$ .

Electrolyte	$V_{\text{OC}}$ (mV)	$J_{\text{SC}}$ ( $\text{mAcm}^{-2}$ )	FF	$\eta(\%)$
$[\text{Cu}(\text{tmby})_2]^{2+/+}$	1028	10.92	0.72	8.20
$[\text{Cu}(\text{tmby})_2]^{2+/+} + \text{TPAA}$	909	8.57	0.70	5.55
$[\text{Cu}(\text{tmby})_2]^{2+/+} + \text{TEMPO}$	986	10.7	0.38	4.09

## 2.6 Conclusions

The performance of tandem electrolytes containing two redox species in the liquid media was analyzed. The organic radical 2-azaadamante-N-oxyl with the corresponding form ( $\text{AZ}^0/\text{AZ}^+$ ) and the well-known redox pair  $[\text{Co}(\text{bpy})_3]^{2+/3+}$ . The highest performance of DSSCs employing tandem electrolytes was reached by the (Co/AZ 1:0.8) tandem electrolyte, while the system (AZ/Co 1:0.9) reached  $V_{\text{OC}}$  values up to 1009 mV. All the tandem electrolytes presented higher performance than the DSSC devices with the single redox mediators. The improvement in  $V_{\text{OC}}$  was determined to be a result of two main factors, the more positive redox potential of the  $\text{AZ}^{+/0}$  redox couple and the lower recombination rates of the electrons from the CB to the electrolyte. From studying different composition systems, an optimal concentration for  $\text{AZ}^0/\text{AZ}^+$  was obtained. It was determined that high concentrations of AZ decrease the fill factor and may also induce the adsorption of  $\text{AZ}^+$  molecules on the oxide surface. These results demonstrate the advantages of using tandem electrolytes containing two redox mediators and indicate that future work could further improve the  $V_{\text{OC}}$  and overall performance of DSSCs.

It was found that the use of small electron donors such as TEMPO and TPAA in conjunction with copper complexes such as  $\text{Cu}(\text{tmby})_2$  causes a detrimental effect on the overall performance of DSSC.

## 2.7 Supporting information

### Experimental methods

All chemicals and solvents were purchased from Sigma-Aldrich and TCI chemicals, if not otherwise noted, and were used without further purification.

**DSSC fabrication:** Glass substrates with fluorine-doped tin oxide (FTO, NSG-10, Nippon Sheet Glass) were cleaned with 0.2% (w/w) detergent solution in an ultrasonic bath for 1 h and rinsed with water, ethanol and acetone, followed by a UV/O<sub>3</sub> (Model no.256-220, Jelight Company, Inc.) treatment for 15 min. The FTO substrates were immersed for 30 min in a 40 mM aqueous  $\text{TiCl}_4$  solution at 70 °C, to form a thin  $\text{TiO}_2$  blocking layer and then washed with water and ethanol, followed by a sintering process at 250 °C for 2 h. Mesoporous  $\text{TiO}_2$  films of 0.25 cm<sup>2</sup> were prepared by screen printing a 4.5 μm thick colloidal  $\text{TiO}_2$  (Dyesol paste DSL 30 NRD-T) layer and drying at 120 °C in air for 5 min. If needed additional transparent colloidal  $\text{TiO}_2$  layers were added to increase the film thickness layers by screen. Subsequently, a 4 μm thick light-scattering layer consisting of 400 nm sized  $\text{TiO}_2$  particles (Dyesol WER2-0) was deposited on top by screen-printing. The films were then gradually heated in air in an oven (Nabertherm controller P320), applying a four-level program: 125 °C (10 min), 250 °C (10 min), 350 °C (10 min), and 450 °C (30 min). After sintering, the electrodes were treated in aqueous  $\text{TiCl}_4$  at 70 °C for 30 min, and washed with water and ethanol. The thickness of the  $\text{TiO}_2$  films was measured with a profilometer (Veeco Dektak 3). A final heating step at 500 °C (30 min) was performed followed by overnight immersion of the electrodes in the dye bath solution. The dye bath composition was 0.1 mM XY1 (Dyename AB chemicals) with 5 mM CDCA (chenodeoxycholic acid) in tert-butyl alcohol and acetonitrile (1:1). After immersion, all films were rinsed in acetonitrile to remove the excess of dye. Solar cells were assembled using a 25 μm thick thermoplastic Surlyn® frame as sealant and spacer between electrodes, with a counter electrode composed of poly (3,4-ethylenedioxythiophene) (PEDOT) deposited on NSG TEC8™ (Pilkington) FTO-type conducting glass. The PEDOT electrodes were prepared by electropolymerization of 3,4-ethylenedioxythiophene (EDOT) from a micellar aqueous solution of 0.1 M sodium n-dodecyl sulfate (SDS) and 0.01 M EDOT. The electrolyte solution was introduced under vacuum through a hole predrilled in the counter electrode, which was sealed with thermoplastic Surlyn® and a glass coverslip. The electrolyte compositions were

**a) the cobalt reference electrolyte:** 0.22 M  $\text{Co}(\text{bpy})_3(\text{TFSI})_2$  (bpy = 2-2'-bipyridine, TFSI =  $\text{N}(\text{CF}_3\text{SO}_2)_2$ ) (Dyename AB chemicals), 0.05 M  $\text{Co}(\text{bpy})_3(\text{TFSI})_3$  (Dyename AB chemicals), 0.1 M LiTFSI, and 0.5 M 4-(5-nonyl)pyridine (NP) in acetonitrile, and the tandem systems consisted of:

**b) Co/AZ 1:1:** 0.22 M of AZ, 0.22 M  $\text{Co}(\text{bpy})_3(\text{TFSI})_2$ , 0.05 M  $\text{Co}(\text{bpy})_3(\text{TFSI})_3$ , 0.1 M LiTFSI, and 0.5 M NP in acetonitrile,

**c) Co/AZ 1:0.8:** 0.17 M of AZADO, 0.22 M  $\text{Co}(\text{bpy})_3(\text{TFSI})_2$ , 0.05 M  $\text{Co}(\text{bpy})_3(\text{TFSI})_3$ , 0.1 M LiTFSI, and 0.5 M NP in acetonitrile,

**d) AZ/Co 1:0.9:** 0.17 M AZ, 0.15 M  $\text{Co}(\text{bpy})_3(\text{TFSI})_2$ , 0.0375 M  $\text{Co}(\text{bpy})_3(\text{TFSI})_3$ , 0.1 M LiTFSI, and 0.5 M NP in acetonitrile and

**e) the  $\text{AZ}^+/\text{AZ}^0$  electrolyte:** 0.25 M AZ, 0.05 M  $\text{AZ}^+$ , 0.1 M CDOA, 0.1 M LiTFSI, and 0.5 M NP. In the latter electrolyte,  $\text{AZ}^+$  is generated by addition of the oxidant 0.05 M  $\text{NOBF}_4$  into an electrolyte containing 0.3M AZ and the other components. The symmetric cells were fabricated with two PEDOT/FTO electrodes sealed together with 35  $\mu\text{m}$  Surlyn<sup>®</sup> and filled with the redox electrolytes to be tested.

**Electrochemical Measurements:** Cyclic voltammetry measurements were performed with a potentiostat Bio Logic SP300, in a three-electrode setup cell. A glassy carbon electrode served as the working electrode (0.07 cm<sup>2</sup> area) and a graphite rod as the counter electrode; a non-aqueous reference electrode of Ag/AgCl (1 M LiCl in ethanol) was used, with an intermediate bridge tube containing the same supporting electrolyte as the working electrode compartment. The electrolyte solutions contained 2 mM of AZ, and 0.1 M of LiTFSI as supporting electrolyte in dry acetonitrile. The scan rate was 100 mV s<sup>-1</sup>, formal potentials were determined vs ferrocenium/ferrocene as a reference system, and then vs SHE (with a value established for  $\text{Fc}^+/\text{Fc} = 0.624$  V versus SHE in acetonitrile and 25 °C).<sup>101</sup> Cyclic voltammetry measurements to determine the current-potential plots of the symmetrical cells were also performed with the Bio Logic SP300 potentiostat.

**Solar Cell Characterization:** Current–voltage (I–V) characteristic curves and photocurrent-dynamics were measured using a 450 W Xenon lamp (Oriel USA) as light source, with a K113 filter Schott Tempax and matched to AM 1.5G solar standard conditions using a reference Si photodiode. The current and voltage were measured and controlled by a Keithley 2400 digital source meter (Keithley, USA) and the current measurement was set up to be delayed 80 ms from applying the potential. A set of metal mesh filters was used to adjust the light intensity to a desired level. A black metal mask with a 0.16 cm<sup>2</sup> aperture was used to define the active area.

**Incident Photon to Current Efficiency, IPCE:** Data were obtained using a modulated light intensity with a frequency of 1 Hz. Light from a 300 W xenon light source (ILC Technology, USA), was focused through a monochromator (JobinYvon Ltd., UK) and directed to the device under test. A white light bias was used to have similar light intensity conditions as during normal operation.

**Electron lifetime measurements:** The measurements were recorded with a Dyenamo AB (Sweden) toolbox using a white LED (Luxeon Star 1W) as light source. Voltage traces were recorded with a 16-bit resolution digital acquisition board (National Instruments); lifetimes were obtained by monitoring photovoltage transients at different light intensities upon applying a small square wave modulation to the base light intensity. The photovoltage

response was fitted using first-order kinetics to obtain time constants. The quasi-Fermi level of  $\text{TiO}_2$  for the devices was calculated by subtracting the reached values of  $V_{\text{OC}}$  to the redox potential of each specific electrolyte

**Electrochemical Impedance Measurements (EIS):** Impedance measurements were performed using a Bio Logic SP300 potentiostat, over a frequency range from 1 MHz down to 0.1 Hz at bias potentials between 0 and 1.1 V (with a 10 mV sinusoidal AC perturbation). All measurements were done at 20 °C. The resulting impedance spectra were analyzed with Z-view software (v2.8b, Scribner Associates Inc.).

**Transient Absorption Spectroscopy:** Nanosecond flash photolysis was used to monitor the microsecond-to-millisecond dynamics. Excitation pulses were generated by frequency-doubled (532nm) Q-switched Nd:YAG laser (Continuum Surelight, 20 Hz repetition rate). The excitation fluence for observing charge recombination was attenuated to less than  $<30 \mu\text{J}/\text{cm}^2$  per pulse, which ideally corresponds to an average of less than 1 electron injected per  $\text{TiO}_2$  particle. A continuous wave, cw, Xe arc lamp was used to generate the probe beam. This beam was passed through various filters, a monochromator and multiple lenses before reaching the sample. The resulting probe signal was set at a wavelength of 735 nm and the beam passing through a sample is collected by a second monochromator and delivered to a fast photomultiplier tube (R9910, Hamamatsu) supplied with 750 V, in which the absorption of photons results in electron emission. To obtain a satisfactory signal-to-noise ratio, a digital signal analyzer (DPO 7104C, Tektronix) records the induced transient voltage signal, and the data acquisition is averaged over 3000 laser shots, resulting in a sensitivity of  $10^{-4} \Delta\text{A}$ .

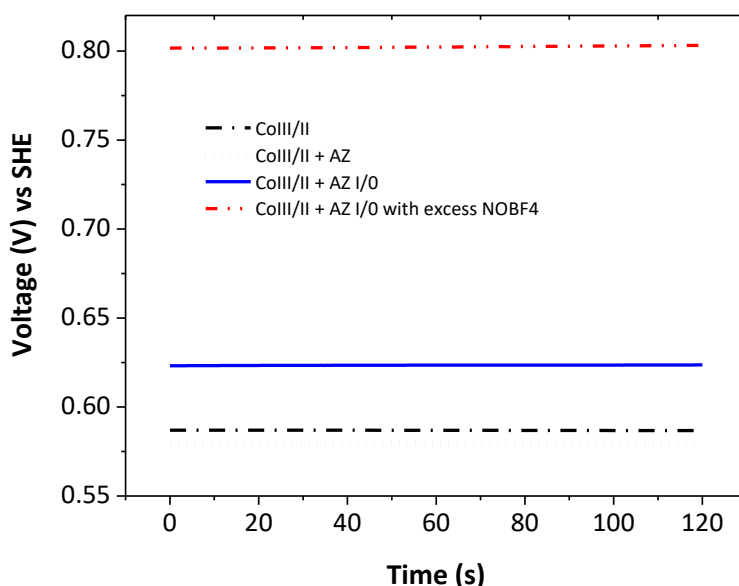


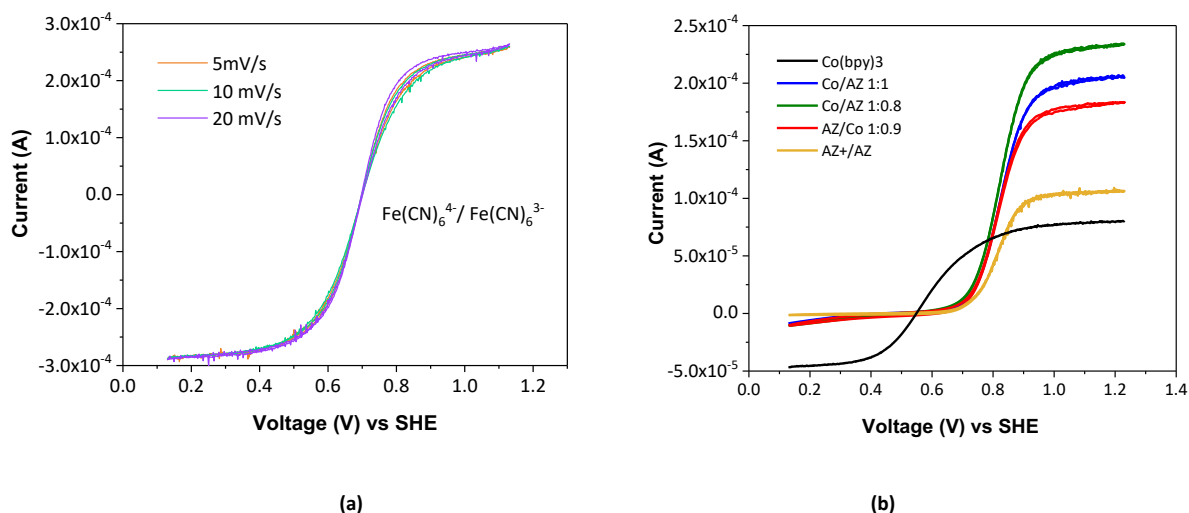
**Figure 2.15.** Plot of voltage vs time in a chronopotentiometry method (zero current) of (a) 2 mM  $\text{Co}(\text{bpy})_3^{2+}$ , 0.5 mM  $\text{Co}(\text{bpy})_3^{3+}$ , 0.1 M LiTFSI (dash-dotted black line), (b) 2 mM  $\text{Co}(\text{bpy})_3^{2+}$ , 0.5 mM  $\text{Co}(\text{bpy})_3^{3+}$ , 0.1 M LiTFSI, 2 mM AZ (dotted red line) and (c) 2 mM  $\text{Co}(\text{bpy})_3^{2+}$ , 0.5 mM  $\text{Co}(\text{bpy})_3^{3+}$ , 0.1 M LiTFSI, 2 mM AZ, 0.1 mM  $\text{AZ}^+$  by adding the corresponding amount of  $\text{NOBF}_4$  (solid blue line), and (d) excess of  $\text{NOBF}_4$ .

### Diffusion coefficients measurements:

Current-voltage measurements were performed via a rotating disk electrode. A potentiostat/galvanostat AUT 71326 Metrom/Autolab, with a three-electrode set-up with a glassy carbon rotating disk electrode as working electrode and a graphite rod as the counter electrode; a non-aqueous reference electrode of Ag/AgCl (1 M LiCl in ethanol) were used, with an intermediate bridge tube containing the same supporting electrolyte as the working electrode compartment. A water flow at 25 °C was used to keep the cell temperature constant at 25 °C. The rotor speed was controlled by a speed control unit (Radiometer Analytical-CVTV101) and set at 1000 rpm for all the experiments. A calibration with an electrolyte of 1 M NaOH,  $1.00 \times 10^{-2}$  M of  $\text{Fe}(\text{CN})_6^{3-}$  and  $1.04 \times 10^{-2}$  M  $\text{Fe}(\text{CN})_6^{4-}$  was performed, using the diffusion coefficients of  $6.77 \times 10^{-6} \text{ cm}^2 \text{ s}^{-1}$  and  $5.81 \times 10^{-6} \text{ cm}^2 \text{ s}^{-1}$  respectively, as reported by Bazán, et.al.<sup>113</sup> The Levich equation (Eq.2.4) was used to determine the diffusion coefficients, where  $i_L$  is the limiting current ( $\text{A cm}^{-2}$ ),  $c_i$  the concentration in  $\text{mol cm}^{-3}$ ,  $\nu$  the kinematic viscosity in  $\text{cm}^2 \text{ s}^{-1}$ ,  $\omega$  the rotation rate in  $\text{rad s}^{-1}$  and  $D$  the diffusion coefficient in  $\text{cm}^2 \text{ s}^{-1}$ , and the electrode area was determined to be  $0.0337 \text{ cm}^2$

$$i_L = \frac{zF}{1.61} c_i \nu^{-1/6} \omega^{1/2} D_i^{2/3}$$

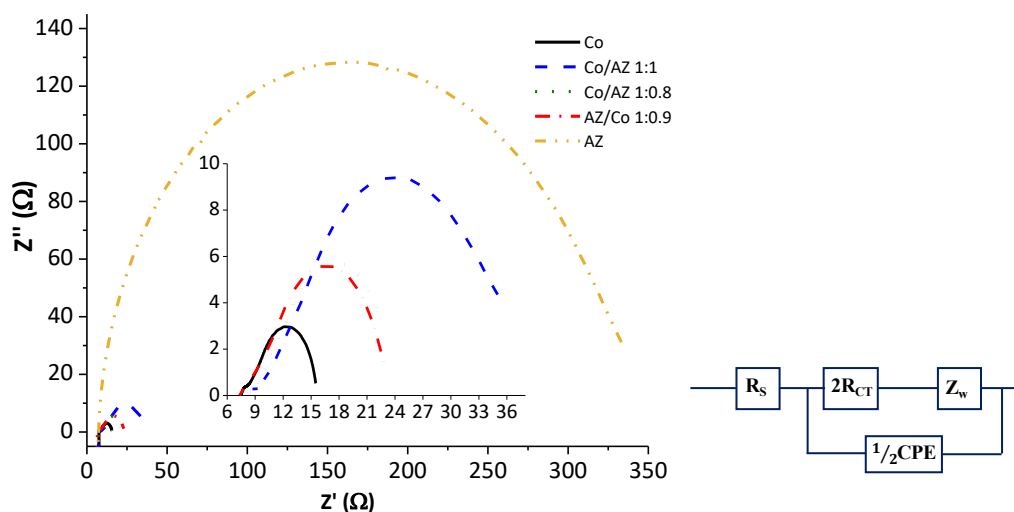
Equation 2.4 Diffusion coefficient from rotatory disk electrode



**Figure 2.16.** Current vs voltage plots measured with a rotatory disk electrode (a) calibration with  $\text{Fe}(\text{CN})_6^{3-}$  and  $\text{Fe}(\text{CN})_6^{4-}$  electrolyte and (b) tandem system electrolytes.

**Table 2.5.** Diffusion coefficients of the active species in acetonitrile, measured with a rotatory disk electrode.

Electrolyte	Active species	Concentration (mM)	$j_{lim}$ (A/cm <sup>2</sup> )	$D$ (cm <sup>2</sup> /s)
Co(bpy) <sub>3</sub>	Co(II)	2.00	$3.91 \pm 0.15E-03$	$7.26 \pm 0.42E-06$
	Co(III)	0.5	$-8 \pm 1E-04$	$1.11 \pm 0.22E-05$
AZ	AZ	2	$3.22 \pm 0.05E-03$	$1.54 \pm 0.02E-05$
	AZ <sup>+</sup>	0.4	$-4.2 \pm 0.2 E-05$	$1.87 \pm 0.1E-07$
Co/AZ 1:1	Co(II)	2	-	-
	AZ	2	-	-
	Total	4	$6.04 \pm 0.07E-03$	$1.39 \pm 0.03E-05$
	Co(III)	0.5	$-2.73 \pm 0.1E-04$	$3.04 \pm 0.1E-06$
Co/AZ 1:0.8	Co(II)	2.4	-	-
	AZ	2	-	-
	Total	4.4	$7.48 \pm 0.04E-03$	$1.67 \pm 0.01E-05$
	Co(III)	0.5	$-3.40 \pm 0.08E-04$	$4.22 \pm 0.1E-06$
AZ/Co 1:0.9	Co(II)	1.8	-	-
	AZ	2	-	-
	Total	3.8	$5.46 \pm 0.05E-03$	$1.40 \pm 0.02E-05$
	Co(III)	0.4	$-3.22 \pm 0.4E-04$	$3.90 \pm 0.7E-06$

**Figure 2.17.** Nyquist plots for symmetric cells containing the tandem electrolyte systems, at 0 V.

**Table 2.6.** Photovoltaic parameters of DSSC with the dye XY1, PEDOT as CE and different electrolyte systems.

Light intensity	Parameter	Co(III/II) Ref	Co(II)/AZ 1:1	Co(II)/AZ 1:0.8	Co(II)/AZ 0.8:1	AZ+/AZ
<b>0.1 Sun</b>	<b>V<sub>oc</sub>(mV)</b>	823 ± 22	839 ± 4	853 ± 9	858 ± 13	811 ± 13
	<b>J<sub>sc</sub>(mAcm<sup>-2</sup>)</b>	1.36 ± 0.09	1.30 ± 0.03	1.33 ± 0.05	1.29 ± 0.05	1.37 ± 0.04
	<b>FF</b>	0.76 ± 0.01	0.73 ± 0.01	0.77 ± 0.03	0.78 ± 0.05	0.73 ± 0.02
	<b>η (%)</b>	8.4 ± 0.4	8.11 ± 0.05	8.4 ± 0.2	8.4 ± 0.1	8.2 ± 0.4
<b>0.5 Sun</b>	<b>V<sub>oc</sub>(mV)</b>	862 ± 21	952 ± 8	947 ± 11	957 ± 17	863 ± 20
	<b>J<sub>sc</sub>(mAcm<sup>-2</sup>)</b>	6.8 ± 0.3	6.4 ± 0.2	6.8 ± 0.2	6.8 ± 0.1	5.8 ± 0.4
	<b>FF</b>	0.71 ± 0.01	0.67 ± 0.01	0.71 ± 0.02	0.70 ± 0.03	0.55 ± 0.06
	<b>η (%)</b>	7.9 ± 0.3	7.8 ± 0.4	8.6 ± 0.2	8.5 ± 0.2	5.3 ± 0.5
<b>1 Sun</b>	<b>V<sub>oc</sub>(mV)</b>	881 ± 18	996 ± 2	992 ± 13	999 ± 20	894 ± 18
	<b>J<sub>sc</sub>(mAcm<sup>-2</sup>)</b>	12.4 ± 0.9	11.8 ± 0.5	12.7 ± 0.2	12.5 ± 0.2	10.2 ± 0.4
	<b>FF</b>	0.68 ± 0.01	0.64 ± 0.01	0.69 ± 0.02	0.68 ± 0.02	0.48 ± 0.07
	<b>η (%)</b>	7.4 ± 0.6	7.5 ± 0.3	8.6 ± 0.3	8.4 ± 0.3	4.4 ± 0.6
# of devices		5	4	6	6	9

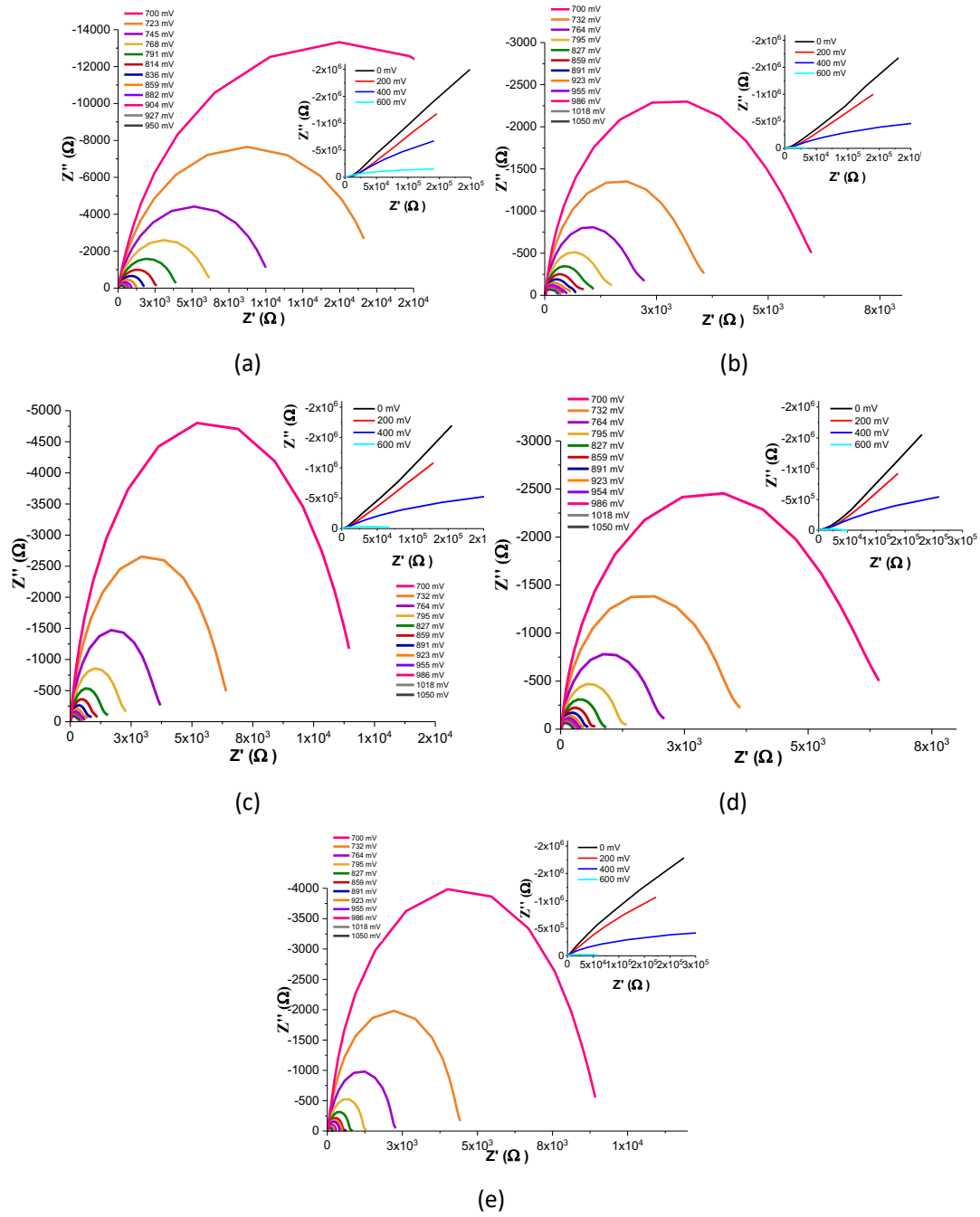


**Figure 2.18.** Nyquist plots under dark conditions for DSSC with electrolytes of a)  $[\text{Co}(\text{bpy})_3]^{3+/2+}$  reference, b) Co/AZ 1:1, c) Co/AZ 1/0.8, d) AZ/Co 1:0.9 and e)  $\text{AZ}^+/\text{AZ}$  electrolyte.



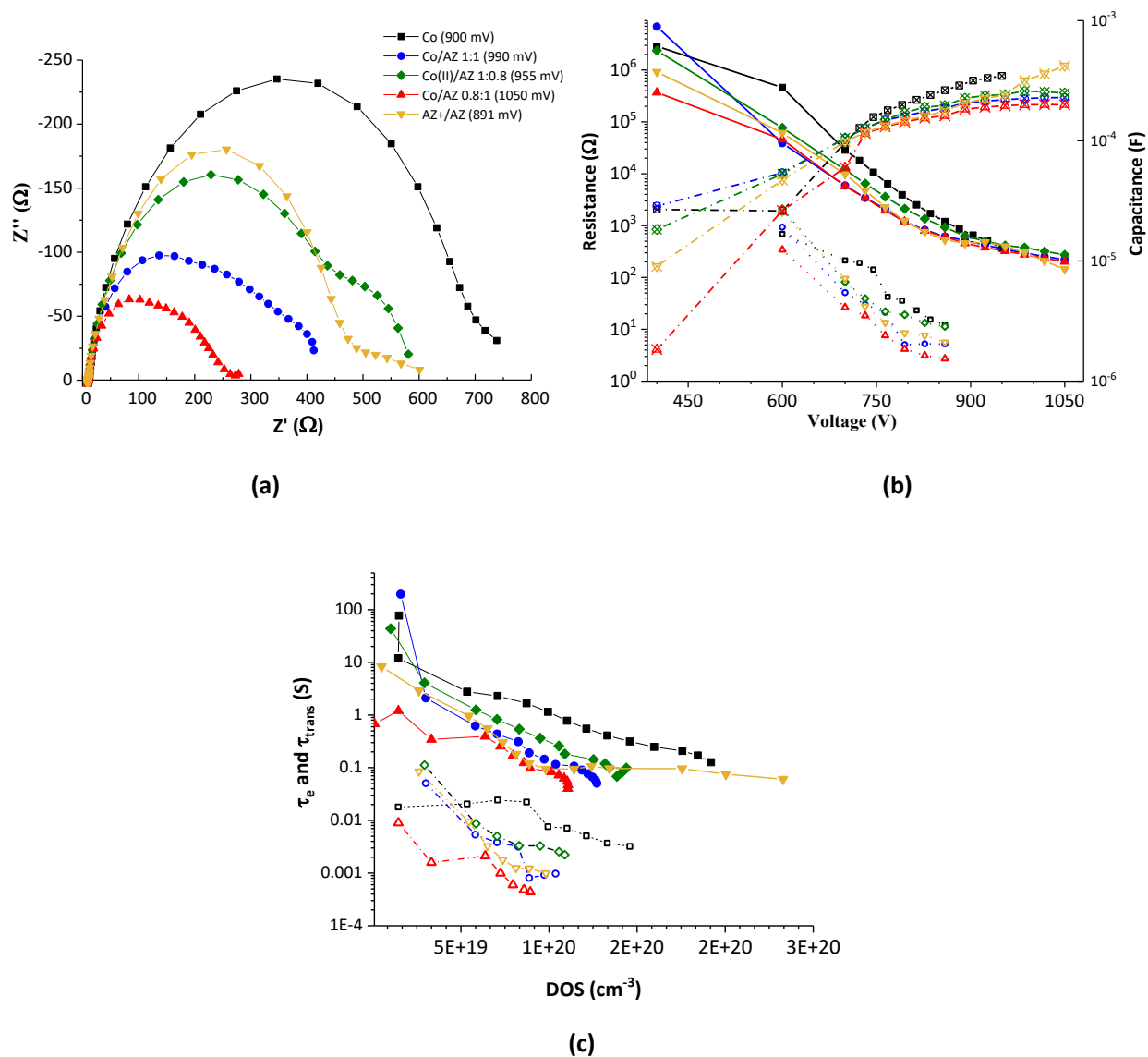


**Figure 2.19.** EIS analysis. (a) Nyquist plots at open-circuit voltage for each electrolyte system, (b) continuous lines with solid markers represent the charge transfer resistance  $R_{CT}$  as a function of applied voltage, the dotted lines with open markers the transport resistance  $R_{trans}$ , dash-dotted lines with and x marker represents capacitance, (c) electron lifetime and transport time vs density of states, DOS. For all the plots, the squares correspond to the  $[\text{Co}(\text{bpy})_3]^{3+/2+}$  reference, the circles to Co/AZ 1:1, diamonds to Co/AZ 1/0.8, triangles to AZ/Co 1:0.9, and inverted triangles to the AZ<sup>+</sup>/AZ electrolyte.



# Chapter 3 In-situ photopolymerization by thiol-ene “click” reaction in cobalt based electrolytes

This chapter is adapted from the paper in manuscript for submission:

***Photopolymerization of hyperbranched networks by thiol-ene “click” reaction in cobalt-based electrolytes for Dye-Sensitized Solar Cells***

*Natalie Flores-Díaz, Sandy Sanchez-Alonso, Jean-David Décoppet, Shaik M. Zakeeruddin, Michael Grätzel, Anders Hagfeldt.*

My contribution was all device preparation and characterization, electrolytes characterization and manuscript writing.

Sandy Sanchez-Alonso contributed with the TGA measurements.

## 3.1 Motivation

The development of cobalt-based solid or quasi-solid electrolytes represents a significant challenge to boost the commercialization of stable DSSC. In-situ polymerization of the electrolytes could potentially lead to highly stable cobalt-based modules.

A strategy to decrease the liquid electrolyte volatility and improve stability is to enclose the redox species in a polymer matrix to create quasi-solid state electrolytes.

For instance, Bella et al. reported the in-situ photopolymerization in cobalt-based electrolytes, using the monomer precursor, BEMA or PEGMA, and a photoinitiator. The precursors are mixed with the cobalt electrolyte and injected into the DSSC. Subsequent UV irradiation through the CE provided the polymerization of cobalt-electrolytes. They performed dark-soaking at 60 °C for 1500 h and soaking at 1 sun irradiation for 300 h at 40 °C. Reporting 90% of the initial PCE of 6% after 300 h.<sup>114</sup>

Hyperbranched polymers (HBPs) are macromolecules with a 3D structure given by multiple branches and inter-connections. They are generally amorphous, with relatively low  $T_g$  values, lower viscosities than linear polymers, and easy to synthesize on a large scale.<sup>115,116</sup> One method to prepare HBPs involves the radical-mediated thiol-ene “click” reaction,<sup>117</sup> which rapidly proceeds to completion with high yields and high selectivity of the desired product.<sup>118,119</sup>

UV-light absorption can initiate the “thiol-ene” reaction between a polyacrylate monomer and a thiol-functionalized polysiloxane.<sup>120</sup> The photopolymerized HBPs generally present low  $T_g$  values, high thermal and electrochemical stability, high conductivity, and hydrophobicity.<sup>121,122</sup> This kind of HBPs have been extensively applied to develop gas separation membranes,<sup>123,124</sup> and flexible membranes and solid polymer electrolytes for lithium-ion batteries.<sup>125,126</sup>

This work aims to apply hyperbranched polymers into cobalt electrolytes for DSSC by in situ photopolymerization of simple polyacrylate monomers and a thiol-functionalized polysiloxane. We chose the simple approach of thiol-click chemistry to produce a polymer network inside the cobalt electrolyte. This reaction is known to be highly stable in the presence of oxygen and water.<sup>123</sup> Polymer membranes formed by photopolymerization of PEGDA and different thiol-siloxanes have been studied for Li-ion batteries and other applications. The acrylate monomer PEGMA has only one reaction site on the terminal acrylate group. The photopolymerization with a thiol will create a more flexible hyperbranched network than PEGDA, which has two possible reaction sides in the terminal acrylate groups.

## 3.2 Thiol-ene reaction

The reaction mechanism is shown in Fig.3.1. It starts with the absorption of a UV photon by a photoinitiator molecule (PI). After absorption, an inter-system crossing from a singlet to a triplet state leads to a radical formation. The former reacts with the thiol-siloxane (hence radical initiated reaction) and creates a thiol-radical, which breaks the acrylate C=C bond, creating the hyperbranched polymer.

The reaction of PEGMA and PEGDA with the thiol-siloxane to form the networks **HB1** (PEGMA+thiol-siloxane) and **HB2** (PEGDA+thiol-siloxane) was monitored by FTIR. For this purpose, the ratio of acrylate monomer to siloxane was fixed as 1:0.2. A 20% of the polymer mixture was added to the cobalt electrolyte and cured it at 350nm in a UV chamber for 120s.

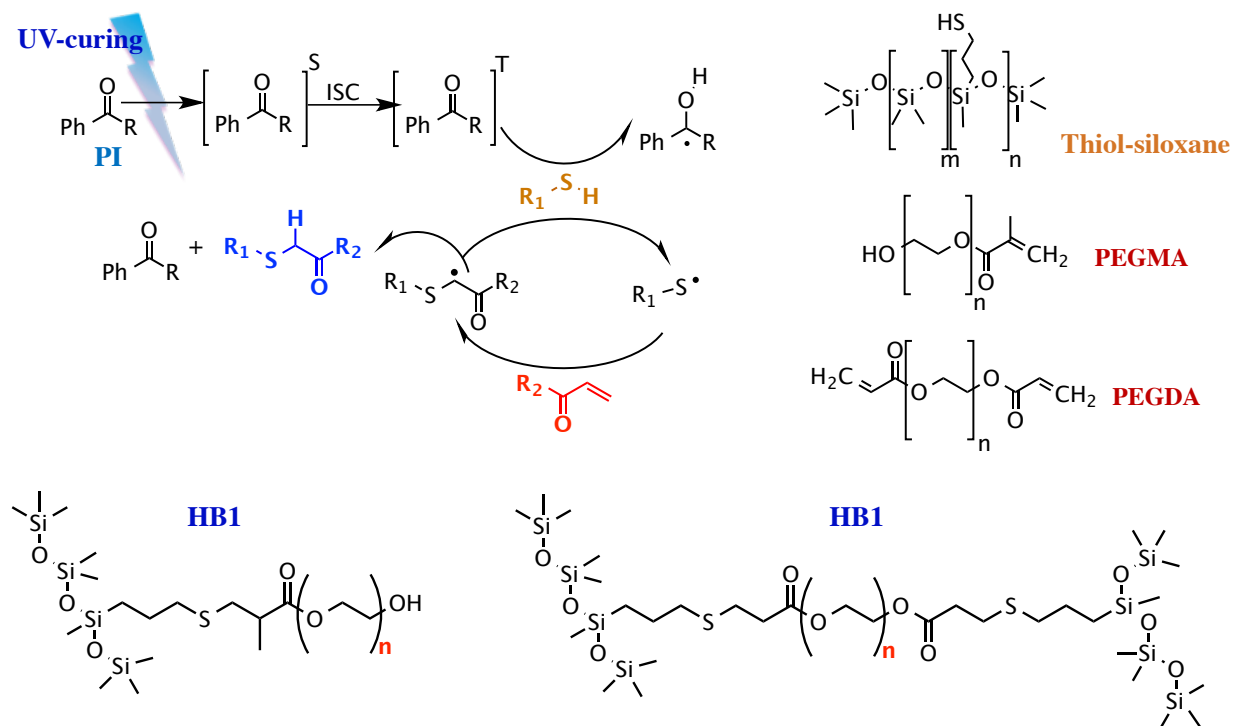


**Figure 3.1.** Thiol-ene reaction and molecular structures of thiol-siloxane, polyacrylate monomers PEGMA, and PEGDA and simplified hyperbranched products, HB1 (PEGMA+thiol-siloxane) and HB2 (PEGDA+thiol-siloxane).

The reactions were monitored from 0s to 240s under UV illumination in ACN to simulate the electrolytes environment. The obtained FTIR are presented in Fig.3.2. The thiol-ene reaction will only happen between the acrylate double bonds and the thiol group. Therefore, to monitor the reactions, we tracked the decrease in intensity of the C=C stretch around 1650 cm<sup>-1</sup>, the S-H peak at 2600 cm<sup>-1</sup>, and the C-H stretch from the alkene groups at 3100 cm<sup>-1</sup>. The typical Si-O-C peak for the siloxane around 1110cm<sup>-1</sup> is overlapped with the C-O-C peak at 1110 cm<sup>-1</sup> and, thus, not used for the reaction monitoring.

It can be noted from Fig 3.2 that the click reaction at room temperature in ACN is reasonably fast and 1 min of UV curing is enough to drive the reaction to completion for both polymers, as expected from previous studies in toluene.<sup>127,128</sup>

The formation of HB polymers would lead to limited mobility of the carbon chain compared to the initial monomers, preventing the complete conversion of the thiol-ene reaction due to mass diffusion constraints.<sup>129</sup> Addi-

tionally, both acrylate monomers PEGMA and PEGDA are only partially miscible with thiol-siloxane in ACN. Nonetheless, as seen in Fig.3.2(a)-(b) for both polymers, the reaction was almost completed after 60 s of UV irradiation for both polymers. The prominent peaks for the acrylate back-bone at  $2800\text{ cm}^{-1}$  from the stretch of C–H bonds in the polymers, the  $\text{C=O}$  stretching at  $1700\text{ cm}^{-1}$  and the  $\text{C=C}$  acrylate band at  $1410\text{ cm}^{-1}$  can still be observed after the photopolymerization, demonstrating that the HB polymers preserve the characteristics of the monomers core.

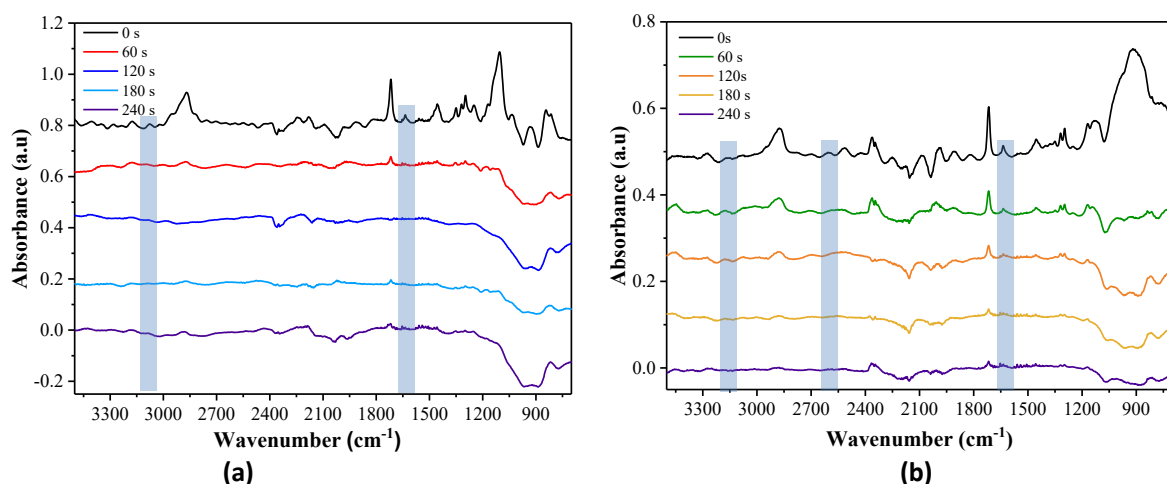


**Figure 3.2.** (a) FTIR of electrolyte with HB1 (PEGMA + thiol-siloxane) in ACN from 0s to 240 s of UV curing. (b) FTIR of HB2 (PEGDA + thiol-siloxane) in ACN from 0s to 240 s of UV curing.

Similarly, the hyperbranched polymer formation by adding 20% (v/v) of the mixtures HB1 and HB2 were monitored in the liquid  $\text{Co}(\text{bpy})_3$ -based electrolytes. The obtained FTIR are presented in Fig.3.3. The  $\text{C=C}$  stretch peak's disappearance could not be tracked due to the aromatic  $\text{C=C}$  bonds from the cobalt complexes and the nonyl-pyridine base. However, the C–H stretch intensity for alkenes at  $3100\text{ cm}^{-1}$  was reduced after 120 s of UV curing. This confirms the formation of the HBs in the presence of the Co-complexes and the additives LiTFSI and 4,5-nonylpyridine.

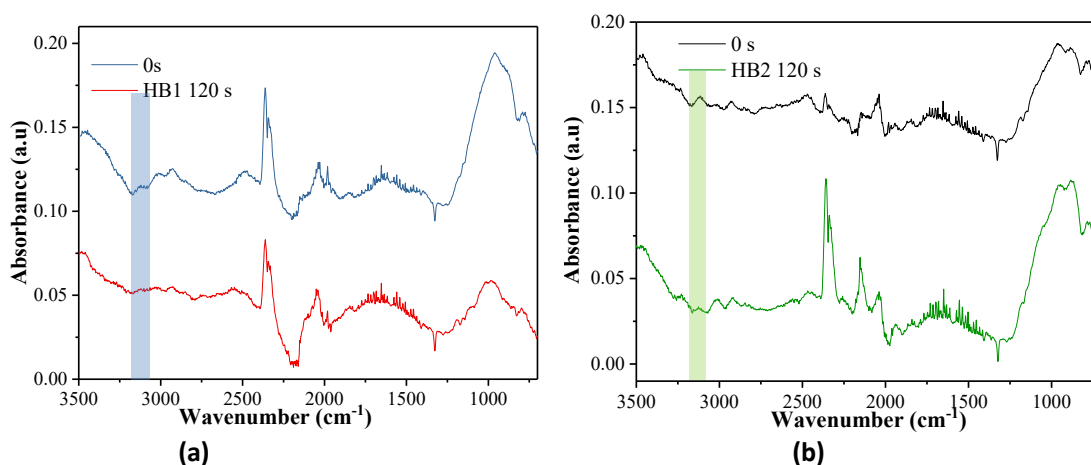


**Figure 3.3.** (a) FTIR of electrolyte with Co ref +HB1 (PEGMA+Thiolsiloxane) 20% (v/v) at 0s and after 120 s of UV curing.(b) FTIR of electrolyte with Co ref+HB2(PEGDA+Thiolsiloxane) 20% (v/v) at 0s and after 120 s of UV curing. The Co ref contains 0.23M Co(bpy)<sub>3</sub>TFSI<sub>2</sub>, 0.05 Co(bpy)<sub>3</sub>TFSI<sub>3</sub>, 0.1 M LiTFSI and 0.6 M 4,5-nonylpyridine.

Thermogravimetric analysis was performed on the acrylate monomers, thiol-siloxane, the co-reference electrolyte, and electrolytes containing 20% of HB1 and HB2 (cured under UV for 120 s). Surprisingly, the in-situ photopolymerization of HB1 and HB2 inside the cobalt electrolyte prevents weight loss up to 150 °C, as noted from Fig.3.4, which could be attributed to an "entrapping" effect by the polymeric network. This behavior is highly beneficial to prevent the volatilization of the ACN solvent in DSSC.

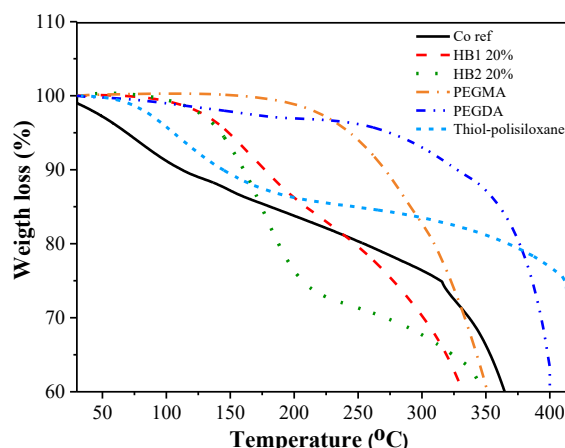


**Figure 3.4.** TGA analysis of the monomers, a [Co(bpy)<sub>3</sub>]<sup>3+/2+</sup> reference electrolyte, and electrolytes containing 20% of HB1 and HB2.

### 3.3 Electrochemical characterization

To study the electrochemical properties of the electrolytes with hyperbranched networks, symmetric cells composed of PEDOT as counter electrode (CE) material, the formed HB1 and HB2 from 10-20% (w/w) in the cobalt reference electrolyte were studied. A schematic representation is presented in Fig.3.5(a). Previous studies with polymeric networks and cobalt electrolytes have demonstrated mass-diffusion limitations with a higher polymer content than 20% (v/v). Thus, We chose to limit the electrolytes' polymer content to a maximum of 20% (v/v).<sup>130</sup>

The Tafel polarization curves are presented in Fig.3.5(b), and the electrochemical parameters are summarized in Table 3.1. As expected, the Cobalt reference exhibits the higher limiting current,  $J_{lim}$ , which is related to the diffusion of the ionic species in the electrolyte. The formation of a polymeric network limits the ionic species' mobility in the electrolyte (Co<sup>2+</sup> and Co<sup>3+</sup>). As a result, the limiting current is drastically decreased with the increase in polymer content.

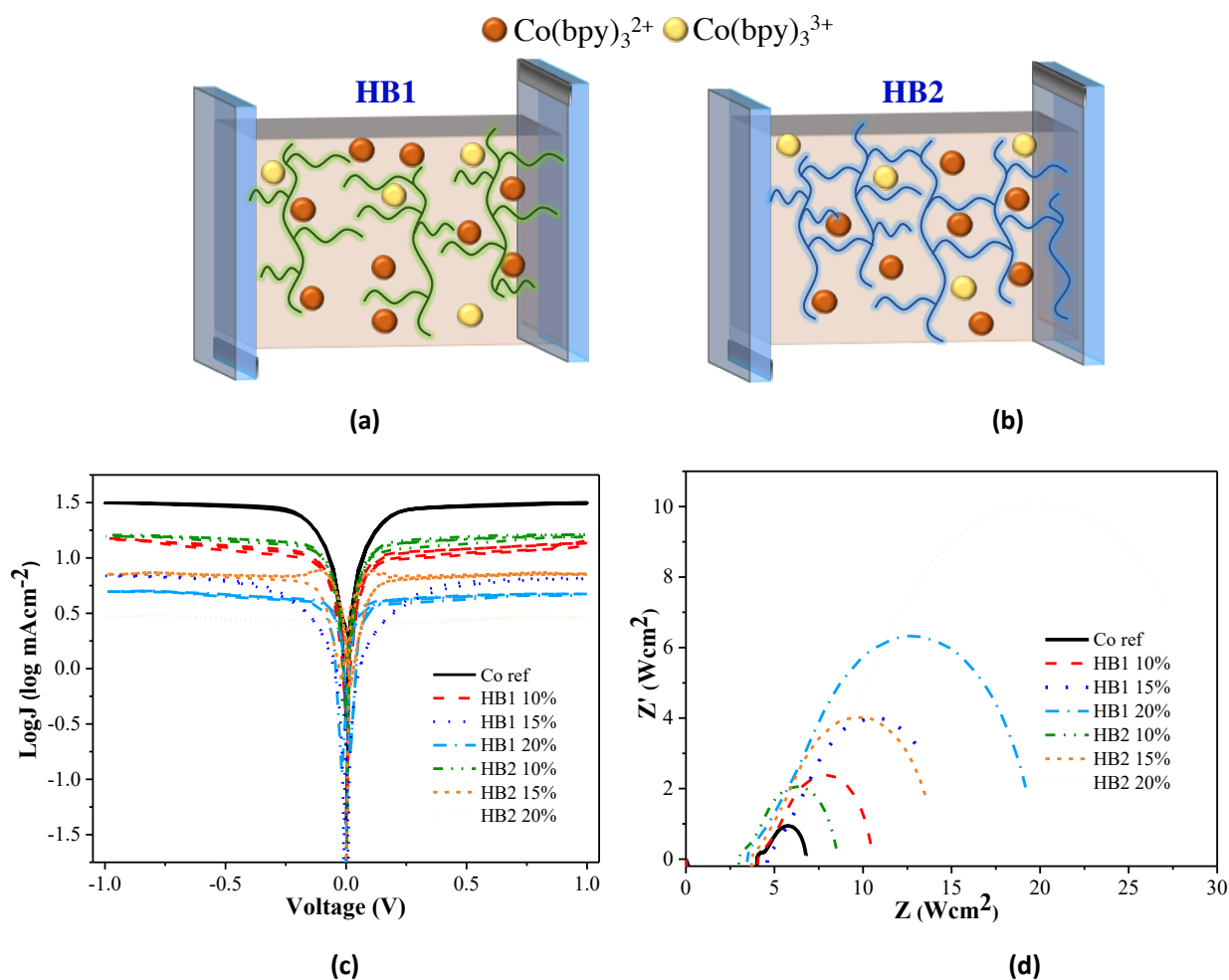


**Figure 3.5.** (a) and (b) Representation of symmetric cells with the photopolymerized electrolytes, (c) Tafel plots, and (d) Nyquist plots at 0 V.

The diffusion coefficients,  $D_n$ , for the  $\text{Co}^{3+}$  species were obtained from the  $J_{\text{lim}}$  and Eq.1.41 and are listed in Table 3.1. The obtained values for the reference electrolyte are in agreement with previous studies reported by several authors.<sup>36,106,107,131</sup> As anticipated, the diffusion coefficients decrease with the percentage of photopolymerized network, which could lead to severe mass-diffusion problems for working DSSC under 1 Sun illumination.

The exchange current,  $J_0$  (intercept at  $V=0$ ), obtained from the Tafel plots is related to the reversibility of electron transfer at the CE with the reduced species. The higher the concentration of polymer content, the more pronounced the decrease of the electron transfer rate at the CE, which at the same time can be related to an increase in the charge transfer resistance,  $R_{\text{CT}}$ , according to Eq.1.42.<sup>105,132</sup> It can be noted that the electrocatalytic ability of the PEDOT electrode is not drastically affected by the addition of 10% of polymer for each HB.

EIS spectra were obtained to further study the electrochemical characteristics of the polymer-containing electrolytes in the symmetric cells. The obtained Nyquist plots Fig.3.5(d), were simulated using the equivalent electrical



model shown in Fig.1.17. We determined the series resistance of the symmetric cell ( $R_s$ ), the charge-transfer resistance ( $R_{CT}$ ), and the diffusion resistance of the active species in the electrolytes ( $Z_w$ ). The obtained values are presented in Table 3.1.

All the symmetrical cells showed similar  $R_s$ , ranging from 3-6  $\Omega\text{cm}^2$  in agreement with previous studies by Bai et al.<sup>133</sup> The obtained  $R_{CT}$  values agree with previous studies by Kang,<sup>134</sup> and remained relatively low for all the electrolytes in contrast to the values obtained from the Taffel plots. The  $Z_w$  was severely affected by a higher polymer content in the electrolyte, as shown by previous quasi-solid cobalt-based electrolytes.<sup>135,136</sup>

**Table 3.1.** Characterization data of symmetric cells from Log(J) vs. potential plots and from EIS analysis

Electrolyte	$J_{lim}$ ( $\text{mAcm}^{-2}$ )	$J_0$ ( $\text{mAcm}^{-2}$ )	$R_{CT}$ ( $\Omega\text{cm}^2$ )	$D_n$ ( $\text{cm}^2\text{s}^{-1}$ )	$R_s$ ( $\Omega\text{cm}^2$ )	$R_{CT}$ ( $\Omega\text{cm}^2$ )	$Z_w$ ( $\Omega\text{cm}^2$ )
[Co(bpy) <sub>3</sub> ] <sup>3+/2+</sup>	31.63	24.55	1.04	8.20E-06	4.01	0.07	2.30
HB1 10%	20.33	10.47	2.44	5.27E-06	4.28	0.23	8.90
HB1 15%	6.59	4.57	5.59	1.70E-06	4.64	0.13	9.73
HB1 20%	5.05	4.07	6.27	1.31E-06	3.48	0.27	11.30
HB2 10%	16.23	12.59	2.03	4.21E-06	4.48	0.07	12.30
HB2 15%	7.80	6.31	4.05	2.02E-06	3.71	0.15	9.75
HB2 20%	3.29	2.66	9.61	8.51E-07	5.48	0.02	24.54

### 3.4 DSSC with HB polymers

The effect of creating hyperbranched networks in the Co-based electrolytes was studied with complete DSSC devices using XY1b as a sensitizer (Fig.3.6) and direct contact of a PEDOT CE sealed with and UV-cured glue. The corresponding J-V curves under 1 sun and 0.1 Sun are presented in Fig.3.7, and the obtained photovoltaic parameters are summarized in Table 3.2.

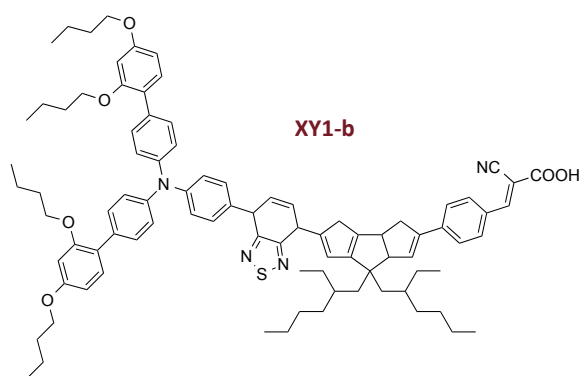


**Figure 3.6.** Molecular structure of XY1-b used as the sensitizer for DSSCs with HB polymers

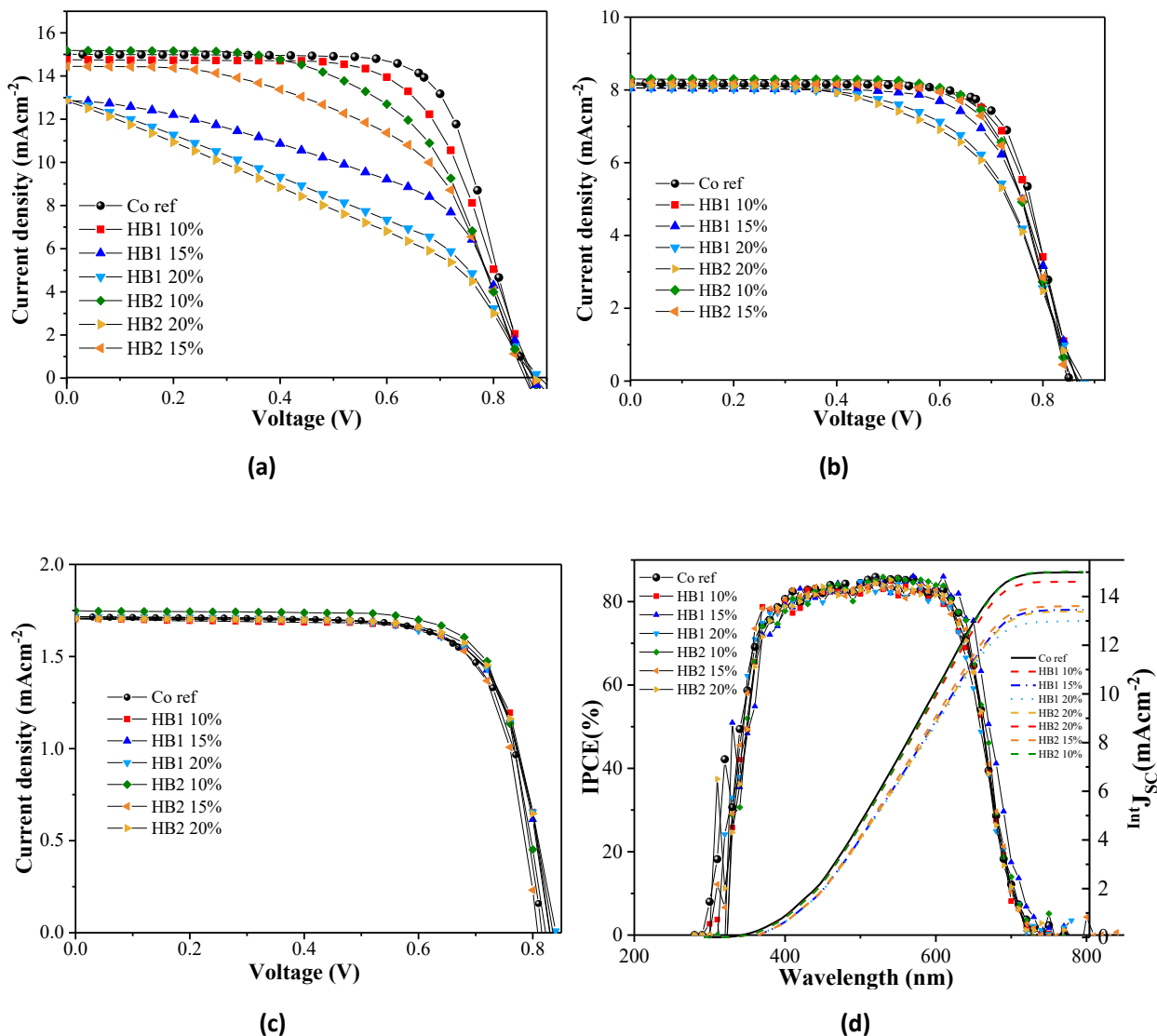


**Figure 3.7.** (a) J-V plots under 1.5 AM, (b) J-V plots under 0.5 Sun and (d) 0.1 Sun and (d) IPCE curves.

The low diffusion coefficients of the cobalt redox mediators in the electrolytes with hyperbranched networks observed from the symmetric cells are expected to be a significant limitation to achieve high performance in DSSC.<sup>137</sup> Nevertheless, as observed in Fig. 3.7, the devices with 10% of HB1 reached an open circuit voltage ( $V_{OC}$ ) of 875 mV, a short circuit current ( $J_{SC}$ ) of 14.75 mAcm<sup>-2</sup>, and a fill factor (FF) of 0.66 for a power conversion efficiency (PCE) of 8.52% under 1 sun illumination. This performance remained very similar to the devices with the cobalt reference electrolyte. For higher polymeric contents, the low PCEs under 1 sun result from mass-diffusion problems reflected in low  $J_{SC}$  and FF due to the lower diffusion coefficients of the Co<sup>3+</sup> species. It is important to note that the in-situ photopolymerization increases the  $V_{OC}$  compared to the cobalt reference. Moreover, the performance at 0.1 Sun for most of the devices surpassed that of the reference device. This behavior can be rationalized by the fact that at low light intensities, the produced photocurrent is very low, and there are enough Co<sup>2+</sup> species in the surrounding to regenerate the dye. Therefore, the mass-diffusion problems of Co<sup>3+</sup> are no

longer an impediment to the device's performance. This is particularly important for designing DSSC for indoor applications, where the photocurrents range from 100-200  $\mu\text{Acm}^{-2}$ , and increasing the  $V_{\text{OC}}$  is crucial to provide power to small electronic devices.

**Table 3.2.** Photovoltaic characteristic parameters for DSSC with photopolymerized electrolytes.

Electrolyte	0.1 Sun				1 Sun				
	$V_{\text{OC}}$ (mV)	$J_{\text{SC}}$ ( $\text{mAcm}^{-2}$ )	FF	$\eta$ (%)	$V_{\text{OC}}$ (mV)	$J_{\text{SC}}$ ( $\text{mAcm}^{-2}$ )	$\text{int}J_{\text{SC}}$ ( $\text{mAcm}^{-2}$ )	FF	$\eta$ (%)
$[\text{Co}(\text{bpy})_3]^{3+/2+}$	816.0	1.72	0.74	9.62	863.7	15.49	14.99	0.72	9.36
HB1 10%	829.9	1.71	0.74	9.74	875.9	14.75	14.60	0.66	8.52
HB1 15%	828.7	1.71	0.74	9.72	874.1	12.86	13.45	0.51	5.72
HB1 20%	841.0	1.72	0.73	9.72	887.4	12.94	12.99	0.39	4.44
HB2 10%	821.7	1.74	0.76	10.08	865.8	15.16	15.00	0.58	7.68
HB2 15%	846.8	1.58	0.76	9.36	895.1	13.52	13.61	0.51	6.17
HB2 20%	835.9	1.71	0.75	9.88	877.7	12.85	13.37	0.36	4.11

The differences observed in the  $V_{\text{OC}}$  for the polymer electrolytes were studied by charge extraction and  $V_{\text{OC}}$  decay measurements as a function of light intensity. The results are presented in Fig.3.8. Under illumination, the  $V_{\text{OC}}$  of a DSSC is the difference between the redox potential of the redox mediator and the quasi-Fermi level,  $E_{\text{F,q}}$ , of the  $\text{TiO}_2$ . The quasi-Fermi level was obtained by the Eq.1.22,<sup>108</sup> where for all the devices, the redox potential of  $[\text{Co}(\text{bpy})_3]^{3+/2+}$  was obtained by the Nernst equation (Eq.1.24). The charge extraction and electron lifetimes are depicted vs.  $E_{\text{F,q}}$  under illumination for complete devices in Fig 3.8.a-b.

It can be observed from Fig. 3.8(a) an upward-shift of the  $\text{TiO}_2$  conduction band (CB), for all the hyperbranched electrolytes compared to the  $[\text{Co}(\text{bpy})_3]^{3+/2+}$  reference. Additionally, we could note from Fig. 3.8(b), that all the HB electrolytes presented longer electron lifetimes than the  $\text{Co}^{3+/2+}$  electrolyte, indicating lower recombination rates for the devices with polymeric networks in the electrolyte. The higher  $V_{\text{OC}}$  obtained for the HB electrolytes can be attributed to a higher quasi-Fermi level and improved recombination resistance. Moreover, the clear effect of using HB polymers in cobalt-based electrolytes reflected in higher  $V_{\text{OC}}$  values was confirmed in Fig. 3.8(c) at different light intensities. It was possible to attribute this behaviour to a  $\text{TiO}_2$  surface passivation effect by the polymers. Thus, shifting the Fermi level of  $\text{TiO}_2$  up and decreasing the recombination of electrons to the electrolyte.

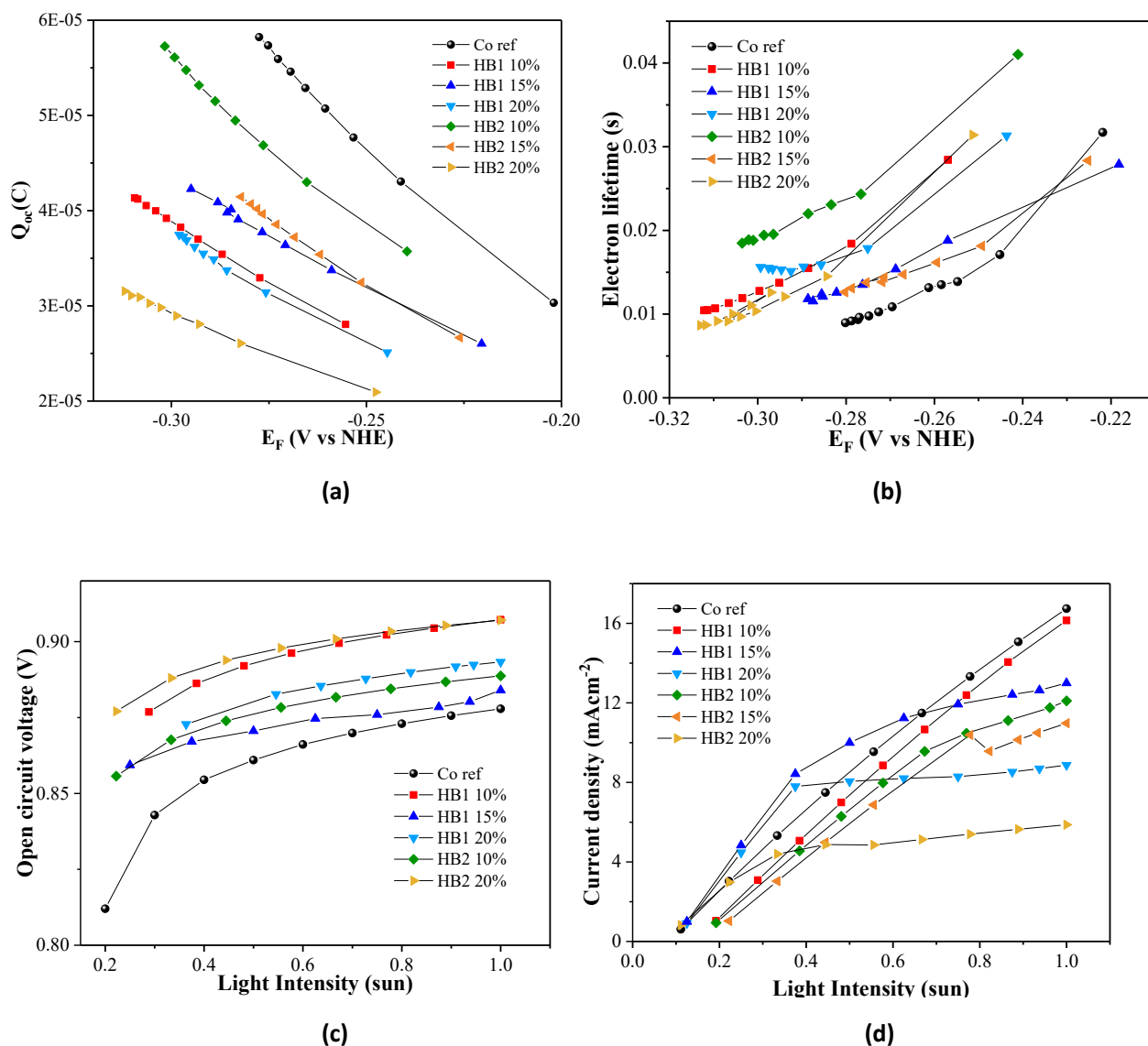


**Figure 3.8.** (a) Charge extraction vs Fermi level (b) electron lifetime vs Fermi (c)  $V_{OC}$  vs light intensity and (d)  $J_{SC}$  vs light intensity of DSSC containing photopolymerized electrolytes. (e) Current density vs voltage for symmetric cells. The quasi-Fermi level was calculated by the relation  $E_{F-q} = E_{redox} - V_{OC}$ .

As expected, the linearity of the current density as a function of light intensity is affected by the photopolymerization due to mass-diffusion limitations at higher intensities, as seen from Fig.3.8(d). However, a polymer content from 10 to 15% of HB1 and HB2 did not affect the photocurrent's linearity up until 60% sun. These findings show that the use of HB electrolytes on DSSC could be beneficial for low-light applications.

To better understand the effect of the in-situ photopolymerization in the internal processes of DSSCs, electrochemical impedance spectroscopy (EIS) was performed.<sup>132,138</sup> To this end, a frequency scan from 0.5 MHz to 0.2 Hz at room temperature was set for a voltage range from 0.6 V to 0.05 V further than that the  $V_{OC}$  of each device (approx. 0.9 V). The alternating current (AC) amplitude of 10 mV. The EIS data recorded at 1 Sun and 0.1 Sun were fitted with the typical three-channel model, using ZView® software.

At 1 Sun illumination conditions, the formation of the polymer network in the electrolytes, slightly enhances the charge transfer resistance compared to the cobalt reference as observed from Fig.3.9(a). This hampers the recombination of electrons from the  $\text{TiO}_2$  CB to the electrolyte. The relation between applied bias and the density of states (DOS) in Fig.3.9(b), shows a shift of the conduction band of  $\text{TiO}_2$  toward higher values for all the electrolytes with polymers compared with the cobalt reference, following the same trends from the  $V_{OC}$  decay measurements from Fig.3.8.(a).

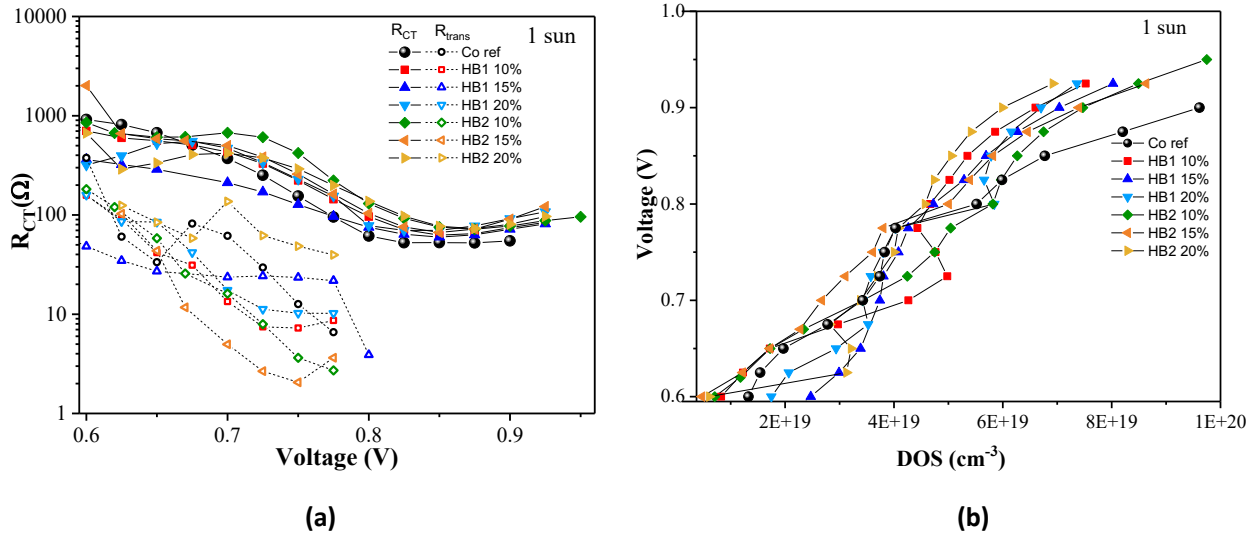


**Figure 3.9.** EIS analysis. (a) continuous lines with solid markers represent the charge transfer resistance  $R_{CT}$  as a function of applied voltage, and the dotted lines with open markers the transport resistance  $R_{trans}$ . (b) voltage vs.  $\text{DOS}/\text{cm}^{-3}$

The higher  $R_{CT}$  values for all the devices containing HB electrolytes can be associated with higher electron lifetimes, confirming that the improved  $V_{OC}$  can be attributed to a slight upward shift of the  $\text{TiO}_2$  CB band edge and higher electron lifetimes (improved recombination resistance). Nonetheless, as observed from the J-V in Fig. 3.7(a), the performance under 1 Sun decreases with polymer content in the electrolyte due to lower  $J_{SC}$  and FF, which we rationalized to be attributed to the lower diffusion coefficients found from the symmetric cells. This was confirmed by EIS analysis and showed in Fig.3.10 where the Warburg resistance for the cobalt species in the electrolytes increased exponentially with the polymer content and was still visible in the Nyquist plots at low voltages.

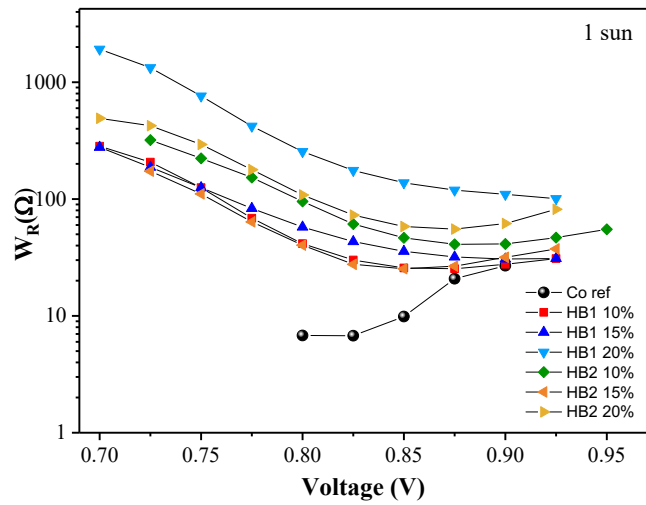


**Figure 3.10.** Warburg resistance of  $\text{Co}^{3+}$  in the studied electrolytes as a function of applied bias.

From the J-V curves in Fig.3.7, we observed that most of the HB-electrolytes presented enhanced performance under 0.1 sun illumination than the cobalt electrolyte. We performed EIS analysis under 0.1 sun illumination to elucidate this behaviour. It can be noted from Fig.3.11(a) that all the polymeric electrolytes presented improved recombination resistance compared to the cobalt reference and also lower resistance to the transport of electrons in the  $\text{TiO}_2$  scaffold to the external circuit. The upward-shift of the  $\text{TiO}_2$  CB is clearly visible for all the polymeric electrolytes in Fig.3.11(b), showing a surface “passivating effect”, decreasing the interfacial recombination. These outcomes suggest that the use of polymeric electrolytes is one of the best ways to improve the performance of DSSC working under low-light intensities.

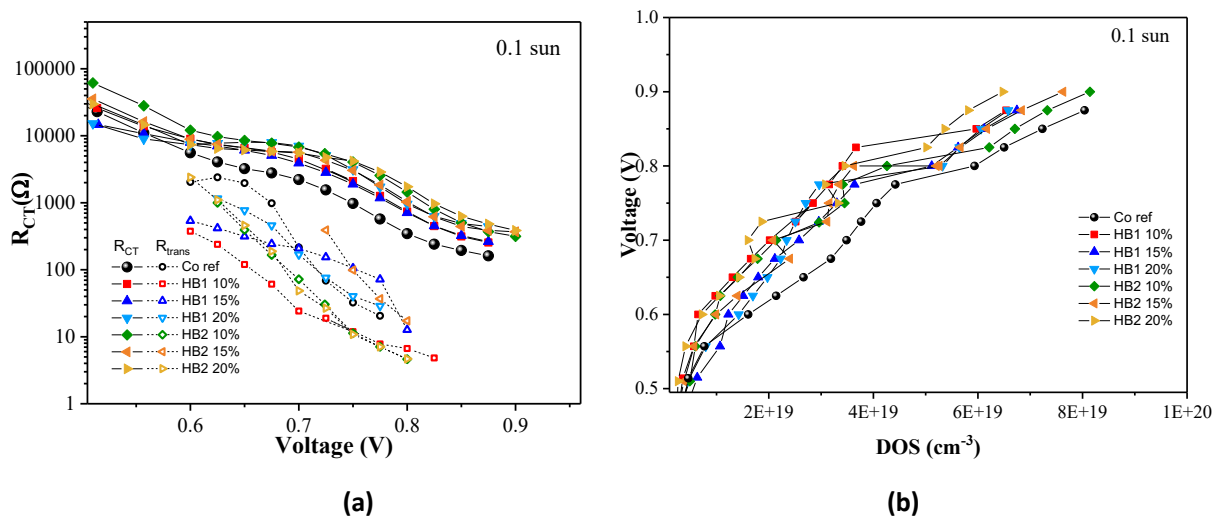


**Figure 3.11.** EIS analysis. (a) continuous lines with solid markers represent the charge transfer resistance  $R_{CT}$  as a function of applied voltage and the dotted lines with open markers the transport resistance  $R_{trans}$ . (b) voltage vs.  $\text{DOS}/\text{cm}^{-3}$

Even though the highest performance for DSSC has been reached by copper-based electrolytes, reaching remarkable efficiencies up to 34% under 1000 lux, the study of DSSC using electrolytes based on cobalt remains a big challenge for building integrated photovoltaics requiring transparent electrolytes. The PCE of polymeric electrolytes based on iodide or cobalt mediators under 1000 Lux illumination range from 19-24%. The polymer content for most studies was set under 20% to avoid mass-diffusion limitations.<sup>139,140</sup>

To study the performance of devices with a larger active area of  $2.8 \text{ cm}^2$  were tested under 1000 lux, and the obtained J-V curves are presented in Fig.3.12(a). As expected from the observed trends under 0.1 Sun illumination, all the devices with hyperbranched networks surpassed that of the cobalt liquid electrolytes. We performed EIS for the best-performing devices for each HB electrolyte, which in both cases was achieved with a 15% of polymeric content. The EIS analysis is shown in Fig.3.12(b) and (c). In agreement with the previous analysis, the photopolymerization of hyperbranched networks on the cobalt-electrolyte improves the recombination resistance, leading to higher electron lifetimes. An overall enhancement of the device's performance was achieved by the polymer electrolytes as shown in Table 3.3.

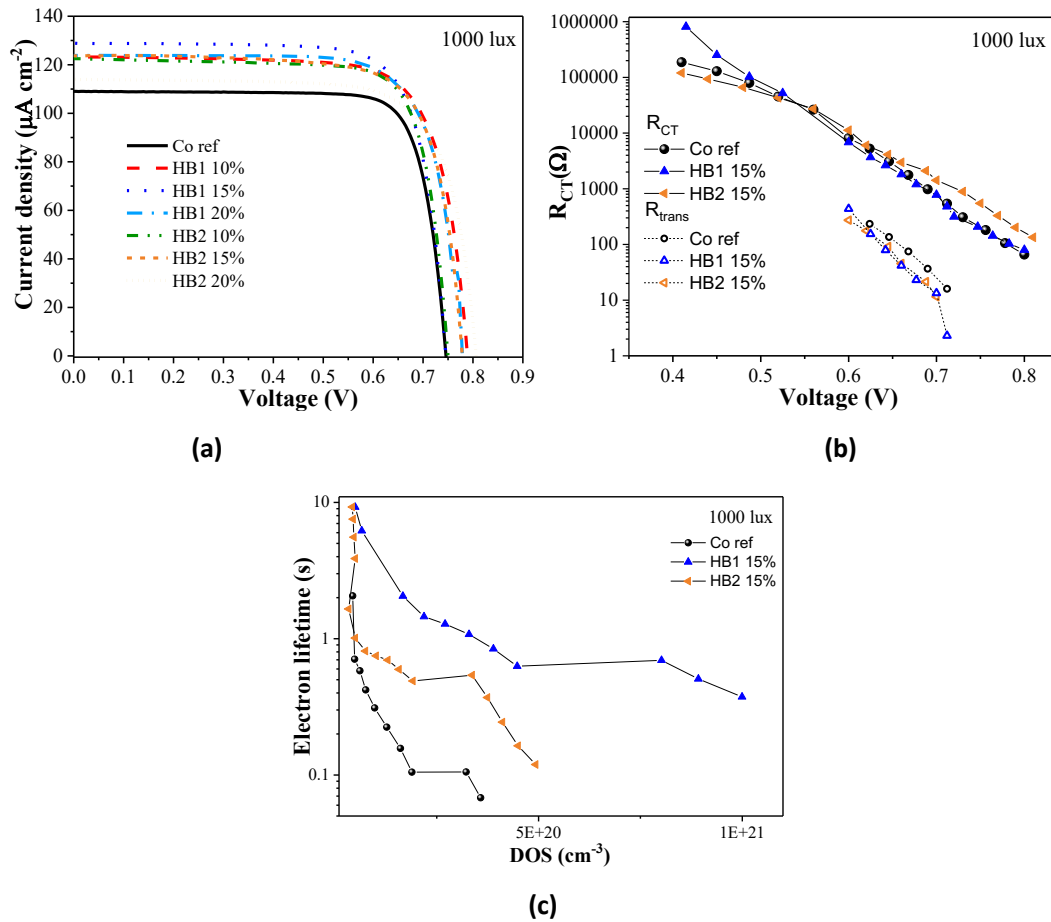


**Figure 3.12.** (a) J-V plots of  $2.8 \text{ cm}^2$  devices under 1000 lux illumination, (b) charge transfer resistance  $R_{CT}$  as function of applied voltage for solid markers and continuous lines, and transport resistance  $R_{trans}$  for the dotted lines with open marker (c) electron lifetime  $\tau_e$  as function of DOS/cm.

**Table 3.3.** Photovoltaic characteristic parameters for DSSC with photopolymerized electrolytes under 1000 lux illumination.

Electrolyte	V <sub>oc</sub> (mV)	J <sub>sc</sub> ( $\mu\text{Acm}^{-2}$ )	FF	W ( $\mu\text{Wcm}^{-2}$ )	$\eta$ (%)
[Co(bpy) <sub>3</sub> ] <sup>3+/2+</sup>	745.92	108.74	0.799	64.83	20.37
HB1 10%	788.87	123.25	0.750	72.97	22.93
HB1 15%	745.32	128.82	0.768	73.82	23.19
HB1 20%	779.38	123.84	0.751	72.46	22.77
HB2 10%	749.73	122.51	0.778	71.49	22.46
HB2 15%	778.51	123.71	0.749	72.11	22.66
HB2 20%	806.29	113.95	0.740	68.03	21.30

### 3.5 Conclusions

The effect of in-situ photopolymerization of a thiol-siloxane with an acrylate monomer, such as PEGMA and PEGDA, via a click thiol-ene reaction in the performance of dye-sensitized solar cells with cobalt-based electrolytes was studied in the present work. The formed hyperbranched networks denoted HB1 (thiol-siloxane and PEGMA) and HB2 (thiol-siloxane and PEGMA). Monitoring the thiol-ene reaction by FTIR revealed that 1 min of UV curing suffices to drive the reactions to completion. TGA analysis showed that electrolytes containing 20% of HB1 and HB2 entrap the liquid ACN-based electrolyte and retain up to 98% of their initial weight up to 150 °C. From symmetrical cells, we found that the diffusion coefficients for Co<sup>3+</sup> in the electrolytes decrease with polymer content. The highest performance was reached by a 10%(v/v) of HB1 with a V<sub>oc</sub> of 875 mV, J<sub>sc</sub> of 14.75 mAcm<sup>-2</sup>, and FF of 0.66 for a PCE of 8.52% under 1 sun illumination, comparable to a PCE of 9.36% for the cobalt reference electrolyte. For higher polymeric contents, the low PCEs under 1 sun result from mass-diffusion problems in the electrolyte. An upward-shift compared to the [Co(bpy)<sub>3</sub>]<sup>3+/2+</sup> electrolyte as a reference was observed for all the electrolytes containing the hyperbranched electrolytes, together with longer electron lifetimes compared to the Co<sup>3+/2+</sup> electrolyte, explaining the higher V<sub>oc</sub> values obtained for the HB electrolytes. EIS analysis under 1 sun illumination revealed that the polymer network formation leads to a slight enhancement in recombination suppression compared to the cobalt reference. Additionally, under 1 sun illumination, the Warburg resistance for the cobalt species in the electrolytes increases exponentially with the polymer content. EIS analysis also revealed that the higher performance for all the devices with HB1 and HB2 under low light intensity is attributed to higher R<sub>CT</sub> and lower R<sub>trans</sub>, leading to a PCE of 23.19% under 1000 lux for devices containing 15% of HB1 compared to 20.37% for the Co-reference.



## 3.6 Supporting Information

### Materials and Methods

All chemicals and solvents were purchased from Sigma-Aldrich and TCI chemicals, if not otherwise noted, and were used without further purification.

**DSSC fabrication:** Glass substrates with fluorine-doped tin oxide (FTO, NSG-10, Nippon Sheet Glass) were cleaned with 0.2% (w/w) detergent solution in an ultrasonic bath for 1 h and rinsed with water, ethanol and acetone, followed by a UV/O<sub>3</sub> (Model no.256-220, Jelight Company, Inc.) treatment for 15 min. A thin TiO<sub>2</sub> blocking layer was deposited on the FTO substrates at 450 °C by spray-pyrolysis of a solution prepared with 0.6 mL titaniumdiisopropoxide bis(acetylacetonate), 75 wt % in IPA, 0.4 mL of acetyl acetone and 9 mL of dry ethanol. Mesoporous TiO<sub>2</sub> films of 0.25 cm<sup>2</sup> were prepared by screen printing a 4.5 μm thick colloidal TiO<sub>2</sub> (Dyesol paste DSL 30 NRD-T) layer and drying at 120 °C in air for 5 min. Subsequently, a 4 μm thick light-scattering layer consisting of 400 nm sized TiO<sub>2</sub> particles (Dyesol WER2-0) was deposited on top by screen-printing. The films were then gradually heated in air in an oven (Nabertherm controller P320), applying a four-level program: 125 °C (10 min), 250 °C (10 min), 350 °C (10 min), and 450 °C (30 min). After sintering, the electrodes were treated in aqueous TiCl<sub>4</sub> at 70 °C for 30 min, and washed with water and ethanol. The thickness of the TiO<sub>2</sub> films was measured with a profilometer (Veeco Dektak 3). A final heating step at 500 °C (30 min) was performed followed by overnight immersion of the electrodes in the dye bath solution. The dye bath composition was 0.1 mM XY1 (Dyename AB chemicals) with 5 mM CDCA (chenodeoxycholic acid) in tert-butyl alcohol and acetonitrile (1:1). After immersion, all films were rinsed in acetonitrile to remove the excess of dye. Solar cells were assembled by direct contact of the sensitized electrodes with pre-drilled counter electrodes composed of poly (3,4-ethylenedioxythiophene) (PEDOT) deposited on NSG TEC8TM (Pilkington) FTO-type conducting glass, sealed with UV-cured glue ThreeBond3035B. The PEDOT electrodes were prepared by electropolymerization of 3,4-ethylenedioxythiophene (EDOT) from a micellar aqueous solution of 0.1 M sodium n-dodecyl sulfate (SDS) and 0.01 M EDOT. The electrolyte solution was introduced under vacuum through a hole predrilled in the counter electrode, sealed with UV-cured glue ThreeBond3035B. The devices containing the polymer mixtures were cured with a Dentmate Traydex™ 18 (375-470 nm) for 2 min to undergo the thiol-ene reaction. The electrolyte compositions were a) the cobalt reference electrolyte: 0.25 M Co(bpy)<sub>3</sub>(TFSI)<sub>2</sub> (bpy = 2-2'-bipyridine, TFSI = N(CF<sub>3</sub>SO<sub>2</sub>)<sub>2</sub>) (Dyename AB chemicals), 0.05 M Co(bpy)<sub>3</sub>(TFSI)<sub>3</sub> (Dyename AB chemicals), 0.1 M LiTFSI, and 0.25 M 4-(5-nonyl)pyridine (NP) in acetonitrile. The polymeric systems consisted of:

- a) **HB1:** 80%(w/w) of Poly(ethylene glycol) methacrylate (PEGMA) and 20% of (mercaptopropyl)methylsiloxane homopolymer from GELEST.
- b) **HB2:** 80%(w/w) of Poly(ethylene glycol) dimethacrylate (PEGDA) and 20% of (mercaptopropyl)methylsiloxane homopolymer from GELEST.

Subsequently, the electrolyte mixtures were prepared by adding HB1 or HB2 from 10-20% (v/v) to the cobalt reference electrolyte, and a 3% (w/w of added HB) of the photoinitiator 2,2-Dimethoxy-2-phenylacetophenone.

The symmetric cells were fabricated with two PEDOT/FTO electrodes sealed together with 35  $\mu\text{m}$  Surlyn® and filled with the redox electrolytes to be tested.

**Electrochemical Measurements:** Cyclic voltammetry measurements were performed with a potentiostat Bio Logic SP300, in a three-electrode setup cell. A glassy carbon electrode served as the working electrode ( $0.07\text{cm}^2$  area) and a graphite rod as the counter electrode; a non-aqueous reference electrode of Ag/AgCl (1 M LiCl in ethanol) was used, with an intermediate bridge tube containing the same supporting electrolyte as the working electrode compartment. The electrolyte solutions contained 2 mM of AZ, and 0.1 M of LiTFSI as supporting electrolyte in dry acetonitrile. The scan rate was  $100\text{ mV s}^{-1}$ , formal potentials were determined vs ferrocenium/ferrocene as a reference system, and then vs SHE (with a value established for  $\text{Fc}^+/\text{Fc} = 0.624\text{ V}$  versus SHE in acetonitrile and  $25\text{ }^\circ\text{C}$ ).<sup>101</sup> Cyclic voltammetry measurements to determine the current-potential plots of the symmetrical cells were also performed with the Bio Logic SP300 potentiostat.

**Solar Cell Characterization:** Current–voltage (I–V) characteristic curves and photocurrent-dynamics were measured using a 450 W Xenon lamp (Oriental Light USA) as light source, with a K113 filter Schott Tempax and matched to AM 1.5G solar standard conditions using a reference Si photodiode. Additionally, the indoor light was delivered by an Osram 930 Warm White tube light or Warm White 3000 K LED (EGLO). The light intensities were calibrated by a light meter (TES-1334, TES). The current and voltage were measured and controlled by a Keithley 2400 digital source meter (Keithley, USA) and the current measurement was set up to be delayed 80 ms from applying the potential. A set of metal mesh filters was used to adjust the light intensity to a desired level. A black metal mask with a  $0.16\text{ cm}^2$  aperture was used to define the active area.

**Incident Photon to Current Efficiency, IPCE:** Data were obtained using a modulated light intensity with a frequency of 1 Hz. Light from a 300 W xenon light source (ILC Technology, USA), was focused through a monochromator (JobinYvon Ltd., UK) and directed to the device under test. A white light bias was used to have similar light intensity conditions as during normal operation.

**Electron lifetime measurements:** The measurements were recorded with a Dyenamo AB (Sweden) toolbox using a white LED (Luxeon Star 1W) as light source. Voltage traces were recorded with a 16-bit resolution digital acquisition board (National Instruments); lifetimes were obtained by monitoring photovoltage transients at different light intensities upon applying a small square wave modulation to the base light intensity. The photovoltage response was fitted using first-order kinetics to obtain time constants. The quasi-Fermi level of  $\text{TiO}_2$  for the devices was calculated by subtracting the reached values of  $V_{\text{oc}}$ , to the redox potential of each specific electrolyte.

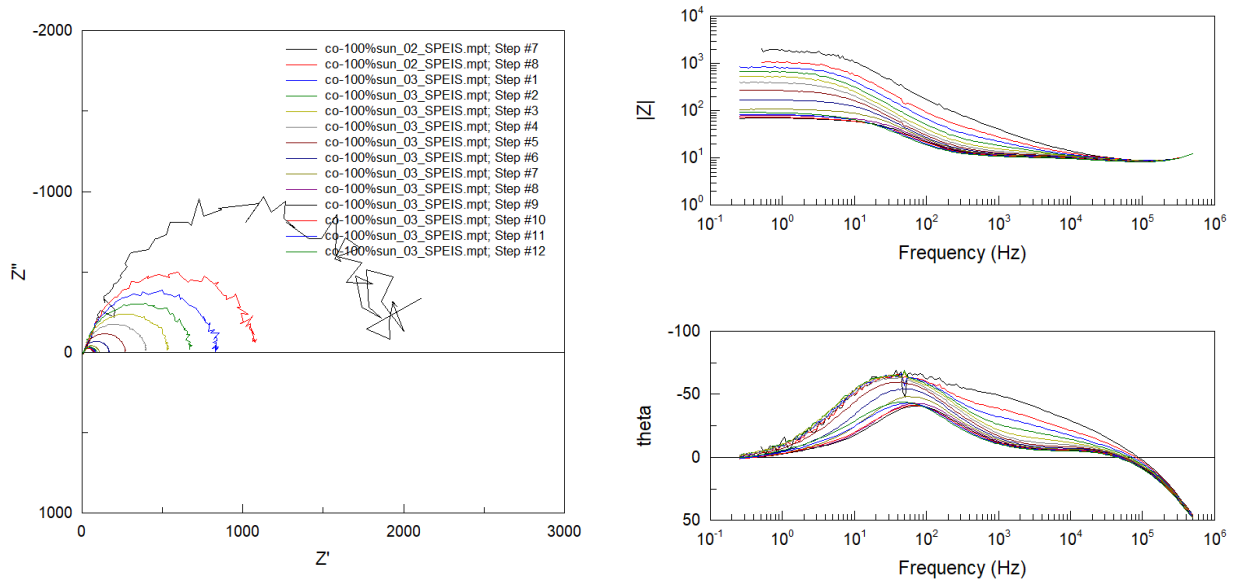
**Electrochemical Impedance Measurements, EIS:** Impedance measurements were performed using a Bio Logic SP300 potentiostat, over a frequency range from 1 MHz down to 0.1 Hz at bias potentials between 0.5 and 1.1 V (with a 10 mV sinusoidal AC perturbation). All measurements were done at 20 °C. The resulting impedance spectra were analyzed with Z-view software (v2.8b, Scribner Associates Inc.).

**Thermogravimetric Analysis, TGA:** Measurements were performed using a Perkin Elmer TGA 4000, with a temperature range of 30 ° C to 950 ° C, with nitrogen gas and a 45-slot autosampler. The measurement was carried out in a cycle of 25 ° C to 400 ° C at a rate of 10 ° C per minute.

**Fourier-transform infrared, FTIR:** Measurements were performed using a FTS 7000 use a He-Ne laser operating at 632.8 nm with a MCT detector for mid-IR measurements and a 896b interferometer. The real panel of the spectrometer is connected for a Far-IR power source, an external source, purged air and water coolant. Infrared measurements were recorded in the 4000–600  $\text{cm}^{-1}$  spectral range with 4  $\text{cm}^{-1}$  spectral and 0.242 s time resolution.

**Table S.3.1.** Statistics for 7 devices per electrolyte

	0.1 Sun				0.5 Sun				1 Sun			
Electrolyte	VOC (mV)	JSC (mAcm <sup>-2</sup> )	FF	$\eta$ (%)	VOC (mV)	JSC (mAcm <sup>-2</sup> )	FF	$\eta$ (%)	VOC (mV)	JSC (mAcm <sup>-2</sup> )	FF	$\eta$ (%)
[Co(bpy) <sub>3</sub> ] <sup>3+/2+</sup>	807±27	1.60±0.1	0.76±0.03	9.3±0.6	849±30	7.7±0.6	0.75±0.02	9.5±0.4	862±32	14 ±1	0.72±0.02	9.1±0.2
HB1 10%	835±9	1.5±0.3	0.77±0.2	9.8±0.4	870±8	7.0±1.0	0.74±0.02	9.40±0.3	877±8	13.24±1	0.69±0.03	8.1±0.4
HB1 15%	833±6	1.61±0.1	0.77±0.04	9.9±0.2	870±6	7.5±0.7	0.71±0.04	8.81±0.1	870±14	12.30±0.4	0.66±0.09	6.86±1.0
HB1 20%	829±15	1.61±0.13	0.75±0.03	9.51±0.3	866±14	7.6±0.6	0.67±0.06	8.05	875±10	12.5±1	0.56±0.16	6±1
HB2 10%	822±10	1.73±0.1	0.74±0.03	9.78±0.3	855±10	8.3±0.6	0.67±0.06	8.9±0.7	861±9	13.4±1.8	0.64±0.1	7.57±1
HB2 15%	828±19	1.61±0.08	0.77±0.02	9.74±0.5	865±18	7.85±0.3	0.71±0.01	9.2±2	870±14	12.73±1	0.65±0.9	7.28±0.6
HB2 20%	814±29	1.67±0.1	0.78±0.02	9.92±0.2	852±17	6.97±0.9	0.7±0.07	7.76±0.6	870±7	11.15±1.7	0.59±0.1	6.31±0.9

**Figure 3.13.** Nyquist plots for a device with Co-reference electrolyte at 1 sun illumination.

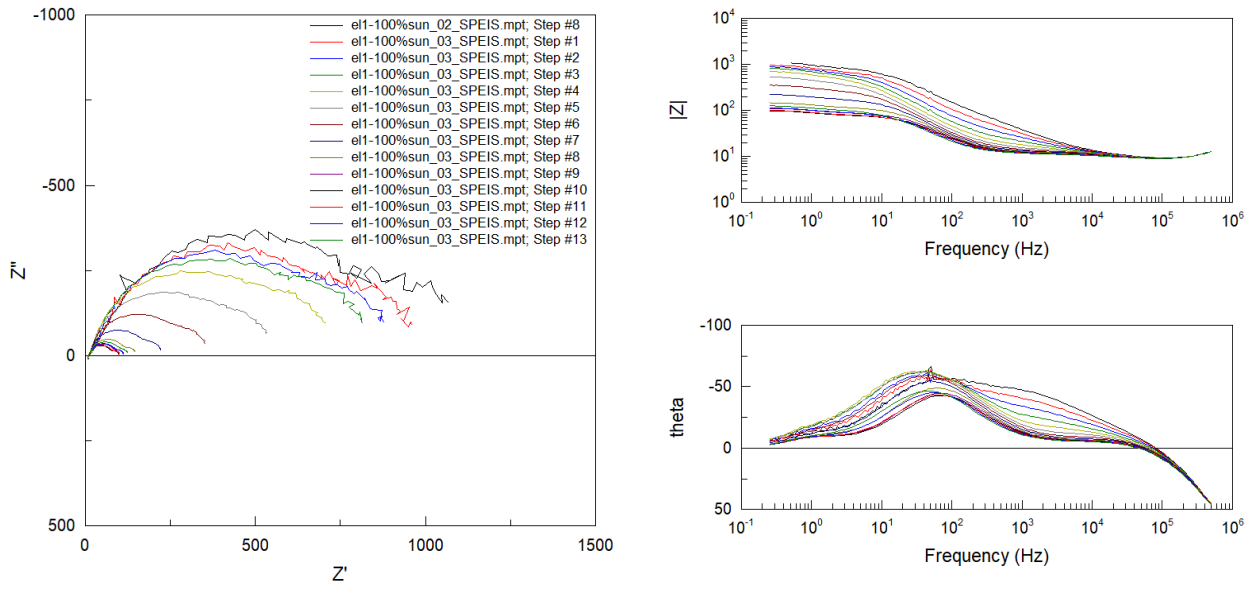


**Figure 3.14.** Nyquist plots for a device with 10% of HB1 electrolyte at 1 sun illumination.

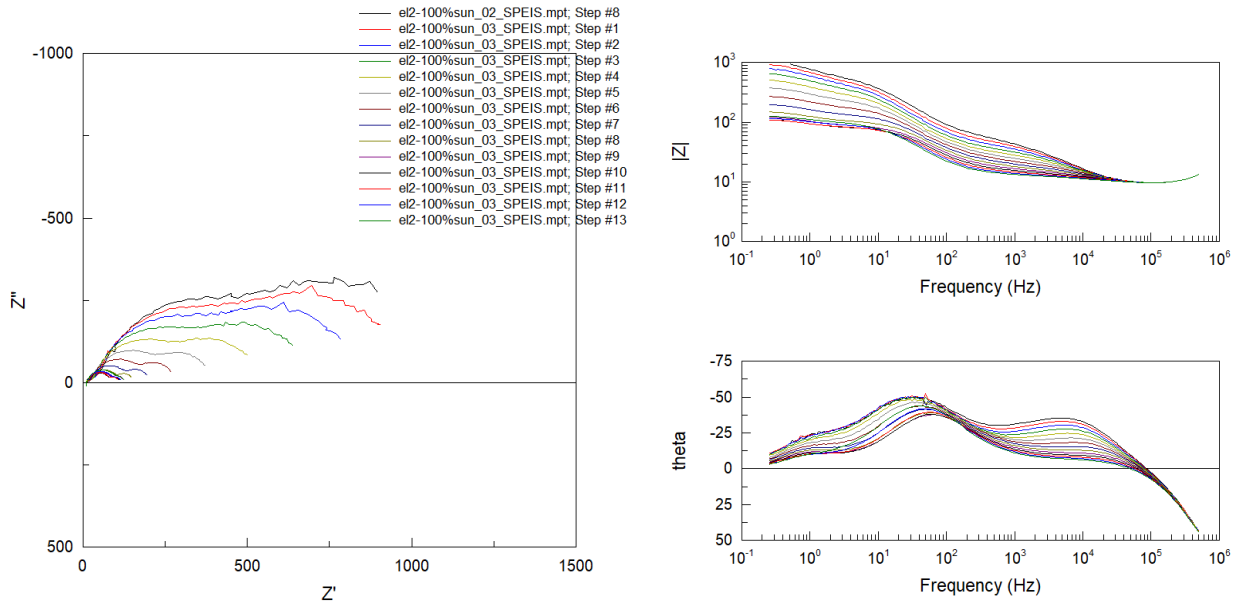


**Figure 3.15.** Nyquist plots for a device with 15% of HB1 electrolyte at 1 sun illumination

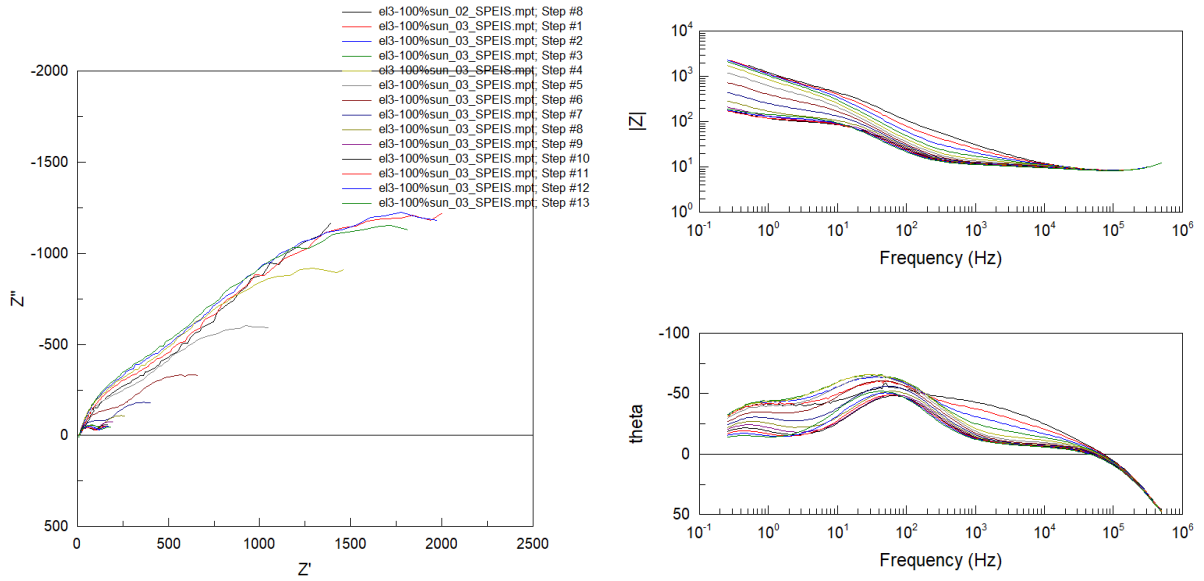


**Figure 3.16.** Nyquist plots for a device with 20% of HB1 electrolyte at 1 sun illumination.

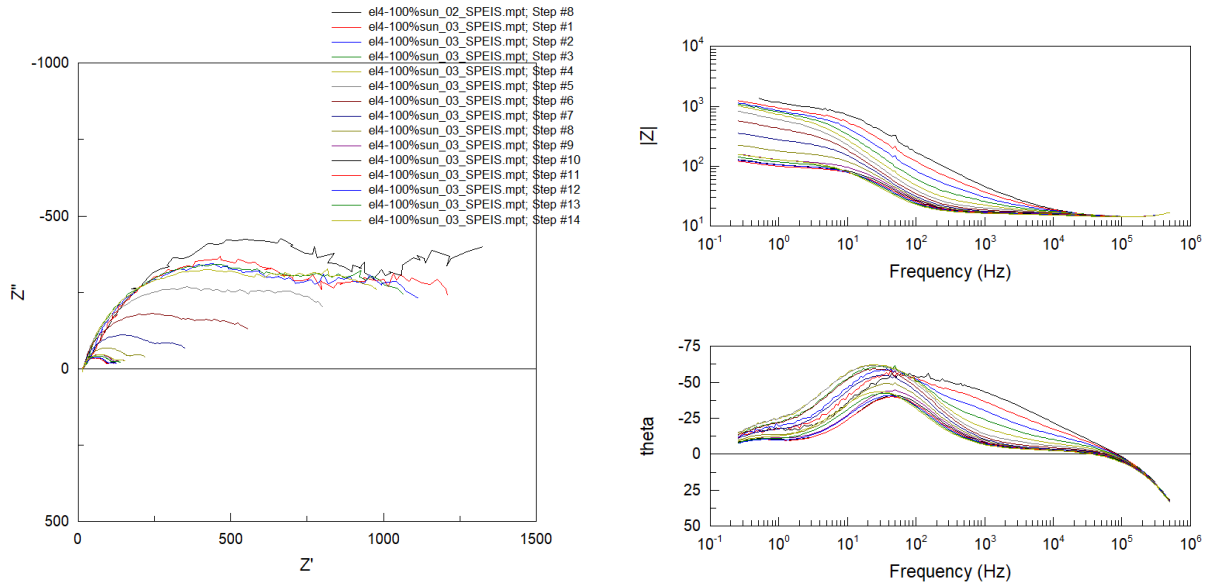


**Figure 3.17.** Nyquist plots for a device with 10% of HB2 electrolyte at 1 sun illumination.

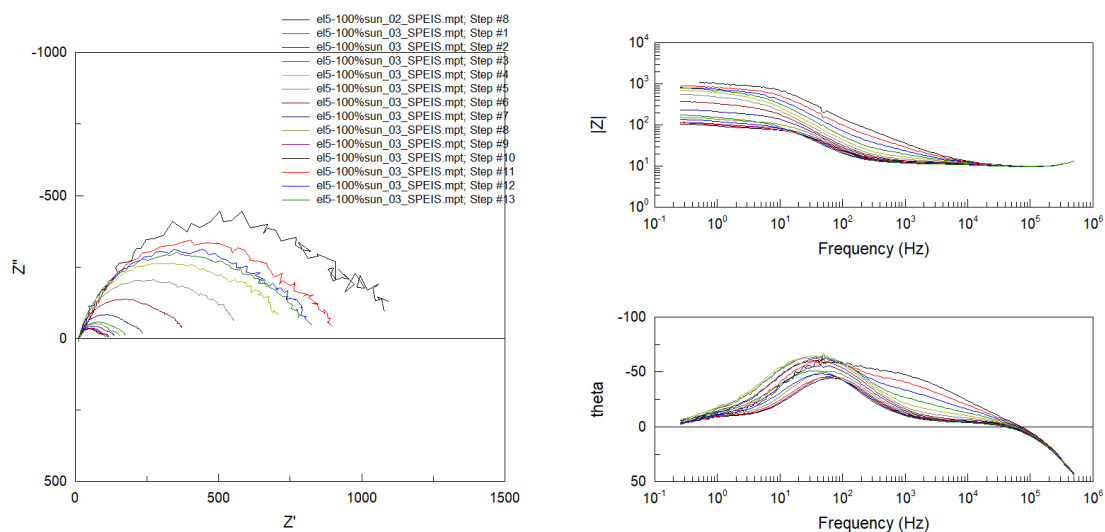


**Figure 3.18.** Nyquist plots for a device with 15% of HB2 electrolyte at 1 sun illumination.

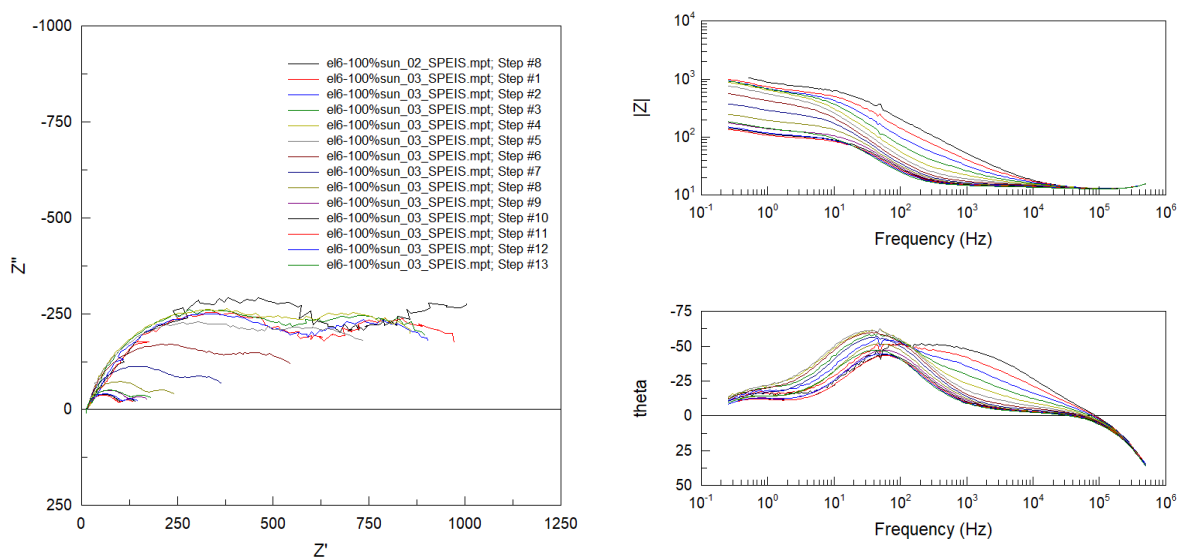


**Figure 3.19.** Nyquist plots for a device with 20% of HB2 electrolyte at 1 sun illumination.

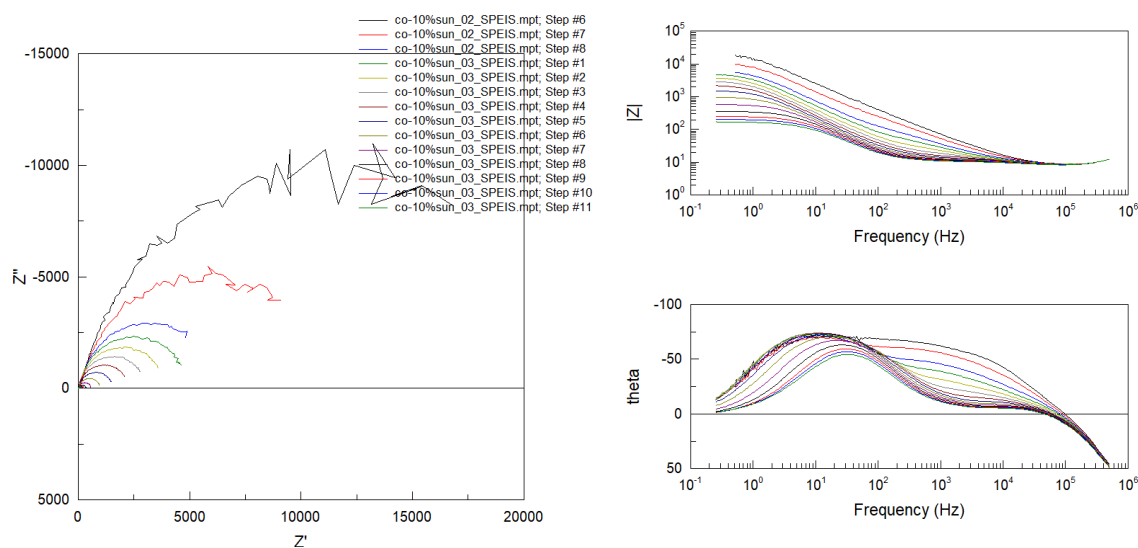


**Figure 3.20.** Nyquist plots for a device with Co-reference electrolyte at 0.1 sun illumination.

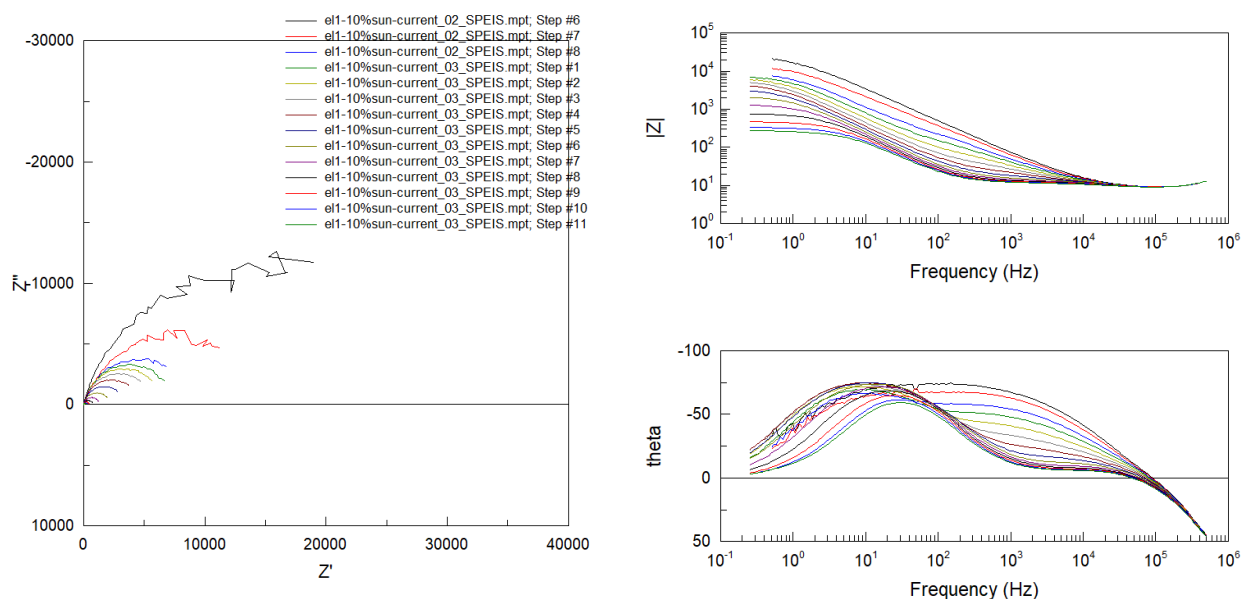


**Figure 3.21.** Nyquist plots for a device with 10% of HB1 electrolyte at 0.1 sun illumination.



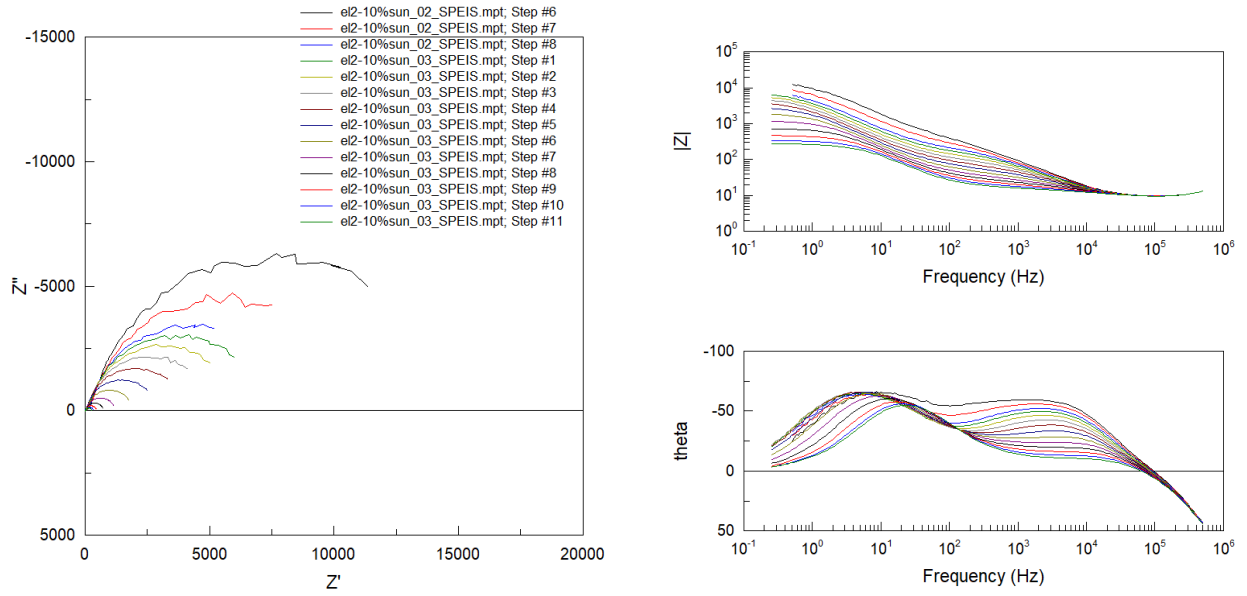


**Figure 3.22.** Nyquist plots for a device with 15% of HB1 electrolyte at 0.1 sun illumination.

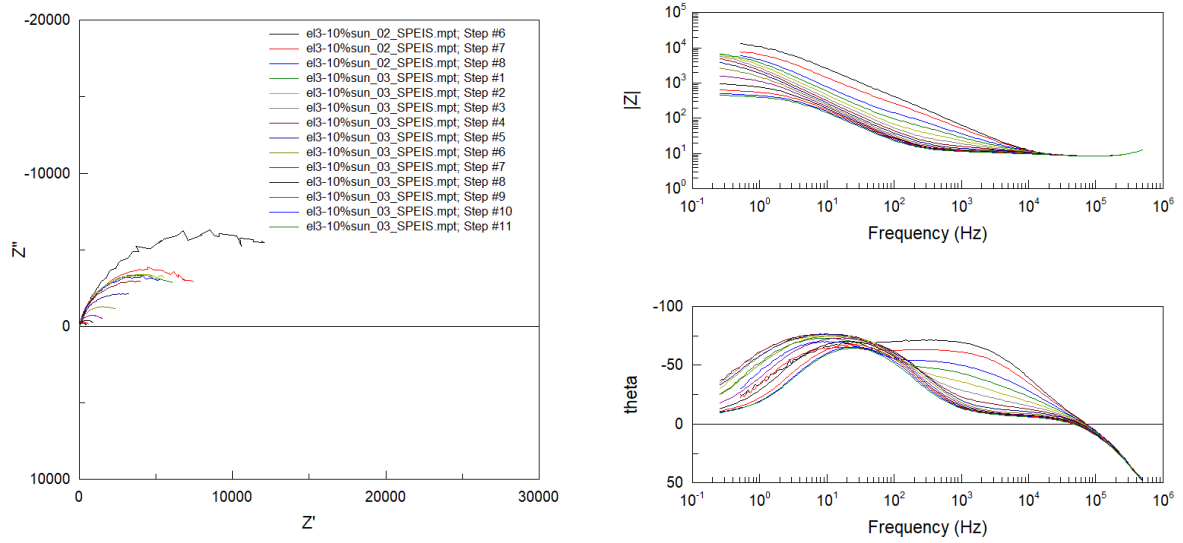


**Figure 3.23.** Nyquist plots for a device with 20% of HB1 electrolyte at 0.1 sun illumination.

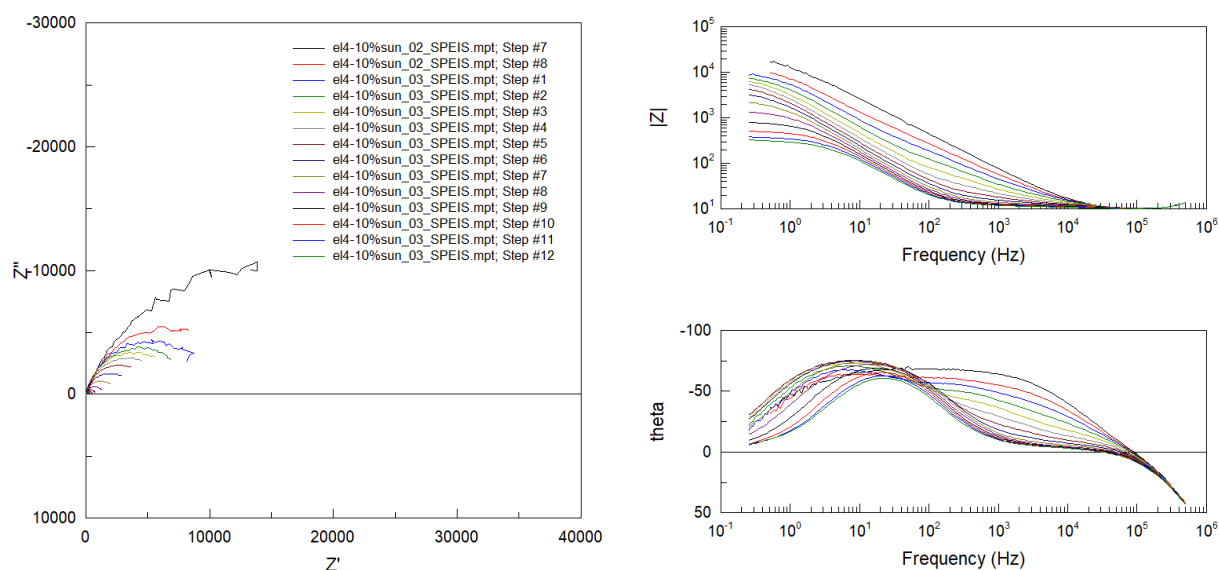


**Figure 3.24.** Nyquist plots for a device with 10% of HB2 electrolyte at 0.1 sun illumination.

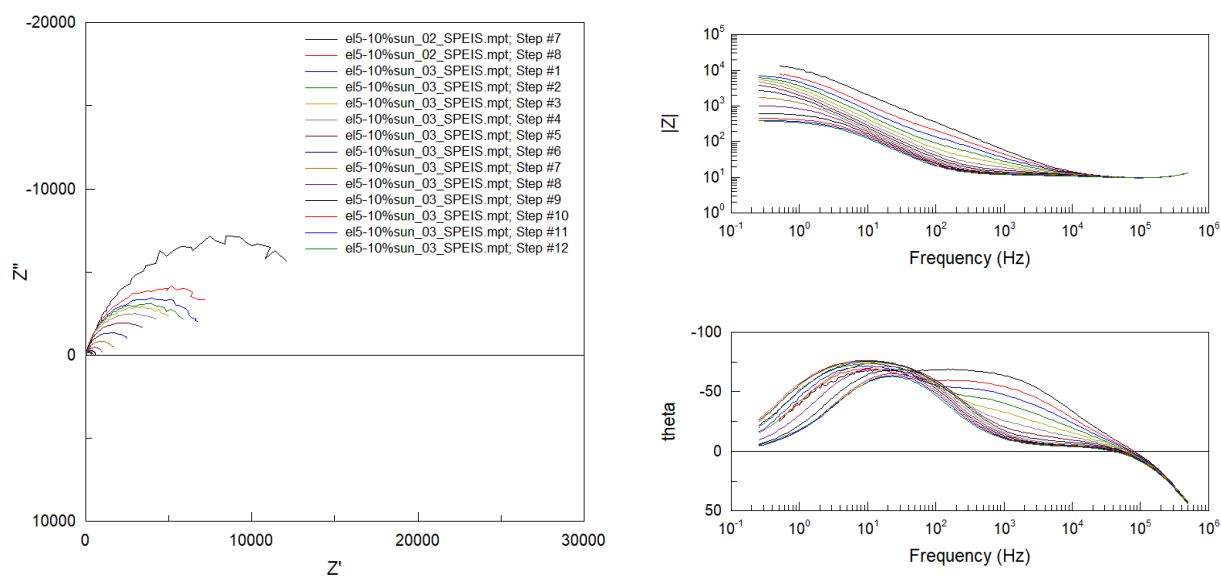


**Figure 3.25.** Nyquist plots for a device with 15% of HB2 electrolyte at 0.1 sun illumination.

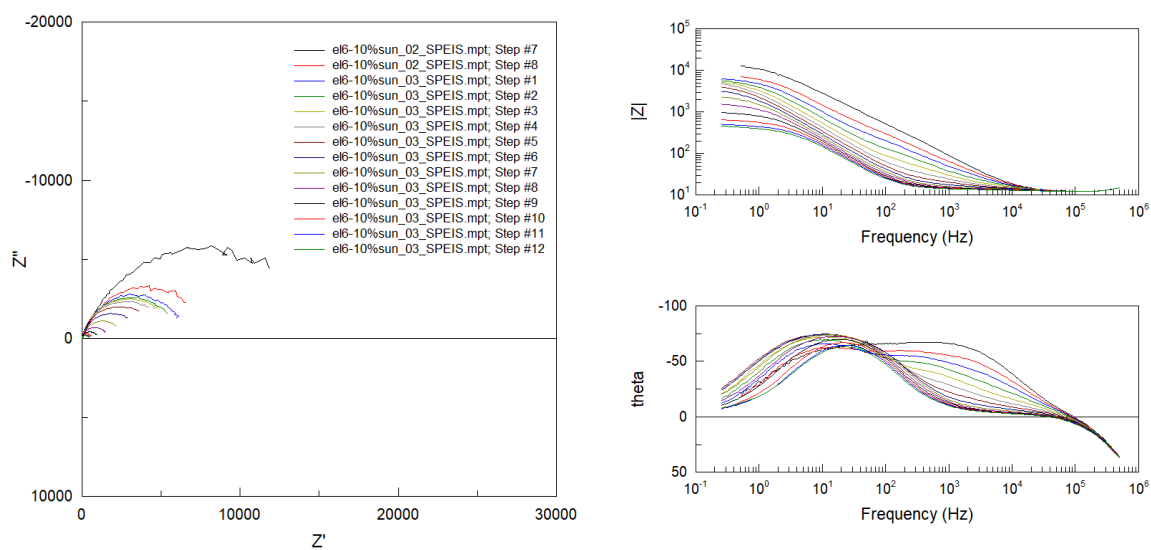


**Figure 3.26.** Nyquist plots for a device with 20% of HB2 electrolyte at 0.1 sun illumination.

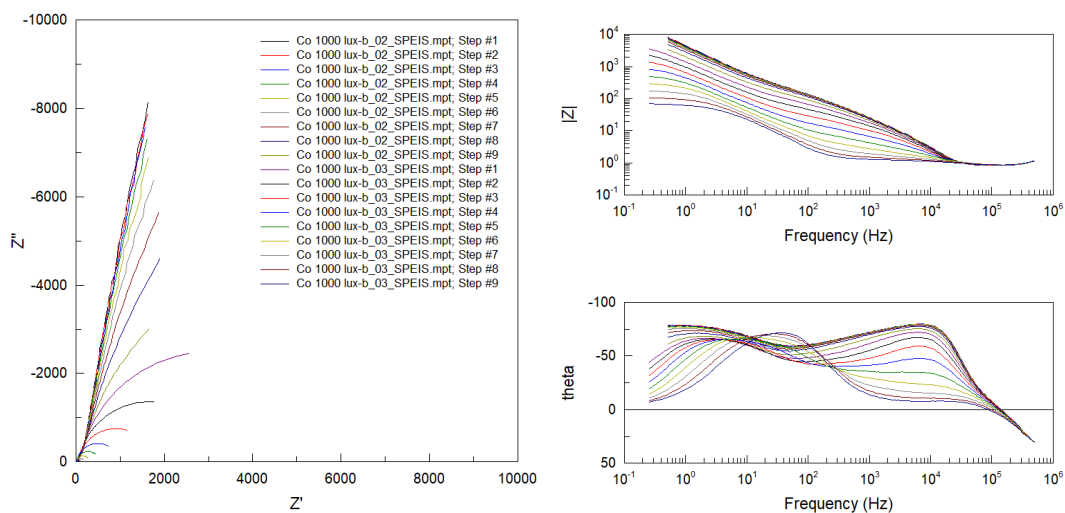


**Figure 3.27.** Nyquist plots for a device Co-reference electrolyte at 1000 lux illumination.

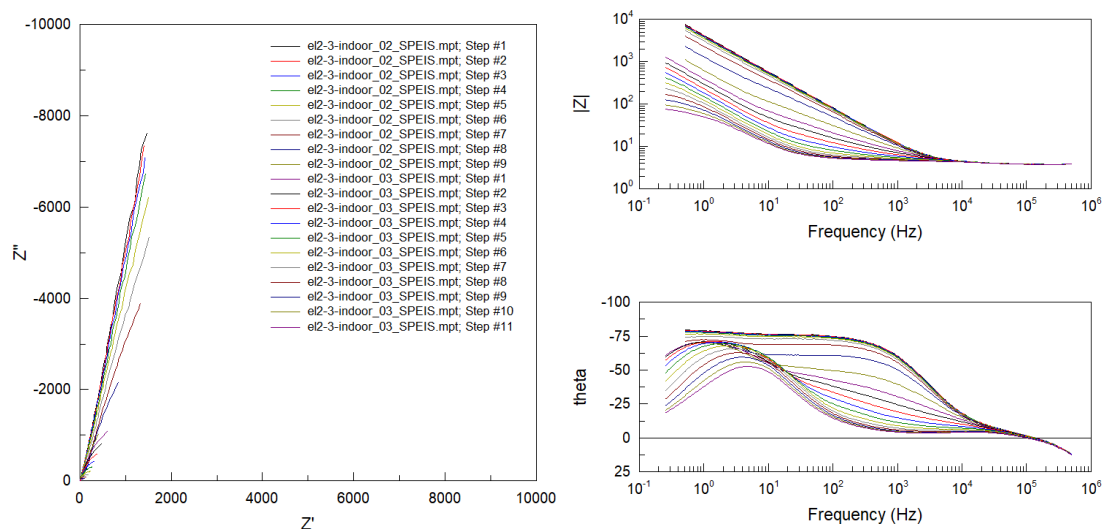


**Figure 3.28.** Nyquist plots for a device 15% of HB1 electrolyte at 1000 lux illumination.

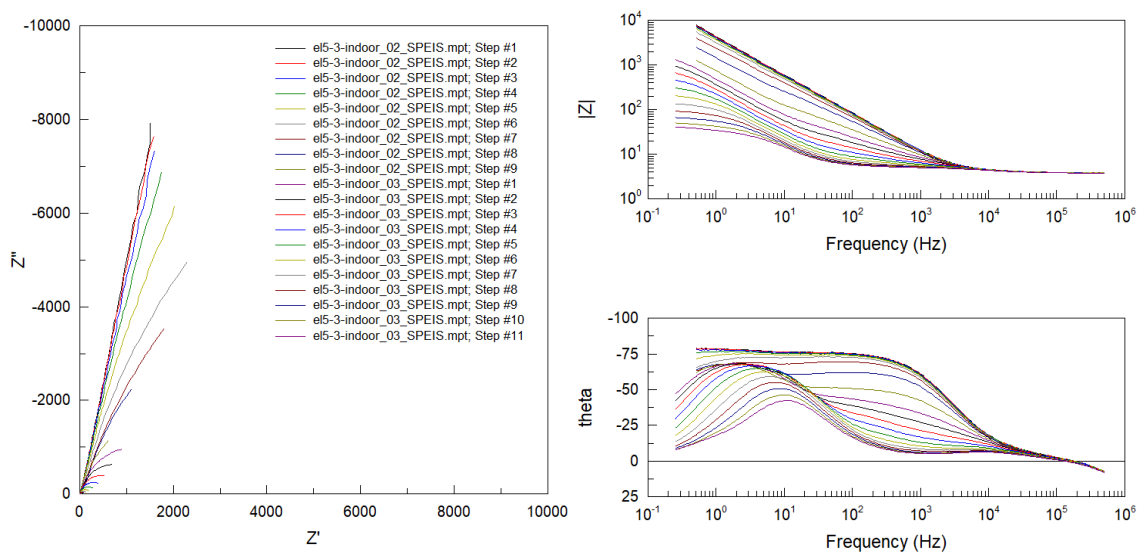


**Figure 3.29.** Nyquist plots for a device 15% of HB2 electrolyte at 1000 lux illumination.

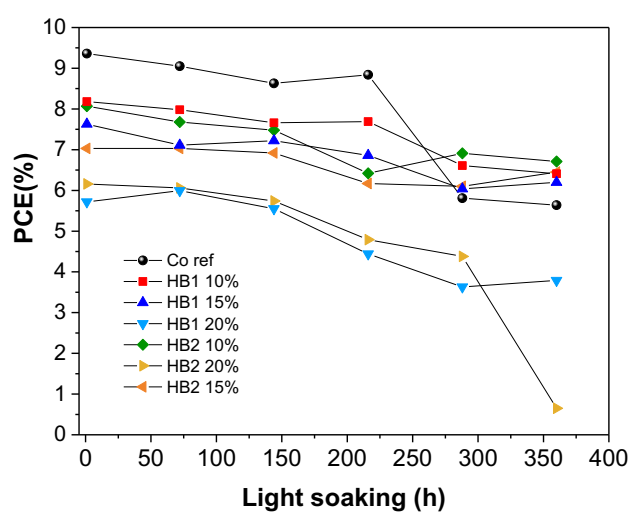


**Figure 3.30.** Light soaking aging at 60 °C and 1 Sun illumination



## Chapter 4 Engineering of a novel blue dye for decreased electron recombination

This chapter is adapted from the paper:

***Blue Photosensitizer with Copper(II/I) Redox Mediator for Efficient and Stable Dye-Sensitized Solar Cells***

*Yameng Ren, Natalie Flores-Díaz, Dan Zhang, Yiming Cao, Jean-David Decoppet, George Cameron Fish, Jacques-E. Moser, Shaik Mohammed Zakeeruddin, Peng Wang, Anders Hagfeldt,\* and Michael Grätzel\**

<https://onlinelibrary.wiley.com/doi/10.1002/adfm.202004804>

My contribution was device preparation, characterization and manuscript writing.

Yameng contributed with the dye synthesis, device preparation and manuscript editing.

### 4.1 Motivation

Replacing the  $I_3^-/I^-$  by copper complexes as redox mediators in DSSCs have remarkably increased the open-circuit voltages ( $V_{oc}$ ) over 1.0 V, due to their higher oxidation potentials compared to iodide/triiodide and cobalt complexes, low internal reorganization energies, fast electron transfer rates, and fast diffusion coefficients.<sup>111,112</sup>

Notably, DSSCs fabricated with organic dyes, and copper-electrolytes have attained PCE of over 13% under 1 sun illumination. Moreover, they have displayed an outstanding PCE over 34% under low light intensities or artificial indoor light,<sup>141</sup> making it one of the best technologies for developing electric power sources for portable electronics and devices for wireless sensor networks or the Internet of Things (IoT).<sup>142</sup>

However, the  $J_{SC}$  values typically attained by DSSC employing copper-based electrolytes are relatively low, limiting the further enhancement in device performance. The development of new dyes specifically tailored to be compatible with copper-based electrolytes, with an extended spectral response, is a crucial strategy for boosting the PCE of DSSCs employing copper complexes.

Previously a strong electron-donating polycyclic aromatic hydrocarbon (PAH) core, 9,19-dihydrobenzo[1',10']phenanthro[3',4':4,5]thieno[3,2-*b*]benzo[1,10]phenanthro[3,4-*d*]thiophene (BPT2), was successfully utilized by Ren *et al.* as the central electron-releasing block of a blue dye R6 with a wide spectral response for efficient and stable cobalt complex-based DSSCs, reaching high PCEs of 12.6%.<sup>143</sup>

Meanwhile, the *N*-(2',4'-bis(hexyloxy)-[1,1'-biphenyl]-4-yl)-2',4'-bis(hexyloxy)-*N*-methyl-[1,1'-biphenyl]-4-amine, commonly referred to as the Hagfeldt (HF) donor, has been shown to efficiently suppress electron recombination from the CB of TiO<sub>2</sub> to the redox shuttle. The HF donor also prevents the sensitizers' aggregation into the TiO<sub>2</sub> films, resulting in high  $V_{OC}$  values for cobalt complex-based DSSCs. On the other hand, the electron acceptor 4-(7-ethynylbenzo[*c*][1,2,5]thiadiazol-4-yl)benzoic acid (EBTBA) has also been successfully used as the electron acceptor for high-efficiency zinc-porphyrin and metal-free organic dyes.<sup>144</sup>

In this regard, a new blue dye was judiciously designed and synthesized and coded R7. The new dye bears an electron-rich PAH block BPT2 functionalized with the HF donor and the acceptor EBTBA for copper complex-based DSSCs. During a preliminary test, the DSSCs with the blue dye R7 in conjunction with Cu(II/I) bipyridyl complexes showed superior performance than to the reference dye R6.

## 4.2 Dye characterization

The effect of the HF donor's introduction into the R6 dye framework on the optical properties of the new dye R7 was studied by UV-Vis spectroscopy of the dyes dissolved in tetrahydrofuran (THF), as shown in Fig. 4.1(b). It can be observed that the absorption spectra of the sensitizers are highly similar, as expected given the structural similarities; only a slight blue-shift of the maximum absorption peak was observed for R7 (626 nm) compared to R6 (631 nm), Fig.4.2(a). The wavelength-dependent molar extinction coefficients ( $\epsilon$ ) reached remarkably high maximum  $\epsilon$  values of  $81.8 \times 10^3 \text{ M}^{-1}\text{cm}^{-1}$  for R6 and  $85.5 \times 10^3 \text{ M}^{-1}\text{cm}^{-1}$  for R7. Therefore, light-harvesting efficiency (LHE) could be expected to be near 100% for these dyes at their maximum peaks.

Cyclic voltammetry was employed to study the effect of the introduction of the HF donor on the highest occupied molecular orbital (HOMO) and lowest unoccupied molecular orbital (LUMO) of R7. The corresponding voltammograms in solution and adsorbed on TiO<sub>2</sub> electrodes are displayed in Fig. 4.3.



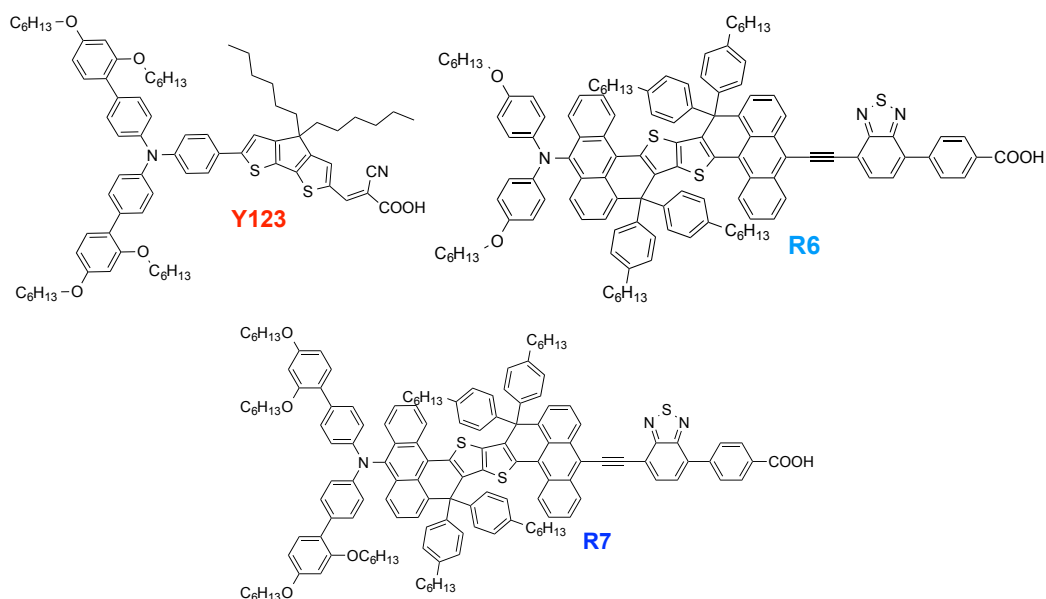


**Figure 4.1.** Molecular structures of the dyes Y123, R6, and R7.

The vacuum energy levels were estimated by the equation  $E = -4.88 - eE_{\text{onset}}$ , where  $E_{\text{onset}}$  is the onset potential of oxidation and reduction of the ground-state molecule. Typically, for D- $\pi$ -A dyes, the HOMO level is mainly delocalized on the dye's donor moiety. In contrast, the LUMO level is mainly delocalized on the acceptor group to ease the injection of electrons into the conduction band (CB) of the  $\text{TiO}_2$ .<sup>106,145,102</sup>

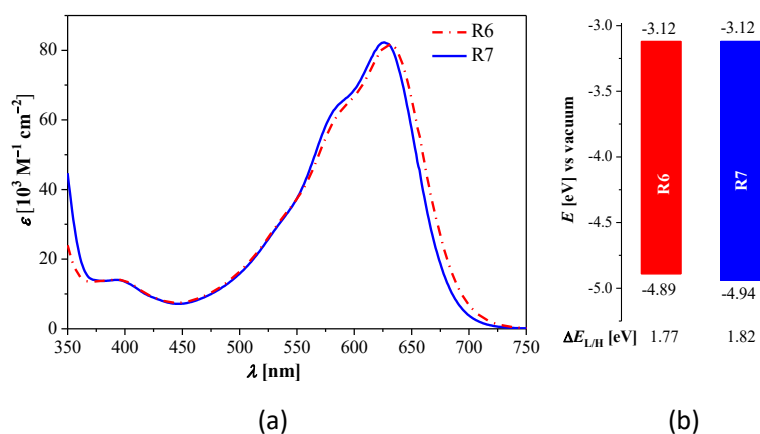


**Figure 4.2.** (a) Stationary UV-vis spectroscopies of R6 and R7 in THF (10  $\mu\text{M}$ ). (b) LUMO energy levels (values above color bars), HOMO energy levels (value under color bars), and energy gaps ( $\Delta E_{LH}$ ) of the dye molecules.

Given the extension only on the donor moiety, while the rest of the R6 dye scaffold remained unchanged, it can be expected that the main effect will be a slight change in the energetic level of the HOMO of the R7 dye. The HOMO and LUMO energies were determined from the onset of the first oxidation and reduction potential. The

measured HOMO energy level for R6 is  $-4.90$  eV and  $-4.95$  for R7. These values lie above the CB edge of  $\text{TiO}_2$  (approx.  $-4.0$  eV vs. vacuum), which implies enough driving force for electron injection from the dye into the CB of  $\text{TiO}_2$ . The same trend in the HOMO/LUMO energetic levels, maximum absorption peaks, and  $\epsilon$  can be reproduced by theoretical calculations, as listed in Table 4.1.

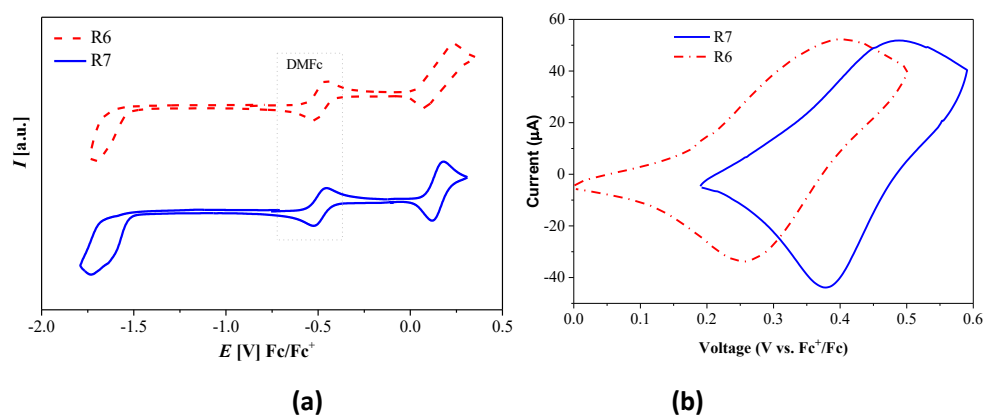


**Figure 4.3.** (a) Cyclic voltammograms of R6 and R7 in THF. Scan rate:  $5 \text{ mV s}^{-1}$ . The internal reference was decamethylferrocene (DMFc), and all potentials were calibrated with the standard ferrocene/ferrocenium ( $\text{Fc}/\text{Fc}^+$ ) redox couple. (b) Cyclic voltammograms of R6 and R7 dyes adsorbed on the  $\text{TiO}_2/\text{FTO}$  electrode in  $0.1 \text{ M}$  LiTFSI + acetonitrile, scan rate  $10 \text{ mV/s}$ .

As observed in Fig. 4.4, the HOMO is delocalized mainly on the donor moiety for both dyes as expected, and the LUMO is localized on the anchoring ligand,<sup>146</sup> displaying an evident characteristic of intramolecular charge-transfer as discerned from the contour plots of molecular orbitals.

**Table 4.1.** Data on frontier orbital energy levels and electronic absorptions.<sup>a</sup>

Dye	$E_L^{\text{CV}}$ [eV]	$E_L^{\text{B3LYP } a)}$ [eV]	$E_H^{\text{CV } a)}$ [eV]	$E_H^{\text{B3LYP}}$ [eV]	$\lambda_{\text{ABS,MAX}}^{\text{MEAS,THF}}$ [nm]	$\lambda_{\text{ABS,MAX}}^{\text{TD-MPW1K,THF}}$ [nm]	$f^{\text{TD-MPW1K}}$	$\epsilon_{\text{ABS,MAX}}^{\text{MEAS,THF}}$ [ $10^3 \text{ M}^{-1} \text{ cm}^{-1}$ ]
<b>R6</b>	-3.35	-3.12	-4.90	-4.89	631	639	1.95	81.82
<b>R7</b>	-3.35	-3.12	-4.95	-4.94	626	637	2.08	82.31

<sup>a</sup> Frontier orbital energies ( $E_L^{\text{CV}}$  and  $E_H^{\text{CV}}$ ) versus vacuum, measured with cyclic voltammetry. Where  $E = -4.88 - eE_{\text{onset}}$ ,  $E_{\text{onset}}$  is the onset oxidation and reduction potentials of a molecule in the ground-state in THF. L and H stand for LUMO and HOMO, respectively. Energy levels ( $E_L^{\text{B3LYP}}$  and  $E_H^{\text{B3LYP}}$ ) are computed at the B3LYP/6-311G(d,p) level of theory for a dye molecule in THF. The maximum absorption wavelength ( $\lambda_{\text{ABS,MAX}}^{\text{MEAS,THF}}$ ) and maximum molar absorption coefficient ( $\epsilon_{\text{ABS,MAX}}^{\text{MEAS,THF}}$ ) are derived from electronic absorption spectroscopies of THF solutions presented in Figure 1. Maximum absorption wavelength ( $\lambda_{\text{ABS,MAX}}^{\text{TD-MPW1K}}$ ) is calculated at the TD-MPW1K/6-311G(d,p) level of theory for a dye molecule in THF.

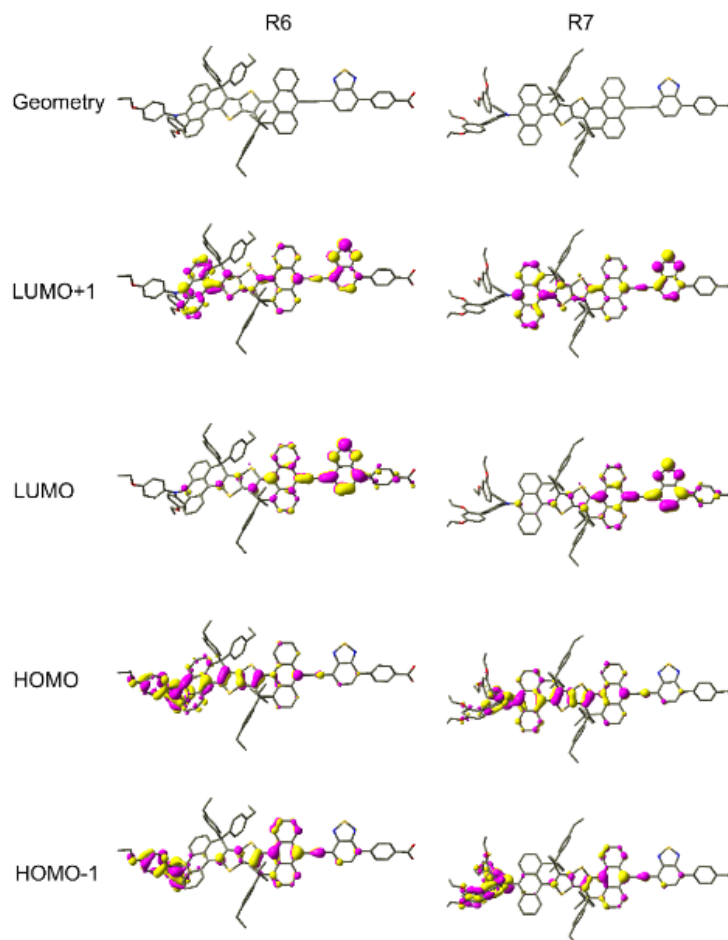


**Figure 4.4.** Contour plots of all the related  $S_1 \leftarrow S_0$  transition molecular orbitals. The orbitals were calculated using DFT/B3LYP/C-PCM(THF). (Isovalue set to 0.03 a.u.). The large hexyl substituents were replaced with ethyl to improve computational efficiency.

### 4.3 DSSC employing the engineered R7 dye

The sensitizers were evaluated in DSCs with the redox mediator  $\text{Cu}(\text{tmbpy})_2^{2+/1+}$  in acetonitrile. The obtained current density vs. voltage (J-V) curves under standard AM 1.5G and the IPCE curves are displayed in Fig 4.5. The characteristic parameters attained by the devices are summarized in Table 4.2.

All the devices fabricated with the dye R6 and copper electrolyte presented low performance. Under 1 sun illumination, R6 obtained a short-circuit current ( $J_{\text{SC}}$ ) of  $12.65 \text{ mA cm}^{-2}$ , an open-circuit voltage ( $V_{\text{OC}}$ ) of 907 mV, and a fill factor (FF) of 0.767 to produce a PCE of 8.8%. These results are significantly lower than those previously reported for the R6 dye with  $\text{Co}(\text{bpy})_3^{3+/2+}$  electrolyte, which obtained a  $J_{\text{SC}}$  of  $19.69 \text{ mA cm}^{-2}$ , a  $V_{\text{OC}}$  of 850 mV, and a FF of 0.754 for a PCE of 12.6%.<sup>143</sup> This is likely due to fast electron recombination or slow regeneration of the

R6 when using a copper-based electrolyte.<sup>102</sup> The bulkier complexes  $\text{Co}(\text{bpy})_3^{3+/2+}$  are more protected from recombination than the smaller  $\text{Cu}(\text{tmby})_2^{2+/1+}$  species.

Nonetheless, devices with the protected dye R7 attained a  $J_{\text{SC}}$  of  $13.91 \text{ mAcm}^{-2}$ , a  $V_{\text{OC}}$  of 980 mV, a FF of 0.785, and a PCE of 10.7% under 1 sun illumination. The higher performance of R7 can be attributed to the insertion of the HF donor, which dramatically reduces the recombination of electrons from the CB of the  $\text{TiO}_2$  to the oxidized form of the electrolyte as expected, leading to significantly higher  $J_{\text{SC}}$ ,  $V_{\text{OC}}$ , and consequently higher PCE.<sup>102</sup> To the best of our knowledge, R7 is the best performing blue sensitizer for a copper complex based DSSCs.<sup>147,148</sup>

Aiming to improve the performance of the dye R7 further, we chose the well-known organic dye Y123 as a co-sensitizer with the blue dye R7.<sup>149,150</sup> Notably, the co-sensitized system with R7+Y123 exhibited outstanding parameters of a  $J_{\text{SC}}$  of  $16.15 \text{ mAcm}^{-2}$ , a  $V_{\text{OC}}$  of 1035 mV, and a FF of 0.76 to achieve a top PCE of 12.7%.

Most highly efficient photosensitizers ( $\text{PCE} > 12\%$ ) compatible with copper-based electrolytes employ the conventional electron acceptor cyanoacrylic acid (CA). Previously, dyes with the new acceptor EBTBA such as R6, showed superior performance compared to dyes with CA as the acceptors for cobalt-based DSSCs. Therefore, to the best of our knowledge, we, for the first time, achieved the highest PCE for copper complex-based DSSCs using a blue dye with an EBTBA acceptor (R7).

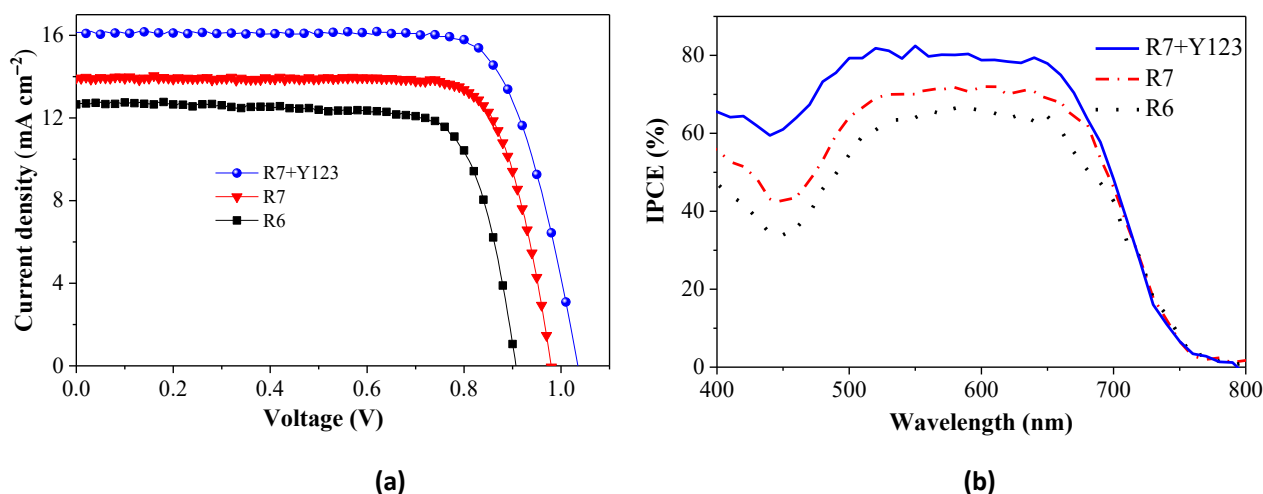


**Figure 4.5.** (a) Current density-voltage ( $J$ - $V$ ) curves measured under simulated full sunlight conditions for DSSCs. (b) Incident photon-to-electron conversion efficiencies (IPCEs) at a set of wavelengths of incident monochromatic lights.

The incident-photon-to-current conversion efficiency (IPCE) for DSCs with R6, R7, and the system R7+Y123 employing  $\text{Cu}(\text{tmby})_2$  electrolyte is shown in Figure 4.5. The IPCE for devices fabricated with dye R6 and the copper-based electrolyte was about 66%, much lower than the IPCE obtained with a cobalt-based electrolyte of 85%.

The introduction of a bulkier moiety on the donor site of the R7 motif leads to an IPCE increase to 72%, which can be attributed to a more efficient regeneration of the oxidized dye by the copper redox mediator and efficient blocking of electron recombination to the electrolyte by the introduction of bulky substituents on the dye.<sup>84</sup> Additionally, the co-sensitized devices with Y123 presented a further improvement in IPCE to 82%, which agrees with the higher  $J_{sc}$  from the J-V curves for this system. The IPCE depends on the yields of light-harvesting efficiency ( $\eta_{LH}$ ), electron injection efficiency ( $\eta_{inj}$ ), and charge collection efficiency ( $\eta_{cc}$ ), as in Eq.1.25.

The  $\eta_{LH}$  can be expected to be very close to 100% at the maximum light absorbance for the dyes R6 and R7 since they present similar high molar extinction coefficients. Therefore the  $\eta_{LH}$  does not explain the differences in the IPCE of the dyes. Moreover, as stated earlier the  $\eta_{inj}$  can be expected to be similar for both R6 and R7 dyes, given the similarities in the dyes' LUMO level. A lower degree of aggregation can be expected for R7 due to the bulkier donor, but the effect of dye aggregation on  $\eta_{inj}$  is almost insignificant.<sup>151</sup> Consequently, the  $\eta_{inj}$  is likely the most crucial reason for a lower IPCE for the dye R6, since higher electron recombination between the CB of TiO<sub>2</sub> and the copper mediators are expected compared to the modified R7, decreasing the  $\eta_{cc}$ , as confirmed from the toolbox measurements and electrochemical impedance spectroscopy (EIS) analysis.

**Table 4.2.** Photovoltaic parameters of the best-performing devices under the simulated AM1.5G sunlight (100 mW cm<sup>-2</sup>).

	Sun [%]	$J_{sc}$ [mA cm <sup>-2</sup> ]	$V_{oc}$ [mV]	FF [%]	PCE [%]
R6	100	12.65	907	76.7	8.8
	52.5	6.62	881	75.5	8.4
	10.2	1.2	803	65.8	6.2
R7	100	13.91	980	78.5	10.7
	52.4	7.30	955	80.3	10.7
	10.1	1.35	889	79.7	9.5
R7+Y123	100	16.15	1035	76.1	12.7
	50.5	8.11	1003	80.1	12.9
	9.9	1.56	940	77.7	11.5

The  $V_{oc}$  differences observed for R6 and R7 dyes were studied by toolbox measurements of the photovoltage response to a small amplitude light modulation. The charge extraction and electron lifetimes are displayed in Fig. 4.6. A slight down-shift compared to R6, was observed for the R7 and R7+Y123 co-sensitized devices. Nonetheless, these measurements do not show significant deviations that possibly explain  $V_{oc}$ 's differences from the J-V measurements. However, it is significant to note from Fig 4.6b, that R7 and R7+Y123 devices presented much longer electron lifetimes as a function of internal potential than R6, which indicates a lower recombination rate for those systems, which does explain the higher  $V_{oc}$  obtained by those devices.

In the case of R7 and the co-sensitized system, the down-shift of the quasi-Fermi level observed from Fig. 4.6(a) implies a larger driving force for electrons' electron injection from the excited dyes to the CB of the  $\text{TiO}_2$ . Consequently, a faster electron injection for these systems can explain the differences observed in the IPCE measurements due to the improved  $\eta_{inj}$  compared to R6.

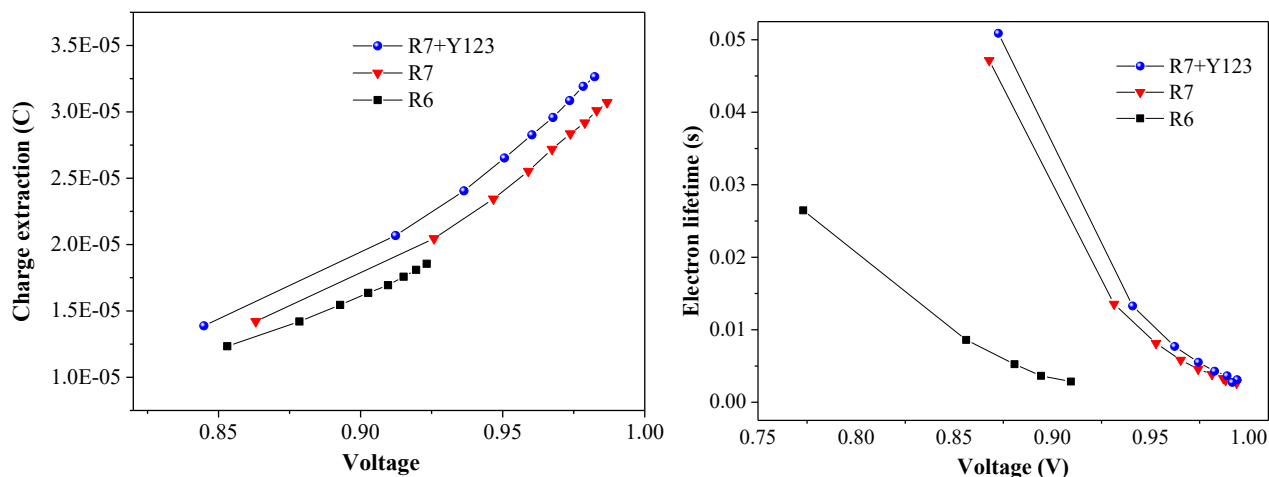


**Figure 4.6.** (a) Charge extraction vs. voltage curves measured (b) electron lifetime vs. voltage of DSCs with the dyes R6, R7 and the co-sensitized system R7+Y123 and  $\text{Cu}(\text{tmby})_2^{2+/1+}$  electrolyte.

EIS on complete devices under 1 sun illumination was performed to get a better insight into the devices' internal phenomena. The typical three-channel model<sup>59</sup> was used to fit the data using ZView® software, where the transmission-line model developed by Bisquert et al.,<sup>48,61,152</sup> was used to fit the Nyquist plots in the medium-voltage range. The results from the fittings are presented in Fig. 4.7.

The EIS analysis displayed that the series resistance,  $R_s$ , for all devices ranged from 5.3-7.9  $\Omega$ , while the counter electrode resistance,  $R_{CE}$ , presented values from 1.5-4.0  $\Omega$ . The recombination resistance is lower for the devices sensitized with R6 compared to R7. These account for the loss in photocurrent observed for R6, and the lower  $V_{OC}$  observed in the J-V curves. Accordingly, the electrons injected from the LUMO of the dye into the CB of  $\text{TiO}_2$  easily recombine with the oxidized forms of the copper redox mediators, decreasing the electron injection rate. Furthermore, R6 presented higher transport resistances than R7, which can be ascribed to slower electron transport in the semiconductor layer and slower injection of electrons to the external circuit, explaining the lower  $J_{SC}$  for this dye. Moreover, higher electron lifetimes were achieved for the R7 dye and the R7+Y123 co-sensitized system, which confirms the beneficial effect of the insertion of the bulkier HF group on the donor side of R7 toward recombination with the copper complex  $[\text{Cu}(\text{tmby})_2]^{2+/1+}$ .

Additionally, in Fig. 4.7(a), the plot for chemical capacitance as a function of applied voltage shows no substantial difference for devices with R6 and R7 and a slight down-shift for the co-sensitized system. The chemical ca-

capacitance estimated from the ESI analysis was associated with the density of states (DOS) of the electrons in the  $\text{TiO}_2$  and plotted as a function of applied potential. In Figure 4.7(b), it can be observed that indeed there is a slight down-shift for the co-sensitized system. However, the movement is minimal and does not explain the differences in  $V_{OC}$ , following the same trend observed from the charge extraction measurements. Thus, we may conclude that the conduction band positions are principally equivalent.

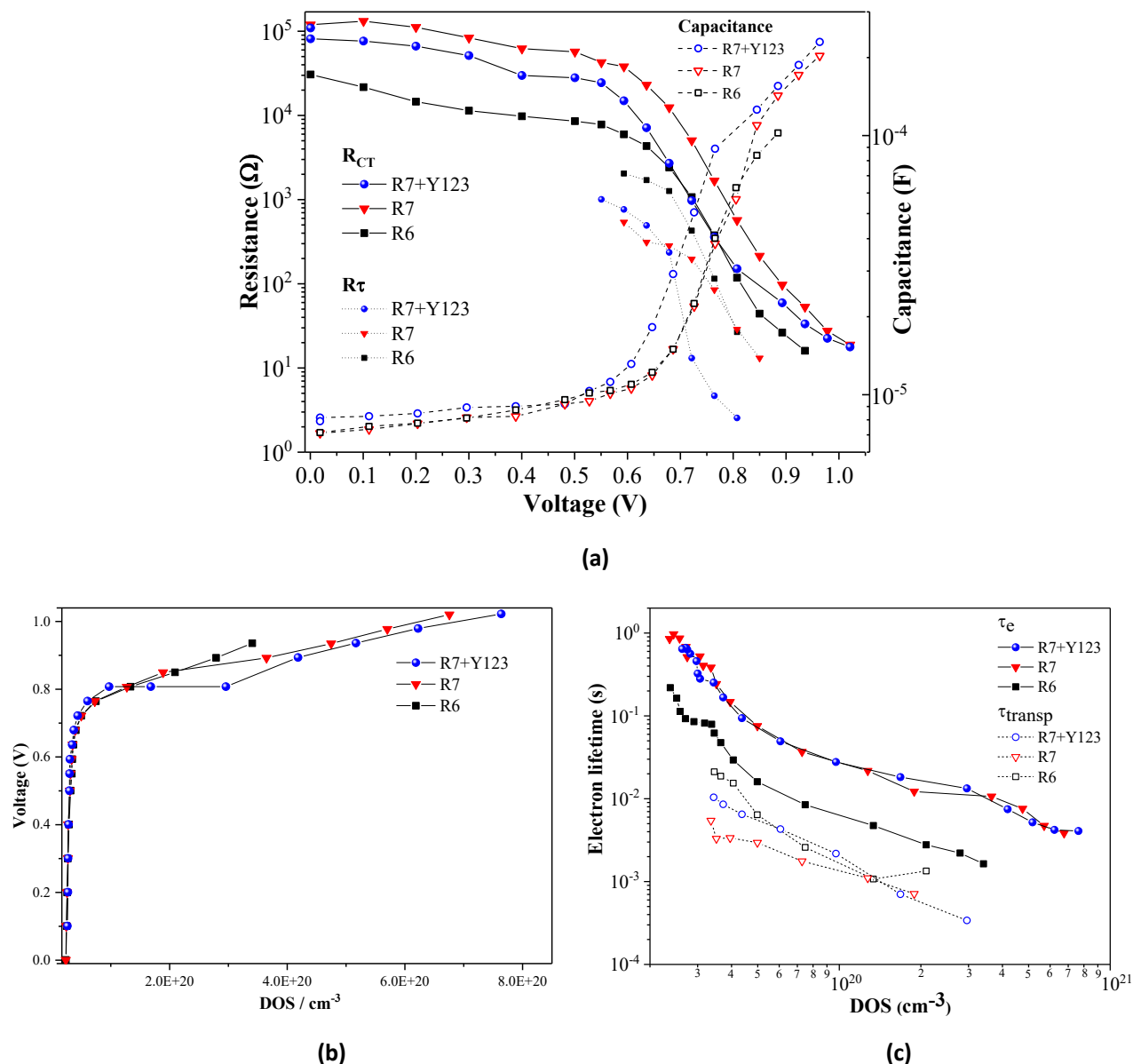


**Figure 4.7.** Electrochemical impedance spectroscopy (EIS) analysis. (a) Continuous lines with solid markers represent the charge transfer resistance ( $R_{CT}$ ) as a function of the applied voltage. The dotted lines with solid markers represent the transport resistance ( $R_{trans}$ ), and the dashed lines with open markers represent the chemical capacitance. (b) Voltage vs. density of states (DOS). (c) Electron lifetime as a function of DOS.

Finally, transient absorption spectroscopy, TAS, was performed to determine the effect of the bulkier donor moiety on the dye regeneration rate of the copper mediators (Fig.4.8). The data was extracted using a MATLAB routine, normalized and fitted with a monoexponential decay function using Igor Pro 7. The dye regeneration efficiency is then calculated using the Eq.1.34.

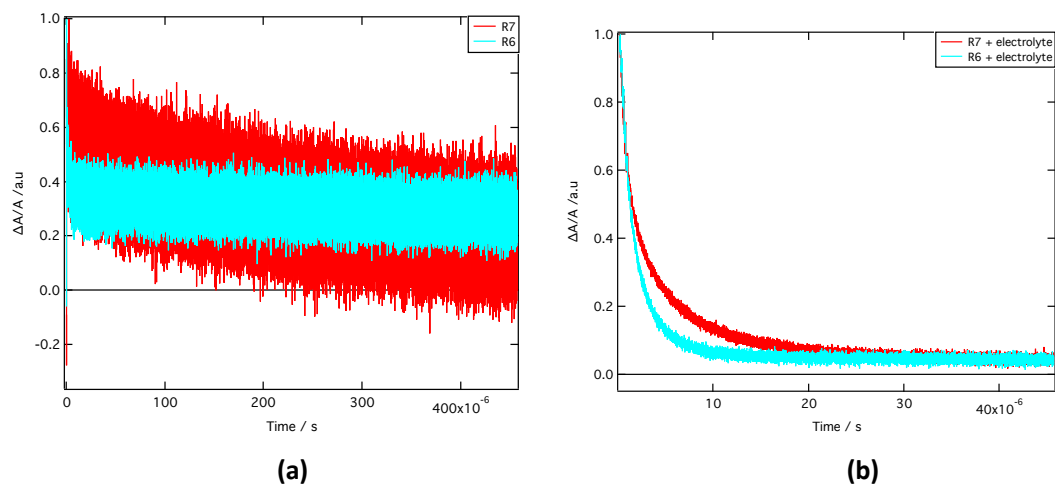


**Figure 4.8.** Transient absorption spectra for a) R6 and R7 with inert electrolyte of 0.1 M LiTFSI and 0.6 M NMB in acetonitrile (ACN), b) with 0.2 M  $[\text{Cu}(\text{tmby})_2]^{1+}\text{TFSI}$ , 0.09 M  $[\text{Cu}(\text{tmby})_2]^{2+}(\text{TFSI})_2$ , 0.1 M LiTFSI and 0.6 M NMB in ACN.

In the case of the dye R6, the photogenerated electrons recombine quite fast to the inert electrolyte, with a recombination half-time ( $\tau_{1/2}$ ) of  $13.4 \pm 0.6 \mu\text{s}$ . Conversely, for the samples with R7 dye with inert electrolyte, the recombination half-time was 13-fold faster with  $\tau_{1/2} = 175 \pm 3 \mu\text{s}$ . As expected, TAS measurements confirmed the marked effect of the HF donor's insertion in R7 for hampering the recombination of electrons in the CB of  $\text{TiO}_2$  to the electrolyte, compared to the bare R6 dye.

The dye's regeneration by the  $\text{Cu}(\text{tmby})_2$  electrolyte was found to be relatively fast for both dyes, with a regeneration half-time of  $1.820 \pm 0.004 \mu\text{s}$  for R6 and  $5.100 \pm 0.009 \mu\text{s}$  for R7. The copper complexes can reach the oxidized state of R6 faster than R7 due to the lack of the bulkier HF donor. Consequently, the regeneration efficiencies are 88.1% and 97.2% for R6 and R7, respectively. These measurements confirmed that for devices with R6 and copper electrolytes, the principal loss pathway is the recombination of electrons to the electrolyte, which ultimately affects the device's overall performance.



## 4.4 Conclusions

A new dye was engineered in combination with the auxiliary bulky HF donor, we have judiciously designed and synthesized a new blue dye R7 with the strong electron-donating PAH core and BPT2 as the central building block. The spectral response of the organic dye was successfully achieved by this strategy, also improving the stability with copper complexes as redox mediators on DSSCs. The photovoltaic performance of R7-based DSSCs with the copper-based electrolyte outperformed their counterpart ones with the dye R6. Our in-depth kinetic studies revealed that the bulky HF donor moiety efficiently suppresses the electron recombination between the TiO<sub>2</sub> surface and the redox shuttle.

Furthermore, the co-sensitized system of R7+Y123 presented outstanding parameters of  $J_{sc}$  of 16.15 mAcm<sup>-2</sup>,  $V_{oc}$  of 1035 mV, FF of 0.76 to achieve a top PCE of 12.7%. To the best of our knowledge, this value of PCE is the highest obtained for copper complex based-DSSCs using a blue photosensitizer not employing the conventional electron acceptor cyanoacrylic acid. So far demonstrating that PAH building block and the HF donor and the electron acceptor EBTBA enable successful spectral extending and interfacial tailoring in copper-based DSSCs. Thus adding a new member to the family of highly efficient organic dyes for copper complex based DSSCs. Our work will shed light on the future molecular engineering of other polycyclic aromatic hydrocarbon-based dyes with bulky HF-donor and other electron-deficient segments.

## 4.5 Supporting Information

### Experimental Section

All chemicals and solvents were purchased from Sigma-Aldrich and TCI chemicals, if not otherwise noted, and were used without further purification.

**DSSC fabrication:** Glass substrates with fluorine-doped tin oxide (FTO, NSG-10, Nippon Sheet Glass) were cleaned with 0.2% (w/w) detergent solution in an ultrasonic bath for 1 h and rinsed with water, ethanol, and acetone, followed by a UV/O<sub>3</sub> (Model no.256-220, Jelight Company, Inc.) treatment for 15 min. The FTO substrates were immersed for 30 min in a 40 mM aqueous TiCl<sub>4</sub> solution at 70 °C, and then washed with water and ethanol, followed by a sintering process at 250 °C for 2 h. Mesoporous TiO<sub>2</sub> films of 0.25 cm<sup>2</sup> were prepared by screen printing a 4.5 μm thick colloidal TiO<sub>2</sub> (Dyesol paste DSL 30 NRD-T) layer and drying at 120 °C in air for 5 min. Afterward, a 4 μm thick light-scattering layer consisting of 400 nm size TiO<sub>2</sub> particles (Dyesol WER2-0) was deposited on top by screen-printing. The films were then gradually heated in an oven (Nabertherm controller P320), applying a four-level program: 125 °C (10 min), 250 °C (10 min), 350 °C (10 min), and 450 °C (30 min).

After sintering, the electrodes were treated in aqueous  $\text{TiCl}_4$  at 70 °C for 30 min and washed with water and ethanol. The thickness of the  $\text{TiO}_2$  films was measured with a profilometer (Veeco Dektak 3). A final heating step at 500 °C (30 min) was performed, followed by overnight immersion of the electrodes in the dye bath solution. The single dye bath composition was 0.1 mM R6, R7, with 5 mM CDCA (chenodeoxycholic acid) in THF/EtOH (1:4). For the dye bath composition of the co-sensitized system was 0.1 mM R7 and 0.1 mM Y123 (Dyename AB chemicals) with 5 mM CDCA in THF/EtOH (1:4). After immersion, all films were rinsed in acetonitrile to remove the excess of dye. Solar cells were assembled using UV glue, with a counter electrode composed of poly (3,4-ethyl-enedioxythiophene) (PEDOT) deposited on NSG TEC8™ (Pilkington) FTO-type conducting glass. The PEDOT electrodes were prepared by electropolymerization of 3,4-ethylenedioxythiophene (EDOT) from a micellar aqueous solution of 0.1 M sodium n-dodecyl sulfate (SDS) and 0.01 M EDOT. The electrolyte solution was introduced under vacuum through a hole predrilled in the counter electrode, which was sealed with thermoplastic Surlyn® and a glass coverslip. The copper-based electrolyte consists of 0.2 M  $[\text{Cu}(\text{tmby})_2]$  (TFSI) and 0.09 M  $[\text{Cu}(\text{tmby})_2](\text{TFSI})_2$  complexes with 0.1 M LiTFSI and 0.6 M 1-Methylbenzimidazole (NMB) in acetonitrile. The inert electrolyte consists of 0.1 M LiTFSI and 0.6 M 1-Methylbenzimidazole (NMB) in acetonitrile (tmby, 4,4',6,6'-tetramethyl-2,2'-bipyridine; TFSI, bis(trifluoromethanesulfonyl)imide).

**Electrochemical Measurements:** electrochemical experiments were carried out in a one-compartment cell using an Autolab Pgstat-30. The working electrode was mesoporous  $\text{TiO}_2$  (4  $\mu\text{m}$  thick film) deposited directly on FTO, i.e., without any underlayer. The counter electrode was platinum, and the reference electrode was a non-aqueous Ag/AgCl (sat. LiCl in ethanol), which was interfaced by a bridge with 0.1 M lithium trifluoromethylsulfonylimide (LiTFSI) in acetonitrile. The potential was calibrated using ferrocene (200  $\mu\text{L}$  of 0.1 M acetonitrile solution per 10 mL of electrolyte solution added and tested using the Pt working electrode; the potential of the standard ( $\text{Fc}^+/\text{Fc}$ ) was fluctuating between 0.499 to 0.510 V vs. the non-aqueous Ag/AgCl).

**DFT and TD-DFT Calculations:** Theoretical calculations were performed with Gaussian 09 program suite employing the 6-311G(d,p) basis set for all atoms. Ground state geometries optimizations for R6 and R7 were executed using the density functional theory (DFT) method with Becke's three-parameter hybrid exchange functionals and the Lee-Yang-Parr correlation functional (B3LYP). The TD-MPW1K hybrid functional, which includes 42% of the Hartree-Fock exchange, was employed for the vertical electron transition calculations. The conductor-like polarizable continuum model (C-PCM) was picked for the simulation of solvent effects.

**Solar Cell Characterization:** Current–voltage (I–V) characteristic curves and photocurrent-dynamics were measured using a 450 W Xenon lamp (Oriel USA) as light source, with a K113 filter (Schott Tempax) and matched to AM 1.5G solar standard conditions using a reference Si photodiode. The current and voltage were measured and controlled by a Keithley 2400 digital source meter (Keithley, USA), and the current measurement was set up to

be delayed 80 ms from applying the potential. A set of metal mesh filters were used to adjust the light intensity to the desired level. A black metal mask with a 0.16 cm<sup>2</sup> aperture was used to define the active area.

**Incident Photon to Current Efficiency, IPCE:** Data were obtained using a modulated light intensity with a frequency of 1 Hz. Light from a 300 W xenon light source (ILC Technology, USA), was focused through a monochromator (JobinYvon Ltd., UK) and directed to the device under test. A white light bias was used to have similar light intensity conditions as during normal operation.

**Electron lifetime measurements:** The measurements were recorded with a Dyenamo AB (Sweden) toolbox using a white LED (Luxeon Star 1W) as the light source. Voltage traces were recorded with a 16-bit resolution digital acquisition board (National Instruments); lifetimes were obtained by monitoring photovoltage transients at different light intensities upon applying a small square wave modulation to the base light intensity. The photovoltage response was fitted using first-order kinetics to obtain time constants. The quasi-Fermi level of TiO<sub>2</sub> for the devices was calculated by subtracting the reached values of V<sub>OC</sub>, to the redox potential of each specific electrolyte

**Electrochemical Impedance Measurements (EIS):** Impedance measurements were performed using a BioLogic SP300 potentiostat, over a frequency range from 1 MHz down to 0.1 Hz at bias potentials between 0 and 1.1 V (with a 10 mV sinusoidal AC perturbation). All measurements were done at 20 °C. The resulting impedance spectra were analyzed with Z-view software (v2.8b, Scribner Associates Inc.).

**Transient Absorption Spectroscopy:** Nanosecond flash photolysis was used to monitor the dynamics. A frequency-tripled (355 nm) Q-switched Nd:YAG laser (continuum Surelite, 20Hz repetition rate) was used to pump an optical parametric oscillator (GWU) allowing the excitation wavelength to be tuned. Both R6 and R7 samples were excited at 650 nm. The samples were probed at 900 nm by a continuous Xenon arc lamp filtered by a monochromator with filters. The probe light was collected by a second monochromator and sent to a Silicon Amplified Photodetector (PDA 100A-EC, Thorlabs), enabling the photons to be converted into electrons. The induced transient voltage was recorded by a digital signal analyzer (DPO 7104C, Tektronix), and the data acquisition was averaged over 3000 shots to obtain a suitable signal-to-noise ratio.

## Materials

LiTFSI, EMITFSI, DMFc, Fc, TBP, tris(dibenzylideneacetone)dipalladium (Pd<sub>2</sub>(dba)<sub>3</sub>), [1,1'-bis(diphenylphosphino)ferrocene]dichloropalladium(II) (Pd(dppf)Cl<sub>2</sub>), palladium(II) acetate (Pd(OAc)<sub>2</sub>), 2-dicyclohexylphosphino-2',6'-dimethoxybiphenyl (Sphos), tris(1,1-dimethylethyl)phosphine (P(*t*-Bu)<sub>3</sub>), *N*-bromosuccinimide (NBS), (triisopropylsilyl)acetylene, sodium *tert*-butoxide (NaOt-Bu), potassium hydroxide (KOH), potassium phosphate (K<sub>3</sub>PO<sub>4</sub>), diethyl 2,5-dibromoterephthalate, 4,4,4',4',5,5,5'-octamethyl-2,2'-bi(1,3,2-dioxaborolane), and cesium carbonate (Cs<sub>2</sub>CO<sub>3</sub>) were purchased from Sigma-Aldrich and used without

further purification. Toluene, THF, dioxane, diisopropylamine, acetonitrile, ethanol, and chloroform were dried and distilled before use. **1** and **2** were synthesized according to the literature procedure. Other chemicals were purchased and used without further purification. The synthetic routes to **R7** are illustrated in Scheme S1 and preparation details are described as follows.

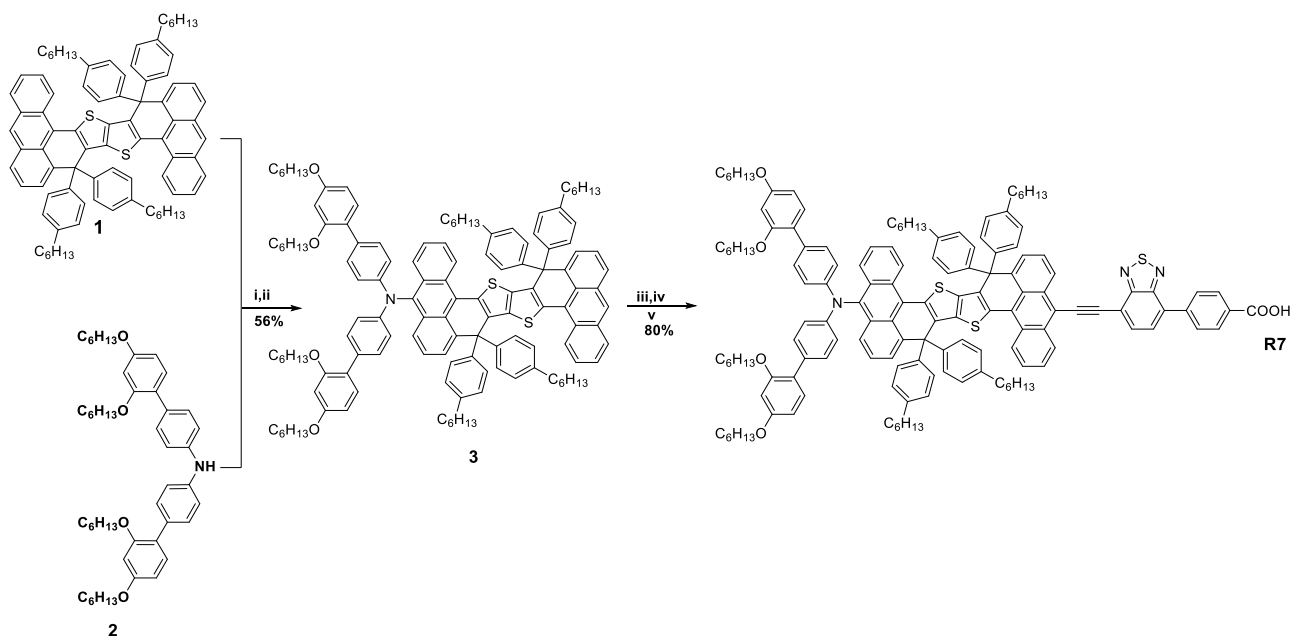


**Figure 4.9.** Synthetic routes to **R7**. Reagents and conditions: (i) NBS, THF, R.T., 10 min.; (ii) bis(2',4'-bis(hexyloxy)-[1,1'-biphenyl]-4-yl)amine, Pd<sub>2</sub>(dba)<sub>3</sub>, P(t-Bu)<sub>3</sub>, NaOtBu, toluene, reflux, 12 h; (iii) NBS, THF, R.T., 8 h; (iv) butyl 4-(7-ethynylbenzo[c][1,2,5]thiadiazol-4-yl)benzoate, Pd<sub>2</sub>(dba)<sub>3</sub>, P(t-Bu)<sub>3</sub>, Cs<sub>2</sub>CO<sub>3</sub>, dioxane, reflux, 10 h; (v) KOH, THF/H<sub>2</sub>O (v/v, 3/1), reflux, 10 h; then phosphoric acid.

*N,N*-bis(2',4'-bis(hexyloxy)-[1,1'-biphenyl]-4-yl)-9,9,19,19-tetrakis(4-hexylphenyl)-9,19-dihydrobenzo[1',10']phenanthro[3',4':4,5]thieno[3,2-*b*]benzo[1,10]phenanthro[3,4-*d*]thiophen-5-amine (**8**)

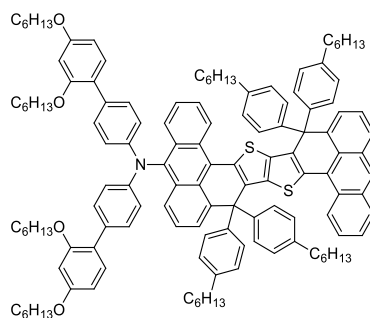


**Figure 4.10.** Molecular structure of bis(2',4'-bis(hexyloxy)-[1,1'-biphenyl]-4-yl)amine.

In a three-neck round bottom flask, **4** (1.5 g, 1.30 mmol) was dissolved in chloroform (35 mL). NBS (463 mg, 2.60 mmol) was added to the reaction mixture, which was stirred at room temperature for 10 min. Then the organic phase was washed with plenty of water and dried over anhydrous sodium sulfate to yield a red solid as the in-

intermediate product 5,15-dibromo-9,9,19,19-tetrakis(4-hexylphenyl)-9,19-dihydrodinaphtho[3,2,1-*de*:3',2',1'-*op*]pentacene, which was used for the next reaction directly. In a dried Schlenk tube were dissolved 5,15-dibromo-9,9,19,19-tetrakis(4-hexylphenyl)-9,19-dihydrobenzo[1',10']phenanthro[3',4':4,5]thieno[3,2-*b*]benzo[1,10]phenanthro[3,4-*d*]thiophene (1.71 g, 1.30 mmol), **6** (3.42 g, 2.60 mmol), and NaOtBu (375 mg, 3.90 mmol) in toluene (20 mL). Then Pd<sub>2</sub>(dba)<sub>3</sub> (48 mg, 0.052 mmol) and P(*t*-Bu)<sub>3</sub> (0.20 mL, 10 wt% in toluene, 0.078 mmol) were added to the reaction mixture in a nitrogen-filled glovebox, which was refluxed under argon for 12 h. The mixture was extracted three times with chloroform before the organic phase was washed with water and dried over anhydrous sodium sulfate. After solvent removal under reduced pressure, the crude product was purified by column chromatography (toluene/petroleum ether 60–90 °C, 1/3, v/v) on silica gel to yield a red solid as the desired product **7** (1.37 g, 56% yield). <sup>1</sup>H NMR (400 MHz, THF-*d*<sub>8</sub>) δ: 8.70 (d, *J* = 8.9 Hz, 1H), 8.62 (d, *J* = 9.1 Hz, 1H), 8.35 (s, 1H), 8.21 (d, *J* = 8.1 Hz, 2H), 7.96–7.93 (m, 2H), 7.46 (t, *J* = 7.6 Hz, 1H), 7.43–7.33 (m, 9H), 7.26 (d, *J* = 7.0 Hz, 2H), 7.15–7.08 (m, 22H), 6.54 (br, 2H), 6.48 (d, *J* = 8.5 Hz, 2H), 3.96–3.91 (m, 8H), 2.61–2.57 (m, 8H), 1.70–1.67 (m, 4H), 1.63–1.60 (m, 8H), 1.48–1.47 (m, 4H), 1.41–1.35 (m, 20H), 1.29–1.27 (m, 28H), 0.93–0.91 (m, 6H), 0.86–0.84 (m, 18H). <sup>13</sup>C NMR (125 MHz, THF-*d*<sub>8</sub>) δ: 160.34, 157.75, 146.83, 144.41, 143.64, 142.99, 142.36, 142.29, 142.10, 141.83, 138.14, 137.95, 137.92, 137.75, 137.34, 133.16, 132.57, 132.09, 131.45, 131.06, 130.93, 130.71, 129.87, 129.69, 128.55, 128.51, 127.97, 127.03, 126.73, 126.29, 125.92, 125.67, 125.47, 124.44, 123.67, 120.22, 105.97, 100.98, 68.79, 68.31, 67.74, 58.94, 58.90, 36.26, 36.23, 32.46, 32.45, 32.41, 32.38, 32.23, 30.45, 30.12, 29.99, 29.93, 29.86, 26.55, 26.47, 25.62, 23.35, 23.25, 23.24, 14.26, 14.23, 14.21. HR-MS (MALDI-TOF) *m/z* calcd. for (C<sub>132</sub>H<sub>149</sub>NO<sub>4</sub>S<sub>2</sub>): 1876.09280. Found: 1876.08848. Anal. Calcd. for C<sub>132</sub>H<sub>149</sub>NO<sub>4</sub>S<sub>2</sub>: C, 84.43%; H, 8.00%; N, 0.75%. Found: C, 84.44%; H, 8.01%; N, 0.76%.

4-(7-((15-(bis(2',4'-bis(hexyloxy)-[1,1'-biphenyl]-4-yl)amino)-9,9,19,19-tetrakis(4-hexylphenyl)-9,19 dihydrobenzo[1',10']phenanthro[3',4':4,5]thieno[3,2-*b*]benzo[1,10]phenanthro[3,4-*d*]thiophen-5-yl)ethynyl)benzo[*c*][1,2,5]thiadiazol-4-yl)benzoic acid (**R7**)

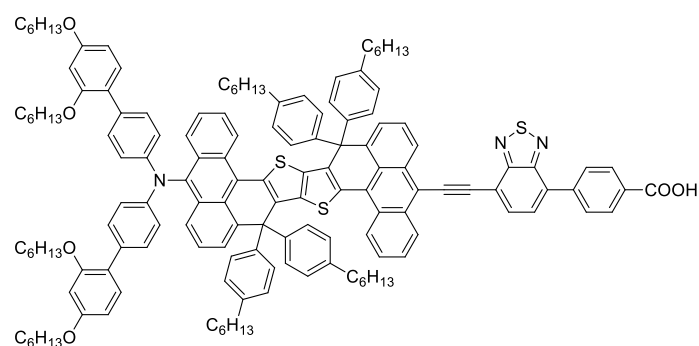


**Figure 4.11.** Molecular structure of **R7**.

In a three-neck round bottom flask, **8** (850 mg, 0.45 mmol) was dissolved in THF (30 mL). NBS (84 mg, 0.47 mmol) was added to the reaction mixture, which was stirred at room temperature for 8 h. Chloroform was added before the organic phase was washed with water and dried over anhydrous sodium sulfate. After solvent removal under reduced pressure, the crude product was purified by column chromatography (toluene/petroleum ether 60–90 °C, 1/3, v/v) on silica gel to yield an purple solid as the intermediate product N,N-bis(2',4'-bis(hexyloxy)-[1,1'-biphenyl]-4-yl)-9,9,19,19-tetrakis(4-hexylphenyl)-9,19-dihydrobenzo[1',10']phenanthro[3',4':4,5]thieno[3,2-*b*]benzo[1,10]phenanthro[3,4-*d*]thiophen-5-amine. In a dried Schlenk tube were dissolved N,N-bis(2',4'-bis(hexyloxy)-[1,1'-biphenyl]-4-yl)-9,9,19,19-tetrakis(4-hexylphenyl)-9,19-dihydrobenzo[1',10']phenanthro[3',4':4,5]thieno[3,2-*b*]benzo[1,10]phenanthro[3,4-*d*]thiophen-5-amine (880 mg, 0.45 mmol), butyl 4-(7-ethynylbenzo[*c*][1,2,5]thiadiazol-4-yl)benzoate (464 mg, 1.38 mmol), and Cs<sub>2</sub>CO<sub>3</sub> (161 mg, 0.50 mmol) in dioxane (25 mL). Then Pd<sub>2</sub>(dba)<sub>3</sub> (25 mg, 0.027 mmol) and P(*t*-Bu)<sub>3</sub> (0.14 mL, 10 wt% in toluene, 0.054 mmol) were added to the reaction mixture in a nitrogen-filled glovebox, which was refluxed under argon for 10 h. The mixture was extracted three times with chloroform before the organic phase was washed with water and dried over anhydrous sodium sulfate. After solvent removal under reduced pressure, the crude product was purified by column chromatography (toluene/petroleum ether 60–90 °C, 1/2, v/v) on silica gel to yield a violet powder as the desired butyl ester. In a three-neck round-bottom flask were dissolved the above butyl ester and KOH (252 mg, 4.50 mmol) in a solvent mixture of THF/H<sub>2</sub>O (20 mL, 3/1, v/v). The reaction mixture was refluxed for 10 h and then cooled to room temperature. Chloroform was added before the organic phase was washed with 0.1 M phosphoric acid and deionized water in turn and then dried over anhydrous sodium sulfate. After solvent removal under reduced pressure, the crude product was purified by column chromatography (chloroform/methanol, 20/1, v/v) on silica gel to yield a purple powder as the desired product **R5** (776 mg, 80% yield). <sup>1</sup>H NMR (500 MHz, THF-*d*<sub>8</sub>) δ: 9.01–8.96(m, 2H), 8.66 (d, *J* = 8.4 Hz, 2H), 8.24–8.18(m, 6H), 8.03 (d, *J* = 7.4 Hz, 1H), 7.83 (d, *J* = 7.4 Hz, 1H), 7.67–7.59(m, 2H), 7.46–7.41(m, 2H), 7.38–7.34(m, 7H), 7.28 (d, *J* = 6.6 Hz, 1H), 7.16–7.08(m, 22H), 6.54–6.47(m, 4H), 3.96–3.91(m, 8H), 2.62–2.57(m, 8H), 1.79–1.76(m, 2H), 1.70–1.66(m, 2H), 1.63–1.56(m, 8H), 1.52–1.44 (m, 4H), 1.42–1.32(m, 20H), 1.29–1.25(m, 28H), 0.93–0.90(m, 6H), 0.88–0.82(m, 18H). <sup>13</sup>C NMR (100 MHz, THF-*d*<sub>8</sub>) δ: 167.20, 160.36, 157.74, 156.37, 153.74, 146.82, 144.31, 144.17, 143.53, 143.39, 143.05, 142.55, 142.45, 142.24, 141.70, 139.24, 138.68, 137.97, 137.71, 134.15, 133.65, 133.25, 132.63, 1321.60, 132.10, 131.51, 131.44, 131.07, 130.95, 130.74, 130.40, 130.03, 129.85, 129.02, 128.67, 128.62, 128.46, 128.27, 127.73, 127.45, 126.98, 126.92, 126.78, 126.72, 126.44, 126.08, 125.98, 124.52, 123.71, 120.25, 117.69, 117.47, 105.978, 100.96, 99.49, 95.39, 68.78, 68.31, 67.78, 67.57, 67.35, 59.11, 58.92, 36.25, 32.48, 32.45, 32.40, 32.38, 32.22, 30.11, 30.00, 29.93, 29.86, 26.55, 26.46, 25.66, 25.46, 25.25, 23.35, 23.28, 23.25, 23.23, 14.26, 14.23, 14.21. HR-MS (MALDI-TOF) *m/z* calcd. for (C<sub>147</sub>H<sub>155</sub>N<sub>3</sub>O<sub>6</sub>S<sub>3</sub>): 2154.10780. Found: 2154.10133. Anal. Calcd. for C<sub>147</sub>H<sub>155</sub>N<sub>3</sub>O<sub>6</sub>S<sub>3</sub>: C, 81.89%; H, 7.25%; N, 1.95%. Found: C, 81.90%; H, 7.26%; N, 1.96%.

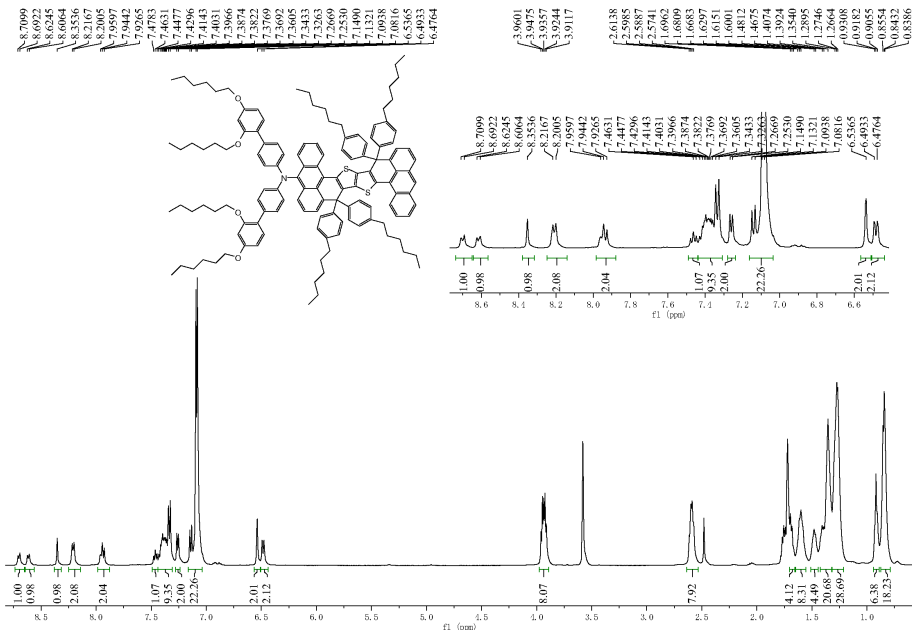


**Figure 4.12.**  $^1\text{H}$  NMR (500 MHz) spectrum of **3** in  $\text{THF-}d_8$ .

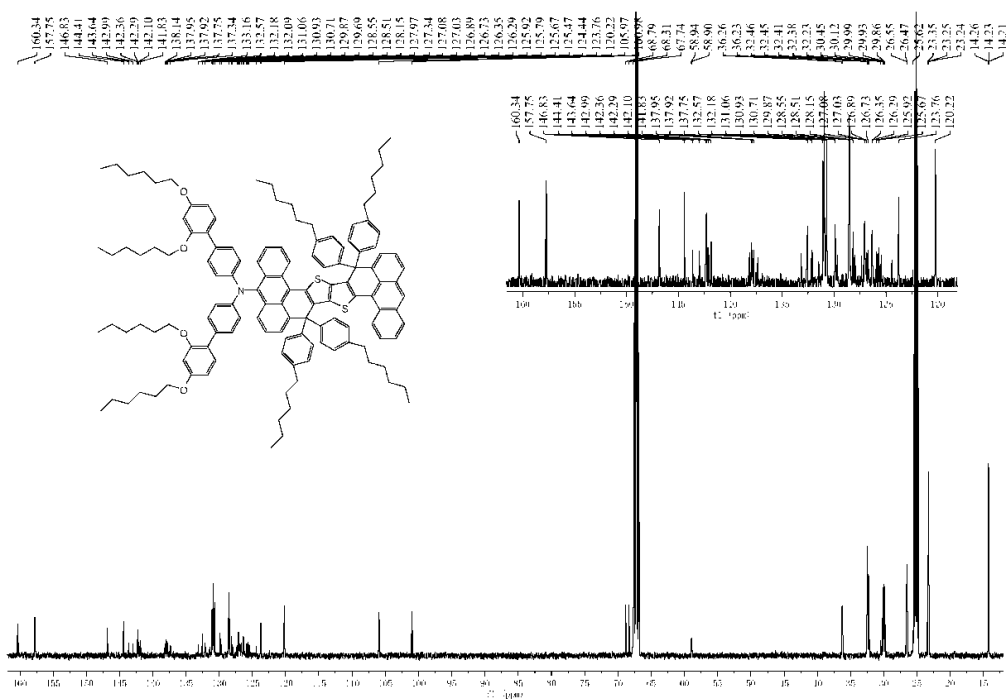


**Figure 4.13.**  $^{13}\text{C}$  NMR (125 MHz) spectrum of **3** in  $\text{THF-}d_8$ .

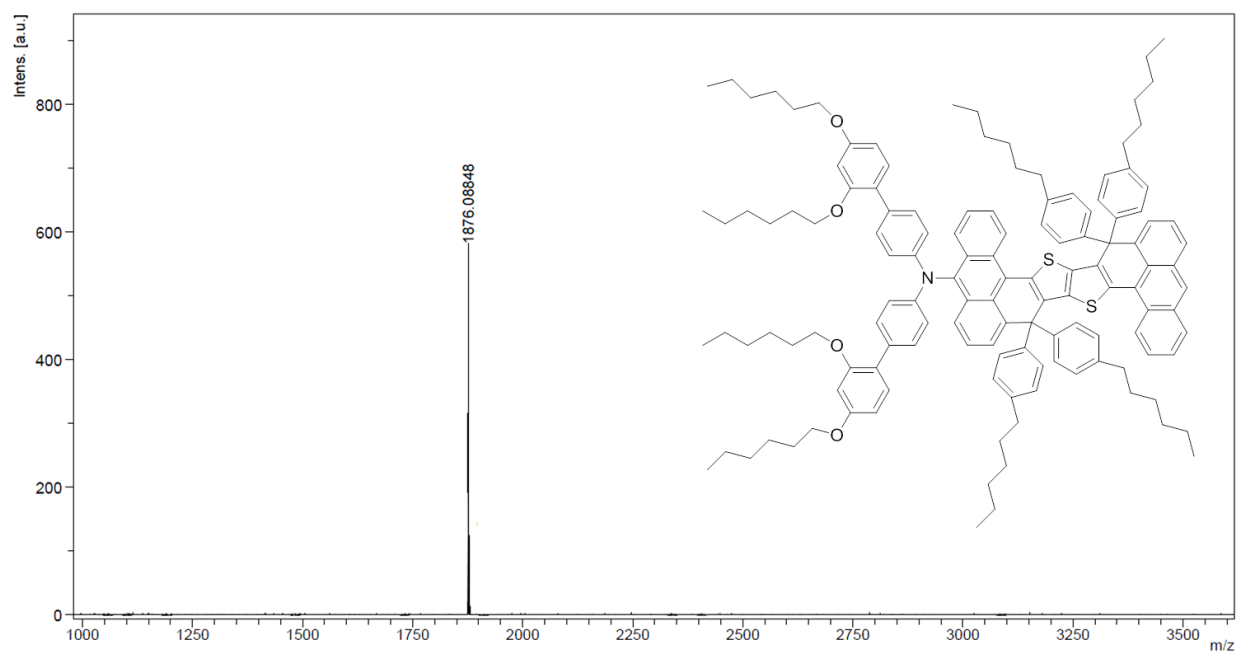


**Figure 4.14.** High resolution mass spectrum (MALDI-TOF) of **3**.

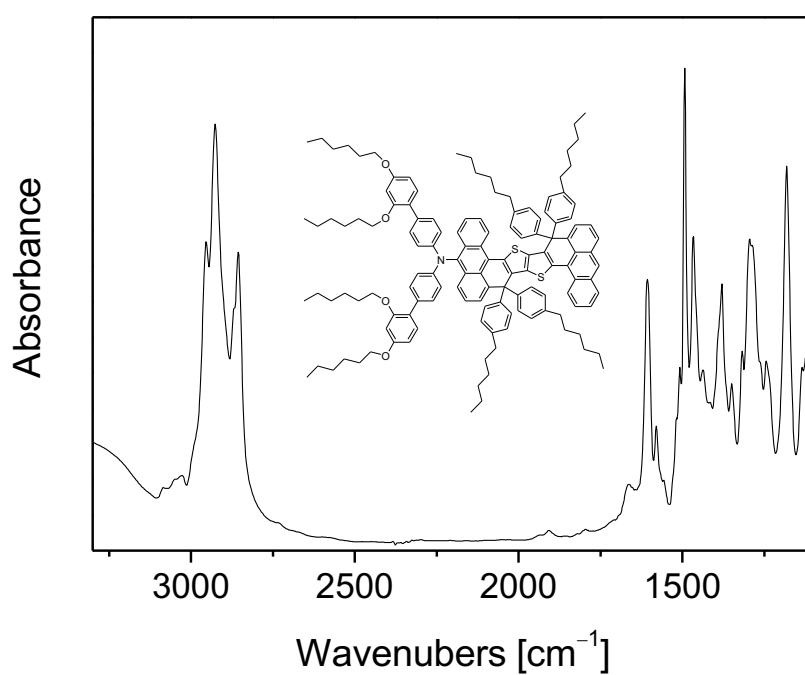


**Figure 4.15.** ATR-FTIR spectrum of **3**.



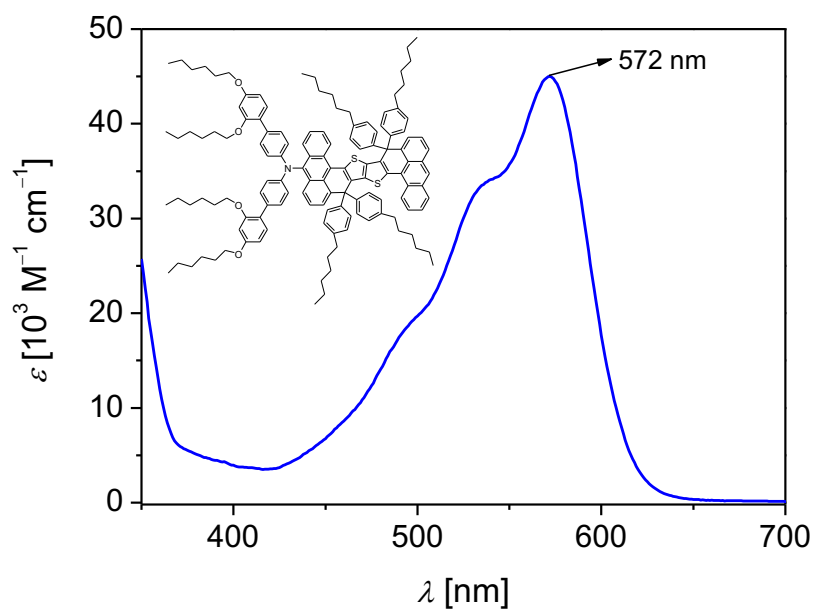
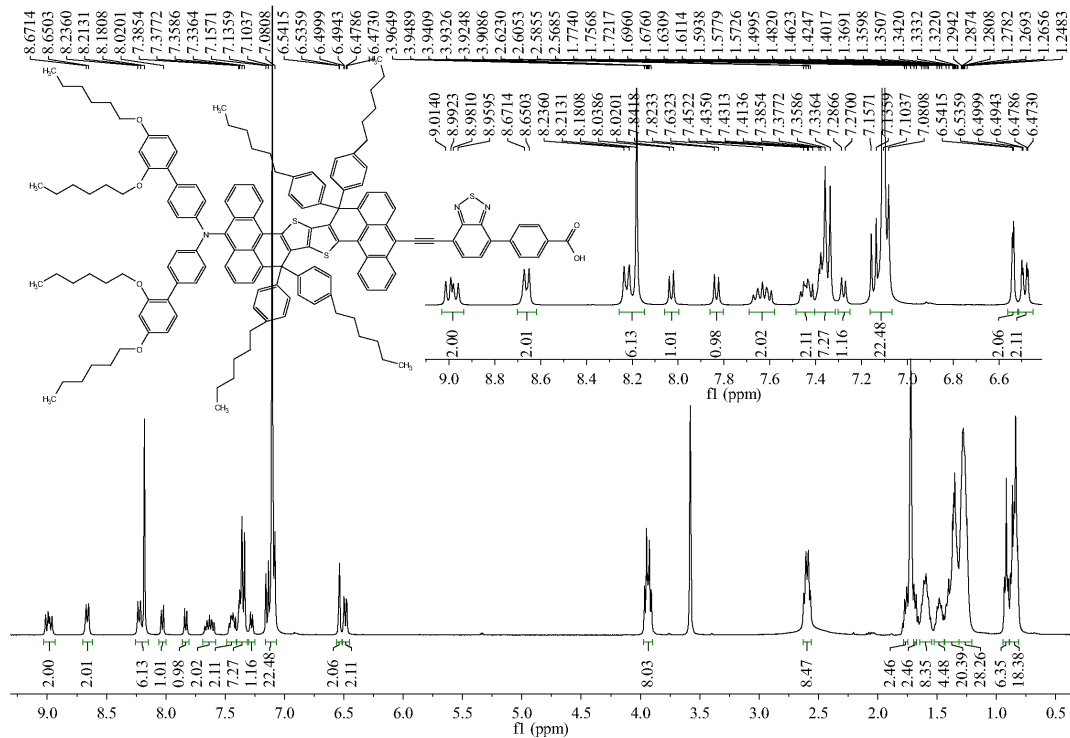


Figure 4.16. UV-Vis spectroscopy of 3 in THF.

Figure 4.17.  $^1\text{H}$  NMR (400 MHz) spectrum of R7 in  $\text{THF-}d_8$ .

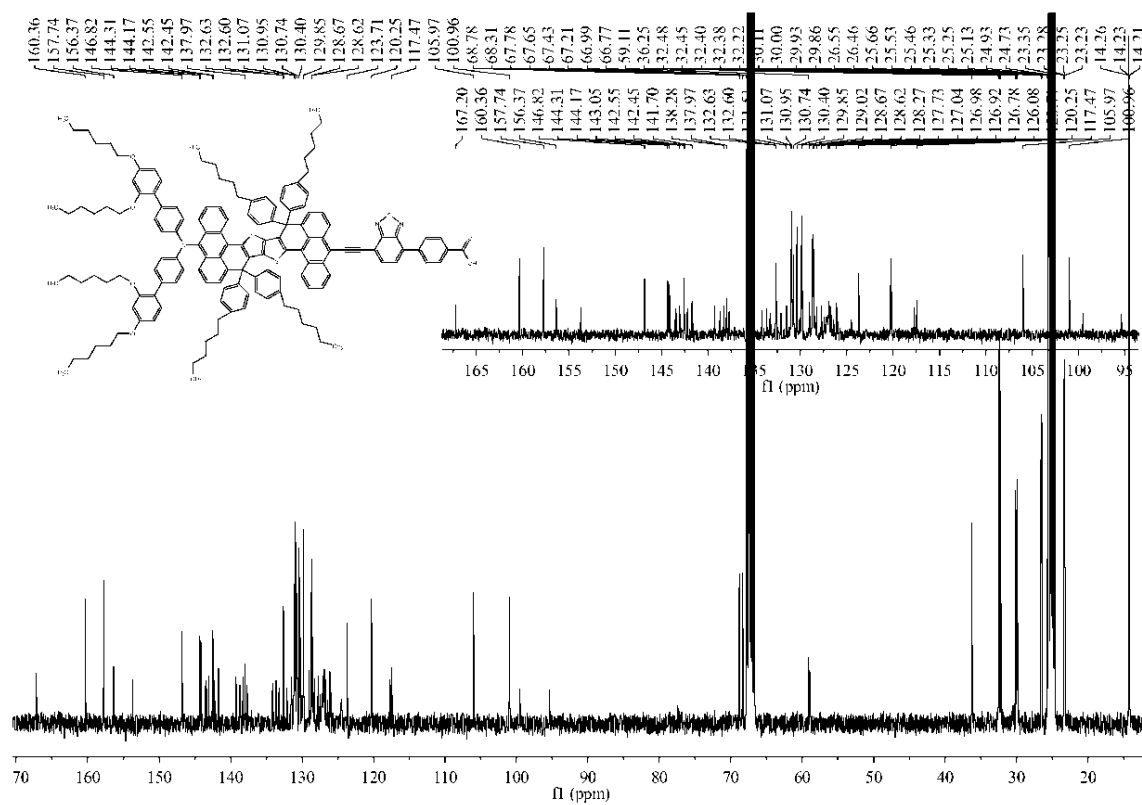


Figure 4.18.  $^{13}\text{C}$  NMR (100 MHz) spectrum of R7 in  $\text{THF-}d_8$ .

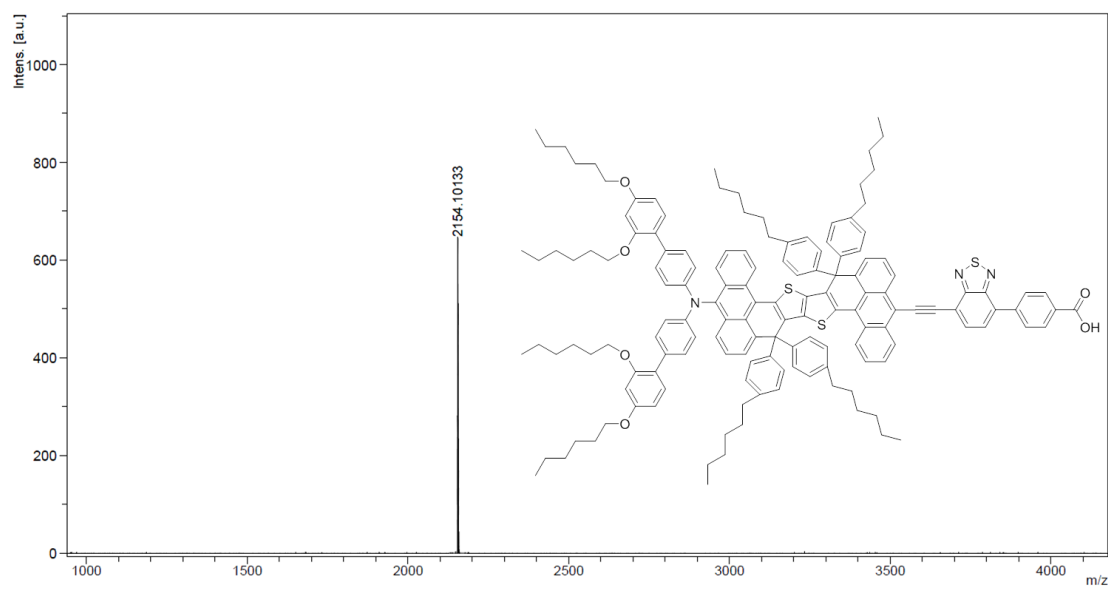
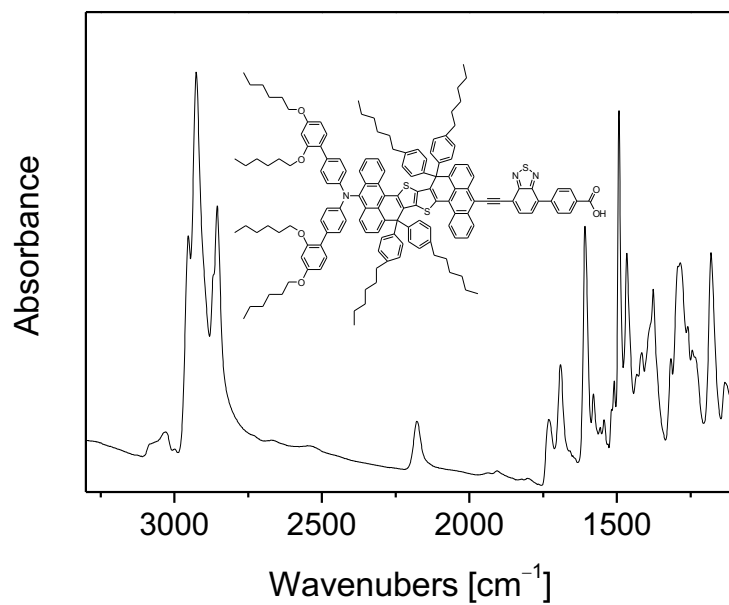
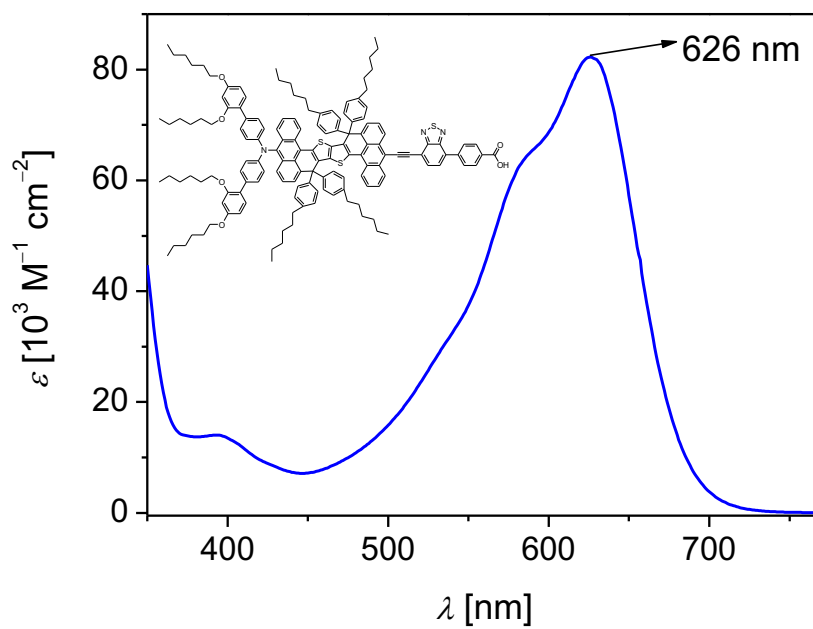


Figure 4.19. High resolution mass spectrum (MALDI-TOF) of R7.



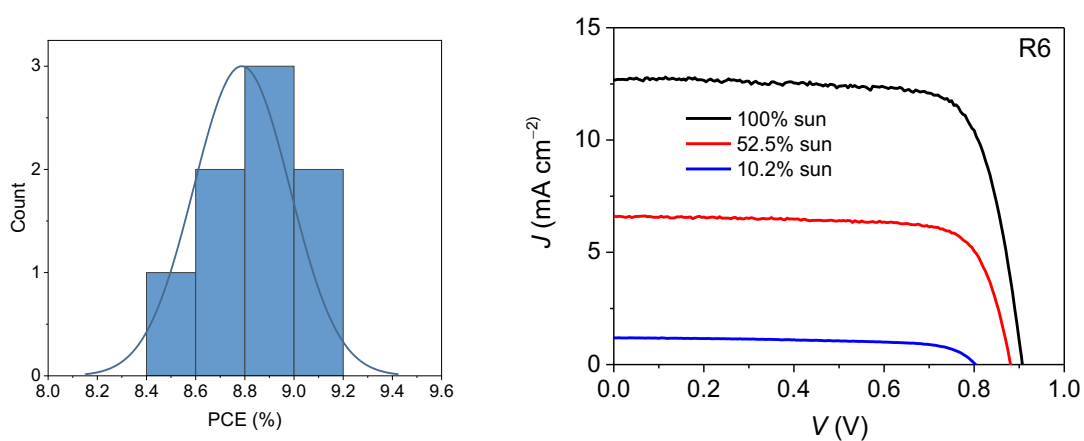
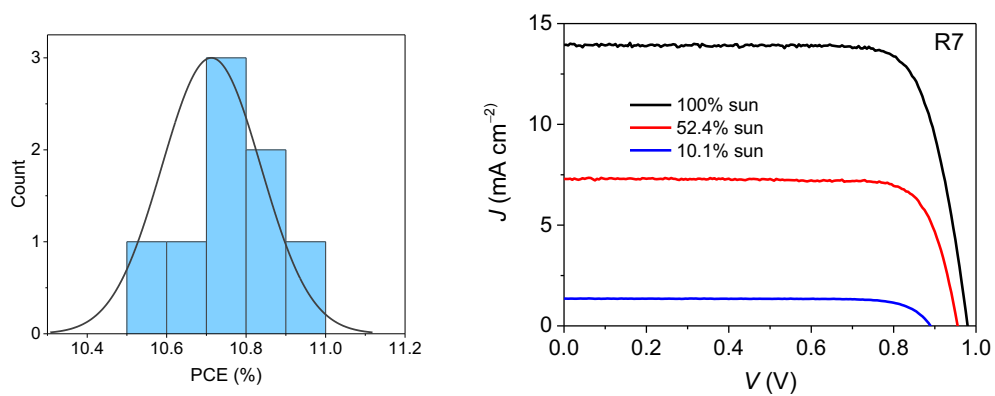
**Figure 4.20.** ATR-FTIR spectrum of R7.



**Figure 4.21.** UV-Vis spectroscopy of R7 in THF.

**Table S.4.1.** Statistics for photovoltaic parameters of eight solar cells measured under the simulated AM1.5G sunlight ( $100 \text{ mW cm}^{-2}$ ).

Dye	$J_{SC}^{EQE}$ [mA cm <sup>-2</sup> ]	$J_{SC}$ [mA cm <sup>-2</sup> ]	$V_{OC}$ [mV]	FF [%]	PCE [%]
R6	12.30±0.04	12.65±0.3	907±2	76.7±0.2	8.8±0.3
R7	13.75±0.04	13.91±0.2	980±3	78.5±0.3	10.7±0.2
R7+Y123	15.84±0.04	16.15±0.25	1035±3	76.1±0.1	12.7±0.2

**Figure 4.22** Histogram of PCE of DSSCs with R6.**Figure 4.23.** Histogram of PCE of DSSCs with R7.

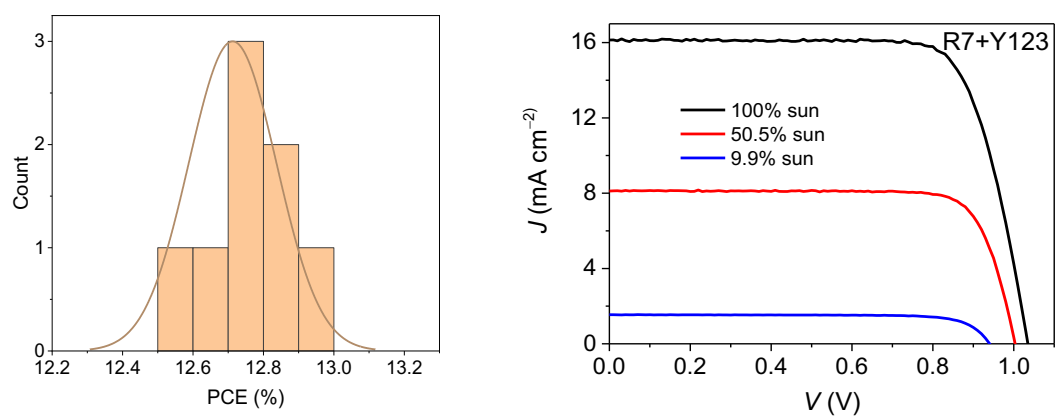


**Figure 4.24.** Histogram of PCE of DSCs with R7 using Y123 as the cosensitizer.

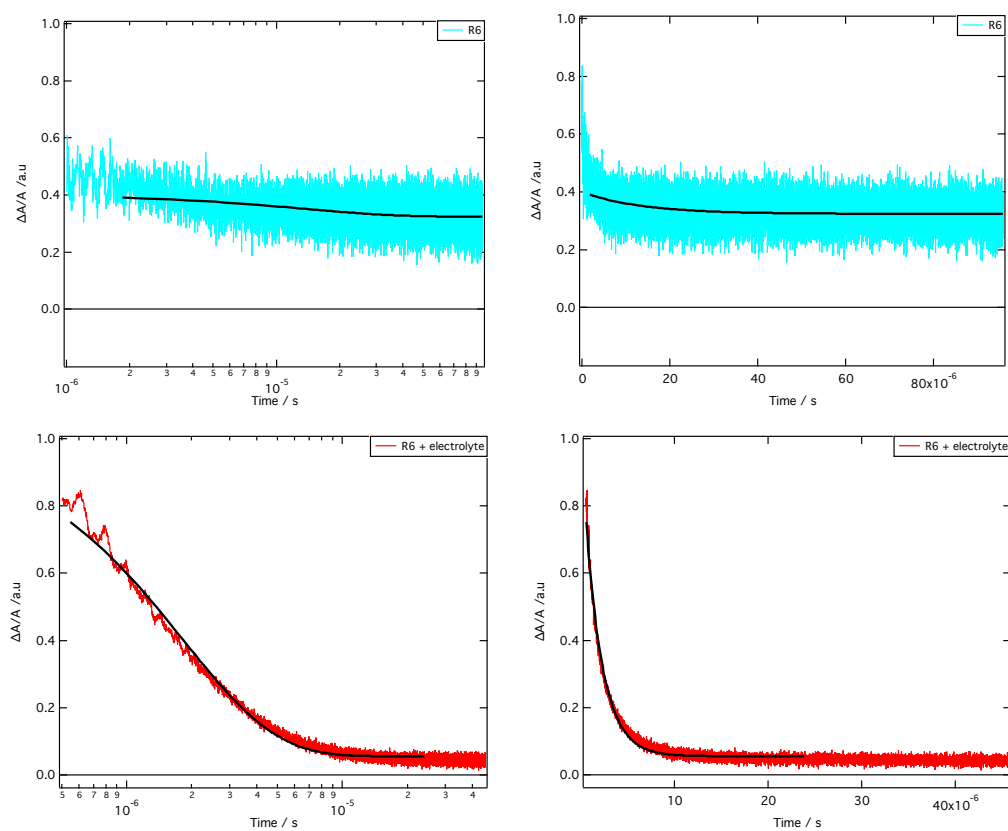


**Figure 4.25.** Exponential fit of transient absorption spectra of dye R6.

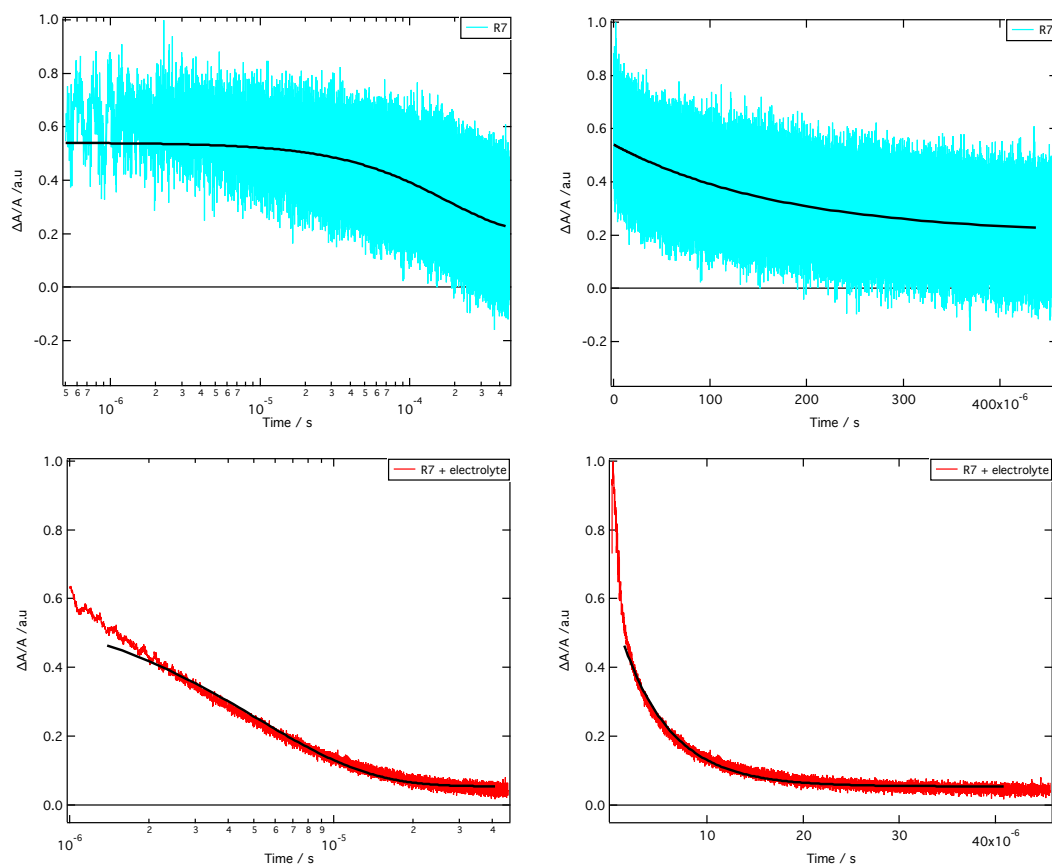


**Figure 4.26.** Exponential fit of transient absorption spectra of dye R7

# Chapter 5 Carbon counter electrodes for copper-based DSSCs

This chapter is adapted from ongoing work

My contribution was device preparation and characterization.

Sandy Sanchez contributed with device preparation and SEM imaging.

## 5.1 Motivation

A particular challenge in the field of DSSCs has been the replacement of the standard iodine redox mediator, which led to substantial potential losses and corrosion. This limitation was successfully addressed by replacing the iodine mediator with Co<sup>106</sup> or Cu<sup>153</sup> coordination complexes, as demonstrated in chapters 2 to 4.

In the past few years, Cu complexes demonstrated rapid electron exchange with the dye molecules with very little energy required (overpotential) of only 0.1 eV.<sup>154,155</sup> Strikingly, under 1000 lux (indoor illumination), their solar to electrical power conversion efficiency (PCE) is 34%.<sup>20</sup> This remarkable PCE opens new areas for applications, such as self-powered electronic devices like the Internet of Things (IoT) that are estimated to grow to 75 billion connected devices by 2025.<sup>142</sup>

The production of all-solid-state devices must be tackled in order to improve the commercial applications of DSSCs. Many studies on solid-state dye-sensitized solar cells (ss-DSSC) have substituted the liquid electrolyte with a solid hole transporting material, HTM.<sup>156</sup> The basic architecture of an ss-DSSC is shown in Fig.5.1(a). Typically, ss-DSSC consists of a thin light-harvesting TiO<sub>2</sub> layer sensitized by a panchromatic dye,<sup>157</sup> a thin layer of an HTM material, and metallic contacts at the CE.

One of the major causes of the instability of ssDSSC is the nature of the hole transporting material (HTM). Additionally, most commonly used HTMs such as spiro-OMETAD present low pore-filling in the TiO<sub>2</sub>+Dye network,

present high electron recombination rates, and poor charge transport at the metallic contacts. All these limitations of the HTM constrain the PCE to values lower than 8%.

Copper-based HTMs have demonstrated remarkable capabilities as an alternative HTM for ss-DSSC, such as improved pore filling, tunable electronic properties, and hydrophobicity. Devices employing Cu complexes as HTM, commonly named “zombie cells,” (Fig.5.1b) have reached impressive PCEs up to 11.7%.<sup>109,149,158,159</sup>

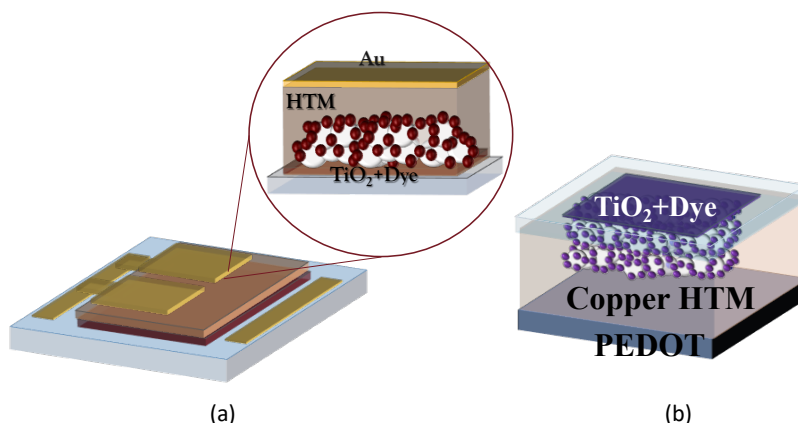


**Figure 5.1.** (a) Schematic representation of a solid-state DSSC (b) Zombie cell employing a Cu complex as HTM

Nonetheless, the use of Cu complexes as HTM in ss-DSSC is limited due to insufficient charge transfer at the CE or back contact material, which profoundly decreases the devices' stability. The commonly used CE materials, such as gold or silver, present two main problems to solve. First, these materials are thermally evaporated under high-vacuum conditions, which is a highly energetic process incompatible with large-scale processes.<sup>160</sup> Secondly, these materials diffuse during the device operation into the light-absorbing layer, significantly decreasing the devices' stability.<sup>161</sup>

Carbon materials such as carbon black, graphite, graphene, and carbon nanotubes have highlighted much attention as the most feasible alternative CE materials for HSCs.<sup>162-163</sup> The critical properties for efficient charge transfer, such as electrical conductivity and work function,<sup>164</sup> can be tailored to each specific copper-based HTM by mixtures of different carbon materials, doping, annealing temperature, and process engineering. Ultimately, the wide range of the sources for these materials, together with their high compatibility with roll to roll and screen printing processing,<sup>165</sup> makes them one of the best choices towards future sustainable commercialization. Recently CCE for hybrid solar cells has been reported with excellent charge transport properties.<sup>166-167</sup>

In this chapter, the use of carbon porous counter electrodes (CCE) in conjunction with Cu(tmby)<sub>2</sub> as an HTM will be studied.



## 5.2 FIRA processing

To meet the aim of sustainable production of materials for solar cells, different techniques employing less energy must be implemented. An excellent strategy to minimize the energy consumed during the thermal calcination process needed in DSSCs' production is to use Flash Infrared Annealing (FIRA). This rapid thermal annealing can achieve high temperatures in impressively low times by implementing short infrared flashes in the range of seconds. Additionally, this low environmental impact technique is compatible with large-area deposition techniques, such as slot dye or roll-to-roll processing.<sup>168</sup> A schematic representation of a FIRA set-up is presented in Fig.5.2. To study the potential use of carbon-based counter electrodes, all the needed materials to ensemble a DSSC were sintered by FIRA annealing.

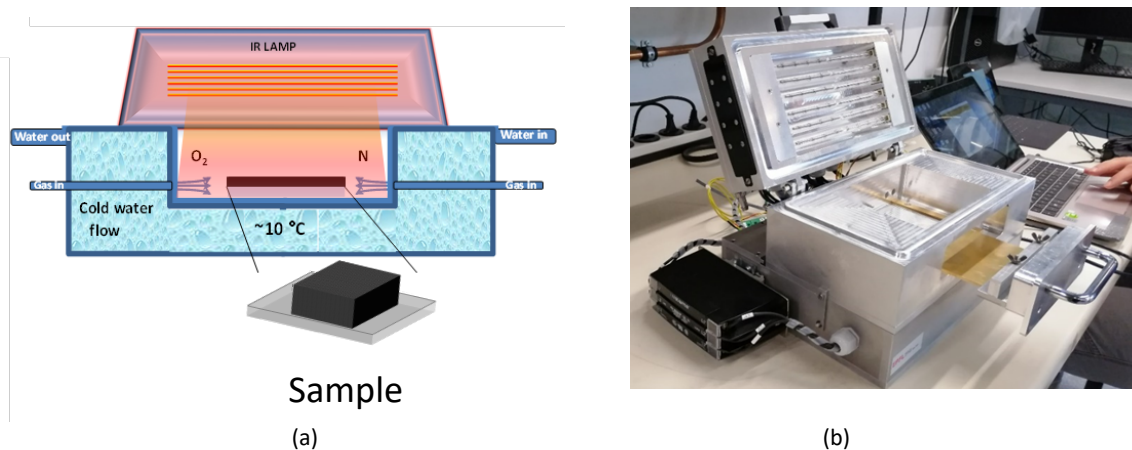


**Figure 5.2.** (a) Schematic representation of the Flash Infrared Annealing set-up. (b) Used equipment

A blocking or spacing layer that insulates the working electrode from the carbon CE is crucial to avoid direct contact of the carbon CE with the electron-selective layer ( $\text{TiO}_2$ ) and prevent the short-circuiting of the devices. We chose to employ  $\text{ZrO}_2$  as a spacer since previous studies demonstrate its ability to suppress the devices' short circuit effectively.<sup>169</sup>

The versatility of FIRA annealing allows to significantly cut down the annealing time compared to a regular hot-plate. Only 30 min at the given temperature is enough to remove all the binders in the pastes. After the heating step is finalized, the substrates' cooling down is relatively fast (less than 5 min) since they are kept at low temperature (10 °C) in the FIRA chamber by using a water recirculatory system through the set-up.

The SEM top-view images of the resulting layers are shown in Fig.5.3. The preliminary results revealed that the use of FIRA annealing can produce highly porous and mechanically stable layers that can be used to produce ss-DSSCs. The  $\text{ZrO}_2$  presented pores in the order of 100 nm, which can later allow the infiltration of the copper-complexes to the sensitized- $\text{TiO}_2$  layer.

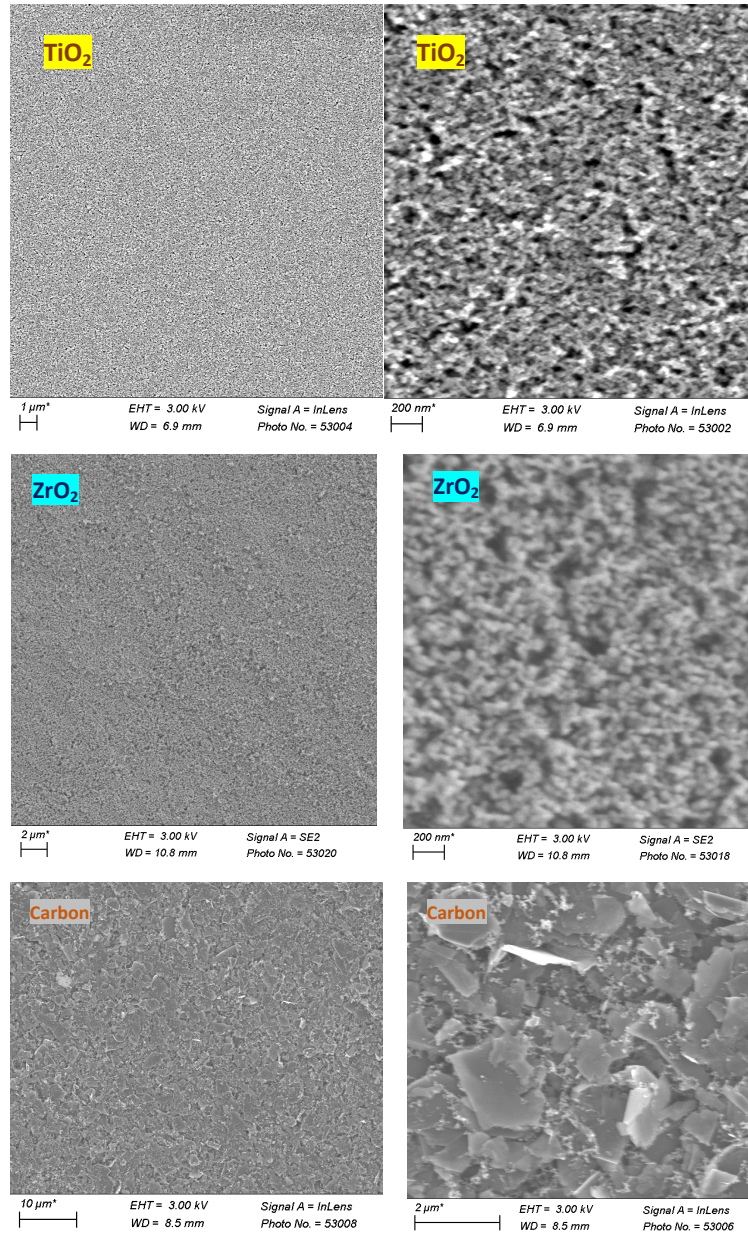


**Figure 5.3.** SEM top view images of TiO<sub>2</sub>, ZrO<sub>2</sub> and Carbon top layers after annealing at FIRA at 450 °C, 500 °C and 400 °C respectively.

### 5.3 DSSC with CCE for indoor light harvesting

To explore the performance of the complex Cu(tmby)<sub>2</sub> in the presence of carbon-based counter-electrodes, we deposited a 10 μm layer of ZrO<sub>2</sub> on top of a 5 μm TiO<sub>2</sub> layer to prepare the WE. Separately, we deposited a 10 μm carbon layer on an FTO glass substrate by blading techniques using a commercially available carbon paste from Solaronix, followed by FIRA annealing. The obtained J-V curves under 1000 lux illumination are shown in Fig.5.4

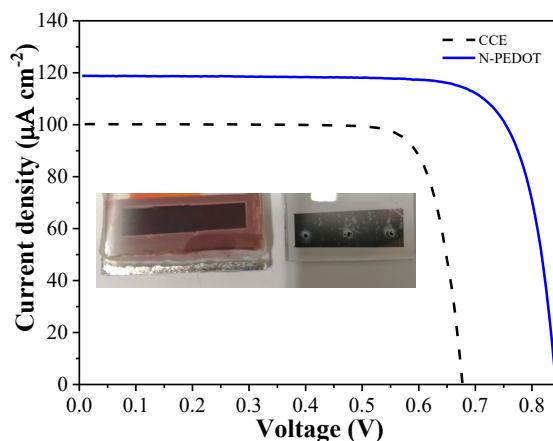


**Figure 5.4.** J-V curve for DSSCs with an active area of 2.8 cm<sup>2</sup>

The characteristic parameters for the best-performing devices are presented in Table 5.1. We found that the devices bearing CCE showed an impressive fill factor of 0.798. These findings demonstrate that carbon-based CE can efficiently transfer charge to regenerate the  $\text{Cu}(\text{tmby})_2^{2+}$  species generated after dye regeneration. Surprisingly, the  $J_{\text{SC}}$  obtained by the devices with CCE is relatively similar to the regular devices with PEDOT CE. Under low lighting conditions, the amount of photoexcited electrons is low, and the copper complexes diffusion does not represent a constraint for the devices' well-functioning. A  $J_{\text{SC}}$  in the same order of magnitude as the reference cells demonstrates that the copper complexes can penetrate the thick 10  $\mu\text{m}$  layer of  $\text{ZrO}_2$  to reduce the dye's oxidized species effectively. However, the  $V_{\text{OC}}$  attained by the devices with CCE showed a drastic decrease compared to the reference cell, leading to a decrease in PCE to 17% compared to 24.5% for the cells with PEDOT counter-electrodes. Though the use of CCEs presented lower PCE under ambient lighting conditions, these results encourage continued research on the use of carbon as a CE material, which can provide higher stability than PEDOT.

**Table 5.1.** Characteristic parameters of 2.8 cm<sup>2</sup> DSSC under 1000 lux illumination

Counter Electrode	$V_{\text{OC}}$ (mV)	$J_{\text{SC}}$ ( $\mu\text{Acm}^2$ )	FF	PCE(%)
PEDOT	837	118.78	0.785	24.5
CCE	676	100.22	0.798	17.01

To better understand the differences in  $V_{\text{OC}}$ , electrochemical impedance spectroscopy (EIS) was performed.<sup>138132</sup> To this end, a frequency scan from 0.5 MHz to 0.2 Hz at room temperature was set for a voltage range from 0.4 V to 0.05 V further than that the  $V_{\text{OC}}$  of each device (approx. 0.9 V). The alternating current (AC) amplitude of 10 mV. The EIS data recorded at 1000 lux illumination were fitted with the typical three-channel model, using ZView® software. The charge transfer resistance at the CE was determined to be 5.75  $\Omega$  for the CCE, and 1.35  $\Omega$  for the PEDOT CCE. The  $R_{\text{CE}}$  value obtained for the CCE is relatively similar to that of PEDOT. These results are

encouraging to develop long-term stable CE for DSSCs, and sheds light to future interfacial engineering to further decrease the charge transfer resistance at the CE.

As observed from Fig.5.5(a), the devices with CCE presented much lower  $R_{CT}$  values compared to the PEDOT reference, meaning higher recombination rates of electrons from the  $TiO_2$  CB to the electrolyte. The low  $R_{CT}$  values can also be attributed to dye adsorption on the  $ZrO_2$  from the spacer layer. The CB edge of  $ZrO_2$  lies at a higher energy level than the LUMO of the dye. Consequently, the photogenerated electrons in the LUMO of the dye cannot be injected and recombine into the electrolyte.<sup>170</sup> On the other hand, devices with CCE presented lower  $R_{trans}$  values than the reference cells, meaning that the electron transport in the  $TiO_2$  is relatively fast.

The relation between applied bias and the density of states (DOS) in Fig 5.5(b) shows a shift of the conduction band of  $TiO_2$  toward lower values for the CCE devices compared to the PEDOT reference. The CB displacement is directly related to the lower electron concentration at the conduction band of  $TiO_2$  due to the high recombination rates, as shown in Eq.1.48. The CB's downward shift and the low  $R_{CT}$  explain the drop in  $V_{OC}$  for the carbon-based CEs.

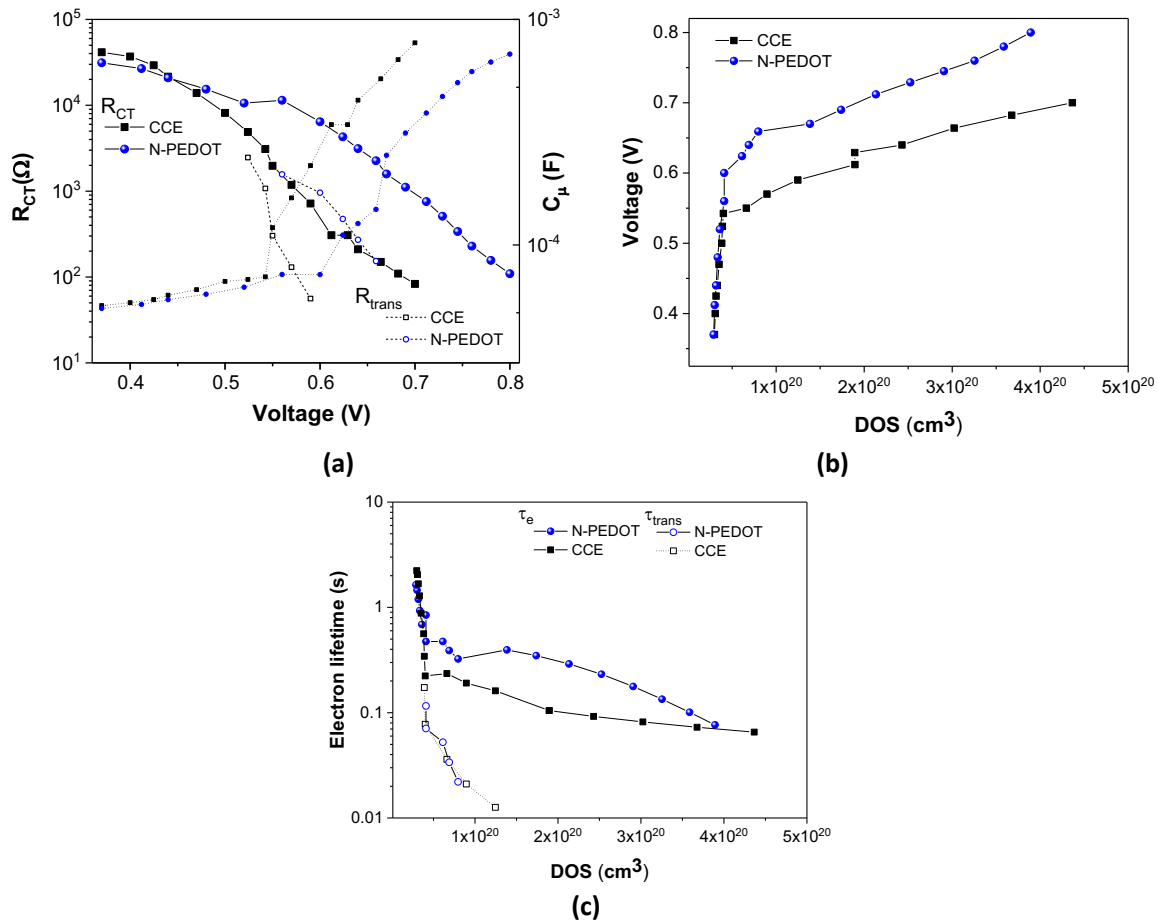


**Figure 5.5.** Electrochemical impedance spectroscopy (EIS) analysis. (a) Continuous lines with solid markers represent the charge transfer resistance ( $R_{CT}$ ) as a function of the applied voltage. The dotted lines with solid markers represent the transport resistance ( $R_{trans}$ ), and the dashed lines with open markers represent the chemical capacitance. (b) Voltage vs. density of states (DOS). (c) Electron lifetime as a function of DOS.

To fairly compare under the same electron occupation, the electron lifetime and transport times are plotted as a DOS function in Fig. 5.5(c). It can be noted that the devices with CCE present lower electron lifetimes, as expected from the low  $R_{CT}$  values. Nonetheless, the transport time is nearly similar for both devices. Our findings demonstrate that carbon can be used as an effective CE material and that the “spacer layer” engineering is crucial to reduce the recombination rate to the electrolyte.

## 5.4 Monolithic DSSC based on copper electrolytes

The so-called monolithic architectural design highlights a promising prospect for fully printable ssDSSC,<sup>171</sup> which uses sustainable carbon materials as CE back contacts and eliminates one glass substrate in the final device, which can substantially decrease the production prices. Additionally, they can easily be adapted to roll-to-roll or screen-printing processes, making them competitive for future commercialization.<sup>172</sup>

CCEs present high electric conductivity and proper work function to be a suitable CE material for monolithic dye-sensitized solar cells (MN-DSSC) employing copper complexes as HTMs, with good charge transfer for rapid collection of electrons as observed from fast electron lifetimes in Fig.5.5(c). CCE also presents excellent hydrophobicity. The so-called monolithic architecture is shown in Fig.5.6(a).<sup>173</sup>

The MD-DSSC were fabricated with  $\text{Cu}(\text{tmby})_2$ -based liquid electrolyte to improve the infiltration through the carbon and zirconia layer. Subsequently, we let the solvent evaporate to form an HTM material. A cross-sectional view of the resulting MN-DSSC is shown in Fig.5.6(b).

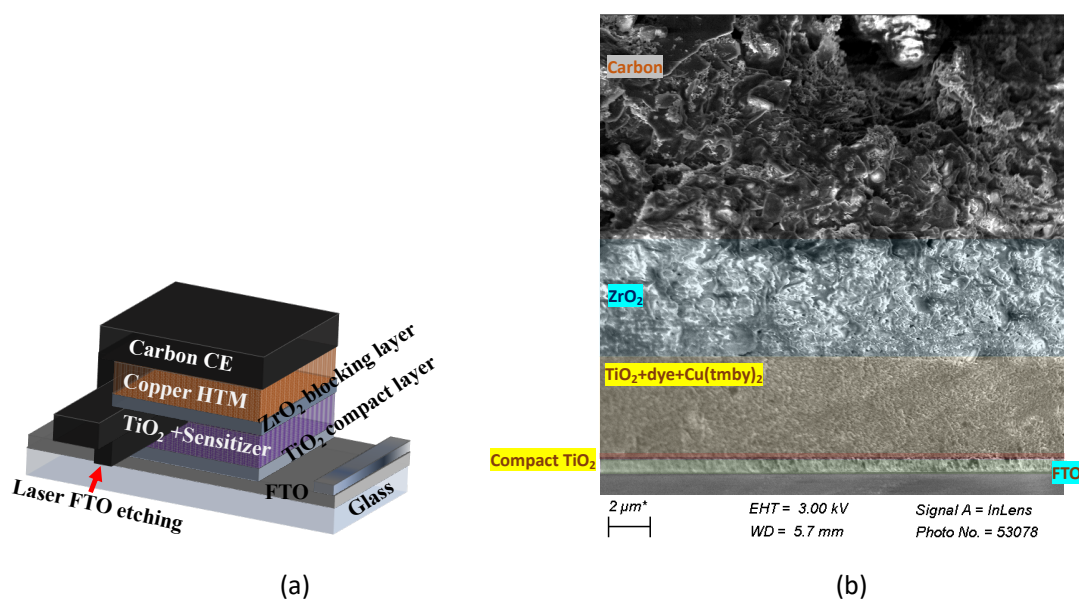


**Figure 5.6.** (a) Schematic representation and (b) cross-sectional SEM of a MN-DSSC with a CCE and copper complex mediator.



The J-V curves under AM1.5 for MN-DSSC, Fig 5.7, showed poor photovoltaic performance (PCE 0.27%) compared to the reference cells employing liquid  $\text{Cu}(\text{tmby})_2$  electrolyte reaching a PCE of 10.27%. The performance under ambient light was not possible to measure due to the low values of photogenerated current. The FF significantly dropped compared to the devices with “regular” architecture and CCE in Fig.4.5, implying poor charge transfer between the carbon layer and the copper mediators. This can also explain the poor efficiency displayed by the MN-devices.

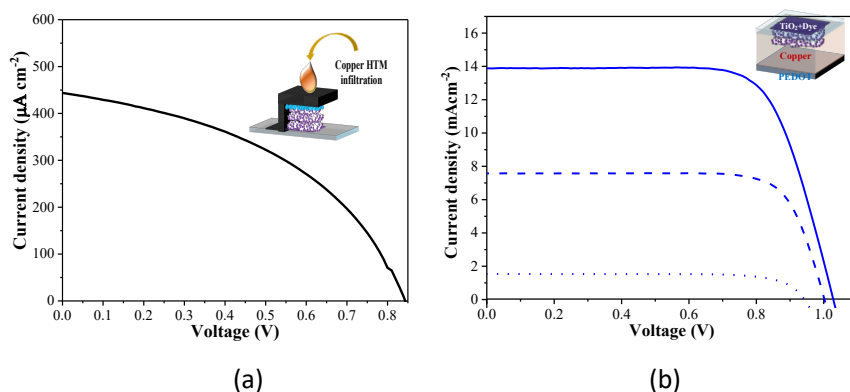


**Figure 5.7.** (a) J-V curve for MN-DSSCs under 1.5 AM and (b) J-V curve for a liquid-based DSSC.

**Table 5.2.** Characteristic parameters of devices DSSC under AM1.5.

Architecture	$V_{oc}$ (mV)	$J_{sc}$ ( $\text{mA cm}^{-2}$ )	FF	PCE(%)
Monolithic DSSC	843.809	0.444	0.439	0.27
Regular DSSC	1028	13.784	0.72	10.27

It can be noted in Fig.5.8, that the  $\text{Cu}(\text{tmby})_2$  complexes filled the pores of the carbon layer. One possible reason for the poor fill factor observed in the monolithic cells employing copper complexes, is the cristalization of the same, decreasing the pore filling through the spacer and the titania layer. This also results in low photogenerated current as the values obtained by the MN-DSSC. the Future work on solvent engineering and design of new copper complexes can enhance the infiltration of the HTM material from the top-carbon CE to the sensitized  $\text{TiO}_2$ .

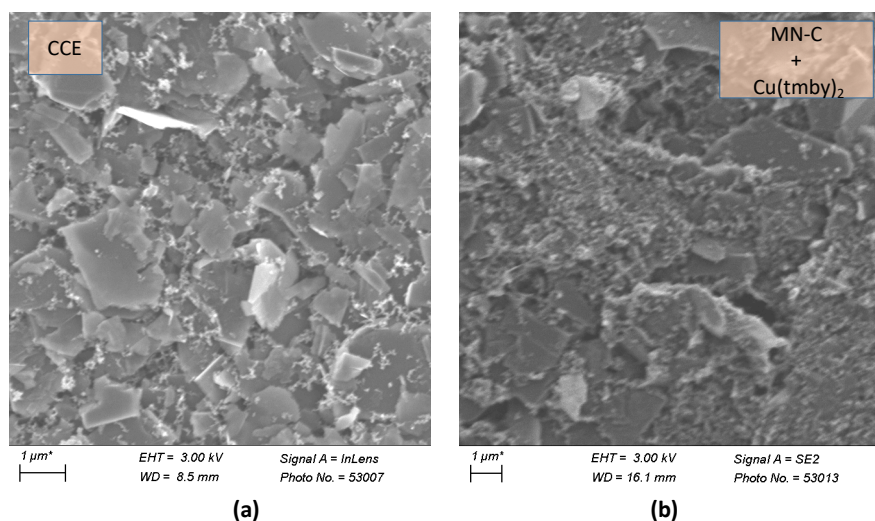


**Figure 5.8.** Top view SEM images of (a) a carbon counter electrode and (b) MS-DSSC with a copper-complex as HTM.

## 5.5 Conclusions

The environmentally friendly carbon material, annealed by the low-impact technique FIRA, can successfully reduce the copper mediator's oxidized species with an excellent fill factor and relatively low  $R_{CE}$  values for charge transfer. Devices employing liquid  $Cu(tmby)_2$ -based electrolyte reached a PCE of 17% under 1000 lux illumination conditions. However, we found a substantial increase in the recombination resistance,  $R_{CT}$ , and a down-shift of the  $TiO_2$  CB, leading to low  $V_{OC}$  values under low-light illumination conditions. The main problem to solve for DSSCs employing copper complexes as HTM and CCEs is the optimization of the “spacer layer”. Future developments include engineering of the layer thickness, surface treatment to avoid dye-adsorption and design of new spacer materials, among others.

## 5.6 Supporting information

### Experimental Section

All chemicals and solvents were purchased from Sigma-Aldrich and TCI chemicals, if not otherwise noted, and were used without further purification.

#### DSSC fabrication:

**Big area cells:** Glass substrates with fluorine-doped tin oxide (FTO, NSG-10, Nippon Sheet Glass) were cleaned with 0.2% (w/w) detergent solution in an ultrasonic bath for 1 h and rinsed with water, ethanol, and acetone, followed by a UV/O<sub>3</sub> (Model no.256-220, Jelight Company, Inc.) treatment for 15 min. The FTO substrates were immersed for 30 min in a 40 mM aqueous TiCl<sub>4</sub> solution at 70 °C, and then washed with water and ethanol, followed by a sintering process at 250 °C for 2 h. Mesoporous TiO<sub>2</sub> films of 2.8 cm<sup>2</sup> were prepared by screen printing a 5 µm thick colloidal TiO<sub>2</sub> (Dyesol paste DSL 30 NRD-T) layer and drying at 120 °C in air for 5 min. The films were then gradually heated in an oven (Nabertherm controller P320), applying a four-level program: 125 °C (10 min), 250 °C (10 min), 350 °C (10 min), and 450 °C (30 min). After sintering, the electrodes were treated in aqueous TiCl<sub>4</sub> at 70 °C for 30 min and washed with water and ethanol. The thickness of the TiO<sub>2</sub> films was measured with a profilometer (Veeco Dektak 3). Subsequently we deposited a 10 µm thick colloidal ZrO<sub>2</sub> by bladding techniques. A sintering process of 450 °C for 30 min was performed by FIRA annealing, and it was followed by overnight immersion of the electrodes in the dye bath solution. The dye bath composition were 0.1 mM XY1b, with 5 mM CDCA (chenodeoxycholic acid) in ACN/t-BuOH (1:41). Solar cells were assembled using UV glue to seal the counter electrode. **PEDOT CE** were prepared by electropolymerization of 3,4-ethylenedioxythiophene (EDOT) from a micellar aqueous solution of 0.1 M sodium n-dodecyl sulfate (SDS) and 0.01 M EDOT on NSG TEC8™ (Pilkington) FTO-type conducting glass. **CCE** were prepared by depositing a 10 µm layer NSG TEC8™ employing the Elcocarb B/SP carbon paste by Solaronix.

The electrolyte solution was introduced through 3 holes predrilled in the counter electrode, which was sealed with UV glue. The copper-based electrolyte consists of 0.2 M [Cu(tmby)<sub>2</sub>] (TFSI) and 0.07 M [Cu(tmby)<sub>2</sub>](TFSI)<sub>2</sub> complexes with 0.1 M LiTFSI and 0.6 M 1-Methylbenzimidazole (NMB) in acetonitrile.

**MN solar cells:** glass substrates from Solaronix were washed with ethanol, and acetone, followed by a UV/O<sub>3</sub> (Model no.256-220, Jelight Company, Inc.) treatment for 15 min. Mesoporous TiO<sub>2</sub> films were prepared by bladding techniques printing a 5 µm thick colloidal TiO<sub>2</sub> (Dyesol paste DSL 30 NRD-T) layer and drying at 120 °C in air for 5 min. The films were sintered at 450 °C by FIRA annealing. The thickness of the TiO<sub>2</sub> films was measured with a profilometer (Veeco Dektak 3). Subsequently, we deposited a 5 µm thick colloidal ZrO<sub>2</sub> by bladding techniques using the Zr-Nanonide ZR/SP from solaronix. A sintering process at 550 °C for 30 min was performed by FIRA annealing. Subsequently, we deposited a carbon layer of 10 µm on top, by bladding techniques followed by annealing at 400 °C for 30 min. The electrode was dip



overnight in the dye bath solution composed of 0.1 mM XY1b, with 5 mM CDCA (chenodeoxycholic acid) in ACN/t-BuOH (1:41). Afterward, 100  $\mu\text{L}$  of a diluted copper-based electrolyte of 0.07 M  $[\text{Cu}(\text{tmby})_2]$  (TFSI) and 0.023 M  $[\text{Cu}(\text{tmby})_2](\text{TFSI})_2$  complexes with 0.1 M LiTFSI and 0.6 M 1-Methylbenzimidazole (NMB) in acetonitrile we deposited on top by drop casting.

**Solar Cell Characterization:** Current–voltage (I–V) characteristic curves and photocurrent-dynamics were measured using a 450 W Xenon lamp (Oriel USA) as light source, with a K113 filter (Schott Tempax) and matched to AM 1.5G solar standard conditions using a reference Si photodiode. Additionally, the indoor light was delivered by an Osram 930 Warm White tube light or Warm White 3000 K LED (EGLO). The light intensities were calibrated by a light meter (TES-1334, TES). The current and voltage were measured and controlled by a Keithley 2400 digital source meter (Keithley, USA), and the current measurement was set up to be delayed 80 ms from applying the potential. A set of metal mesh filters were used to adjust the light intensity to the desired level. A black metal mask with a 0.16  $\text{cm}^2$  aperture was used to define the active area.

**Electrochemical Impedance Measurements (EIS):** Impedance measurements were performed using a BioLogic SP300 potentiostat, over a frequency range from 1 MHz down to 0.1 Hz at bias potentials between 0 and 1.1 V (with a 10 mV sinusoidal AC perturbation). All measurements were done at 20 °C. The resulting impedance spectra were analyzed with Z-view software (v2.8b, Scribner Associates Inc.).

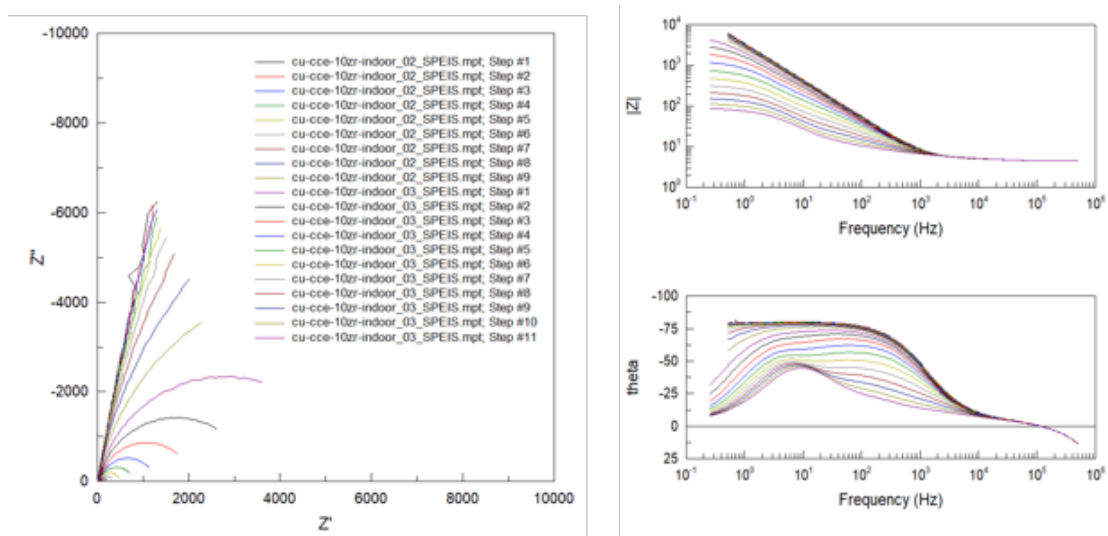


**Figure 5.9.** Nyquist plots for a device Cu-reference electrolyte with CCE at 1000 lux illumination.

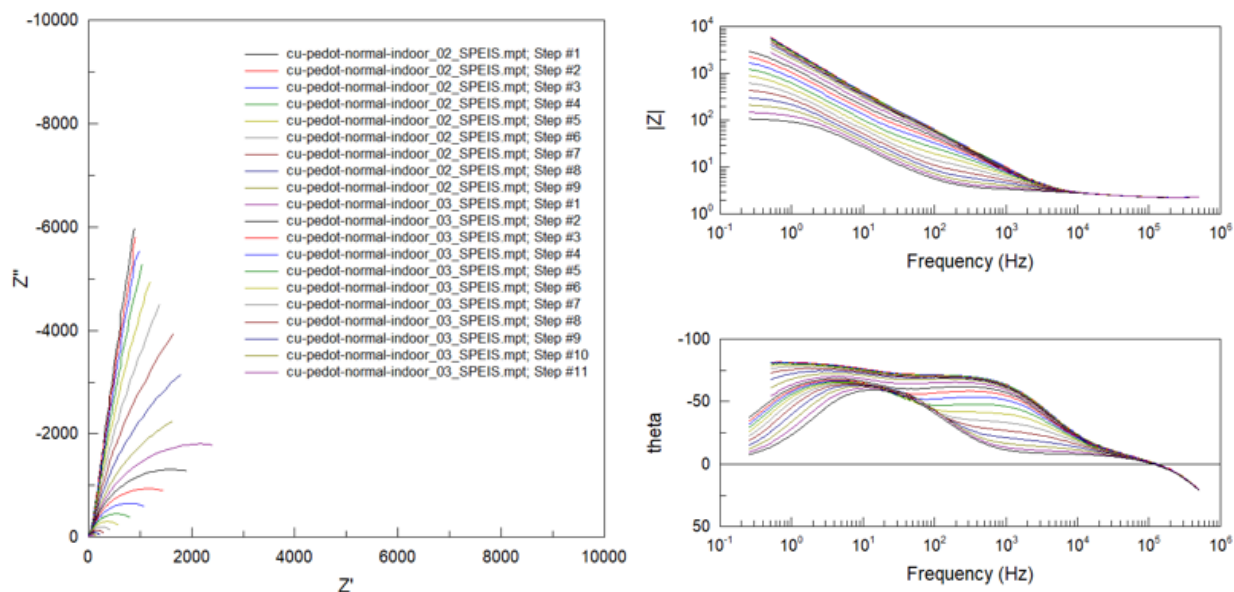


**Figure 5.10.** Nyquist plots for a device Cu-reference electrolyte with PEDOT CE at 1000 lux illumination

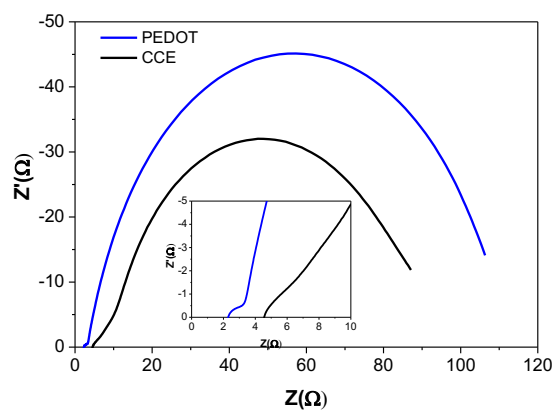


**Figure 5.11.** Nyquist plots at 700 mV for DSSCs fabricated with a copper-based electrolyte under 1000 lux.

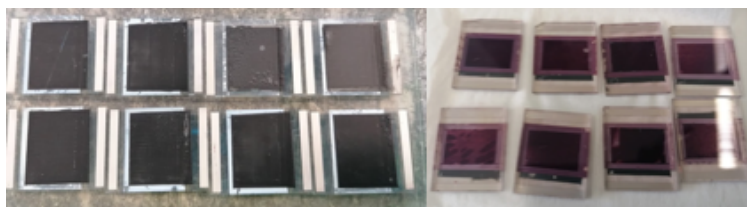


**Figure 5.12.** Monolithic solar cells.

## Chapter 6 Conclusions

### 6.1 Achieved results

Decreasing the recombination rates from the electrons in the conduction band of the  $\text{TiO}_2$  layer to the redox mediator in the electrolyte is vital to improve the performance of DSSCs and boost its commercialization. Interfacial engineering approaches can provide significant enhancements. We successfully demonstrated that the charge transfer processes at the  $\text{TiO}_2$ +dye/electrolyte interface could be tuned to enhance the devices' overall performance.

We engineered tandem electrolytes containing two redox species in the liquid solvent; the organic radical 2-azaadamante-N-oxyl ( $\text{AZ}^0/\text{AZ}^+$ ) and the well-known redox pair  $[\text{Co}(\text{bpy})_3]^{2+/3+}$ . DSSCs fabricated with this electrolyte reached  $V_{\text{OC}}$  values up to 1007 mV and higher performance than the DSSC devices with single redox mediators. It was determined that the  $V_{\text{OC}}$  improvement is due to two main factors, the more positive redox potential of the  $\text{AZ}^{+/0}$  redox couple and the lower recombination rates of the electrons from the CB to the electrolyte. From studying different composition systems, an optimal concentration for  $\text{AZ}^0/\text{AZ}^+$  was obtained. It was determined that high concentrations of AZ decrease the fill factor and may also result in the adsorption of  $\text{AZ}^+$  molecules on the oxide surface. The advantages of using tandem electrolytes containing two redox mediators to enhance of the dye regeneration rates and for recombination suppression at the  $\text{TiO}_2$ 's interface with the electrolyte were demonstrated. Future work improving the steric hindrance of small "auxiliary" donors could further improve the  $V_{\text{OC}}$  and overall performance of DSSCs. Additionally, it was determined that the use of small electron donors such as TEMPO and TPAA in conjunction with copper complexes such as  $\text{Cu}(\text{tmby})_2$  causes a detrimental effect on the overall performance of DSSC. Future studies on tandem electrolytes with copper complexes should include the design of new small mediators that do not react with  $\text{Cu}(\text{I})$  species.

Another strategy to decrease the electron recombination rates was hyperbranched networks' design by in-situ photopolymerization of a thiol-siloxane with an acrylate monomer, such as PEGMA and PEGDA. The formed hyperbranched networks denoted HB1 (thiol-siloxane and PEGMA), and HB2 (thiol-siloxane and PEGMA) were studied in conjunction with  $[\text{Co}(\text{bpy})_3]^{2+/3+}$ -based electrolyte. It was found that the diffusion coefficients for  $\text{Co}^{3+}$

in the electrolytes decrease with polymer content. The highest performance was reached by a 10%(w/w) of HB1 with a  $V_{OC}$  of 875 mV,  $J_{SC}$  of  $14.75 \text{ mAcm}^{-2}$ , and FF of 0.66 for a PCE of 8.52% under 1 sun illumination, comparable to a PCE of 9.36% for the cobalt reference electrolyte. For higher polymeric contents, the low PCEs under 1 sun result from mass-diffusion problems in the electrolyte. An upward-shift compared to the  $[\text{Co}(\text{bpy})_3]^{3+/2+}$  electrolyte as a reference was observed for all the electrolytes containing the hyperbranched electrolytes, together with longer electron lifetimes compared to the  $\text{Co}^{3+/2+}$  electrolyte, explaining the higher  $V_{OC}$  values obtained for the HB electrolytes. EIS analysis under 1 sun illumination revealed that the polymer network formation leads to a slight enhancement in recombination suppression compared to the cobalt reference. Additionally, under 1 sun illumination, the Warburg resistance for the cobalt species in the electrolytes increases exponentially with the polymer content. EIS analysis also revealed that the higher performance for all the devices with HB1 and HB2 under low light intensity is attributed to higher  $R_{CT}$  and lower  $R_{trans}$ , leading to a PCE of 23.19% under 1000 lux for devices containing 15% of HB1 compared to 20.37% for the Co-reference.

To increase the recombination resistance of blue dyes in devices with copper complexes, we judiciously designed and synthesized a new blue dye R7 with the strong electron-donating PAH core and BPT2 as the central building block and the auxiliary bulky HF donor. The spectral response of organic dyes was successfully enhanced with this strategy, also improving the stability with copper complexes as redox mediators on DSSCs. The photovoltaic performance of R7-based DSSCs with copper-based electrolyte outperformed their counterpart ones with the dye R6. Our in-depth kinetic studies revealed that the bulky HF donor moiety efficiently suppresses the electron recombination between the  $\text{TiO}_2$  surface and the redox shuttle. Furthermore, the co-sensitized system of R7+Y123 presented outstanding parameters of  $J_{SC}$  of  $16.15 \text{ mAcm}^{-2}$ ,  $V_{OC}$  of 1035 mV, FF of 0.76 to achieve a top PCE of 12.7%. To the best of our knowledge, this value of PCE is the highest obtained for copper complex based-DSSCs using a blue photosensitizer not employing the conventional electron acceptor cyanoacrylic acid. We demonstrated that the HF donor and the electron acceptor EBTBA could successfully extend the dye's spectral response and improve and interfacial electron recombination.

Lastly, to implement environmentally friendly carbon-based materials, the use of carbon as CE for DSSC employing copper complexes in the electrolyte was studied. The low-impact technique FIRA to anneal the carbon counter electrodes was implemented in the fabrication of DSSCs. The CCEs were found to successfully reduce the copper mediator's oxidized species with an excellent fill factor and relatively low  $R_{CE}$  values for charge transfer. Devices employing liquid  $\text{Cu}(\text{tmby})_2$ -based electrolyte reached a PCE of 17% under 1000 lux illumination conditions. However, we found a substantial increase in the recombination resistance,  $R_{CT}$ , and a down-shift of the  $\text{TiO}_2$  CB, leading to low  $V_{OC}$  values under low-light illumination conditions.

## 6.2 Future development

The use of tandem systems can potentially lead to  $V_{OC}$  exceeding 1.2 V. The synthesis of new organic stable radicals or small electron donors with improved steric hindrance can also boost the regeneration rate, with improved recombination rates could lead to PCEs beyond 15%. Future work on small electron donors judiciously design for enhanced stability in conjunction with copper complexes should also be the next interfacial engineering strategy for highly-efficient devices.

One of the best approaches for decreasing the electron recombination at the interface  $TiO_2$ /electrolyte is designing new polymeric materials for their use in electrolytes. Future work should address the polymerization of copper-based electrolytes, with improved recombination rates to boost the  $V_{OC}$  beyond 1.2 V.

The main problem for DSSCs employing copper complexes as HTM and carbon counter electrodes is optimizing the “spacer layer”. Future developments include engineering the layer thickness, surface treatment to avoid dye-adsorption, and design of new materials.

The next breakthrough in ssDSC requires efficient counter electrodes based on carbon-blend materials. They should overcome charge-transport limitations, high recombination rates, limited tunability, and processability. This can be achieved by innovating carbon porous-composites with all the necessary credentials for printable solar cell production. The formation of the hybrid-composites can be achieved by adding functionalized carbon allotropes such as graphite, graphene, reduced graphene oxides, and carbon nanotubes to carbon black. This approach can improve the charge transfer at the CE in MN-DSSC. The use of carbon black as a base material is vital for maintaining high porosity and low sheet resistance. At the same time, the additives can enhance the charge transfer rates with the copper complexes.

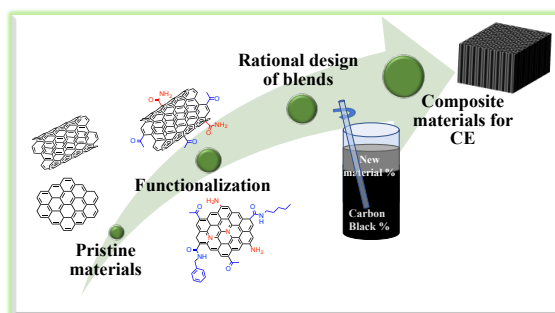


**Figure 6.1.** Rational design of new carbon-based materials with enhanced charge transfer properties.

## References

- (1) BP. Statistical Review of World Energy 2020. **2020**, 66.
- (2) Bett, A. W. *Sustainable PV Manufacturing in Europe*; 2020.
- (3) World Energy Investment 2020. *World Energy Invest. 2020* **2020**.
- (4) Kober, T.; Schiffer, H. W.; Densing, M.; Panos, E. Global Energy Perspectives to 2060 – WEC’s World Energy Scenarios 2019. *Energy Strateg. Rev.* **2020**, *31* (December 2019), 100523.
- (5) World Energy Council. *World Energy Scenarios: Composing Energy Futures to 2050*; 2020.
- (6) Strapasson, A.; Woods, J.; Pérez-Cirera, V.; Elizondo, A.; Cruz-Cano, D.; Pestiaux, J.; Cornet, M.; Chaturvedi, R. Modelling Carbon Mitigation Pathways by 2050: Insights from the Global Calculator. *Energy Strateg. Rev.* **2020**, *29*, 100494.
- (7) Hagfeldt, A.; Boschloo, G.; Sun, L.; Kloo, L.; Pettersson, H. Dye-Sensitized Solar Cells. *Chem. Rev.* **2010**, *110* (11), 6595–6663.
- (8) Ise, F. *Photovoltaics Report*; 2020.
- (9) Ehrler, B.; Alarcón-Lladó, E.; Tabernig, S. W.; Veeken, T.; Garnett, E. C.; Polman, A. Photovoltaics Reaching for the Shockley-Queisser Limit. *ACS Energy Lett.* **2020**, *5* (9), 3029–3033.
- (10) Tayebjee, M. J. Y.; McCamey, D. R.; Schmidt, T. W. Beyond Shockley–Queisser: Molecular Approaches to High-Efficiency Photovoltaics. *J. Phys. Chem. Lett.* **2015**, *6* (12), 2367–2378.
- (11) Zhao, C.; Wang, J.; Zhao, X.; Du, Z.; Yang, R.; Tang, J. Recent Advances, Challenges and Prospects in Ternary Organic Solar Cells. *Nanoscale* **2021**, 2181–2208.
- (12) Duan, J.; Zhang, H.; Tang, Q.; He, B.; Yu, L. Recent Advances in Critical Materials for Quantum Dot-Sensitized Solar Cells: A Review. *J. Mater. Chem. A* **2015**, *3* (34), 17497–17510.
- (13) Massiot, I.; Cattoni, A.; Collin, S. Progress and Prospects for Ultrathin Solar Cells. *Nat. Energy* **2020**, *5* (12), 959–972.
- (14) Hagfeldt, A.; Vlachopoulos, N. Dye-Sensitized Solar Cells. In *The Future of Semiconductor Oxides in Next-Generation Solar Cells*; Elsevier, 2018; pp 183–239.
- (15) Hiramoto, M.; Izawa, S. *Organic Solar Cells*; Hiramoto, M., Izawa, S., Eds.; Springer Singapore: Singapore, 2021; Vol. 1.
- (16) European Commission. *A New Circular Economy Action Plan For a Cleaner and More Competitive Europe*; 2020.
- (17) O’Reagan, B.; Grätzel, M. A Low-Cost, High-Efficiency Solar Cell Based on Dye-Sensitized Colloidal TiO<sub>2</sub> Films. *Nature* **1991**, *353*, 737–740.

- (18) Kakiage, K.; Aoyama, Y.; Yano, T.; Oya, K.; Fujisawa, J.; Hanaya, M. Highly-Efficient Dye-Sensitized Solar Cells with Collaborative Sensitization by Silyl-Anchor and Carboxy-Anchor Dyes. *Chem. Commun.* **2015**, 51 (88), 15894–15897.
- (19) Huauilmé, Q.; Mwalukuku, V. M.; Joly, D.; Liotier, J.; Kervella, Y.; Maldivi, P.; Narbey, S.; Oswald, F.; Riquelme, A. J.; Anta, J. A.; Demadrille, R. Photochromic Dye-Sensitized Solar Cells with Light-Driven Adjustable Optical Transmission and Power Conversion Efficiency. *Nat. Energy* **2020**, 5 (June).
- (20) Michaels, H.; Rinderle, M.; Freitag, R.; Benesperi, I.; Edvinsson, T.; Socher, R.; Gagliardi, A.; Freitag, M. Dye-Sensitized Solar Cells under Ambient Light Powering Machine Learning: Towards Autonomous Smart Sensors for the Internet of Things. *Chem. Sci.* **2020**, 11 (11), 2895–2906.
- (21) Kalyanasundaram, K.; Hagfeldt, A.; Boschloo, G.; Sun, L.; Kloo, L.; Pettersson, H. Dye-Sensitized Solar Cells. *Chem. Rev.* **2010**, 110 (11), 6595–6663.
- (22) Bisquert, J. Hopping Transport of Electrons in Dye-Sensitized Solar Cells. *J. Phys. Chem. C* **2007**, 111 (46), 17163–17168.
- (23) Teuscher, J.; Marchioro, A.; Andrès, J.; Roch, L. M.; Xu, M.; Zakeeruddin, S. M.; Wang, P.; Grätzel, M.; Moser, J. E. Kinetics of the Regeneration by Iodide of Dye Sensitizers Adsorbed on Mesoporous Titania. *J. Phys. Chem. C* **2014**, 118 (30), 17108–17115.
- (24) Boschloo, G.; Hagfeldt, A. Characteristics of the Iodide/Triiodide Redox Mediator in Dye-Sensitized Solar Cells. *Acc. Chem. Res.* **2009**, 42 (11), 1819–1826.
- (25) Ito, S.; Liska, P.; Comte, P.; Charvet, R.; Péchy, P.; Bach, U.; Schmidt-Mende, L.; Zakeeruddin, S. M.; Kay, A.; Nazeeruddin, M. K.; Grätzel, M. Control of Dark Current in Photoelectrochemical (TiO<sub>2</sub>/I<sup>-</sup>/I<sub>3</sub><sup>-</sup>) and Dye-Sensitized Solar Cells. *Chem. Commun. (Camb)*. **2005**, No. 34, 4351–4353.
- (26) Sun, Z.; Liang, M.; Chen, J. Kinetics of Iodine-Free Redox Shuttles in Dye-Sensitized Solar Cells: Interfacial Recombination and Dye Regeneration. *Acc. Chem. Res.* **2015**, 48 (6), 1541–1550.
- (27) Moehl, T.; Tsao, H. N.; Wu, K.-L.; Hsu, H.-C.; Chi, Y.; Ronca, E.; De Angelis, F.; Nazeeruddin, M. K.; Grätzel, M. High Open-Circuit Voltages: Evidence for a Sensitizer-Induced TiO<sub>2</sub> Conduction Band Shift in Ru(II)-Dye Sensitized Solar Cells. *Chem. Mater.* **2013**, 25 (22), 4497–4502.
- (28) Vlachopoulos, N.; Zhang, J.; Hagfeldt, A. Dye-Sensitized Solar Cells: New Approaches with Organic Solid-State Hole Conductors. *Chim. Int. J. Chem.* **2015**, 69 (1), 41–51.
- (29) Kalyanasundaram, K. *Dye Sensitized Solar Cells*; 2003.
- (30) Aghazada, S.; Nazeeruddin, M. Ruthenium Complexes as Sensitizers in Dye-Sensitized Solar Cells. *Inorganics* **2018**, 6 (2), 52.
- (31) Mahmood, A. Triphenylamine Based Dyes for Dye Sensitized Solar Cells: A Review. *Sol. Energy* **2016**, 123, 127–144.
- (32) Vlachopoulos, N.; Hagfeldt, A.; Benesperi, I.; Freitag, M.; Hashmi, G.; Jia, G.; Wahyuono, R. A.; Plentz, J.; Dietzek, B. New Approaches in Component Design for Dye-Sensitized Solar Cells. *Sustain. Energy Fuels* **2021**, 5 (2), 367–383.
- (33) Iftikhar, H.; Sonai, G. G.; Hashmi, S. G.; Nogueira, A. F.; Lund, P. D. Progress on Electrolytes Development in Dye-Sensitized Solar Cells. *Materials (Basel)*. **2019**, 12 (12), 1998.
- (34) Wu, J.; Lan, Z.; Lin, J.; Huang, M.; Huang, Y.; Fan, L.; Luo, G. Electrolytes in Dye-Sensitized Solar Cells. *Chem. Rev.* **2015**, 115 (5), 2136–2173.
- (35) Ellis, H.; Vlachopoulos, N.; Häggman, L.; Perruchot, C.; Jouini, M.; Boschloo, G.; Hagfeldt, A. PEDOT Counter Electrodes for Dye-Sensitized Solar Cells Prepared by Aqueous Micellar Electrodeposition. *Electrochim. Acta*

**2013**, 107, 45–51.

- (36) Kavan, L.; Yum, J.-H.; Nazeeruddin, M. K.; Grätzel, M. Graphene Nanoplatelet Cathode For. *ACS Nano* **2011**, 5 (11), 9171–9178.
- (37) Chen, M.; Shao, L. L. Review on the Recent Progress of Carbon Counter Electrodes for Dye-Sensitized Solar Cells. *Chem. Eng. J.* **2016**, 304, 629–645.
- (38) Mariotti, N.; Bonomo, M.; Fagiolari, L.; Barbero, N.; Gerbaldi, C.; Bella, F.; Barolo, C. Recent Advances in Eco-Friendly and Cost-Effective Materials towards Sustainable Dye-Sensitized Solar Cells. *Green Chem.* **2020**.
- (39) Stergiopoulos, T.; Falaras, P. Minimizing Energy Losses in Dye-Sensitized Solar Cells Using Coordination Compounds as Alternative Redox Mediators Coupled with Appropriate Organic Dyes. *Adv. Energy Mater.* **2012**, 2 (5), 616–627.
- (40) Saygili, Y.; Stojanovic, M.; Flores-Díaz, N.; Zakeeruddin, S. M.; Vlachopoulos, N.; Grätzel, M.; Hagfeldt, A. *Metal Coordination Complexes as Redox Mediators in Regenerative Dye-Sensitized Solar Cells*; 2019; Vol. 7.
- (41) Bisquert, J.; Zaban, A.; Greenshtein, M.; Mora-Seró, I. Determination of Rate Constants for Charge Transfer and the Distribution of Semiconductor and Electrolyte Electronic Energy Levels in Dye-Sensitized Solar Cells by Open-Circuit... *J. Am. Chem. Soc.* **2004**, 126 (41), 13550–13559.
- (42) Feldt, S. M.; Lohse, P. W.; Kessler, F.; Nazeeruddin, M. K.; Grätzel, M.; Boschloo, G.; Hagfeldt, A. Regeneration and Recombination Kinetics in Cobalt Polypyridine Based Dye-Sensitized Solar Cells, Explained Using Marcus Theory. *Phys. Chem. Chem. Phys.* **2013**, 15 (19), 7087.
- (43) Grampp, G. The Marcus Inverted Region from Theory to Experiment. *Angew. Chemie Int. Ed. English* **1993**, 32 (5), 691–693.
- (44) Rosso, K. M.; Rustad, J. R. Ab Initio Calculation of Homogeneous Outer Sphere Electron Transfer Rates: Application to  $M(OH_2)6^{3+/2+}$  Redox Couples. *J. Phys. Chem. A* **2000**, 104 (29), 6718–6725.
- (45) Feldt, S. M.; Wang, G.; Boschloo, G.; Hagfeldt, A. Effects of Driving Forces for Recombination and Regeneration on the Photovoltaic Performance of Dye-Sensitized Solar Cells Using Cobalt Polypyridine Redox Couples. *J. Phys. Chem. C* **2011**, 115 (43), 21500–21507.
- (46) Tress, W. *Organic Solar Cells*; 2014; Vol. 208.
- (47) Pootrakulchote, N. Investigation on Functionalized Ruthenium-Based Sensitizers to Enhance Performance and Robustness of Dye-Sensitized Solar Cells, ÉCOLE POLYTECHNIQUE FÉDÉRAL DE LAUSANNE, 2012, Vol. 5376.
- (48) Fabregat-Santiago, F.; Garcia-Belmonte, G.; Mora-Seró, I.; Bisquert, J. Characterization of Nanostructured Hybrid and Organic Solar Cells by Impedance Spectroscopy. *Phys. Chem. Chem. Phys.* **2011**, 13 (20), 9083.
- (49) Ronca, E.; Pastore, M.; Belpassi, L.; Tarantelli, F.; De Angelis, F. Influence of the Dye Molecular Structure on the  $TiO_2$  Conduction Band in Dye-Sensitized Solar Cells: Disentangling Charge Transfer and Electrostatic Effects. *Energy Environ. Sci.* **2013**, 6 (1), 183–193.
- (50) Grätzel, M.; Hara, K.; Arakawa, H.; DssC, C.; Grätzel, M. Dye-Sensitized Solar Cells. *J. Photochem. Photobiol. C Photochem. Rev.* **2003**, 4 (2), 145–153.
- (51) Krishnan Rajeshwar. Fundamentals of Semiconductor Electrochemistry and Photoelectrochemistry. In *Encyclopedia of Electrochemistry*; Wiley, 2002.
- (52) Trasatti, S. INTERNATIONAL UNION OF PURE AND APPLIED CHEMISTRY COMMISSION ON ELECTROCHEMISTRY \* THE ABSOLUTE ELECTRODE POTENTIAL : AN EXPLANATORY NOTE. *Pure Appl. Chem.* **1986**, 58 (7), 955–966.
- (53) Hagfeldt, A.; Cappel, U. B.; Boschloo, G.; Sun, L. *Dye-Sensitized Photoelectrochemical Cells*, Second Edi.; Elsevier Ltd, 2012.



- (54) Pazoki, M.; Cappel, U. B.; Johansson, E. M. J.; Hagfeldt, A.; Boschloo, G. Characterization Techniques for Dye-Sensitized Solar Cells. *Energy Environ. Sci.* **2017**, *10* (3), 672–709.
- (55) Berera, R.; van Grondelle, R.; Kennis, J. T. M. Ultrafast Transient Absorption Spectroscopy: Principles and Application to Photosynthetic Systems. *Photosynth. Res.* **2009**, *101* (2–3), 105–118.
- (56) Elgrishi, N.; Rountree, K. J.; McCarthy, B. D.; Rountree, E. S.; Eisenhart, T. T.; Dempsey, J. L. A Practical Beginner's Guide to Cyclic Voltammetry. *J. Chem. Educ.* **2018**, *95* (2), 197–206.
- (57) Memming, R. *Semiconductor Electrochemistry*; Wiley-VCH: Weinheim, Germany, 2001.
- (58) Kalyanasundaram, K. *Dye-Sensitized Solar Cells*, First.; EPFL Press: Lausanne, Switzerland, 2010.
- (59) Bisquert, J.; Grätzel, M.; Wang, Q.; Fabregat-Santiago, F. Three-Channel Transmission Line Impedance Model for Mesoscopic Oxide Electrodes Functionalized with a Conductive Coating. *J. Phys. Chem. B* **2006**, *110* (23), 11284–11290.
- (60) Bisquert, J. Theory of the Impedance of Charge Transfer via Surface States in Dye-Sensitized Solar Cells. *J. Electroanal. Chem.* **2010**, *646* (1–2), 43–51.
- (61) Fabregat-Santiago, F.; Bisquert, J.; Garcia-Belmonte, G.; Boschloo, G.; Hagfeldt, A. Influence of Electrolyte in Transport and Recombination in Dye-Sensitized Solar Cells Studied by Impedance Spectroscopy. *Sol. Energy Mater. Sol. Cells* **2005**, *87* (1–4), 117–131.
- (62) Bisquert, J.; Fabregat-Santiago, F.; Mora-Seró, I.; Garcia-Belmonte, G.; Barea, E. M.; Palomares, E. A Review of Recent Results on Electrochemical Determination of the Density of Electronic States of Nanostructured Metal-Oxide Semiconductors and Organic Hole Conductors. *Inorganica Chim. Acta* **2008**, *361* (3), 684–698.
- (63) Mora-sero, I.; Bisquert, J. Fermi Level of Surface States in TiO<sub>2</sub> Nanoparticles. *Nano Lett.* **2003**, *3* (7), 945–949.
- (64) Wang, Q.; Moser, J.-E.; Grätzel, M. Electrochemical Impedance Spectroscopic Analysis of Dye-Sensitized Solar Cells. *J. Phys. Chem. B* **2005**, *109* (31), 14945–14953.
- (65) Sharma, K.; Sharma, V.; Sharma, S. S. Dye-Sensitized Solar Cells: Fundamentals and Current Status. *Nanoscale Res. Lett.* **2018**, *13* (1), 381.
- (66) Bentley, C. L.; Bond, A. M.; Hollenkamp, A. F.; Mahon, P. J.; Zhang, J. Voltammetric Determination of the Iodide/Iodine Formal Potential and Triiodide Stability Constant in Conventional and Ionic Liquid Media. *J. Phys. Chem. C* **2015**, *119* (39), 22392–22403.
- (67) Snaith, H. J. Estimating the Maximum Attainable Efficiency in Dye-Sensitized Solar Cells. *Adv. Funct. Mater.* **2010**, *20* (1), 13–19.
- (68) Sauvage, F. A Review on Current Status of Stability and Knowledge on Liquid Electrolyte-Based Dye-Sensitized Solar Cells. *Adv. Chem.* **2014**, *2014*, 1–23.
- (69) Clifford, J. N.; Palomares, E.; Nazeeruddin, M. K.; Grätzel, M.; Nelson, J.; Li, X.; Long, N. J.; Durrant, J. R. Molecular Control of Recombination Dynamics in Dye-Sensitized Nanocrystalline TiO<sub>2</sub> Films: Free Energy vs Distance Dependence. *J. Am. Chem. Soc.* **2004**, *126* (16), 5225–5233.
- (70) Stojanović, M.; Flores-Diaz, N.; Ren, Y.; Vlachopoulos, N.; Pfeifer, L.; Shen, Z.; Liu, Y.; Zakeeruddin, S. M.; Milić, J. V.; Hagfeldt, A. The Rise of Dye-Sensitized Solar Cells: From Molecular Photovoltaics to Emerging Solid-State Photovoltaic Technologies. *Helv. Chim. Acta* **2021**, hlca.202000230.
- (71) Góes, M. S.; Joanni, E.; Muniz, E. C.; Savu, R.; Habeck, T. R.; Bueno, P. R.; Fabregat-Santiago, F. Impedance Spectroscopy Analysis of the Effect of TiO<sub>2</sub> Blocking Layers on the Efficiency of Dye Sensitized Solar Cells. *J. Phys. Chem. C* **2012**, *116* (23), 12415–12421.
- (72) Cameron, P. J.; Peter, L. M. Characterization of Titanium Dioxide Blocking Layers in Dye-Sensitized Nanocrystalline Solar Cells. *J. Phys. Chem. B* **2003**, *107* (51), 14394–14400.

- 
- (73) Chen, C. Y.; Wang, M.; Li, J. Y.; Pootrakulchote, N.; Alibabaei, L.; Ngoc-Le, C. H.; Decoppet, J. D.; Tsai, J. H.; Grätzel, C.; Wu, C. G.; Zakeeruddin, S. M.; Grätzel, M. Highly Efficient Light-Harvesting Ruthenium Sensitizer for Thin-Film Dye-Sensitized Solar Cells. *ACS Nano* **2009**, *3* (10), 3103–3109.
- (74) Yu, Q.; Wang, Y.; Yi, Z.; Zu, N.; Zhang, J.; Zhang, M.; Wang, P. High-Efficiency Dye-Sensitized Solar Cells: The Influence of Lithium Ions on Exciton Dissociation, Charge Recombination, and Surface States. *ACS Nano* **2010**, *4* (10), 6032–6038.
- (75) Wang, P.; Yang, L.; Wu, H.; Cao, Y.; Zhang, J.; Xu, N.; Chen, S.; Decoppet, J.-D.; Zakeeruddin, S. M.; Grätzel, M. Stable and Efficient Organic Dye-Sensitized Solar Cell Based on Ionic Liquid Electrolyte. *Joule* **2018**, *2* (10), 2145–2153.
- (76) Tuikka, M.; Hirva, P.; Rissanen, K.; Korppi-Tommola, J.; Haukka, M. Halogen Bonding—a Key Step in Charge Recombination of the Dye-Sensitized Solar Cell. *Chem. Commun.* **2011**, *47* (15), 4499–4501.
- (77) Bella, F.; Sacco, A.; Massaglia, G.; Chiodoni, A.; Pirri, C. F.; Quaglio, M. Dispelling Clichés at the Nanoscale: The True Effect of Polymer Electrolytes on the Performance of Dye-Sensitized Solar Cells. *Nanoscale* **2015**, *7* (28), 12010–12017.
- (78) Saygili, Y.; Stojanovic, M.; Flores-Díaz, N.; Zakeeruddin, S. M.; Vlachopoulos, N.; Grätzel, M.; Hagfeldt, A. Metal Coordination Complexes as Redox Mediators in Regenerative Dye-Sensitized Solar Cells. *Inorganics* **2019**, *7* (3), 30.
- (79) Bella, F.; Galliano, S.; Gerbaldi, C.; Viscardi, G. Cobalt-Based Electrolytes for Dye-Sensitized Solar Cells: Recent Advances towards Stable Devices. *Energies* **2016**, *9* (5), 384.
- (80) Mosconi, E.; Yum, J. H.; Kessler, F.; Gómez García, C. J.; Zuccaccia, C.; Cinti, A.; Nazeeruddin, M. K.; Grätzel, M.; De Angelis, F. Cobalt Electrolyte/Dye Interactions in Dye-Sensitized Solar Cells: A Combined Computational and Experimental Study. *J. Am. Chem. Soc.* **2012**, *134* (47), 19438–19453.
- (81) De Angelis, F. Modeling Materials and Processes in Hybrid/Organic Photovoltaics: From Dye-Sensitized to Perovskite Solar Cells. *Acc. Chem. Res.* **2014**, *47* (11), 3349–3360.
- (82) Feldt, S. M.; Lohse, P. W.; Kessler, F.; Nazeeruddin, M. K.; Grätzel, M.; Boschloo, G.; Hagfeldt, A. Regeneration and Recombination Kinetics in Cobalt Polypyridine Based Dye-Sensitized Solar Cells, Explained Using Marcus Theory. *Phys. Chem. Chem. Phys.* **2013**, *15* (19), 7087.
- (83) Ørnsø, K. B.; Jónsson, E. O.; Jacobsen, K. W.; Thygesen, K. S. Importance of the Reorganization Energy Barrier in Computational Design of Porphyrin-Based Solar Cells with Cobalt-Based Redox Mediators. *J. Phys. Chem. C* **2015**, *119* (23), 12792–12800.
- (84) Feldt, S. M.; Wang, G.; Boschloo, G.; Hagfeldt, A. Effects of Driving Forces for Recombination and Regeneration on the Photovoltaic Performance of Dye-Sensitized Solar Cells Using Cobalt Polypyridine Redox Couples. *J. Phys. Chem. C* **2011**, *115* (43), 21500–21507.
- (85) Yum, J.-H.; Baranoff, E.; Kessler, F.; Moehl, T.; Ahmad, S.; Bessho, T.; Marchioro, A.; Ghadiri, E.; Moser, J.-E.; Yi, C.; Nazeeruddin, M. K.; Grätzel, M. A Cobalt Complex Redox Shuttle for Dye-Sensitized Solar Cells with High Open-Circuit Potentials. *Nat. Commun.* **2012**, *3* (1), 631.
- (86) Yella, A.; Lee, H.-W.; Tsao, H. N.; Yi, C.; Chandiran, A. K.; Nazeeruddin, M. K.; Diau, E. W.-G.; Yeh, C.-Y.; Zakeeruddin, S. M.; Grätzel, M. Porphyrin-Sensitized Solar Cells with Cobalt (II/III)-Based Redox Electrolyte Exceed 12 Percent Efficiency. *Science* **2011**, *334* (6056), 629–634.
- (87) Mathew, S.; Yella, A.; Gao, P.; Humphry-Baker, R.; Curchod, B. F. E.; Ashari-Astani, N.; Tavernelli, I.; Rothlisberger, U.; Nazeeruddin, M. K.; Grätzel, M. Dye-Sensitized Solar Cells with 13% Efficiency Achieved through the Molecular Engineering of Porphyrin Sensitizers. *Nat. Chem.* **2014**, *6* (3), 242–247.
- (88) Colombo, A.; Dragonetti, C.; Roberto, D.; Fagnani, F. Copper Complexes as Alternative Redox Mediators in Dye-Sensitized Solar Cells. *Molecules* **2021**, *26* (1), 194.

- (89) Fürer, S. O.; Milhuisen, R. A.; Kashif, M. K.; Raga, S. R.; Acharya, S. S.; Forsyth, C.; Liu, M.; Frazer, L.; Duffy, N. W.; Ohlin, C. A.; Funston, A. M.; Tachibana, Y.; Bach, U. The Performance-Determining Role of Lewis Bases in Dye-Sensitized Solar Cells Employing Copper-Bisphenanthroline Redox Mediators. *Adv. Energy Mater.* **2020**, *10* (37), 1–13.
- (90) Cao, Y.; Liu, Y.; Zakeeruddin, S. M.; Hagfeldt, A.; Grätzel, M. Direct Contact of Selective Charge Extraction Layers Enables High-Efficiency Molecular Photovoltaics. *Joule* **2018**, *2* (6), 1108–1117.
- (91) Mathew, S.; Yella, A.; Gao, P.; Humphry-Baker, R.; Curchod, B. F. E.; Ashari-Astani, N.; Tavernelli, I.; Rothlisberger, U.; Nazeeruddin, M. K.; Grätzel, M. Dye-Sensitized Solar Cells with 13% Efficiency Achieved through the Molecular Engineering of Porphyrin Sensitizers. *Nat. Chem.* **2014**, *6* (3), 242–247.
- (92) Yella, A.; Lee, H.-W.; Tsao, H. N.; Yi, C.; Chandiran, A. K.; Nazeeruddin, M. K. M. K.; Diau, E. W.-G.; Yeh, C.-Y.; Zakeeruddin, S. M.; Grätzel, M.; Grätzel, M.; Grätzel, M. Porphyrin-Sensitized Solar Cells with Cobalt (II/III)-Based Redox Electrolyte Exceed 12 Percent Efficiency. *Science* **2011**, *334* (6056), 629–634.
- (93) Liu, Y.; Jennings, J. R.; Huang, Y.; Wang, Q.; Zakeeruddin, S. M.; Grätzel, M. Cobalt Redox Mediators for Ruthenium-Based Dye-Sensitized Solar Cells: A Combined Impedance Spectroscopy and near-IR Transmittance Study. *J. Phys. Chem. C* **2011**, *115* (38), 18847–18855.
- (94) Kato, F.; Hayashi, N.; Murakami, T.; Okumura, C.; Oyaizu, K.; Nishide, H. Nitroxide Radicals for Highly Efficient Redox Mediation in Dye-Sensitized Solar Cells. *Chem. Lett.* **2010**, *39* (5), 464–465.
- (95) Zhang, Z.; Chen, P.; Murakami, T. N.; Zakeeruddin, S. M.; Grätzel, M. The 2,2,6,6-Tetramethyl-1-Piperidinyloxy Radical: An Efficient, Iodine-Free Redox Mediator for Dye-Sensitized Solar Cells. *Adv. Funct. Mater.* **2008**, *18* (2), 341–346.
- (96) Cong, J.; Hao, Y.; Boschloo, G.; Kloo, L. Electrolytes Based on TEMPO-Co Tandem Redox Systems Outperform Single Redox Systems in Dye-Sensitized Solar Cells. *ChemSusChem* **2015**, *8* (2), 264–268.
- (97) Hao, Y.; Yang, W.; Zhang, L.; Jiang, R.; Mijangos, E.; Saygili, Y.; Hammarström, L.; Hagfeldt, A.; Boschloo, G. A Small Electron Donor in Cobalt Complex Electrolyte Significantly Improves Efficiency in Dye-Sensitized Solar Cells. *Nat. Commun.* **2016**, *7*, 13934.
- (98) Yang, W.; Söderberg, M.; Eriksson, A. I. K.; Boschloo, G. Efficient Aqueous Dye-Sensitized Solar Cell Electrolytes Based on a TEMPO/TEMPO<sup>+</sup> Redox Couple. *RSC Adv.* **2015**, *5* (34), 26706–26709.
- (99) Kato, F.; Kikuchi, A.; Okuyama, T.; Oyaizu, K.; Nishide, H. Nitroxide Radicals as Highly Reactive Redox Mediators in Dye-Sensitized Solar Cells. *Angew. Chemie* **2012**, *124* (40), 10324–10327.
- (100) Shibuya, M.; Tomizawa, M.; Suzuki, I.; Iwabuchi, Y. 2-Azaadamantane N-Oxyl (AZADO) and 1-Me-AZADO: Highly Efficient Organocatalysts for Oxidation of Alcohols. *J. Am. Chem. Soc.* **2006**, *128* (26), 8412–8413.
- (101) Pavlishchuk, V. V.; Addison, A. W. Conversion Constants for Redox Potentials Measured versus Different Reference Electrodes in Acetonitrile Solutions at 25 °C. *Inorganica Chim. Acta* **2000**, *298* (1), 97–102.
- (102) Gabrielsson, E.; Ellis, H.; Feldt, S.; Tian, H.; Boschloo, G.; Hagfeldt, A.; Sun, L. Convergent/Divergent Synthesis of a Linker-Variied Series of Dyes for Dye-Sensitized Solar Cells Based on the D35 Donor. *Adv. Energy Mater.* **2013**, *3* (12), 1647–1656.
- (103) Zhang, X.; Xu, Y.; Giordano, F.; Schreier, M.; Pellet, N.; Hu, Y.; Yi, C.; Robertson, N.; Hua, J.; Zakeeruddin, S. M.; Tian, H.; Grätzel, M. Molecular Engineering of Potent Sensitizers for Very Efficient Light Harvesting in Thin-Film Solid-State Dye-Sensitized Solar Cells. *J. Am. Chem. Soc.* **2016**, *138* (34), 10742–10745.
- (104) Hao, Y.; Saygili, Y.; Cong, J.; Eriksson, A.; Yang, W.; Zhang, J.; Polanski, E.; Nonomura, K.; Zakeeruddin, S. M.; Grätzel, M.; Hagfeldt, A.; Boschloo, G. Novel Blue Organic Dye for Dye-Sensitized Solar Cells Achieving High Efficiency in Cobalt-Based Electrolytes and by Co-Sensitization. *ACS Appl. Mater. Interfaces* **2016**, *8* (48), 32797–32804.

- (105) Chen, M.; Shao, L.; Xia, Y.; Huang, Z.-Y.; Xu, D.-L.; Zhang, Z.-W.; Chang, Z.-X.; Pei, W.-J. Construction of Highly Catalytic Porous TiOPC Nanocomposite Counter Electrodes for Dye-Sensitized Solar Cells. *ACS Appl. Mater. Interfaces* **2016**, *8* (39), 26030–26040.
- (106) Feldt, S. M.; Gibson, E. a; Gabrielsson, E.; Sun, L.; Boschloo, G.; Hagfeldt, A. Design of Organic Dyes and Cobalt Polypyridine Redox Mediators for High-Efficiency Dye-Sensitized Solar Cells. *J. Am. Chem. Soc.* **2010**, *132* (46), 16714–16724.
- (107) Kavan, L.; Yum, J.-H.; Grätzel, M. Graphene Nanoplatelets Outperforming Platinum as the Electrocatalyst in Co-Bipyridine-Mediated Dye-Sensitized Solar Cells. *Nano Lett.* **2011**, *11* (12), 5501–5506.
- (108) Yang, W.; Vlachopoulos, N.; Hao, Y.; Hagfeldt, A.; Boschloo, G. Efficient Dye Regeneration at Low Driving Force Achieved in Triphenylamine Dye LEG4 and TEMPO Redox Mediator Based Dye-Sensitized Solar Cells. *Phys. Chem. Chem. Phys.* **2015**, *17* (24), 15868–15875.
- (109) Freitag, M.; Daniel, Q.; Pazoki, M.; Sveinbjörnsson, K.; Zhang, J.; Sun, L.; Hagfeldt, A.; Boschloo, G. High-Efficiency Dye-Sensitized Solar Cells with Molecular Copper Phenanthroline as Solid Hole Conductor. *Energy Environ. Sci.* **2015**, *8* (9), 2634–2637.
- (110) Freitag, M.; Giordano, F.; Yang, W.; Pazoki, M.; Hao, Y.; Zietz, B.; Grätzel, M.; Hagfeldt, A.; Boschloo, G. Copper Phenanthroline as a Fast and High-Performance Redox Mediator for Dye-Sensitized Solar Cells. *J. Phys. Chem. C* **2016**, *120* (18), 9595–9603.
- (111) Saygili, Y.; Söderberg, M.; Pellet, N.; Giordano, F.; Cao, Y.; Muñoz-García, A. B.; Zakeeruddin, S. M.; Vlachopoulos, N.; Pavone, M.; Boschloo, G.; Kavan, L.; Moser, J.-E.; Grätzel, M.; Hagfeldt, A.; Freitag, M. Copper Bipyridyl Redox Mediators for Dye-Sensitized Solar Cells with High Photovoltage. *J. Am. Chem. Soc.* **2016**, *138* (45), 15087–15096.
- (112) Cao, Y.; Saygili, Y.; Ummadisingu, A.; Teuscher, J.; Luo, J.; Pellet, N.; Giordano, F.; Zakeeruddin, S. M.; Moser, J.-E.; Freitag, M.; Hagfeldt, A.; Grätzel, M. 11% Efficiency Solid-State Dye-Sensitized Solar Cells with Copper(II/I) Hole Transport Materials. *Nat. Commun.* **2017**, *8*, 15390.
- (113) Bazàn, J. C.; Arvia, A. J. The Diffusion of Ferro- and Ferricyanide Ions in Aqueous Solutions of Sodium Hydroxide. *Electrochim. Acta* **1965**, *10* (December 1964), 1025–1032.
- (114) Bella, F.; Vlachopoulos, N.; Nonomura, K.; Zakeeruddin, S. M.; Grätzel, M.; Gerbaldi, C.; Hagfeldt, A. Direct Light-Induced Polymerization of Cobalt-Based Redox Shuttles: An Ultrafast Way towards Stable Dye-Sensitized Solar Cells. *Chem. Commun.* **2015**, *51* (91), 16308–16311.
- (115) Gao, C.; Yan, D. Hyperbranched Polymers: From Synthesis to Applications. *Prog. Polym. Sci.* **2004**, *29* (3), 183–275.
- (116) Hobzová, R.; Peter, J.; Sysel, P. Hyperbranched Polymers. *Chem. List.* **2008**, *102* (10), 906–913.
- (117) Crivello, J. V.; Reichmanis, E. Photopolymer Materials and Processes for Advanced Technologies. *Chem. Mater.* **2014**, *26* (1), 533–548.
- (118) Hoyle, C. E.; Lowe, A. B.; Bowman, C. N. Thiol-Click Chemistry: A Multifaceted Toolbox for Small Molecule and Polymer Synthesis. *Chem. Soc. Rev.* **2010**, *39* (4), 1355.
- (119) Kolb, H. C.; Finn, M. G.; Sharpless, K. B. Click Chemistry: Diverse Chemical Function from a Few Good Reactions. *Angew. Chemie - Int. Ed.* **2001**, *40* (11), 2004–2021.
- (120) Hoyle, C. E.; Lowe, A. B.; Bowman, C. N. Thiol-Click Chemistry: A Multifaceted Toolbox for Small Molecule and Polymer Synthesis. *Chem. Soc. Rev.* **2010**, *39* (4), 1355–1387.
- (121) Nakahara, H.; Yoon, S.-Y.; Nutt, S. Effect of an Additive to Polysiloxane-Based Electrolyte on Passive Film Formation on a Graphite Electrode. *J. Power Sources* **2006**, *158* (1), 600–607.

- (122) Yuasa, S.; Imoto, H.; Naka, K. Synthesis and Properties of Hyperbranched Polymers by Polymerization of an AB<sub>3</sub>-Type Incompletely Condensed Cage Silsesquioxane (IC-POSS) Monomer. *Polym. J.* **2018**, *50* (9), 879–887.
- (123) Kusuma, V. A.; Roth, E. A.; Clafshenkel, W. P.; Klara, S. S.; Zhou, X.; Venna, S. R.; Albenze, E.; Luebke, D. R.; Mauter, M. S.; Koepsel, R. R.; Russell, A. J.; Hopkinson, D.; Nulwala, H. B. Crosslinked Poly(Ethylene Oxide) Containing Siloxanes Fabricated through Thiol-Ene Photochemistry. *J. Polym. Sci. Part A Polym. Chem.* **2015**, *53* (13), 1548–1557.
- (124) Kwisnek, L.; Heinz, S.; Wiggins, J. S.; Nazarenko, S. Multifunctional Thiols as Additives in UV-Cured PEG-Diacrylate Membranes for CO<sub>2</sub> Separation. *J. Memb. Sci.* **2011**, *369* (1–2), 429–436.
- (125) Piedrahita, C.; Kusuma, V.; Nulwala, H. B.; Kyu, T. Highly Conductive, Flexible Polymer Electrolyte Membrane Based on Poly(Ethylene Glycol) Diacrylate-Co-Thiosiloxane Network. *Solid State Ionics* **2018**, *322* (April), 61–68.
- (126) Wang, F. M.; Hu, C. C.; Lo, S. C.; Wang, Y. Y.; Wan, C. C. The Investigation of Electrochemical Properties and Ionic Motion of Functionalized Copolymer Electrolytes Based on Polysiloxane. *Solid State Ionics* **2009**, *180* (4–5), 405–411.
- (127) Zuo, X.; Liu, X. M.; Cai, F.; Yang, H.; Shen, X. D.; Liu, G. A Novel All-Solid Electrolyte Based on a Co-Polymer of Poly-(Methoxy/ Hexadecyl-Poly(Ethylene Glycol) Methacrylate) for Lithium-Ion Cell. *J. Mater. Chem.* **2012**, *22* (41), 22265–22271.
- (128) Kusuma, V. A.; Roth, E. A.; Clafshenkel, W. P.; Klara, S. S.; Zhou, X.; Venna, S. R.; Albenze, E.; Luebke, D. R.; Mauter, M. S.; Koepsel, R. R.; Russell, A. J.; Hopkinson, D.; Nulwala, H. B. Crosslinked Poly(Ethylene Oxide) Containing Siloxanes Fabricated through Thiol-Ene Photochemistry. *J. Polym. Sci. Part A Polym. Chem.* **2015**, *53* (13), 1548–1557.
- (129) Piedrahita, C.; Kusuma, V.; Nulwala, H. B.; Kyu, T. Highly Conductive, Flexible Polymer Electrolyte Membrane Based on Poly(Ethylene Glycol) Diacrylate-Co-Thiosiloxane Network. *Solid State Ionics* **2018**, *322* (May), 61–68.
- (130) Zhang, W.; Yuan, C.; Guo, J.; Qiu, L.; Yan, F. Supramolecular Ionic Liquid Gels for Quasi-Solid-State Dye-Sensitized Solar Cells. *ACS Appl. Mater. Interfaces* **2014**, *6* (11), 8723–8728.
- (131) Ellis, H.; Vlachopoulos, N.; Haggman, L.; Perruchot, C.; Jouini, M.; Boschloo, G.; Hagfeldt, A. PEDOT Counter Electrodes for Dye-Sensitized Solar Cells Prepared by Aqueous Micellar Electrodeposition. *Electrochim. Acta* **2013**, *107*, 45–51.
- (132) Halme, J.; Vahermaa, P.; Miettunen, K.; Lund, P. Device Physics of Dye Solar Cells. *Adv. Mater.* **2010**, *22* (35), E210–34.
- (133) Bai, Y.; Xu, Y.; Wang, J.; Gao, M.; Zhu, J.; Rehman, W. ur. Electrochemically Prepared Poly(3,4-Ethylenedioxy-Thiophene)/Polypyrrole Films with Hollow Micro-/Nanohorn Arrays as High-Efficiency Counter Electrodes for Dye-Sensitized Solar Cells. *ChemElectroChem* **2016**, 1–9.
- (134) Kang, J. S.; Kim, J.; Kim, J. Y.; Lee, M. J.; Kang, J.; Son, Y. J.; Jeong, J.; Park, S. H.; Ko, M. J.; Sung, Y. E. Highly Efficient Bifacial Dye-Sensitized Solar Cells Employing Polymeric Counter Electrodes. *ACS Appl. Mater. Interfaces* **2018**, *10* (10), 8611–8620.
- (135) Masud; Kim, K. M.; Kim, H. K. Polymer Gel Electrolytes Based on PEG-Functionalized ABA Triblock Copolymers for Quasi-Solid-State Dye-Sensitized Solar Cells: Molecular Engineering and Key Factors. *ACS Appl. Mater. Interfaces* **2020**, *12* (37), 42067–42080.
- (136) Kumar Shah, D.; Son, Y. H.; Lee, H. R.; Shaheer Akhtar, M.; Kim, C. Y.; Yang, O. B. A Stable Gel Electrolyte Based on Poly Butyl Acrylate (PBA)-Co-Poly Acrylonitrile (PAN) for Solid-State Dye-Sensitized Solar Cells. *Chem. Phys. Lett.* **2020**, *754* (July), 137756.
- (137) Yella, A.; Mathew, S.; Aghazada, S.; Comte, P.; Grätzel, M.; Nazeeruddin, M. K. Dye-Sensitized Solar Cells Using Cobalt Electrolytes: The Influence of Porosity and Pore Size to Achieve High-Efficiency. *J. Mater. Chem. C* **2017**, *5* (11), 2833–2843.

- (138) Sarker, S.; Ahammad, A. J. S.; Seo, H. W.; Kim, D. M. Electrochemical Impedance Spectra of Dye-Sensitized Solar Cells: Fundamentals and Spreadsheet Calculation. *Int. J. Photoenergy* **2014**, 2014.
- (139) Venkatesan, S.; Liu, I. P.; Tseng Shan, C. M.; Teng, H.; Lee, Y. L. Highly Efficient Indoor Light Quasi-Solid-State Dye Sensitized Solar Cells Using Cobalt Polyethylene Oxide-Based Printable Electrolytes. *Chem. Eng. J.* **2020**, 394 (March), 124954.
- (140) Masud; Kim, K. M.; Kim, H. K. Polymer Gel Electrolytes Based on PEG-Functionalized ABA Triblock Copolymers for Quasi-Solid-State Dye-Sensitized Solar Cells: Molecular Engineering and Key Factors. *ACS Appl. Mater. Interfaces* **2020**, 12 (37), 42067–42080.
- (141) Michaels, H.; Rinderle, M.; Freitag, R.; Benesperi, I.; Edvinsson, T.; Socher, R.; Gagliardi, A.; Freitag, M. Dye-Sensitized Solar Cells under Ambient Light Powering Machine Learning: Towards Autonomous Smart Sensors for the Internet of Things. *Chem. Sci.* **2020**.
- (142) Khan, W. Z.; Rehman, M. H.; Zangoti, H. M.; Afzal, M. K.; Armi, N.; Salah, K. Industrial Internet of Things: Recent Advances, Enabling Technologies and Open Challenges. *Comput. Electr. Eng.* **2020**, 81, 106522.
- (143) Ren, Y.; Sun, D.; Cao, Y.; Tsao, H. N.; Yuan, Y.; Zakeeruddin, S. M.; Wang, P.; Grätzel, M. A Stable Blue Photosensitizer for Color Palette of Dye-Sensitized Solar Cells Reaching 12.6% Efficiency. *J. Am. Chem. Soc.* **2018**, 140 (7), 2405–2408.
- (144) Yao, Z.; Zhang, M.; Wu, H.; Yang, L.; Li, R.; Wang, P. Donor/Acceptor Indenoperylene Dye for Highly Efficient Organic Dye-Sensitized Solar Cells. *J. Am. Chem. Soc.* **2015**, 137 (11), 3799–3802.
- (145) Baumann, A.; Watson, J.; Delcamp, J. H. Robust, Scalable Synthesis of the Bulky Hagfeldt Donor for Dye-Sensitized Solar Cells. *ChemSusChem* **2020**, 13 (2), 283–286.
- (146) Aghazada, S.; Gao, P.; Yella, A.; Moehl, T.; Teuscher, J.; Moser, J. E.; Grätzel, M.; Nazeeruddin, M. K. Unraveling the Dual Character of Sulfur Atoms on Sensitizers in Dye-Sensitized Solar Cells. *ACS Appl. Mater. Interfaces* **2016**, 8 (40), 26827–26833.
- (147) Hao, Y.; Saygili, Y.; Cong, J.; Eriksson, A.; Yang, W.; Zhang, J.; Polanski, E.; Nonomura, K.; Zakeeruddin, S. M.; Grätzel, M.; Hagfeldt, A.; Boschloo, G. Novel Blue Organic Dye for Dye-Sensitized Solar Cells Achieving High Efficiency in Cobalt-Based Electrolytes and by Co-Sensitization. *ACS Appl. Mater. Interfaces* **2016**, 8 (48), 32797–32804.
- (148) Yum, J.-H.; Holcombe, T. W.; Kim, Y.; Rakstys, K.; Moehl, T.; Teuscher, J.; Delcamp, J. H.; Nazeeruddin, M. K.; Grätzel, M. Blue-Coloured Highly Efficient Dye-Sensitized Solar Cells by Implementing the Diketopyrrolopyrrole Chromophore. *Sci. Rep.* **2013**, 3 (1), 2446.
- (149) Zhang, W.; Wu, Y.; Bahng, H. W.; Cao, Y.; Yi, C.; Saygili, Y.; Luo, J.; Liu, Y.; Kavan, L.; Moser, J. E.; Hagfeldt, A.; Tian, H.; Zakeeruddin, S. M.; Zhu, W.; Grätzel, M. Comprehensive Control of Voltage Loss Enables 11.7% Efficient Solid-State Dye-Sensitized Solar Cells. *Energy Environ. Sci.* **2018**, 10 (i), 8–10.
- (150) Yella, A.; Lee, H.-W.; Tsao, H. N.; Yi, C.; Chandiran, A. K.; Nazeeruddin, M. K. M. K.; Diau, E. W.-G.; Yeh, C.-Y.; Zakeeruddin, S. M.; Grätzel, M.; Grätzel, M.; Grätzel, M. Porphyrin-Sensitized Solar Cells with Cobalt (II/III)-Based Redox Electrolyte Exceed 12 Percent Efficiency. *Science* **2011**, 334 (6056), 629–634.
- (151) Zhang, L.; Cole, J. M. Dye Aggregation in Dye-Sensitized Solar Cells. *J. Mater. Chem. A* **2017**, 5 (37), 19541–19559.
- (152) Marinado, T.; Nonomura, K.; Nissfolk, J.; Karlsson, M. K.; Hagberg, D. P.; Sun, L.; Mori, S.; Hagfeldt, A. How the Nature of Triphenylamine-Polyene Dyes in Dye-Sensitized Solar Cells Affects the Open-Circuit Voltage and Electron Lifetimes. *Langmuir* **2010**, 26 (4), 2592–2598.
- (153) Freitag, M.; Daniel, Q.; Pazoki, M.; Sveinbjörnsson, K.; Zhang, J.; Sun, L.; Hagfeldt, A.; Boschloo, G. High-Efficiency Dye-Sensitized Solar Cells with Molecular Copper Phenanthroline as Solid Hole Conductor. *Energy Environ. Sci.* **2015**, 8 (9), 2634–2637.

- (154) Saygili, Y.; Söderberg, M.; Pellet, N.; Giordano, F.; Cao, Y.; Muñoz-García, A. B.; Zakeeruddin, S. M.; Vlachopoulos, N.; Pavone, M.; Boschloo, G.; Kavan, L.; Moser, J.-E.; Grätzel, M.; Hagfeldt, A.; Freitag, M. Copper Bipyridyl Redox Mediators for Dye-Sensitized Solar Cells with High Photovoltage. *J. Am. Chem. Soc.* **2016**, *138* (45), 15087–15096.
- (155) Freitag, M.; Teuscher, J.; Saygili, Y.; Zhang, X.; Giordano, F.; Liska, P.; Hua, J.; Zakeeruddin, S. M.; Moser, J.-E.; Grätzel, M.; Hagfeldt, A. Dye-Sensitized Solar Cells for Efficient Power Generation under Ambient Lighting. *Nat. Photonics* **2017**, *11* (6), 372–378.
- (156) Benesperi, I.; Michaels, H.; Freitag, M. The Researcher's Guide to Solid-State Dye-Sensitized Solar Cells. *J. Mater. Chem. C* **2018**, *6* (44), 11903–11942.
- (157) Zhang, X.; Xu, Y.; Giordano, F.; Schreier, M.; Pellet, N.; Hu, Y.; Yi, C.; Robertson, N.; Hua, J.; Zakeeruddin, S. M.; Tian, H.; Grätzel, M. Molecular Engineering of Potent Sensitizers for Very Efficient Light Harvesting in Thin-Film Solid-State Dye-Sensitized Solar Cells. *J. Am. Chem. Soc.* **2016**, *138* (34), 10742–10745.
- (158) Cao, Y.; Saygili, Y.; Ummadisingu, A.; Teuscher, J.; Luo, J.; Pellet, N.; Giordano, F.; Zakeeruddin, S. M.; Moser, J. E.; Freitag, M.; Hagfeldt, A.; Grätzel, M. 11% Efficiency Solid-State Dye-Sensitized Solar Cells with Copper(II/I) Hole Transport Materials. *Nat. Commun.* **2017**, *8*, 1–8.
- (159) Saygili, Y.; Stojanovic, M.; Kim, H. S.; Teuscher, J.; Scopelliti, R.; Freitag, M.; Zakeeruddin, S. M.; Moser, J. E.; Grätzel, M.; Hagfeldt, A. Liquid State and Zombie Dye Sensitized Solar Cells with Copper Bipyridine Complexes Functionalized with Alkoxy Groups. *J. Phys. Chem. C* **2020**, *124* (13), 7071–7081.
- (160) He, S.; Qiu, L.; Son, D.-Y.; Liu, Z.; Juarez-Perez, E. J.; Ono, L. K.; Stecker, C.; Qi, Y. Carbon-Based Electrode Engineering Boosts the Efficiency of All Low-Temperature-Processed Perovskite Solar Cells. *ACS Energy Lett.* **2019**, *4* (9), 2032–2039.
- (161) Liu, S.; Huang, W.; Liao, P.; Pootrakulchote, N.; Li, H.; Lu, J.; Li, J.; Huang, F.; Shai, X.; Zhao, X.; Shen, Y.; Cheng, Y. B.; Wang, M. 17% Efficient Printable Mesoscopic PIN Metal Oxide Framework Perovskite Solar Cells Using Cesium-Containing Triple Cation Perovskite. *J. Mater. Chem. A* **2017**, *5* (44), 22952–22958.
- (162) Aitola, K.; Sveinbjörnsson, K.; Correa-Baena, J. P.; Kaskela, A.; Abate, A.; Tian, Y.; Johansson, E. M. J.; Grätzel, M.; Kauppinen, E. I.; Hagfeldt, A.; Boschloo, G. Carbon Nanotube-Based Hybrid Hole-Transporting Material and Selective Contact for High Efficiency Perovskite Solar Cells. *Energy Environ. Sci.* **2016**, *9* (2), 461–466.
- (163) Li, G. R.; Gao, X. P. Low-Cost Counter-Electrode Materials for Dye-Sensitized and Perovskite Solar Cells. *Adv. Mater.* **2020**, *32* (3), 1–20.
- (164) Li, G.; Gao, X. Low-Cost Counter-Electrode Materials for Dye-Sensitized and Perovskite Solar Cells. *Adv. Mater.* **2020**, *32* (3), 1806478.
- (165) Mariani, P.; Vesce, L.; Di Carlo, A. The Role of Printing Techniques for Large-Area Dye Sensitized Solar Cells. *Semicond. Sci. Technol.* **2015**, *30* (10), 104003.
- (166) Babu, V.; Fuentes Pineda, R.; Ahmad, T.; Alvarez, A. O.; Castriotta, L. A.; Di Carlo, A.; Fabregat-Santiago, F.; Wojciechowski, K. Improved Stability of Inverted and Flexible Perovskite Solar Cells with Carbon Electrode. *ACS Appl. Energy Mater.* **2020**, *3* (6), 5126–5134.
- (167) Aftabuzzaman, M.; Lu, C.; Kim, H. K. Recent Progress on Nanostructured Carbon-Based Counter/Back Electrodes for High-Performance Dye-Sensitized and Perovskite Solar Cells. *Nanoscale* **2020**, *12* (34), 17590–17648.
- (168) Sánchez, S.; Vallés-Pelarda, M.; Alberola-Borràs, J. A.; Vidal, R.; Jerónimo-Rendón, J. J.; Saliba, M.; Boix, P. P.; Mora-Seró, I. Flash Infrared Annealing as a Cost-Effective and Low Environmental Impact Processing Method for Planar Perovskite Solar Cells. *Mater. Today* **2019**, *31* (December), 39–46.
- (169) Thompson, S. J.; Duffy, N. W.; Bach, U.; Cheng, Y. B. On the Role of the Spacer Layer in Monolithic Dye-Sensitized Solar Cells. *J. Phys. Chem. C* **2010**, *114* (5), 2365–2369.

- 
- (170) Renuka, L.; Anantharaju, K. S.; Sharma, S. C.; Nagabhushana, H.; Vidya, Y. S.; Nagaswarupa, H. P.; Prashantha, S. C. A Comparative Study on the Structural, Optical, Electrochemical and Photocatalytic Properties of ZrO<sub>2</sub>nanooxide Synthesized by Different Routes. *J. Alloys Compd.* **2017**, *695*, 382–395.
- (171) Han, H.; Bach, U.; Cheng, Y.-B.; Caruso, R. A.; MacRae, C. A Design for Monolithic All-Solid-State Dye-Sensitized Solar Cells with a Platinized Carbon Counterelectrode. *Appl. Phys. Lett.* **2009**, *94* (10), 103102.
- (172) Kokkonen, M.; Talebi, P.; Zhou, J.; Asgari, S.; Soomro, S. A.; Elsehrawy, F.; Halme, J.; Ahmad, S.; Hagfeldt, A.; Hashmi, S. G. Advanced Research Trends in Dye-Sensitized Solar Cells. *J. Mater. Chem. A* **2021**.
- (173) Santos, F.; Hora, C.; Bernardo, G.; Ivanou, D.; Mendes, A. Efficient Monolithic Dye Sensitized Solar Cells with Eco-Friendly Silica-Titania Spacer Layers. *Sol. Energy* **2019**, *183* (January), 419–424.



## Curriculum Vitae

---

### Personal information

---

Name : Natalie Flores Díaz Birth date :15/10/1988

ORCID: 0000-0002-3761-348X ResearcherID: AAX-4117-2020

Phone: +41 786290137 Email: [natalie.floresdiaz@epfl.ch](mailto:natalie.floresdiaz@epfl.ch), [nathy5815@gmail.com](mailto:nathy5815@gmail.com)

Work Address: EPFL SB ISIC LSPM, Station 6. CH-1015 Lausanne. Switzerland.

Home Address: Route Cantonale 37, Saint-Sulpice, 1025. Switzerland.

---

### Employment history

---

Spring semesters of 2019 and 2020. École Polytechnique Fédérale de Lausanne

Teaching assistant of the laboratory of Introduction to Chemical Engineering, ChE203, with the Prof. Kevin Sivula. (+41) 21 693 7979

Fall semester 2019. École Polytechnique Fédérale de Lausanne

Teaching assistant of the exercise sessions for the master course Heterogeneous reaction engineering, ChE403, with the Prof. Jeremy Luterbacher. (+41) 21 693 3114

Academic year 2016-2017. University of Costa Rica

Junior Assistant Professor of Theory and exercises session of the bachelor course Thermodynamics-I. University of Costa Rica, UCR. Supervisor Prof. Esteban Durán Herrera, (+506) 25116633.

Academic years 2009-2011. University of Costa Rica

Laboratory Assistant of General and Organic chemistry. Supervisor, Prof. Heilen Arce (+506) 25118520

---

### Education

---

**Ph.D. (Chemistry and Chemical Engineering). 23/02/2017 - 26/03/2021.**

École Polytechnique Fédérale de Lausanne, EPFL. Switzerland. Supervised by Prof. Anders Hagfeldt.

Dissertation entitled "Interphase engineering to minimize energetic losses in highly performing Dye Sensitized Solar Cells", defense date will take place 20/03/2021.

I am currently at the end of the doctoral program of Chemistry and Chemical Engineering (EDCH) at EPFL, with a duration of 4 years. Through these years I developed several skills, such as scientific writing, project management, teaching and mentoring students, Dye sensitized solar cells (DSC) and Perovskite Solar Cells (PSC) fabrication and device optimization. I learn several characterization techniques such as, IPCE, "toolbox", SEM, XRD, TAS, EIS, TRPL, among others. To date I have 3.2 years of research experience at the Laboratory of Photomolecular Science, LSPM. During my master's I spent one full year in research activities for the completion of my thesis at

the Research Center for Electrochemistry and Chemical Energy (CELEQ) at University of Costa Rica. Through these studies I developed several skills, such as organic synthesis of electroactive materials and characterization techniques, UV-vis, CV, NMR, IR and Raman spectroscopy, and basic solar cells characterization such as J-V. Combined, I have 4.2 years in academic research, and the private defence of my doctoral dissertation took place the 26/03/21, and the public defense on 07/05/2021 .

**M.Sc. (Chemistry). 10/03/2014 - 21/12/2016.**

University of Costa Rica, UCR. Costa Rica. Supervised by Prof. Leslie. W. Pineda.

Dissertation entitled "Synthesis of new organic redox systems: application on Dye Sensitized Solar Cells". Final mark:10/10

The degree date is issued on 06/10/2017. I moved to Switzerland for my Ph.D. studies and could not attend the official graduation at UCR in Costa Rica, and I had to process a graduation through the Embassy of Costa Rica in Switzerland. For this reason, the master degree was issued after the completion of the same, and the degree that allowed the Ph.D. is the Chemical Engineering Licentiate from 2014.

**Licentiate (Chemical Engineering) 06/03/2006 - 07/10/2012.**

University of Costa Rica. UCR. Supervised by Prof. Cindy Torres.

The degree comprises 4 years equivalent to a bachelor's in chemical engineering, 1 year of advanced courses, and a final graduation project of minimum 1.5 years. Dissertation entitled "Determination of the power conversion efficiency of Dye Sensitized Solar Cells sensitized with pigments obtained from natural extracts, microbiological processes and germanium nanoparticles". Final mark 10/10

---

**Publications**

---

- (1) **Flores-Díaz, N.**; Soto-Navarro, A.; Freitag, M.; Lamoureux, G.; Pineda, L. W. Neutral Organic Redox Pairs Based on Sterically Hindered Hydroquinone/Benzoquinone Derivatives for Dye-Sensitized Solar Cells. *Sol. Energy* 2018, 167 (January), 76–83. <https://doi.org/10.1016/j.solener.2018.03.084>.
- (2) **Flores-Díaz, N.**; Bahng, H.-W.; Vlachopoulos, N.; Moser, J.-E.; Zakeeruddin, S. M.; Grätzel, M.; Hagfeldt, A. A Tandem Redox System with a Cobalt Complex and 2-Azaadamantane- N -Oxyl for Fast Dye Regeneration and Open Circuit Voltages Exceeding 1 V. *J. Mater. Chem. A* 2019, 7 (18), 10998–11006. <https://doi.org/10.1039/C9TA00490D>.
- (3) Saygili, Y.; Stojanovic, M.; **Flores-Díaz, N.**; Zakeeruddin, S. M.; Vlachopoulos, N.; Grätzel, M.; Hagfeldt, A. Metal Coordination Complexes as Redox Mediators in Regenerative Dye-Sensitized Solar Cells; 2019; Vol. 7. <https://doi.org/10.3390/inorganics7030030>.
- (4) Molina, D.; Ruiz-Preciado, M. A.; Carlsen, B.; Eickemeyer, F. T.; Yang, B.; **Flores-Díaz, N.**; Álvaro-Martins, M. J.; Nonomura, K.; Hagfeldt, A.; Sastre-Santos, Á. Zinc Phthalocyanine Conjugated Dimers as Efficient Dopant-Free Hole Transporting Materials in Perovskite Solar Cells. *ChemPhotoChem* 2020, 4 (4), 307–314. <https://doi.org/10.1002/cptc.201900245>.
- (5) Ren, Y.; **Flores-Díaz, N.**; Zhang, D.; Cao, Y.; Decoppet, J.; Fish, G. C.; Moser, J.; Zakeeruddin, S. M.; Wang, P.; Hagfeldt, A.; Grätzel, M. Blue Photosensitizer with Copper(II/I) Redox Mediator for Efficient and Stable Dye-Sensitized Solar Cells. *Adv. Funct. Mater.* 2020, 30 (50), 2004804. <https://doi.org/10.1002/adfm.202004804>.

(6) Soto-Montero, T.; **Flores-Díaz, N.**; Molina, D.; Soto-Navarro, A.; Lizano-Villalobos, A.; Camacho, C.; Hagfeldt, A.; Pineda, L. W. Dopant-Free Hole-Transport Materials with Germanium Compounds Bearing Pseudohalide and Chalcogenide Moieties for Perovskite Solar Cells. *Inorg. Chem.* 2020, 59 (20), 15154–15166. <https://doi.org/10.1021/acs.inorgchem.0c02120>.

(7) Stojanovi, M.; **Flores-díaz, N.**; Ren, Y.; Vlachopoulos, N.; Pfeifer, L.; Liu, Y.; Zakeeruddin, S. M.; Milic, J.; Hagfeldt, A. The Rise of Dye-Sensitized Solar Cells : From Molecular Photovoltaics to Emerging Solid-State Photovoltaic Technologies Historical Development of DSSCs. *Helv. Chim. Acta* 2021, **Just accepted**.

#### Ready for submission:

**Flores-díaz, N.**; Sánchez-Alonso, S., Déccoppet, J.D., Zakeeruddin, S. M.; Grätzel, M.; Hagfeldt, A. Photopolymerization of hyperbranched networks by thiol-ene “click” reaction in cobalt-based electrolytes for Dye-Sensitized Solar Cells. On Manuscript.

Stojanovi, M.; Ren, Y.; **Flores-díaz, N.**, Ouellett, O., N.; Pfeifer, L.; Wei, M., Jing, F., Socie, E., Moser, J.-E.; Zakeeruddin, S. M.; Meng, S., Grätzel, M.; Hagfeldt, A. From benzo-thiadiazole to benzo-oxadiazole: the effect of atom substitution on two photosensitizers containing a dithienopyrrole  $\pi$ -bridge on the performances of dye solar cells with copper redox couple.

---

#### Conferences

---

Poster: “Photopolimerization of quasi-solid electrolytes by in-situ thiol-ene “click” reaction for stable cobalt-based electrolytes for DSSC”. 14/10/2019. Dyenamo DSSC Strikes on. Uppsala, Sweden.

Poster: “TEMPO electrolytes to enhance dye regeneration in dye sensitized solar cells”. 15/10/2017. Dyenamo DSSC Strikes back. Uppsala, Sweden.

Oral presentation: “Synthesis of new organic redox systems for dye sensitized solar cells”. 14/03/2016. Iberoamerican Electrochemistry Society, SIBAE San José, Costa Rica

Poster: “Photoelectrochemical properties of natural pigments for dye sensitized solar cells”. 14/03/2016. Iberoamerican Electrochemistry Society, SIBAE San José, Costa Rica

Poster: “Synthesis and modeling of new biomimetic redox systems, and their application in Dye Sensitized Solar Cells”. 04/05/2014. NanoGe Hybrid and Organic Photovoltaics. HOPV2014. Lausanne, Switzerland.

---

#### Workshops

---

22/09/2020 - 15/12/2020. Innosuisse Business concept training. École Polytechnique Fédérale de Lausanne.

22/04/2020. Dyenamo web-workshop No.2. Dye sensitized solar cells using Cu redox mediators

08/04/2020. Dyenamo web-Workshop No.1. Perovskite Solar Cells using paste DNCP-01

13/10/2019 Dyenamo workshop Dye sensitized solar cells fabrication. Uppsala, Sweden

05/05/2014 École Polytechnique Fédérale de Lausanne, HOPV Dye sensitized Solar Cells Workshop

07/01/2013-10/01/2013 University of Costa Rica. Nanofabrication Workshop

---

13/9/2011-10/12/2011 University of Costa Rica and Miravalles University Center. Professional Developing Program.

08/10/2011.University of Costa Rica. Team building towards productivity workshop.

---

### Supervision and Mentoring

---

During my Ph.D. studies at EPFL, I supervised the master student, Tatiana Soto Montero from 01.09.2018 to 20.12.2018 during her research stay at the Laboratory of Photomolecular Science, LSPM. I guided her through the assembly process of Perovskite Solar Cells (PSC) and the optimization of the deposition of her new Germanium-based HTM materials. I tutored her on basic characterization techniques such as J-V, IPCE, PL, and SEM imaging.

---

### Awards

---

The Network of Research and Development on Energetic Efficiency and Renewable Energy (RIDER) from University of Costa Rica, UCR, granted me a scholarship to fully complete the doctoral program of Chemistry and Chemical Engineering (EDCH) at École Polytechnique Fédérale de Lausanne, Switzerland. This scholarship aims to increase the knowledge exchange in the specific areas of energy efficiency and renewable energy deployment, and make technology transfer to the industry possible.

Recently awarded a Marie Skłodowska Curie Actions Fellowship for Early Postdoc career under the supervision of Prof. Marina Freitag in Newcastle University, starting from May 2021.

---

### Personal Skills

---

Language:

Native: Spanish

Second: English: Proficient, French: B2 level.

Academic Skills:

- **Networking:** Through the attendance of several conferences, I have learned to approach people to express my interest in possible collaborations and engage in scientific conversations.
- **Communication skills:** After several group-meeting presentations I have gain several valuable skills to engage the interest of the public and deliver a good presentation. From slides content-design and animations, to body language during the presentation, voice tone, confidence and openness to questions and criticism.
- **Leadership and management:** I have learned to supervise master students by offering as much help as needed while providing them with plenty of independence to develop their own ideas. I have also managed most of the projects I have worked during my Ph.D. studies, since experiment design, to materials purchase and decision making.
- **Writing:** I have learned to write scientific papers, reviews, and grant proposals.

**Research Skills:** design and implementation of experiments, responsible conduct with data management, meticulous attention during experimental work, proper statistical analysis for accurate interpretation of results, critical evaluation of literature.

Interpersonal skills:

- Teamwork abilities to collaborate with colleagues from multidisciplinary areas
- Enthusiasm and personal drive to engage in difficult tasks
- Initiative to propose new research projects, methods, approaches to existing problems, and to look for possible collaborations
- Management and organisational skills to propose activities in the research group
- Willingness to learn and resilience to adapt the actual work to new findings in science and to the work environment
- Positive manners to deal with conflicts in highly competitive environments